NEW METHOD FOR ESTIMATING LOCAL STRAINS USING NANOINDENTATION AND ATOMIC FORCE MICROSCOPY

By

SONY VARGHESE

Bachelor of Engineering in Mechanical Engineering
Basaveshwar Engineering College
Bagalkot, Karnataka, India
1996

Master of Engineering in Materials Engineering
Karnataka Regional Engineering College
Suratkal, Karnataka, India
1998

Submitted to the Faculty of the
Graduate College of the
Oklahoma State University
in partial fulfillment of
the requirements for
the Degree of
DOCTOR OF PHILOSOPHY
July, 2006

NEW METHOD FOR ESTIMATING LOCAL STRAINS

USING NANOINDENTATION AND ATOMIC

FORCE MICROSCOPY

Dissertation Approved:

Dr. Ranga Komanduri
Dissertation Adviser

Dr. Hongbing Lu

Dr. C. E. Price

Dr. Jay C. Hanan

Dr. Satish T.S. Bukkapatnam

Dr. A. Gordon Emslie
Dean of the Graduate College

PREFACE

Strain measurements have been an important part of engineering design since reliability of structures became an important criterion in design. Effects of strain on a structural part have played an important role in the design and testing of most components in use today. Depending on the size and scale of the source of strain, several methods of strain measurement have been developed.

One major application in which strain measurement is important is for the measurement of residual stress. Residual stresses, in general, are estimated by determining the strains that are associated with it. They may be categorized by cause (e.g. elastic or thermal mismatch), or by the scale over which the stresses exist or by the method by which they are estimated. Residual stresses are present widely in materials that have been subjected to some processing during their manufacture. Miniaturization in MEMS and similar technologies has seen problems due to strains from residual stresses that would be negligible in similar larger macro-mechanical systems. Increasing use of coatings, layered arrangements, and composites in structural components have also brought about the need for measuring strains in small regions.

Some common strain measurement techniques used in practice are strain gauges, X-ray diffraction, optical fiber sensors, Moire´ interferometry,

thermoelastic stress analysis (TSA), photoelasticity, and shearography. Even though these methods have been effective in estimating strains, there are some inherent problems associated with them. Most of these methods can be used to determine only average strains over an area and nanometer-scale strain measurements are difficult. Some of these methods are considered destructive and render the part unusable. The development of MEMS and even smaller systems, such as NEMS, has brought up the need for the measurement of strains due to residual stresses in very small areas. The effect of the magnitude of residual stresses become more pronounced as the scale gets smaller. Several researchers have attempted to use nanoindentation as a technique for measuring residual stresses.

Macro-, micro-, and nanoindenters can aid in measuring both short range and long range strains due to residual stresses at different size scales. It is a flexible tool for measuring local (short range) and volume averaged (long range) residual stresses. Estimation of strains in thin films and graded materials, where microstructure, composition, and properties vary spatially are possible. Since the indentation size is small, the method is almost nondestructive. This is similar to micro-scale indentation at macrolevel when the size of the indent does not affect its properties or performance.

Presently known methods of strain measurement using indentation, usually consider subtle differences in hardness and elastic modulus to get an estimate of the stresses. The hardness estimates are made by determining the load applied by the projected area of a residual indent. These methods are based

on estimating the projected areas of the residual indents using optical or scanning electron microscopes which made the method time consuming and somewhat error prone due to possible errors in calculating the projected area in presence of pile-up or sink-in. It was found that when compressive stresses were applied, the hardness measured was higher and when a tensile stress was applied the hardness measured was lower.

Even though several methods have been developed to estimate strains using nanoindentation, none of these methods have considered the effect of stresses on the shape of the residual indents. Moreover, the depths of nanoindents used to estimate stresses have been on the order of a few hundred nanometers. It is possible to perform nanoindentation using a diamond nanoindenter with an atomic force microscope (AFM). The AFM also has the added advantage of being able to image the surface before and after nanoindentation.

An attempt is made in this investigation to estimate strains associated with stresses at an intergranular (Type II) and transgranular (Type III) scale by investigating the change in shape of the residual nanoindents. *In-situ* atomic force microscopy of tensile experiments were conducted on polycrystalline copper samples to investigate their microscopic deformation behavior. An *in-situ* tensile testing setup, originally built for use inside a SEM, was adapted to perform tensile experiments under an AFM. The surface of the sample can be imaged or indented at various stages of tensile loading. Nanoindentations were performed on polycrystalline copper samples using an AFM nanoindenter at

various stages during the tensile test, to study the effect of local strains on the shape of the residual image of the nanoindent.

A method was developed to compare the residual images to estimate strains locally. It was seen that the shape of the residual indent was dependent on the orientation of the slip bands formed in individual grains. In order to determine the strains in a relatively large area, an array of nanoindentations were made on a polycrystalline copper sample using an MTS nanoindenter system (600 nm deep) and an AFM (75 nm deep indents) as markers to estimate strains locally when the sample is under tension. Strains were estimated by analyzing the relative displacements of the nanoindents with increasing tensile loads. The former indents were made on multiple grains while the latter was on an individual grain. Strains associated with the formation of a slip band were estimated by this technique. The strains estimated were validated using a digital image correlation method.

ACKNOWLEDGEMENTS

First and foremost I would like to thank my advisor, Dr. Ranga Komanduri, for his insight, guidance, advice and support during my research at the Oklahoma State University. Working with him has been a great pleasure and honor for me which will last me a whole lifetime. I would like to thank Dr. Hongbing Lu, Dr. C.E. Price, Dr. Jay C. Hanan, and Dr. Satish T.S. Bukkapatnam for their suggestions and for agreeing to serve on my thesis committee.

I am deeply indebted to my wife Ms. Neethu Abraham for her encouragement and support in all aspects of my life. I would like to acknowledge my parents, Mr. K. V. Varghese and Mrs. Mariamma Varghese and my wife's parents Mr. Thomas Abraham and Mrs. Molly Abraham for their support and encouragement. My thanks are also due to my brother Bony Varghese for his support. I would like to thank my friend Mr. Anil Raghavan for software related help. I would also like to thank my family and friends for the wonderful support I have had so far.

This project is sponsored by grants from the Micron Foundation (Dr. N. Chandrasekaran) and the Air Force Office of Scientific Research (AFOSR) – Dr. Craig S. Hartley, Dr. Jamie Tilley and Dr. Brett Conner Program Managers for the Metallic Materials Program(DEPSCoR grant No. F49620-03-1-0281).

Special thanks are also due to my colleagues at ATRC: Mr. Rutuparna Narulkar, Mr. Milind Malshe, Mr. Prahlad Rao, and Ms. Yang Liu. I would like to thank Dr. Jin Ma and Mr. Nitin Daphlapurkar for helping me with the MTS nanoindenter system. I would also like to thank all other colleagues, both former and present, at ATRC, with whom I have been fortunate to work with, during my stay at OSU.

Thanks are also due to Mr. Jerry Dale for his help during my research. I would like to thank Ms. Kyong Edwards, Ms. Sharon Green, Ms. Daleene Caldwell and other MAE staff for their help.

TABLE OF CONTENTS

LIST OF TABLES

LIST OF FIGURES

LIST OF SYMBOLS

AFM	Atomic Force Microscope
X	Transverse direction
Y	Longitudinal direction or tensile axis
Z	Vertical direction
FA	Front angle of AFM diamond indenter
BA	Back angle of AFM diamond indenter
SA	Side angle of AFM diamond indenter
H	Hardness of a material
a	Contact radius of the cylindrical punch i.e. contact radius of cone at maximum depth
h_t	Maximum depth of indentation and maximum load
P_t	Maximum load
h_r	Depth of residual impression
h_{rp}	Depth of residual impression for an equivalent punch
h_e	Elastic displacement after unloading
h_{ep}	Elastic displacement after unloading for an equivalent punch
h_a	Distance from the edge of the contact to the surface and maximum load

h_p	Depth of circle of contact measured from maximum depth h_t
E^*	Combined or reduced elastic modulus
h_p	Depth of circle of contact and maximum depth h_t
ε	Strain in a material
σ	Stress in a material
S	Elastic stiffness of contact
v	Poisson's ratio
P	Load applied on nanoindenter tip
A	Area of residual indent
LSCT	Linear shrinkage curve displacement transducer
UNS	Unified Numbering System for Metals and Alloys
DIC	Digital Image Correlation

CHAPTER 1

INTRODUCTION

Strain measurements have been an important part of engineering design since reliability of structures became a critical criterion in design. Effect of strain on a structural part have played an important role in the design and testing of most components in use these days. Strain is the deformation caused due to the action of stresses on a body. When stresses built up, due to release of geological strain in the earth's crust occur, earthquakes are caused. On the other extreme end of the size scale, the release of stresses due to strains in crystals results in the generation of dislocations and formation of slip. This gives us a fairly good idea of why strain measurements are important for engineers and geologists as well.

Depending on the size and scale of the strain source, several methods for strain measurement have been developed. Some common strain measurement techniques include strain gauges, X-ray diffraction, optical fiber sensors, Moire´ interferometry, thermoelastic stress analysis (TSA), photoelasticity, and shearography among several others.

One major application in which strain measurement is important is residual stress measurement. Residual stresses in general are estimated by determining the strains that are associated with it. They may be categorized by cause (e.g.

elastic or thermal mismatch), or by the scale over which the stresses exist or by the method by which they are estimated. These stresses can be classified as Type I (or macro-stresses) which vary continuously over large distances, Type II (or intergranular stresses) that vary over the grain scale and Type III which vary at the atomic scale.

Residual tensile stresses exist widely in materials that have been subjected to some processing during their manufacture. Equi-biaxial residual stresses exist in thin films and coatings on different substrates and mainly occur due to differences in the thermal expansion coefficients between the two materials. Other reasons for the existence of residual stresses in materials, include, non uniform cooling down from processing temperatures, mechanical shot peening, laser shot peening, bending or normal loading, mechanical working, or even phase transformations. Pre-existing residual tensile stresses often result in peeling and warping of coatings. Miniaturization in MEMS and similar technologies has experienced problems due to residual stresses that would probably be negligible in similar larger mechanical systems. Increasing use of coatings, layered arrangements, and composites in structural components have also brought about the need for measuring residual stresses.

Several residual stress measuring techniques have been developed over the years[1]. Some of the most common techniques used are the following.

1. X-ray and neutron diffraction
2. μ-Raman spectroscopy
3. Strain curvature measurements

4. Hole drilling
5. Layer removal
6. Optical fluorescence
7. Chemical etching
8. Nanoindentation

Some of these techniques have several limitations associated with them, including:

1. Measurement accuracy
2. Spatial resolution
3. Ease of measurement
4. Applicability to a broad range of materials and geometries
5. Feasibilty for use as a quality control device in mass production or during service
6. Flexibility for scaling-up from small to large components.
7. Mostly give an average measure of the residual stress.
8. Variation of residual stresses at different depths cannot be easily measured
9. Sub-micrometer stress measurements are difficult
10. Nanometer scale residual stress measurements are difficult.

The development of MEMS and even smaller systems (NEMS) has brought about the need for the measurement of strain in very small areas. The effect of the magnitudes of residual stresses become more pronounced as the scale gets smaller. Several researchers have attempted to use indentation as a

technique for measuring strains and thereby residual stresses [2-7]. Some of the advantages of using indentation for measuring strains and residual stresses are the following:

1. Macro-, micro-, and nanoindenters can facilitate in measuring short range and long range residual stresses at different size scales
2. Extraction of residual stresses in thin films
3. Flexible tool for measuring local (short range) and volume averaged (long range) residual stresses
4. Residual stress measurement for graded materials where microstructure, composition, and properties vary spatially
5. Non-destructive testing/evaluation

Though several researchers have used nanoindentation for strain and residual stress measurements [2-7], no account of the same have been found for nanoindentation using AFM. There are several advantages of using AFM for strain measurements, including:

1. Extremely localized measurements can be made
2. Area in which strain measurements are to be made can be selected and imaged before and after measurements
3. Measurements can be made at very low depths
4. Measurements can be made at different depths
5. Lower loads can be used, compared to commonly used nanoindentors
6. Smaller and sharper indenter – greater depths at lower loads

7. Multiple indents can be made on surfaces to determine average residual strain or make residual strain maps.

8. Local residual strains due to different phases can be measured.

In this investigation, AFM was used as a tool to determine local strains in very small areas. *In-situ* imaging of the surface is done as the tensile load is applied at different stages. Strains have been estimated by measuring the relative displacement of nanoindentations performed on the surface of a tensile specimen. Nanoindentations were also performed using a tetrahedral AFM diamond indenter and the influence of the applied load on the shape of the residual indent was investigated.

CHAPTER 2

LITERATURE REVIEW

2.1 Introduction

The main aim of this investigation is to develop a method to estimate strains in very small regions using residual images of nanoindents using atomic force microscopy. This investigation, therefore, involves the development of a strain measurement technique (nanoindentation) using AFM (*in-situ* examination of surface deformation) by examining a tensile specimen of a material (copper) that finds applications in areas where strains are encountered in very small regions (microelectronics) are of importance or critical to the functioning of the system. Keeping this in perspective, this literature review will concentrate on available literature on the measurement of strain in general, estimation of strain and residual stresses, application of indentation for the determination of strains and residual stresses, tensile testing of copper and study of *in-situ* surface deformation using atomic force microscope. A significant amount of literature exists on the topics listed here except for the application of indentation for the determination of strains and residual stresses and the study of *in-situ* surface deformation using AFM. This literature review covers these two topics in some detail compared to other topics.

2.2 Strain and residual stress measurement techniques

As mentioned in Chapter 1, several techniques have been developed over the years to determine strain in structures. Some common strain measurement techniques used in practice include strain gauges, X-ray diffraction, optical fiber sensors, Moire´ interferometry, thermoelastic stress analysis (TSA), photoelasticity and shearography. Since residual stresses are often determined from strains, a review of residual stress measurement techniques is also included in this document. A brief review of the capability and accuracy of these techniques is given in Table 2-1 (after Withers and Bhadeshia[1]).

The most common method used for estimating strains is the strain gauge or systems that use strain gauges. In general, strains gauges consist of a metallic foil pattern embedded in an insulating material. When a body to which the strain gauge is attached deforms, it causes the resistance of the metal in the strain gauge to change. This change in resistance of the strain gauge can be measured and calibrated so that the relative deformation in material can be estimated to determine the strains experienced by it.

Rather than looking for changes in electrical resistance, one can monitor stresses and strains by measuring the changes in the properties of light. This is the principle employed in fiber optic sensor strain measurement systems. The fiber optic sensor can be embedded into the material that it is monitoring, so that if the material is stretched or heated then the sensor would also experience the same too. When the shape of the sensor changes it alters the way the light

travels down the fiber. One can monitor how the light changes and use this information to estimate how the material is deformed.

Table 2-1: Summary of various residual stress measurement techniques[1]

Method	Penetration	Spatial resolution
Hole drilling (distortion caused by stress relaxation)	~1·2 × hole diameter	50 μm depth
Curvature (distortion as stresses arise or relax)	0·1 – 0·5 of thickness	0·05 of thickness; no lateral resolution
X-ray diffraction (atomic strain gauge)	<50 μm (Al); <5 μm (Ti); <1 mm (with layer removal)	1 mm laterally; 20 μm depth
Hard X-rays (atomic strain gauge)	150 – 50 mm (Al)	20 μm lateral to incident beam; 1 mm parallel to beam
Neutrons (atomic strain gauge)	200 mm (Al); 25 mm (Fe); 4 mm (Ti)	500 μm
Ultrasonics (stress related changes in elastic wave velocity)	>10 cm	30 μm
Magnetic (variations in magnetic domains with stress)	10 mm	1 mm
Raman	<1 μm	<1 μm approx.

Method	Accuracy	Comments
Hole drilling (distortion caused by stress relaxation)	±50 MPa, limited by reduced sensitivity with increasing depth	Measures in-plane type I stresses; semidestructive
Curvature (distortion as stresses arise or relax)	Limited by minimum measurable curvature	Unless used incrementally, stress field not uniquely determined; measures in-plane type I stresses
X-ray diffraction (atomic strain gauge)	±20 MPa, limited by non-linearities in $\sin^2\psi$ or surface condition	Non-destructive only as a surface technique; sensitive to surface preparation; peak shifts: types I, ⟨II⟩; peak widths: type II, III
Hard X-rays (atomic strain gauge)	$\pm 10 \times 10^{-6}$ strain, limited by grain sampling statistics	Small gauge volume leads to spotty powder patterns; peak shifts: type I, ⟨II⟩, II; peak widths: types II, III
Neutrons (atomic strain gauge)	$\pm$ 25 x 10^{-6} strain, limited by counting statistics and reliability of stress free references	Access difficulties; low data acquisition rate; costly; peak shifts: type I, ⟨II⟩ (widths rather broad)
Ultrasonics (stress related changes in elastic wave velocity)	10%	Microstructure sensitive; types I, II, III
Magnetic (variations in magnetic domains with stress)	10%	Microstructure sensitive; for magnetic materials only; types I, II, III
Raman	$\Delta\lambda \approx 0{\cdot}1\ \mathrm{cm}^{-1} \equiv 50$ MPa	Types I, II

Fiber optic sensors are used in bridges to monitor static and dynamic strains to monitor structural integrity and to detect macro- strains that are a result of seismic activity[8]. It is interesting to note that fiber optic sensors are also used to measure strains in the testing of soft biological tissues[9].

Strains, and thereby stresses within coatings of materials such as copper[10] are often determined by curvature measurements. This is based on the fact that the deposition of a coating layer will result in stresses that cause the substrate to curve. Curvature can be measured using contact methods, such as profilometry[10], strain gauges or non contact ones, such as laser scanning and grids. The resulting change in the curvature during deposition is used to calculate the corresponding variations in strain as a function of coating thickness.

Moiré interferometry is an optical interference technique with high resolution and high sensitivity that is often used for measuring surface strains. A grating, which typically has a pitch ~ 5 μm for large strain measurements, and smaller for elastic strain measurements is deposited on the surface of the specimen using photolithography. Two laser beams are then used to illuminate the specimen surface and two of the diffracted beams from the grating are collected and interfered which produces a fringe pattern. Using a grid with two perpendicular gratings and by collecting fringe patterns for both gratings the three components of surface strains can be determined. This method often finds applications in studying strains due to thermal deformation in microelectronic chip applications that use copper coatings[11]

To look for warning signs of de-lamination or thinning in composite panels, engineers can use a laser interferometric method, developed originally for full-field observation of surface strains of components, called shearography. This method employs a speckle-shearing camera, in which a thin glass wedge covers one half of the lens. The surface to be examined is illuminated by laser light, and

the camera produces two sheared images that interfere with each other producing a random interference, known as a speckle pattern. The speckle pattern changes when the object is deformed and this is captured on high-resolution film both before and after the object is deformed. The two speckle patterns interfere to produce a fringe pattern that can be used to determine the strain distribution on the surface. A modification of this method is digital speckle shearing interferometry in which digital images are captured and the fringe patterns are processed using computers. This method is used in thin film applications for determining the debonding properties between coatings such as copper and the silicon substrate[12]. Guelorget *et al.*[13] used in-plane electronic speckle pattern interferometry during tensile testing of semi-hard copper sheets to measure the strain rate. They determined that strain rate measurement before fracture was dependent on localization of strains and the active slip systems.

The X-ray or neutron stress evaluation methods are based on the use of lattice spacing as a strain gauge. Changes in interplanar spacing due to stresses can be used in the Bragg equation to detect elastic strain through the knowledge of the incident wavelength and the change in the Bragg scattering angle. To measure the strain in different directions at the same point, the sample is rotated about its surface normal to coincide the direction of interest with the diffraction plane. X-ray diffraction is probably the most common method used for determining surface strains and has been widely used for determining strains in copper samples [14-17]. Strains determined are usually average strains over the area that is being examined (depends on size and intensity of the beam)[1]. More

recently, diffraction has been coupled with tomography to analyze controlled stresses, like the one employed by Hanan *et al.*[18] for determining residual stresses at the interface of a ceramic layered composite. The use of imaging along with diffraction enabled them to precisely position the X-ray beam for the measurement of residual strains.

Rizzo *et al.*[19] developed an inexpensive device for measuring the strain in thin films during deposition, by measuring the electrical resistance of a commercial strain gauge for determining the strain and thereby the stresses at the film/substrate interface. They deposited thin films of copper over temperatures ranging from 22 to 100 ºC. By plotting residual strain after cooling, they obtained the thermal strain as well as the intrinsic component strain. They observed that the generic stress evolved from compressive to tensile, then back to compressive stress as the film thickness is increased.

2.3 Strain and residual stress measurement using a sharp nanoindentor

The effect of residual stresses on the measurement of hardness and other mechanical properties had been recognized for a long time. For example, in 1932, Kokubo[20] investigated various materials that were subjected to tensile and compressive uniaxial stresses and found that the Vickers hardness values of several commercial metals and alloys varied when a bending stress was applied. Several studies have been carried out since then, using Brinell, Rockwell, and Vickers indentation methods under both uniaxial and biaxial stresses to determine the influence of stresses on the hardness measured. As early as 1952, it was suggested by Sines and Carlson[21] that indentation could be used as a

method to determine residual stresses in materials. They observed from their hardness measurements on a high carbon steel bar, loaded in 4-point bending, that the effects of the stresses were small and the hardness values did not change much. They also found that when compressive stresses were applied, the hardness measured was higher and when tensile stresses were applied the hardness measured was lower.

Since thin films often have large built-in residual stresses in them, it is not surprising that the study of the effect of residual stresses on the hardness measured was done by researchers who were attempting to obtain the mechanical properties of thin films. Doerner *et al.* [22] reported that there was about 10% variance in the hardness measurements for 1.1 μm thick aluminum films stressed to 128 MPa in biaxial tension and 55 MPa in biaxial compression. Since the variations were minimal, their findings were not conclusive. LaFontaine *et al.*[23, 24] examined the nanoindentation hardness of thin aluminum films (0.30 μm thick) that had a high biaxial tensile stress of 380 MPa caused due to thermal processing. Using X-ray diffraction to measure residual stresses, they found that over a period of about 100 h, the tensile stresses relaxed by about 50% and the measured hardness doubled. In a similar study, they also found that nanoindentation hardness of thin copper films decreased after the relaxation of large compressive stresses.

Tsui *et al*.[7] conducted several nanoindentation tests on an aluminum alloy specimen (8009) subjected to well controlled bending to determine if the load vs. depth curves are affected by stresses and subsequently the hardness measured.

They reported that stresses influenced not only the hardness determined but also the elastic modulus. They also found the real area of contact measured by optical methods to be higher than those determined from nanoindentation data. This resulted in error in the measured values of hardness. They reported that the real contact area did not get affected significantly by tensile stresses but by ~ 15% for compressive stresses. In subsequent finite element simulations, they found that the change in hardness was not real and that it was an artifact caused by the pileup of the surface[5].

Suresh and Giannakopulos[25] found that although the hardness is not influenced by the presence of residual stresses when the real contact area is used for hardness measurements, the pileup of aluminum was found to increase with increasing compressive stresses and decrease with increasing tensile stresses. Based on these observations, they developed a theoretical model for the determination of surface residual stresses by a sharp indentor by making some assumptions on the local stress and deformation fields in the contact region. Using FEM analysis, they found that the real contact area of indentation on materials with a compressive residual stress is larger than that of the virgin material and it was smaller for tensile residual stresses. Venkatesh *et al.*[26] conducted experiments on alloys of zinc and aluminum to assess the validity of the theoretical framework developed by Suresh and Giannakopulos[25] for the estimation of elasto-plastic properties through sharp indentation. They reported values of the Young's modulus, hardness, and compressive yield strength of several materials with good accuracy.

Dahmani *et al*.[3] used instrumented nanoindentation to measure the residual stress field around a laser-induced crack in fused silica. They derived a simple theoretical model based on change in the nanoindentation penetration depth as well as the change in Young's modulus and hardness of the material. The contact area was calculated based on the geometry of the indenter.

Even though several techniques were developed to measure the residual stresses some important problems have yet to be solved. In particular, the effect of residual stress fields on global indentation parameters (hardness and the ratio between actual and nominal contact area) for rigid-plastic conditions. This problem was analyzed by Carlsson and Larsson[20, 27] using FEM for Vicker's indentation. They made a parametric study in which numerical methods were used to investigate the effects of different quantities to arrive at simple quantitative relations suitable for experiments. They found the residual stresses to have a small effect on the hardness but residual plastic strain fields to have substantial affect on the hardness values. They performed Vicker's indentation tests on samples exposed to standard four-point bending tests. They reported good agreement between experiments and numerical results especially in situations where no or little plastic deformation occurred due to preloading.

Lee and Kwon[28] designed a concentric bending apparatus to generate equi-biaxial elastic tensile and compressive stresses on an isotropic single crystal tungsten in the (100) orientation. The elastically bent specimen had a stress gradient from tensile on one side to compressive on the other. They used a nanoindenter to obtain load - displacement curves on the unstressed, tensile

stressed, and compressively stressed surfaces. They evaluated the stresses based on a theoretical relaxation model in which a reduced modulus was used that was estimated from the real contact area measured using an AFM. They reported a reasonably good estimation of the residual stresses using this technique compared to the strain gauge measurements made during loading of the specimen.

Nanoindentation was used by Taylor *et al.*[6] to determine residual stresses in thin carbon films. They determined the contact area values based on a methodology presented by Suresh and Giannakopoulos[25]. The residual stress values estimated showed good agreement with stresses estimated using μ-Raman spectroscopy. They also found that residual stresses of materials with unknown properties could be better determined using nanoindentation. Atar *et al.*[29] estimated the residual stresses in ceramic thin films using nanoindentation as well as X-ray diffraction. They reported that the residual stress measured by the former technique was three times higher than the latter. This was attributed to errors in the estimation of a geometrical factor (associated with the Vicker's indenter) they used in the theory developed by Suresh and Giannakopulos[25]. They made modifications to this theory by introducing correction factors for estimating the residual stresses in ceramic thin films.

Guelorget *et al*.[30] used microindentation as local damage measurement technique and found that variations in Young's modulus can be used to quantify local damage. Microindentations (~ 500 nm) were performed on a longitudinal section of a semi-hard copper sheet that was broken in a tensile test. They found

the hardness to be higher (close to fracture) due to work-hardening and that the Young's modulus decreased by 36% within a distance of 300 μm from the fracture and it was constant beyond that.

2.4 Tensile Testing of copper

Copper is one of the earliest known metals to man and has been in use for many centuries[31]. It has excellent thermal and electrical conductivities which has given it a wide range of applicability. It is used extensively in architecture, industry, automotive, marine, and electrical applications among several others. Thin films of copper have been used for the metallization of circuits in the microelectronic industry for sometime[32-35]. Microelectronic applications often involve the generation of heat during use and therefore uneven cooling of the substrate and the coating can take place. This results in the generation of thermo-mechanical stresses in these coatings[35]. Several techniques have, therefore, been used over the years to determine strains and stresses in thin films of copper [10,16,24,36,37]. In order to develop new methods for determining strains in materials, it is often necessary to generate these strains in a controlled manner and tensile testing is often used for this [20, 23]. This investigation employs a tensile testing setup for the generation of strains in the test sample. In the following, tensile testing experiments performed by various researchers on different types of copper samples, are discussed along with their findings.

Tensile testing of copper has been performed on several different types of samples ranging from single crystal to nano-crystalline copper to thin films[14, 16, 37-42]. The deformation behavior of pure polycrystalline copper was investigated by

in-situ X-ray micro-diffraction using synchrotron radiation by Joo *et al.*[14]. They observed the tensile axis to rotate several positions of the same grain which they attributed to the local position of a grain in the sample and the orientation relationship between neighboring grains.

Tensile testing of pure single crystal copper was performed by Kim and Koo[15] to study the deformation behavior. They used scanning electron microscopy and reflection Laue method, using synchrotron radiation, for *in-situ* examination of the tensile test specimen. They determined that the $(\bar{1}11)[101]$ and $(\bar{1}11)[0\bar{1}1]$ slip systems operated mainly in the middle region of the sample and the $(111)[\bar{1}01]$ and $(\bar{1}\bar{1}1)[011]$ are activated in the corner regions of the tensile sample. Borbely *et al.*[38] studied the local crystallographic orientation of copper single crystals under uniaxial tension by the electron backscattering technique. Statistical evaluation of their data revealed the presence of an increased crystallographic correlation at the transition point between stages II and III of work-hardening.

Thin copper foils of varying thickness (10 – 250 μm) were tested in tension by Simons *et al.* [39] at room temperature. They examined the surface of two types of samples, namely, the as-received samples and the annealed samples using SEM. When they compared samples of the same processing condition they found a dependence of the mechanical behavior on the thickness of the foils in the tensile test. When the thickness was reduced from 250 μm to 10 μm, the fracture strain decreased for the as-received foils from approximately 20% to 0.2% and for the samples with heat treatment from 35% to 15%.

Kretschmann *et al.*[16] studied the plastic deformation of 1 μm thick copper films sputtered on nickel substrates. Tensile experiments were performed on a special microtensile tester built into a theta-theta diffractometer. The substrate and film were deformed together to avoid problems normally associated with tensile testing of free-standing films. They performed *in-situ* X-ray measurements of the lattice spacings and distribution of lattice spacing to determine both elastic and plastic strains. To reduce the effect of metal substrates on the tensile properties of copper thin films, Denis and Spaepen[40] vapor deposited copper films ~0.1 to 3 μm thick on thin (~7.6 – 12.7 μm) polyimide (Kapton) substrates. Tensile tests were perfomed in a microtensile tester in which strain was measured by optical diffraction from a microlithographically applied grid. They determined the Young's Modulus to be independent of the film thickness and was ~ 20% less than the values calculated using single crystal elastic constants. The microstructure of the films was examined using focused ion-beam microscopy. They found that the grains were heavily twinned and the grain size, twin spacing, and twin width depended weakly on the thickness of the films. They also determined that the yield strength of the films was strongly dependant on the films thickness.

Some researchers [37,36] have gone a step further by performing tensile tests on free standing copper films. Keller *et al.*[37] performed *in-situ* straining experiments using a transmission electron microscope on electron beam evaporated copper films suspended over windows etched in a silicon substrate. The films had low ductility (< 1%) and fracture occurred both in an intergranular

as well as transgranular manner. Cheng *et al.*[36] developed a tensile-testing technique for micrometer-sized, free-standing thin films whose major components included a three-axis micromanipulator, a force sensor, and an optical microscope. They calculated strains from the images obtained using the optical microscope by digital image correlation (DIC) technique. The yield strength of 60 nm thick copper films was determined to be ~ 224 MPa with an elongation of ~ 2%.

Interest in nano-cystalline copper has grown over the years because of the high tensile strength of these materials[41-45]. Wang *et al.*[42] characterized the tensile properties of nanocrystalline (nc) copper with grain sizes < 100 nm using a microsample tensile testing machine. The bow-tie shaped nano-crystalline microsamples were produced by surface mechanical attrition treatment. The initial strain rate of the tensile tests was 5×10^{-4} / s. They reported that nano-crystalline copper with fine grain sizes and high angle grain boundaries had very high tensile strengths (~ 760 MPa). They also reported that the ductility of these samples was low with a total plastic strain of only ~ 3%.

Kalidindi *et al*.[46] studied the deformation of several large aluminum grains (0.75mm) in a sample of high purity aluminum with a columnar grain structure. Aluminum, like copper, has an FCC structure. Plastic deformation was imposed using a channel die setup in which compression was imposed along the length of the sample which resulted in reduction in width and increase in length. They used orientation imaging microscopy (OIM) in an SEM that had a spatial resolution of 1 μm. Using this technique, they characterized the local rotations of the

polycrystalline sample. They identified the local strain histories of the individual grains which they found to be in agreement with the measured changes in orientations. They initially mapped several areas of the sample to determine the grain orientations and using the OIM software assigned colors to different grains with different orientations. Grains that had orientation mismatch within 5% of each other were assigned the same color. They used micro-indentations as markers to track specific crystals during deformation.

Using the OIM technique, they reported three kinds of crystals based on their orientations in a deforming polycrystalline material.

1. In the first category of crystals, the misorientations were only marginally higher than the misorientations in the same grain in the undeformed state. They do not fragment during deformation and continue to exhibit a roughly homogeneous lattice orientation field. These types of grains were reported to be relatively harder than their neighbors and they are most common in the material. These crystals or grains had several shear bands locally that resulted in a decrease in the plastic energy dissipation rate. They reported that the local deformation history of these crystals was largely governed by the need for the sample to minimize its plastic energy dissipation rate.

2. The second category of grains exhibited a characteristic banded orientation fields where the orientation bands repeated at least once within the same crystal and were oriented at ±45º to the transverse direction. These grains were reported to have slip taking place in different slip systems within the same grain. They concluded that certain crystal orientations were inherently unstable

resulting in these crystals having orientation fields repeated at various stages of deformation after having different orientation fields in between these repetitions.

3. The third category of grains exhibited multiple, non-repeating orientations within the crystal indicating the grains to be fragmented. These were found to be relatively softer crystals compared to their neighbors. The shear bands in these crystals were greatly influenced by the shear bands formed in their harder crystal neighbors. They found that the final orientation of these crystals differed significantly from the original orientations before deformation, which led them to conclude that different regions of these crystals were greatly influenced by their neighbors.

Slip, within most crystals, takes place in two ways[47].

1. Fairly uniformly distributed slip on individual lattice planes: This can be attributed to a large number of dislocations that might be individually generated at grain boundaries.

2. Localized concentration of slip within certain stacks of slip planes giving rise to slip bands which are caused by large bursts of dislocations within concentrated areas.

Numerous investigations have shown that slip directions are definite, and in the case of FCC metals, the slip system is $[\bar{1}10](111)$. Some studies have shown that when slip is suppressed on the {111} planes in FCC metals, a small amount of slip can occur on {123} planes[48].

In polycrystalline materials, multiple slip takes place in nearly every grain, if each grain is to remain coherent with its neighboring grains. Thus, to enable

each grain to match the deformation of its neighbors along grain boundaries, theoretically slip has to occur on a minimum of five planes[47]. In addition to all this, individual grains of a polycrystal are stressed in irregular ways due to the fact that each grain is faced by a different grain with a possible change in the orientation at each boundary.

Modelling and simulations have also been used to study the deformation behavior of copper [49,50,51,52]. A review of this topic is beyond the scope of this investigation due to limitations in space and the relevance to the present investigation.

2.5 *In-situ* imaging of deformations using Atomic Force Microscope (AFM)

In-situ imaging of tensile testing of copper samples has been performed primarily using optical microscope, scanning electron microscope[42], transmission electron microscope[37, 53], X-ray diffraction[15], focused ion-beam microscopy[40]. However, very little work is reported on *in-situ* AFM imaging of deforming surfaces. The earliest known setup (1995) in which an AFM was used for *in-situ* imaging of deformation was by Small *et al.*[54] who imaged the deformation of a LiF crystal under compression. They modified the motorized stage of a standalone AFM (SAAFM) with a manual adjustment system that had three fine threaded screws with rounded edges that came in contact with the sample. The LiF crystal could be compressed by two piezoelectric crystals and the surface could be imaged by the AFM tip. They imaged dislocations as the crystal deformed. Goken *et al.*[55] studied the effect of deformation on crack tips in NiAl using an AFM in ultra-high vacuum. They developed a mini 4-point bending

device to bend the crystal. An *in-situ* examination of the surface of an Al-5%Mg alloy under a tensile load was performed by Tong *et al.*[56] using an AFM. They used a tensile sub-stage that was fixed on the X-Y stage of the AFM that could measure both the force applied as well as the strain. They studied the deformation of two grains on the surface of the sample as the load on the sample was increased. The grains were imaged in intermittent steps during which loading was halted.

Bobji and Bushan[57] used an AFM to investigate microcracking of magnetic thin films under tension. A left-right combination screw was used to stretch the sample on a tensile stage that was specially developed so that the area being observed did not move away from the scanning area of the AFM. They made small indents made using a diamond indenter as markers so that the same area could be imaged during the tension experiment. A support was also used below the sample during the imaging of the surface which was performed in strain steps of 0.16%. The supports were removed when the tension experiment was performed. Renault *et al.*[58] used a tensile testing setup in which a micrometer was used to control the deformation of a 125 μm-thick polyimide coupons. They used an X-ray diffractometer and an AFM to study the mechanical behavior as well as the microstructure of the sample during the tension experiment. Some experiments were also performed by George *et al.*[59] to study the behavior of metallic films on polymeric substrates using the same tension test setup.

AFM *in-situ* experiments were performed by Tambe and Bushan[60] to study nano-cracking in magnetic tapes under monotonic and fatigue loading conditions.

A stepper motor driven linear stage was used for both tensile as well as fatigue experiments. The tension experiments were performed at a constant strain rate of 8.33×10^{-3} /s. For fatigue loading experiments, the tape sample was first loaded to a mean stress and then a cyclically varying (constant amplitude) load was applied by programming the stepper motor controller. Bamberg *et al.*[61] developed a tensile testing setup in conjunction with an AFM to study the effect of uniaxial tensile loads on polymers. One of the salient features of their equipment was the use of three piezoelectric load cells with maximum loads of 25 N, 250 N and 4.4 kN so that experiments could be performed over a wide range of loads depending on the accuracy required. The dynamics of slip-lines on the surface of a polycrystalline copper specimen was studied by *in-situ* scanning tunneling microscopy by Vettegren and Svetlov[62]. They performed a creep test that lasted 450 hours and determined that the formation, evolution and disappearance of slip lines were caused by the motion of material bands several nanometers wide.

CHAPTER 3

PROBLEM STATEMENT AND OBJECTIVES

The ever increasing demand for fabricating smaller and smaller devices to enable savings in material costs, operational costs, space, and weight has lead to the miniaturization of components. The processing technologies involved in the fabrication and the working environments of these devices have resulted in stresses and thereby strains in highly localized regions. The need to improve designs of devices so that they have better reliability has brought about the need for determining strains in very small regions. A review of literature showed that residual stress measurement techniques, such as X-ray diffraction and μ-Raman spectroscopy have been in use for some time for strain estimation, but attempts at relating local strains with global strains were somewhat limited. Also, measurement of global strains in micrometer to sub-micrometer scale was practically non existent.

More recently, nanoindentation has been used to determine local strains and residual stresses. Current methods of strain measurement using indentation, usually consider subtle differences in hardness and elastic modulus to get an estimate of the strains. The hardness estimates are made by dividing the applied load with the projected area of the residual indent. They are based on estimating the projected areas of the residual indent using optical or scanning electron

microscopes. These techniques are somewhat time consuming and error prone due to possible errors in calculating the projected area due to pile-up or sink-in. Moreover, it is not easy to locate the residual indents after the experiments are performed.

This led us to the need for the development of a new method for determining strains in very small regions. It had been observed during some nanoindentation experiments of thin films, using an atomic force microscope (AFM), that the shape of residual images of nanoindents on stressed surfaces appeared different than the nanoindents made on unstressed surfaces. A set of indentation tests are planned to investigate possible effect of stresses on the shape of a residual indent and to develop a method to determine strains in very small regions using this information. This method should be able to identify a very small area of interest with relative ease and image the selected area before and after the analysis. Such a technique has to be relatively fast and less error prone and had to be achieved using an existing surface imaging methods, such as AFM.

A new method was developed for determining strains which required the use of a micro-tensile apparatus that could make controlled displacements at known strain intervals on a test specimen. Strains are introduced in the samples via a small *in-situ* tensile testing system, originally developed for *in-situ* SEM, and modified and adapted here for use with the AFM. A method will also be developed for determining the difference between bulk strains (test sample as a

whole) and local strains (strains in individual grains) of the test specimen under tensile loading.

This investigation deals with the development of a new method for determining residual strains by studying the effect of stresses on the shape of the residual images of the nanoindents performed on the surface. To accomplish this, the following specific tasks will be undertaken.

1. An *in-situ* tensile testing stage, originally designed for use for *in-situ* tensile testing inside an SEM, will be modified and adapted so that *in-situ* tension experiments on a sample can be performed under an AFM.
2. The stress-strain behavior and mechanical properties of polycrystalline copper sample will be estimated to determine various stages at which AFM experiments are to be performed.
3. *In-situ* tension experiments will be performed using an optical interference microscope (MicroXam) to examine the deformed surface.
4. Images acquired at different strain intervals will be analyzed using a digital image correlation (DIC) method[63] to determine the variation in local strains.
5. *In-situ* tension experiments will be performed using an AFM to study the microscopic surface deformation at various locations.
6. Nanoindentation tests will be conducted using a diamond nanoindenter in an AFM at various stages of the tension experiment starting from the initial elastic deformation to the final necking of the sample. Images of the residual indents will be acquired at each stage.

7. A new method called the indent shape change (ISC) method will be developed to compare the residual indent images acquired at various deformation intervals to the image of the indent when no deformation takes place.
8. A technique known as virtual “digital“ tensile testing will be used by digitally altering an image of the residual indent by known values in the longitudinal (tensile) and transverse directions and comparing it to the strains estimated by the ISC and DIC methods.
9. Strains associated with change in size and shape of the residual indent on the deformed surfaces will be estimated using the ISC method.
10. The influence of grain orientation on the shape of the residual indent will be investigated by performing nanoindentation experiments on various grains with different orientations.
11. A set of 9 nanoindents (75 nm deep and 500 nm apart) in a 3 x 3 array will be made in the center of a tensile sample on a single grain. The nanoindents will be tracked and imaged under increasing tensile loads. The relative displacements of the nanoindents will be analyzed, by a method called relative indent movement (RIM) method to determine strains. This will result in the estimation of strains associated with the formation of slip bands. A Digital Image Correlation (DIC) software[63] will be used to determine the distribution of strains around the indents.
12. Theoretical validation of the method will be done by virtual “digital” tensile testing consisting of digital modification of an image of the residual indents

by simultaneously stretching in the longitudinal (tensile) direction and shrinking in the transverse direction by known values and comparing it to the strains estimated by the RIM and DIC methods.

13. Experimental validation of the RIM and DIC methods will be accomplished by analyzing images of nanoindents on a polycarbonate sample during tensile loading. The strains measured using a linear shrinkage curve (LSC) transducer will be compared to the strains estimated using the RIM and DIC methods.
14. Experiments will also be performed using nanoindents made using an MTS nanoindenter system to estimate strains in multiple grains under the influence of tensile loading. The nanoindents will be 600 nm deep and 10 μm apart arranged in a 3 x 3 array. The DIC software will be used to estimate the strain distribution around the nanoindents.

CHAPTER 4

EXPERIMENTAL SETUP AND EQUIPMENT USED

Several characterization equipment, including a Digital Instruments atomic force microscope (AFM), MTS Nanoindenter, and optical interference microscope (Microxam) were used in this investigation. Some details on the operation of AFM and MTS Nanoindenter are given in the following.

4.1 Digital Instruments (D3100) Atomic Force Microscope (AFM)

A Digital Instruments D3100 AFM was used in this investigation. Specifications of the AFM are given in Table 4-1. An Atomic Force Microscope (AFM) produces high-resolution, 3D images by scanning the sample surface with a sharp probe. The probe is part of a flexible cantilever which is mounted on one end of a cylindrical piezoelectric tube. The piezo-tube is rigidly mounted near the top of the microscope. Voltages applied to the X- and Y- electrodes on the piezoelectric tube deflect the tube horizontally to produce a precise raster scan over the sample surface. The vertical height of the probe is controlled by a voltage applied to the Z-electrode on the piezo-tube. A stepper motor coupled to a lead screw translates the slide to which the sample is attached. A separate motor drive enables the height of the microscope and probe to be adjusted relative to the sample surface.

Table 4-1: DI3100 Atomic Force Microscope specifications[64]

X-Y imaging area approx	90 μm x 90 μm
Z range approx.	6 μm
Sample Size	Up to 150 mm diameter, 12 mm thick
Inspectable area - Stage	125 mm x 100 mm
Tips Used	Silicon and silicon nitride for imaging, Diamond Tip for nanoindentation
AFM Resolution	~ 10 nm (Depends on tip radius)
Nanoindentation(load controlled)	< 50 μN
Scratch length	< 3 μm
Optical microscope viewing area	150 μm to 675 μm
Optical microscope resolution	1.5 μm

There are several scanning options available in an AFM depending on the type of material being viewed and the type of characterization required. Some of the scanning techniques commonly used are listed in the following:

- Contact Mode
- Tapping Mode
- Non-contact Mode
- Phase Imaging
- Lateral Force Microscopy (LFM)
- Magnetic Force Microscopy (MFM)
- Electric Force Microscopy (EFM)
- Scanning Capacitance Microscopy (SCM)
- Scanning Spreading Resistance Microscopy (SSRM)
- Scanning Tunneling Microscopy (STM)

The two most commonly used imaging techniques are the contact mode and the tapping mode. In this investigation, we have used the tapping mode of imaging, as this causes minimal damage to the surface being viewed.

Tapping mode AFM operates by scanning a tip attached to the end of an oscillating cantilever across the sample. Figure 4.1 is a schematic of the tapping mode showing the cantilever and parts of the scanning head. The cantilever is oscillated at or near its resonant frequency with amplitude ranging typically from 20 to 100 nm. The tip lightly taps on the surface being imaged during scanning, contacting the surface at the end of its swing downwards. A feedback loop maintains constant oscillatory amplitude by maintaining a constant RMS of the signal acquired by a split photo-detector diode. The vertical position of the scanner at each data point is stored in the computer to form a topographical image of the sample surface. Imaging can be done both in air as well as in liquids. While imaging in air, the tip contacts the surface through an adsorbed liquid layer that is found on the surface of all materials and this prevents the tip from getting stuck to the surface.

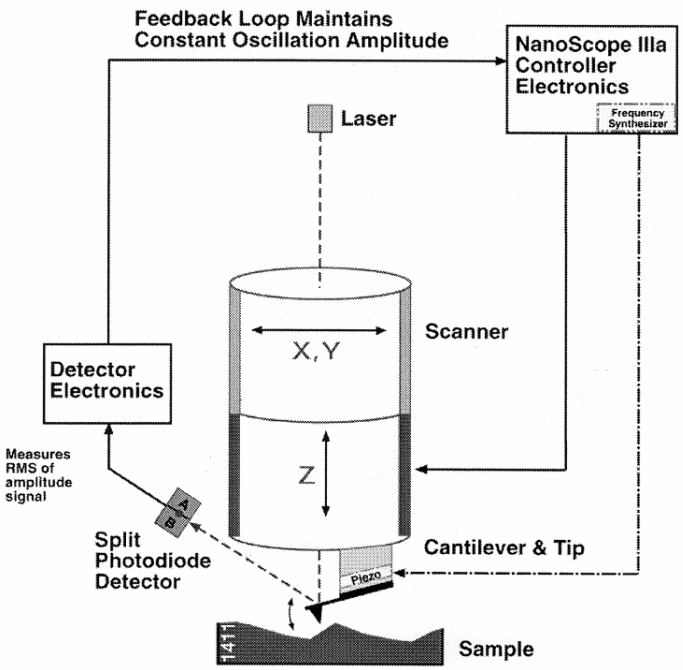

Figure 4.1: Schematic of TappingMode AFM [64]

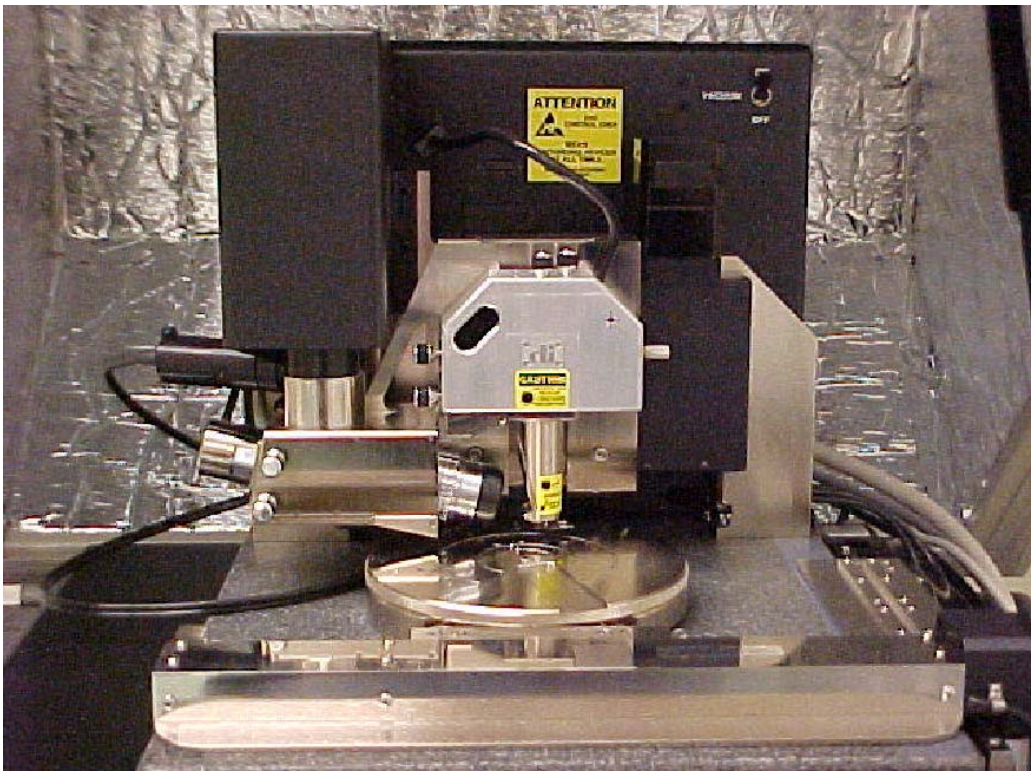

Figure 4.2: Digital Instruments Dimension 3100 Atomic Force Microscope (AFM)

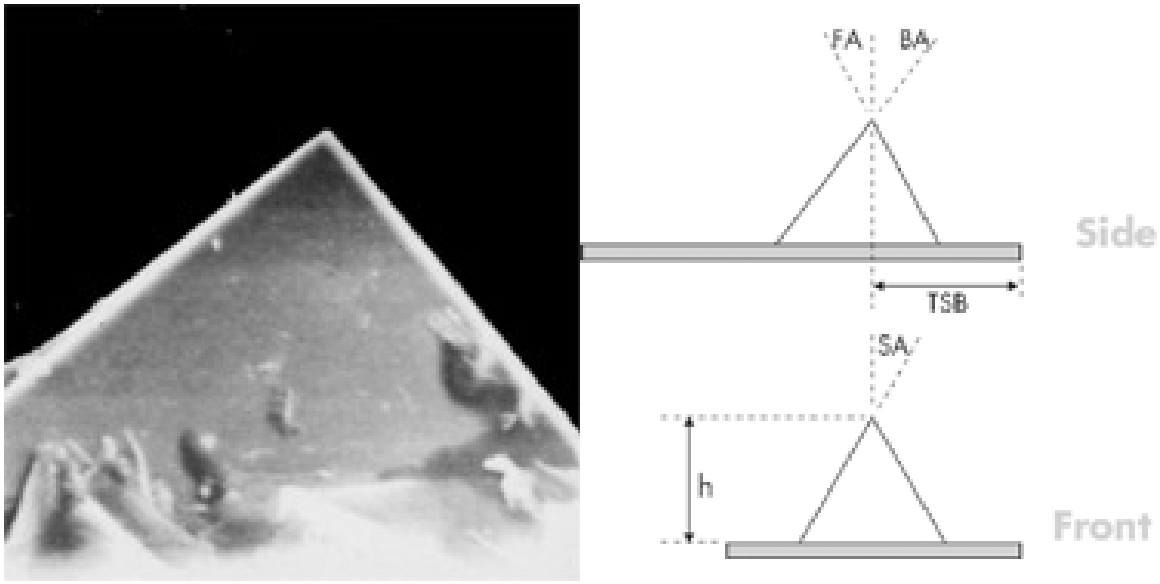

Figure 4.3: Tetrahedral Diamond indentor[64]

4.2 Nanoindentaion using an AFM

Nanoindentation tests were conducted on tensile samples using a Digital Instruments (Dimension 3100) Atomic Force Microscope (AFM) (see Figure 4.2). Details of the tensile stage used in these experiments are given in Section 4.3. A Berkovich indenter with a diamond tip mounted on a stiff stainless steel cantilever was used. Spring constant of the cantilever is 230 N/m. Figure 4.3 is an SEM micrograph of a typical AFM diamond tip (provided by Digital Instruments) with a tip radius of ~ 25 nm.

In the AFM, the indentations were made by gradually bringing the piezo in the AFM head into the material (see Figure 4.4). This results in the deflection of the cantilever as well as penetration into the material. The AFM senses the distance moved by the piezo and the deflection of the cantilever. Subtracting the cantilever deflection from the piezo movement gives the penetration depth.

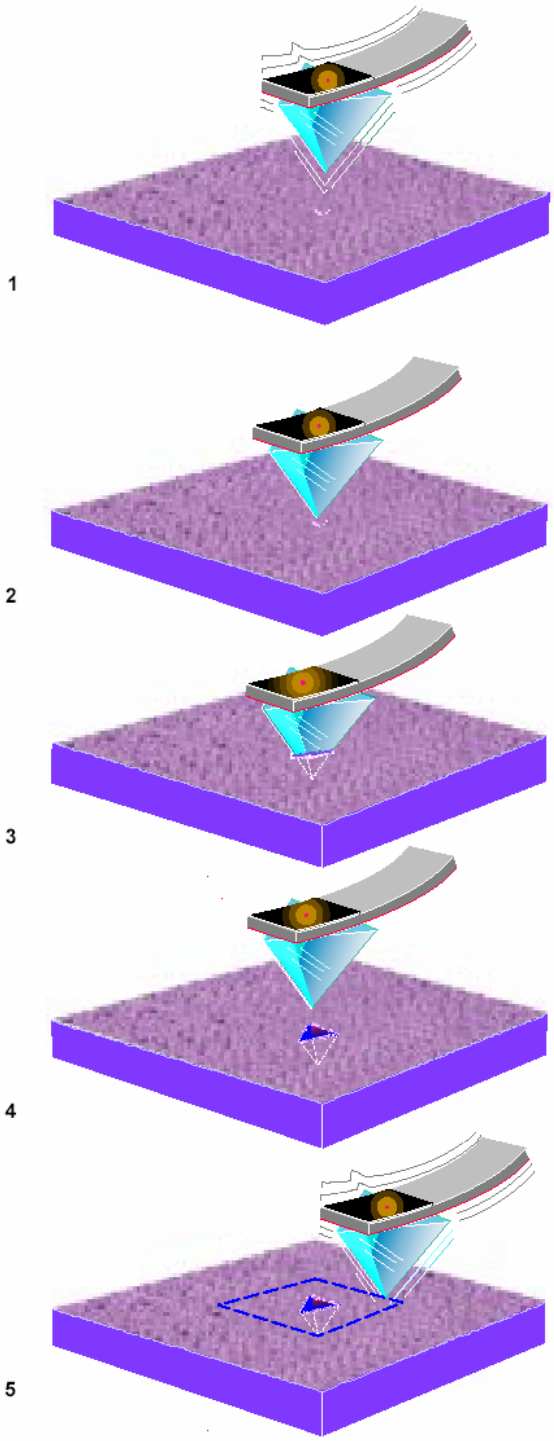

Figure 4.4: Nanoindentation sequence: (1) engagement; (2-4) indentation; (5) imaging[64]

The residual depth is measured using a cross-sectional plot from the AFM image obtained thereafter. Force is calculated by multiplying the deflection with the spring constant. Hardness is calculated based on the projected area of the indent, which is dependent on the penetration depth.

Table 4-2 Specifications of the diamond AFM tip[64]

Geometry:	Anisotropic
Tip Height:	50 μm – 150 μm
Front Angle (FA):	30°
Back Angle (BA):	30°
Side Angle (SA):	30°
Tip Radius (Nom.):	25 nm
Tip Radius (max.):	50 nm
Tip Set Back (Nom.):	13 um
Tip Set Back (Range):	5 μm to 20 μm

The three sided pyramidal indenter in Figure 4.3 has a face or front angle (FA), θ of 30º. This indenter is similar to a cube corner indenter which is a modification of the Berkovich indenter. The semi-angle of the faces of a cube corner indenter, θ is 35.26º compared to a Berkovich indenter that has an angle, θ of 65.03º.

The elastic modulus and hardness of a specimen material can be determined from the load versus displacement measurements obtained in a nanoindentation test. An important quantity in determining indentation hardness is the mean contact pressure that can be determined by dividing the load on the indenter by the projected area of contact. The mean contact pressure under a fully established plastic zone is considered to be the hardness, H of the specimen material. The depth of penetration of the indenter below the surface is measured as the load is being applied. From the known geometry of the indenter

the projected area of the indent can be estimated and there by the hardness. The modulus of elasticity of the specimen can also be established from the load versus penetration data. When the load is removed from the indenter, the material attempts to regain its original form but is prevented from doing so because of the plastic deformation around the indent. Some amount of recovery does take place due to relaxation of the elastic strains within the material. The stiffness of the specimen can be determined from the rate of change of load with depth during the initial unloading of the indenter. One important assumption made for determining the hardness and elastic modulus of a specimen is that during the indentation there is elastic-plastic loading followed by an elastic unloading with no plastic deformation occurring during the unloading.

There is an important difference between the hardness determined by conventional techniques and the hardness obtained from depth sensing nanoindentation techniques. In conventional hardness determination techniques, such as Brinell hardness test hardness is determined from the area of the residual impression on the surface indented while for depth sensing indentation, such as nanoindentation the size of the contact area under full load is obtained from the penetration depth of the indenter and the shape of the elastic recovery during initial unloading. Usually the areas obtained by both these techniques are similar except for cases when there is considerable elastic recovery which results in the former technique giving higher hardness compared to the latter.

The analysis of the AFM nanoindenter can be done in a similar way as the analysis of a Berkovich indenter which is also a pyramidal indenter. In order to

extract useful information from the load versus penetration depth data for a pyramidal indenter, it would be easier to analyze a conical indenter which has the advantage of being axi-symmetric[2].

Consider the elastic-plastic loading and elastic unloading of specimen material with a conical indenter as shown in Figure 4.5 (a). As the indenter is unloaded from its maximum load, the contact radius remains constant until the surface of the material is no longer shaped like the indenter. As the contact radius is almost constant during the initial unloading, the unloading curve is linear. Therefore, the initial part of the unloading is similar to the unloading of a cylindrical punch indentation. A cylindrical flat punch indentation is shown in Figure 4.6. Even though this type of indentation is very rarely used, it illustrates a good elastic unloading response and is assumed to be fully elastic.

Different terms used in this analysis are given in the following:

a = contact radius of the cylindrical punch i.e. contact radius of cone at maximum depth

h_t = maximum depth of indentation and maximum load

P_t = maximum load

h_r = depth of residual impression

h_{rp} = depth of residual impression for an equivalent punch

h_e = elastic displacement after unloading

h_{ep} = elastic displacement after unloading for an equivalent punch

h_a = distance from the edge of the contact to the surface and maximum load

h_p = depth of circle of contact measured from maximum depth h_t

E^* = Combined or reduced elastic modulus

h_p = depth of circle of contact and maximum depth h_t

In Figure 4.5 (b), the initial unloading of the cone, which acts like a punch in terms of its constant contact area as the initial unloading, appears to be linear. Now, if the contact area remains constant throughout unloading (as in the case of a cylindrical punch), the unloading curve would be linear from point P_t to P = 0. This elastic displacement of the imaginary punch would be the distance from point D to maximum depth of the indent h_t denoted by the term h_{ep}. This is equal to the distance h_a for the actual initial unloading of the cone. From this, we can say that the distance $h_{rp,}$ which is the depth of circle of contact for an equivalent punch would be equivalent to h_p, which is the depth of penetration measured from the edge of the area of contact. Once h_p is estimated, the area of contact, the hardness, and the elastic modulus can be estimated.

The equivalent projected area of contact between a pyramidal indenter and a conical indenter is obtained from the relationship:

$$A = \pi h_p^{\,2} \tan^2 \alpha \qquad (4.1)$$

where α is the cone angle. The representative strain in the specimen material, using geometrically similar indentations, such as that made by Vickers or Berkovich indenters, depends only on the effective cone angle of the indenter. The sharper the angle, the greater is the strain. According to Tabor[65], the representative strain (ε) for a conical indenter is given by:

$$\varepsilon = 0.2 \cot \alpha \qquad (4.2)$$

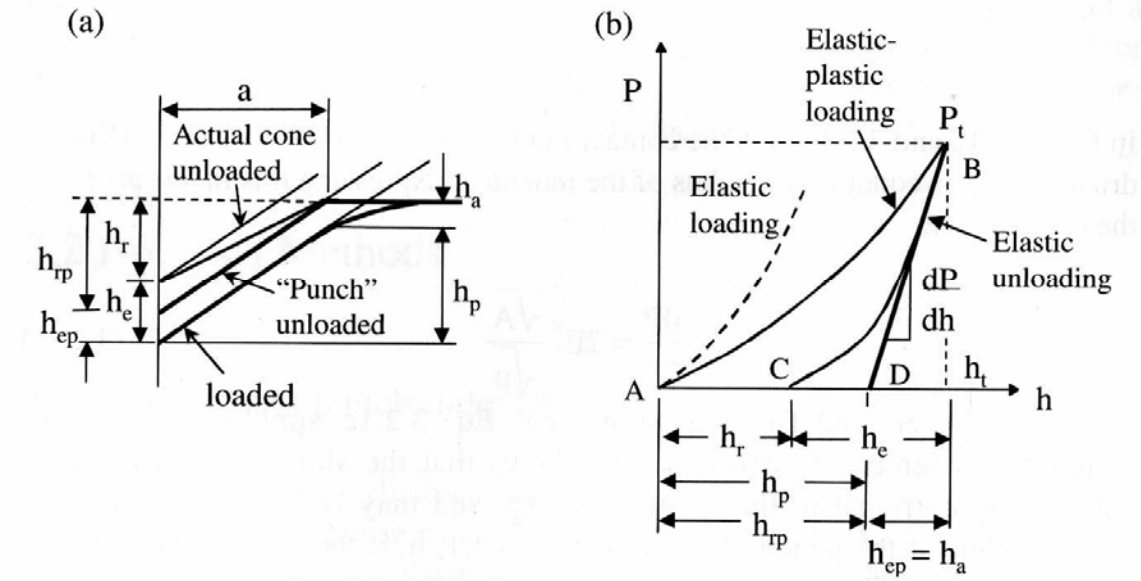

Figure 4.5:(a) Schematic of indenter and specimen surface at maximum loading and unloading for an equivalent axial-symmetric cone indenter with the same area to depth ratio as a triangular pyramidal indenter (b) Load versus displacement for elastic-plastic loading followed by elastic unloading[2].

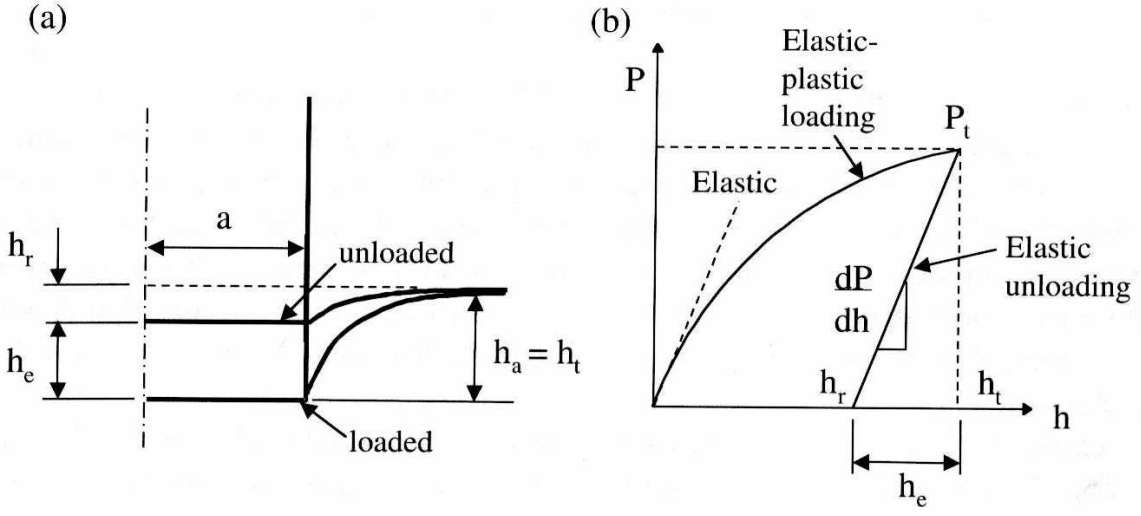

Figure 4.6: Schematic of indenter and specimen surface at maximum loading and unloading for a cylindrical punch indenter (b) Load versus displacement for elastic-plastic loading followed by elastic unloading[2].

The analysis of this indenter with reference to an axi-symmetric conical indenter that results in the same area to depth ratio can now be considered. The semi-angle of the cone, α = 36.59º that gives the same area to depth ratio as the triangular pyramidal indenter with a semi-angle θ = 30º can be determined from Eqns. 4,1 and 4.2 which results in the relationship:

$$\tan\alpha = \sqrt{\frac{3\sqrt{3}\tan^2 30°}{\pi}} \tag{4.3}$$

The representative strain for this indenter from Eqn. 4.2 would, therefore, be ~ 27%. Indentations made with sharp indenters would thereby induce plasticity from the very moment of contact. On unloading, the contact can be considered elastic and the relationship between the load and the penetration depth for a cone indenter is given by the relation:

$$P = \frac{2}{\pi} E^* h_e^{\,2} \tan\alpha' \tag{4.4}$$

α' is the combined angle of the indenter and the residual impression. The normal displacement h of points on the surface below the indenter is a function of the radial distance r from the axis of symmetry and is given by the relationship

$$h = \left(\frac{\pi}{2} - \frac{r}{a}\right) a \cot\alpha' \quad r \le a \tag{4.5}$$

Now from Figure 4.5, it can be seen that as the indenter is unloaded, the tip of the indenter, where r = 0, moves through a distance h_e and the edge of the circle of contact with specimen surface, at r = a, moves through a distance equal to h_e.

Thus, from Eqn. 4.5, at maximum load P_t, the displacements h_a and h_e can be expressed as

$$h_e = \frac{\pi}{2} a \cot \alpha'$$
$$h_a = \left(\frac{\pi}{2} - 1 \right) a \cot \alpha' \tag{4.6}$$

Therefore, h_a in terms of h_e can be written as

$$h_a = \left(\frac{\pi - 2}{\pi} \right) h_e \tag{4.7}$$

and

$$h_t = h_p + h_a \tag{4.8}$$

From Eqns. 4.7 and 4.8, we get

$$h_t = h_p + \left(\frac{\pi - 2}{\pi} \right) h_e \tag{4.9}$$

Since $h_e = h_t - h_r$

$$h_t = h_p + \left(\frac{\pi - 2}{\pi} \right) (h_t - h_r) \tag{4.10}$$

$$h_p = h_t - \left[\frac{\pi - 2}{\pi} \right] h_t + \left[\frac{\pi - 2}{\pi} \right] h_r \tag{4.11}$$

The relationship between the projected area A of the indent and the depth h_p below the contact for triangular pyramidal indenter with θ = 30° is given by the relationship

$$A = 3\sqrt{3} h_p^{\,2} \tan^2 30° \tag{4.12}$$
$$= \sqrt{3} h_p^{\,2}$$

The slope or the stiffness, S of the unloading part of the load versus penetration depth can be determined from the relation

$$S = \frac{dP}{dh} = \frac{P_t}{h_t - h_p} \tag{4.13}$$

The reduced elastic modulus of the specimen material can thus be determined from

$$E^* = \frac{\sqrt{\pi} * S}{2\sqrt{A}} \tag{4.14}$$

$$\frac{1}{E^*} = \frac{\left(1 - \nu^2\right)}{E} + \frac{\left(1 - \nu_i^2\right)}{E_i} \tag{4.15}$$

where E is the elastic modulus of the material that has to be determined, E_i is the elastic modulus of the indenter, ν and ν_i are the Poisson's ratios of the material and indenter, respectively. For a diamond indenter the constants used are E_i =1141 GPa and ν_i = 0.07.

4.2.1 Calibration of Atomic Force Microscope

The main imaging part in an AFM is the scanner which is a hollow tube made of a piezoelectric material, such as PZT (lead zirconium titanate). These materials contract or elongate when a positive or negative voltage is applied to it, respectively. All scanners do not react in exactly the same way when the same voltage is applied because of variations in the orientation and size of the piezoelectric grain structure and other factors. Sensitivity of a scanner is the ratio of applied piezo voltage to the movement of the piezo.

Figure 4.7 represents the sensitivity of the AFM piezoelectric scanner over its full range of movement. Since piezoelectric scanners exhibit more sensitivity at higher voltages than at lower voltages, the sensitivity curve is not linear. Piezoelectric materials also exhibit hysteresis which here means that the response of the crystal when the voltage is increased is not the same as when the voltage is decreased. In order to have sharp and linear movements when a surface is being scanned the applied voltage must compensate for increased effects of hysteresis. This is achieved by controlling the applied voltage using a set of mathematical functions that compensate for errors in the measured dimensions using necessary inputs from the user. Moreover, as the scanner ages, its sensitivity will slightly decrease making it necessary to periodically recalibrate the scanner [66].

Piezoelectric scanners seen in the AFM scanning head (Figure 4.1) need to be recalibrated every three to four months to maintain high accuracy. The

Dimension 3100 AFM employs a software guided procedure for calibration that includes the following main steps.

1. Image a calibration reference that has surface features with precisely known dimensions
2. Compare the known dimensions on the reference with the one's estimated by the AFM software
3. Make the required corrections necessary in the calibration parameters of the AFM until the values measured by the software are within acceptable tolerances with the actual dimension of the reference.

To test linearity and sensitivity of the scanner, images are captured at two calibration points, namely, the maximum range at 440 V (90 µm x 90 µm) and at a medium range of 150 V (25 µm x 25 µm) for the scanner. The user then inputs in the software the distance between features on the reference surface and correction parameters are recorded to compensate for the scanners movements.

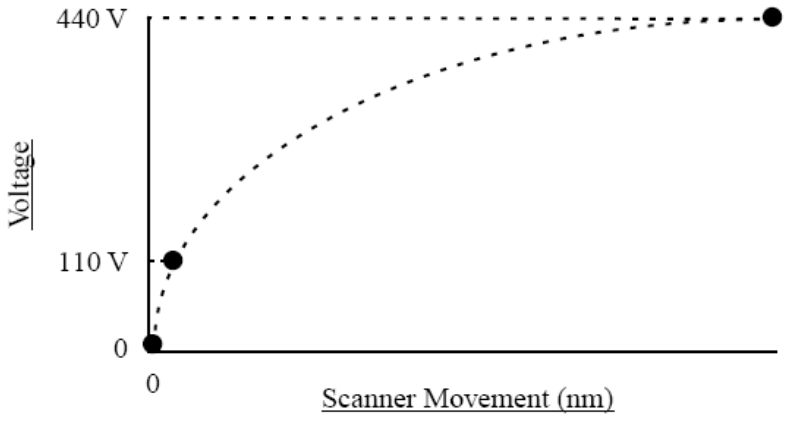

Figure 4.7: AFM piezoelectric scanner sensitivity curve[64]

To calibrate the scanner, a calibration sample with square holes of known depths and lengths are used. The calibrations reference is a platinum coated silicon substrate with a grating that has a regular series of 180 nm pits, 10 µm apart. Figure 4.8 is an AFM 3D image of platinum coated silicon reference showing its dimensions. The AFM should be capable of measuring features on the surface of the reference with an accuracy of ~2 % or better at the maximum scan size.

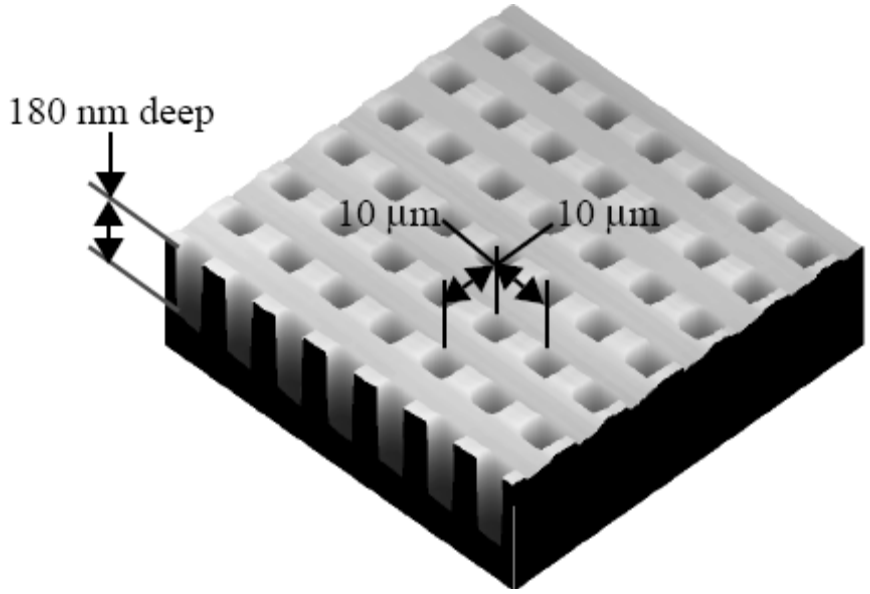

Figure 4.8: Digital Instruments platinum coated silicon calibration reference[64]

The AFM scanner used in this investigation is calibrated every three months to maintain accuracy of the values measured using it. Figure 4.9 shows the results of calibration performed on the scanner. Figure 4.9 (a) is an AFM 3D image of the calibration reference performed at a maximum scan size of 90 µm x 90 µm. Figures 4.9 (b) and (c) show the cross sectional analysis of an image of an area on the reference. The measured values show that the calibration has been performed correctly. The variation in the values measured by the AFM

software in the X- and Y- directions with the actual dimensions of the calibration reference were only ~ 0.1%, which is well within the accuracy required. The variation in depth was also < 1%.

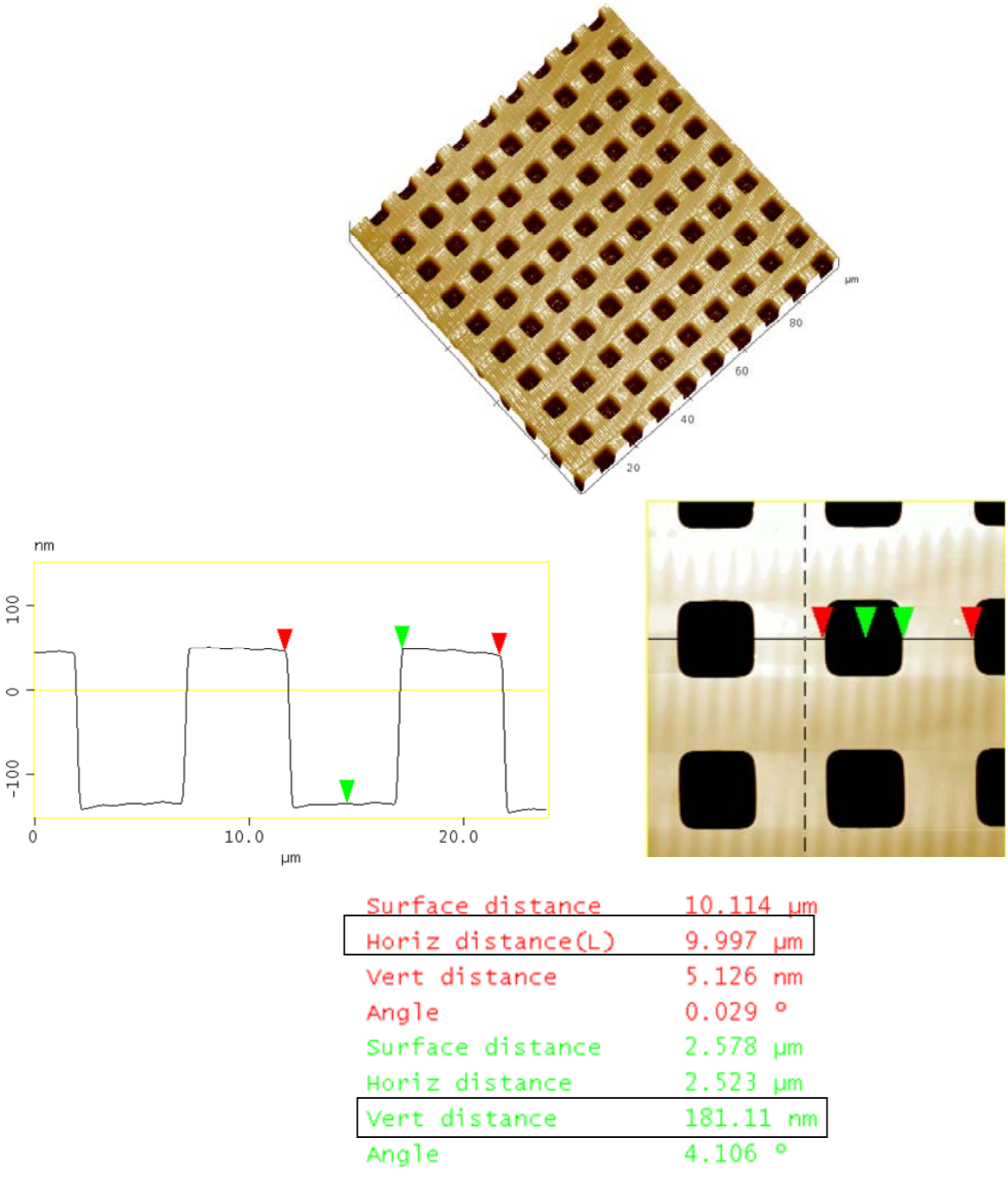

Figure 4.9: Calibration of AFM scanner

4.3 MTS Nanoindenter

As mentioned earlier, nanoindentations were made on tensile specimens using an MTS Nanoindenter prior to the tension experiments. Specifications of the nanoindenter system are given in Table 4-3. Salient features of the MTS Nanoindenter system (Figure 4.10) are given in the following. Briefly stated, the indenter system has the following components: a means for translating the specimen, a means for applying a known force to the indenter shaft, and a means for measuring the resultant displacement. In the following, some of these features are elaborated.

4.3.1 Sample Translation

Desired locations are selected on the specimen while observing its surface through an optical microscope. The sample is then automatically translated to the indenter, and tests are performed at the desired locations. Translation stages are screw-driven. Theoretical resolution for site selection is 45 nm with a real accuracy of 1.5 μm. The motion of this stage is guided by highly pre-loaded, cross-roller bearing slides that provide excellent linearity and stiffness. Translating the sample while the indenter maintains in contact with the surface under a prescribed load is the basis for all instrumented scratch testing.

4.3.2 Force Application

Force is imposed on the indenter by passing current through a coil that sits within a circular magnet as illustrated in Figure 4.11. The force imposed on the indenter shaft in this way is directly proportional to the current passed

through the coil. The theoretical force resolution is 50 nN.

Table 4-3 Specifications of MTS nanoindenter[67]

Displacement resolution	<0.01 nm
Maximum indentation depth	00 μm
Maximum load	500 mN (50.8 gm)
Maximum load (w/high load system)	10 N (1 kg)
Position control	Robotic mouse
Load resolution	50 nN (5.1 μgm)

Figure 4.10: MTS Nano Indenter XP System

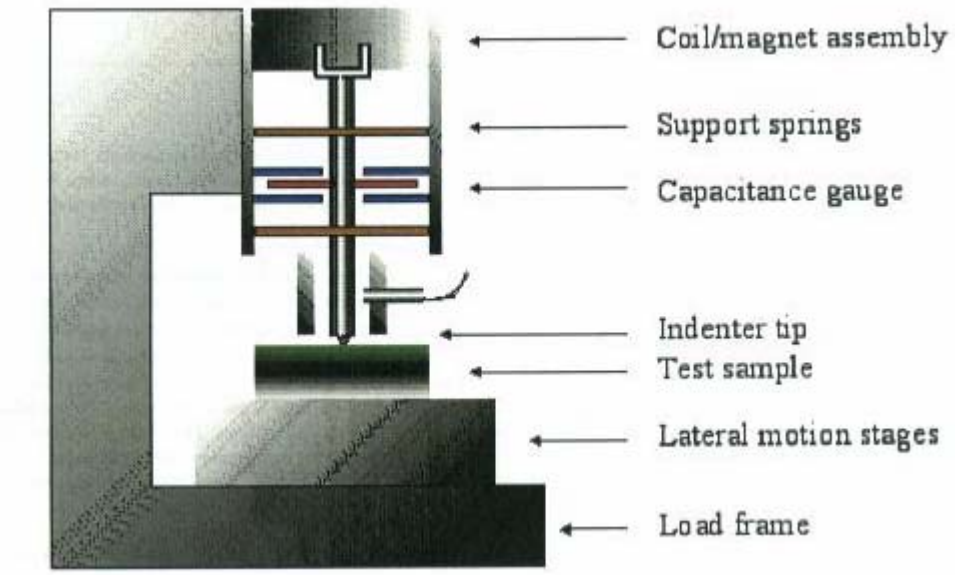

Figure 4.11: Schematic of a nanoIndenter system[67]

4.3.3 Displacement Sensing

The displacement sensing system consists of three-plate capacitive arrangement as shown in Figure 4.11. All three plates are circular disks. The two outside plates are fixed to the head and have holes in the center just large enough to accommodate the indenter shaft. The center plate is fixed to the indenter shaft and is free to move vertically between the two outside plates. The position of the indenter column within the gap is determined by observing the differences in voltage between the center plate and either of the two outside plates. The displacement sensor is calibrated at the factory using laser interferometry. The theoretical displacement resolution is < 0.01 nm. This plate-and-indenter assembly is supported by two leaf springs which are designed to have very low stiffness in the vertical direction and very high stiffness in the horizontal direction.

4.3.4 Indentation Tips

For reliable measurement of hardness by nanoindentation, two conditions need to be satisfied. First, an accurate function relating indentation depth to the projected area of contact is needed. Second, a plastically deformed indentation is required. The first calls for an effective way of determining the shape of the diamond tip; the second implies some minimum indentation depth before hardness may be accurately measured. A Berkovich indenter was used in this investigation.

4.3.5 Instrumented Indentation Testing (IIT)

Instrumented-indentation testing (IIT) was developed for probing the mechanical properties of materials at very low depths (<1 μm)[67]. IIT is ideal for mechanically characterizing thin films, coatings, and surface layers. Because indents can be positioned to within ~ 1 μm, it also provides the ability to map the spatial distribution of surface mechanical properties with good resolution. For example, one could map the mechanical properties within and around a weld site. Even when the material sample is sufficiently large to be tested by other means, IIT often remains the method of choice because it requires little or no sample preparation.

At its most basic level, IIT employs a high-resolution actuator to force an indenter into a test surface, and a high-resolution sensor to continuously measure the resulting penetration. One of the advantages of this technique is that the contact area under load can often be inferred from the continuous load-displacement data alone. In other words, the residual hardness impression does

not have to be directly imaged, thus facilitating mechanical property measurement at the sub-micrometer scale.

Hardness *(H)* and elastic modulus *(E)* are properties most frequently measured by IIT. As the indenter is driven into the material, both elastic and plastic deformations cause the formation of a hardness impression conforming to the shape of the indenter to some contact depth. As the indenter is withdrawn, only the elastic portion of the displacement is recovered. It is this recovery which allows one to determine the elastic properties of a material (see Figure 4.12).

Figure 4.13 presents a set of continuous load-displacement data. Some important quantities are the peak load and displacement, the residual depth after unloading and the slope of the initial portion of the unloading curve, S= *dP/dh.* Note that S has the dimensions of force per unit distance, and so it is also known as the elastic stiffness of the contact.

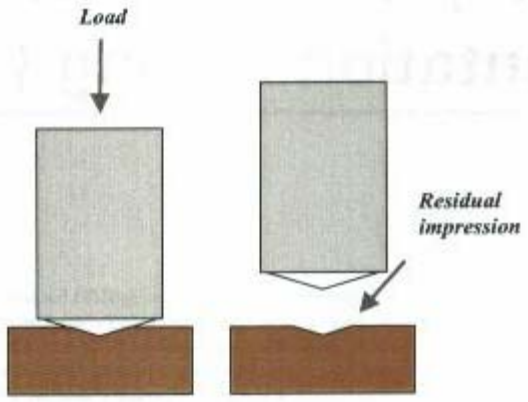

Figure 4.12: Indenter tip surface interaction[67]

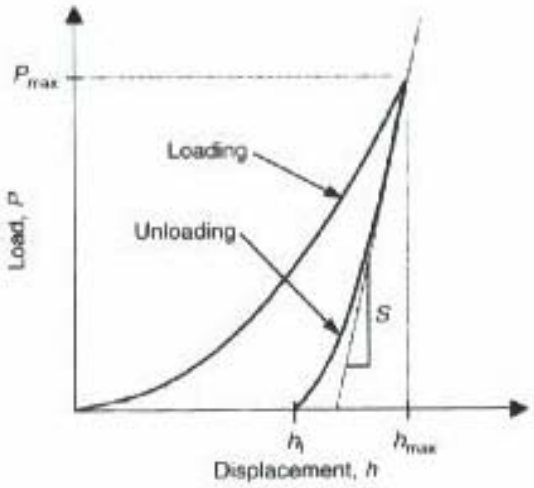

Figure 4.13: Typical load displacement curve[67]

The hardness of the test surface *(H)* is determined using equation

$$H = \frac{P}{A} \tag{4.16}$$

where P is the load applied to the test surface and A is the projected contact area at that load. The elastic modulus of the test sample, *E* is determined from the reduced modulus, E_r, given by:

$$E_r = \frac{(\sqrt{\pi}.S)}{2\beta\sqrt{A}} \tag{4.17}$$

where β is a constant that depends only on the geometry of the indenter. The elastic modulus of the test material, *E,* is calculated using the expression:

$$\frac{1}{E_r} = \frac{(1-\nu^2)}{E} + \frac{(1-\nu^2)}{E_i} \tag{4.18}$$

where ν is the Poisson's ratio for the test material and E_i and ν_i are the elastic modulus and Poisson's ratio, of the indenter, respectively. For a diamond

indenter, the elastic constants are E_i = 1141 GPa and ν_i = 0.07.

Equation 4.18 is based on elastic contact theory and holds for any indenter that can be described as a body of revolution of a smooth function. Because the equation was derived for an axisymmetric indenter, it formally applies only to circular contacts, and β =1. However, it has been shown that the equation works well even when the geometry is not axisymmetric, provided that different values of b̩ are used. For indenters with a square cross section, such as the Vickers pyramid, β = 1.012; for triangular cross sections, such as the Berkovich and the cube-corner indenters, β = 1.034.

4.3.6 Determination of the Contact Stiffness and Contact Area

From Eqns. 4.16 to 4.18, it is clear that in order to calculate the hardness and elastic modulus from indentation load-displacement data, one must have an accurate measurement of the elastic contact stiffness (S) and the projected contact area under load *(A).* One of the primary distinctions between IIT and traditional hardness testing is the manner in which the contact area is derived. Rather than by imaging, the area is established from an analysis of the indentation load-displacement data.

4.3.7 The Power Law Relationship

The most widely used method for calculating the contact area was developed by Oliver and Pharr[68]. Their data analysis procedure begins with fitting the load-displacement data acquired during unloading to the power-law relationship

$$P = B(h - h_f)^m \tag{4.19}$$

where *P* is the load applied to the test surface, h is the resulting penetration, *B* and m are empirically determined fitting parameters, and h_f is the final displacement after complete unloading (also determined by curve fitting). The unloading stiffness, S, is then established by analytically differentiating the above and evaluating at the maximum depth of penetration, $h = h_{max}$

$$S = \frac{Bm(h - h_f)^{m-1}}{h = h_{\max}} \tag{4.20}$$

Experience has shown that this equation does not always provide an adequate description of the entire unloading curve, especially for films on substrates. It is thus a prudent practice to determine the contact stiffness by fitting only the upper portion of the unloading data; fitting the upper 25% to 50% of the data is usually sufficient.

The next step in the procedure is to determine the depth over which the test material makes contact with the indenter, h_c. The contact depth, h_c, is generally different from the total penetration depth, and is estimated using

$$h_c = h - \frac{\varepsilon P}{S} \tag{4.21}$$

where ε is a constant which depends on the indenter geometry. For cones, ε is 0.72, and for spheres, ε = 0.75. There is ample justification for using ε = 0.75 for Berkovich and Vickers indenters as well. This is based on elastic contact theory but it works surprisingly well, even when the contact causes significant plastic

deformation. For example, a soft metal experiences very little elastic recovery as the indenter is withdrawn, and so the unloading curve is nearly vertical (very large S). Thus, the second term in this equation is small and the contact depth is approximately equal to the total depth as one might expect. The contact depth is always less than the total depth of penetration; it cannot account for the plastic phenomenon of pile-up.

Finally, the projected contact area, *A,* is calculated by evaluating an empirically determined area function at the contact depth, h_c*;*

$$A = f(h_c) \tag{4.22}$$

i.e. the area function, *f(d)*, also known as the shape function or tip function, relates the cross-sectional area of the indenter to the distance, *d,* from its tip.

4.4 Tensile Sub-stage with AFM

To study the effect of tensile stresses on indentation, a tensile testing substage developed for *in-situ* SEM [manufactured by Ernest F Fullam Inc. (No.18211)], was adapted to work in conjunction with the Digital Instruments (D3100) atomic force microscope.

The tensile testing substage can exert a maximum load of 1000 lb (454 Kg) on a suitable test specimen. Figure 4.14 (a) is a photograph of the tensile stage. Important elements of the stage are: (1) two left-right combination screws, (2) two gripping heads with removable grips (3) a Honeywell Sensotec sub-miniature load cell (Model-11) with high resolution and a maximum load of 1000 lbs and (4) a linear shrinkage curve (LSC) displacement transducer to measure the change in length of the tensile specimen. Loads are applied to the stage using a detachable drive motor assembly through a flexible coupling and telescoping square drive shafts. The motor speed can be varied from 0 to 300 rpm. The total gear reduction of the substage is 600:1 which translates to ~7 μm of sample strain or elongation for each revolution of the shaft. In this investigation experiments were performed at an average motor speed of ~120 rpm which translates to an elongation rate of ~14 μm/s.

To study the deformation of a tensile sample, the tensile stage was mounted under an AFM [see Figure 4.14 (b)]. The existing X-Y stage with the AFM (seen in Figure 4.2) was removed and a new stage that accommodates the tensile stage was fabricated. The weight and the roughness of the surface in contact with the main granite stage of the AFM assembly of the new stage were

similar to that of the original AFM stage. The weight of the stage was an important factor in its development as this contributes to the rigidity of the entire system and thereby facilitating in the fine X-Y translations.

The tensile stage also underwent some modifications so that it can be accommodated with the new AFM stage. This setup can be easily disassembled so that the AFM can be used for other experiments. The new AFM stage with the tensile stage can be placed under the AFM in such a way that the AFM tip cantilever would always be perpendicular to the tensile loading axis.

The speed of the drive motor translates to the rate at which the tensile sample is stretched (strain rate) and this is set using a controller. The strain and the load applied are constantly measured using digital readouts. The tensile test can be stopped at any time so that the surface of the tensile surface can be examined using the AFM. Since the mechanism used to stretch the sample uses left and right combination screws that simultaneously move the grippers in opposite directions and thus stretch both sides of the sample equally, very little displacement of the area being examined occurs relative to the AFM tip. Such displacement can be corrected using the modified X-Y AFM stage.

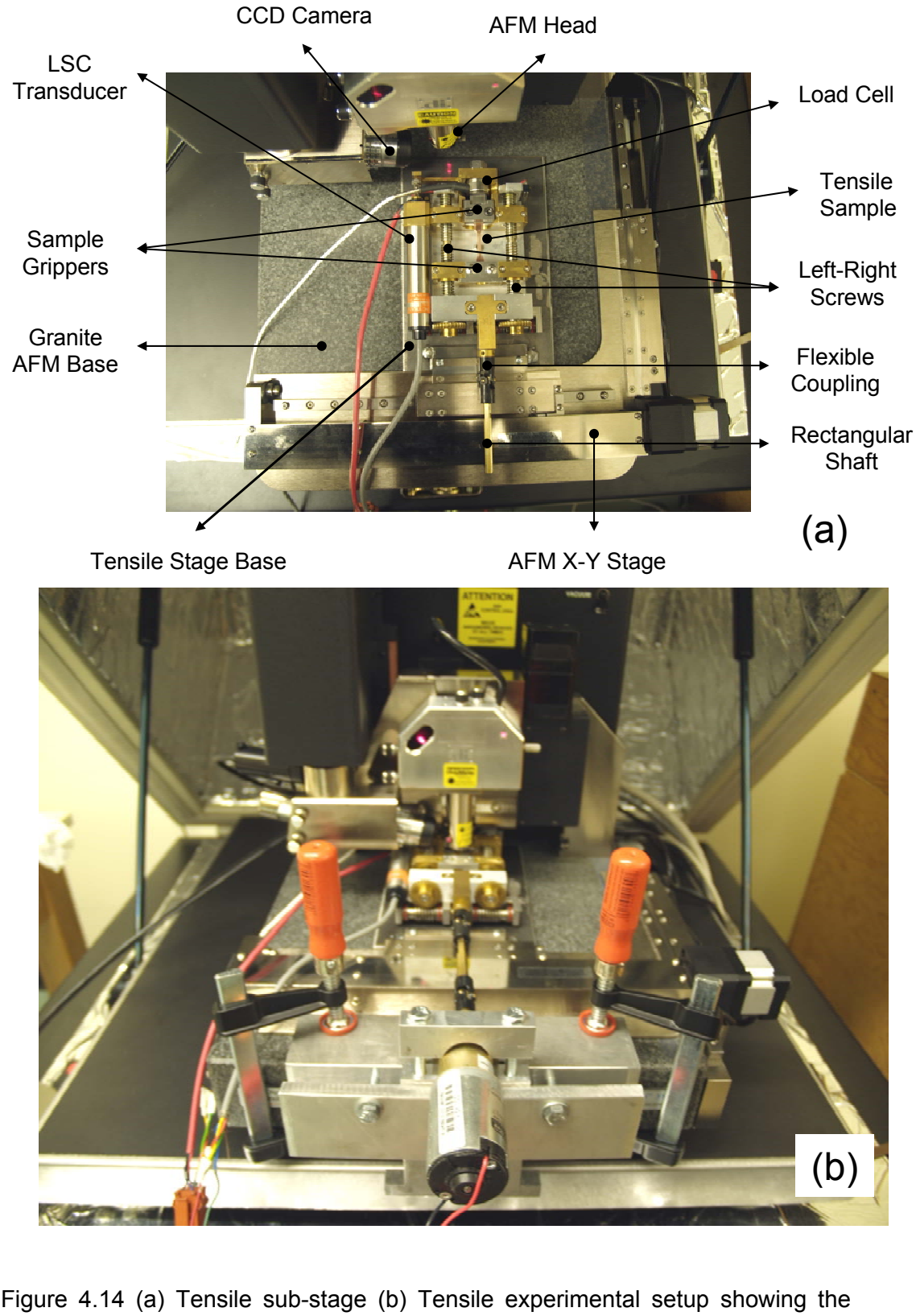

Figure 4.14 (a) Tensile sub-stage (b) Tensile experimental setup showing the AFM, tensile sub-stage and motor assembly

4.5 Sample preparation

The tensile sample used has the following dimensions: length 45 mm, width 6.35 mm and thickness 3 mm. The gauge length is 19 mm with a square cross section of 3 mm. The samples have a grip length of 12.7 mm on both sides with radius corners at the smaller cross section to eliminate stress concentrations. Experiments were performed on electrolytic tough pitch copper (UNS C11000 H01 temper). The samples were machined as per the specifications of Ernest F Fullam Inc. The tensile samples were used as supplied by the manufacturer. Any residual strains present in the sample as a result of processing were not considered in this investigation as this did not affect the strain estimation method being developed. Some nominal properties of the tensile sample (as supplied by the manufacturer from online database) are given in Table 4-4.

One side of the tensile specimen was polished down gradually by using 200 - 600 grit coated abrasive papers and finally with a 0.3 μm alumina powder suspension. The sample was then boiled in isopropyl alcohol (which has a boiling point of 82ºC) for 5 minutes in a beaker and then ultrasonicated by placing the same beaker in warm water to remove any grease or other foreign material on the surface.

The dried sample was then electro-polished in a bath with 85% orthophosphoric acid and distilled water in a 4.7:1 ratio[69] using an Electromet III (Buehler Ltd.) polishing cell, Several electropolishing experiments were performed based on the recommendations given in the ASM Handbook[69] to

obtain a polished surface for AFM examination. After electropolishing, the tensile samples were washed in distilled water, then in isopropyl alcohol, and then air dried.

Table 4-4 Mechanical properties of ETP copper (C11000) tensile specimen[70]

Property	
Heat treatment	H01 Temper
Chemical composition	99.9% Cu 0.04% O
Hardness, Rockwell F	70
Tensile Strength, Ultimate, MPa	260
Tensile Strength, Yield, MPa	205
Modulus of Elasticity, GPa	115-130
Poissons Ratio	0.33
Shear Modulus, GPa	44-49
Shear Strength, MPa	170

AFM images of surfaces obtained under different electropolishing conditions are shown in Figure 4.15. Electropolishing for longer durations and different voltages resulted in the formation of surfaces that appeared shinier to the naked eye but on examination under the AFM revealed small etch pits and asperities [see Figures 4.15 (b) – (e)]. The best surface for nanoindentation was obtained when electropolishing was performed at ~1.7 V for 15 - 30 sec [see Figure 4.15 (f)]. This removed small scratches and burrs but did not remove the bigger scratches. Even though the surface showed some scratches when viewed under an optical microscope, examination using an AFM showed that surface was relatively smooth in the regions of interest. Table 4-5 shows the roughness values obtained for the images in Figure 4.15.

Depending on the experiments being performed, some samples were etched with an acidified ferric chloride etchant[71]. Figure 4.16 shows the images of etched copper tensile samples obtained using a MicroXam optical Interference microscope and an AFM at different magnifications. The grains are large and equiaxed with an average size of about 20-40 μm.

Table 4-5 Roughness values for electropolised surfaces

Electopolishing Conditions	Mean Roughness Ra (nm)	RMS Rq (nm)
After polishing using 0.3μm alumina suspension	8.56	11.26
2V- 5min	5.27	7.07
2V – 10min	3.43	4.6
2V – 15min	2.76	3.35
1.7V – 45sec	1.55	1.97
1.7V – 15sec	0.85	1.09

4.6 . Experimental procedure

Six types of experiments were performed on the tensile samples after they were electropolished. They are briefly presented in the following.

4.6.1 Tensile testing of samples to determine their stress-strain relationship

The tensile specimen was mounted on the tensile substage between the grippers in such a way that the grippers covered about 10 mm of the sample on either side. The tensile stage has a limit switch that can be set to the required length. After each tension experiment, the motor can be driven in the opposite direction to bring the grippers closer. The motor stops when the required length is reached after the limit switch is activated. This ensures that the length of

specimen in between the grippers is the same for all experiments. Once the tensile sample is mounted and aligned, the grippers are tightened and the experiment is performed. As mentioned earlier, the elongation rate at which the tension experiments were conducted was ~14 μm/sec. The loads and displacements are constantly recorded during the experiment and photographs of the tensile specimen were also taken at different stages of extension.

4.6.2 Examination of the tensile sample surface using optical interference microscope (MicroXam)

After electropolishing and etching, the tensile sample is mounted on the tensile stage as described earlier. The stage is positioned under the microscope and the experiment is started. Images were acquired at various stages of deformation at magnifications of 100x and 500x after the drive motor is stopped.

4.6.3 *In-situ* examination of the tensile sample surface using atomic force microscope (AFM)

The electropolished sample is mounted on the tensile stage and installed under the AFM head. The drive motor was stopped at various stages of the tensile experiment and the AFM tip (silicon) was engaged to image the surface. Several images at different magnifications were obtained by scanning the areas of interest.

4.6.4 AFM imaging of nanoindents made with MTS nanoindenter

Using a Berkovich indenter and an MTS nanoindenter system, several nanoindentation experiments were made on the tensile sample. They were made

in such a manner that one of the sides of the indenter was parallel to the length (tensile axis) of the sample. After the nanoindentations were made, the sample was mounted on the tensile stage and installed under the AFM head. The nanoindents were then located with the help of AFM's CCD camera and the X-Y stage. The nanoindents on the surface of the tensile sample were then imaged using an AFM, as described earlier.

4.6.5 Nanoindentation and imaging using AFM

In this experiment a set of indentations were made on the electropolished sample mounted on the tensile stage using a tetrahedral diamond AFM indenter. After the indents were made, the tension experiment was started and the indents were imaged at various stages of the experiment after stopping the drive motor. AFM images were acquired as described earlier.

4.6.6 Nanoindentation and imaging of tensile sample at various stages of the tensile experiment using AFM

This experiment differs from experiments in Section 4.6.5 in that the nanoindentations were conducted on the sample surface every time the drive motor was stopped. After the indentation was made, the indents were imaged using AFM.

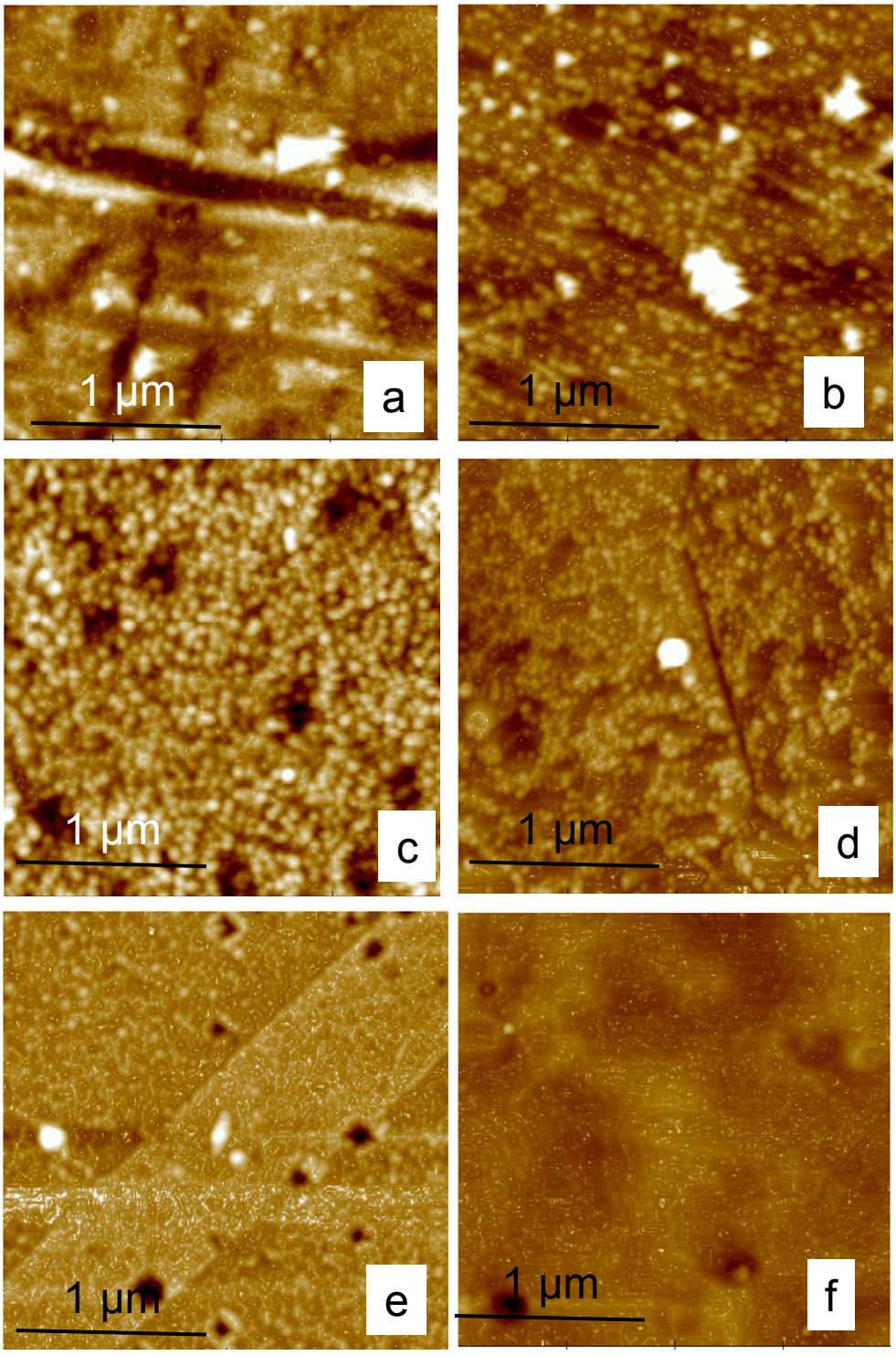

Figure 4.15: AFM 3D images of the surface of C11000 copper after electropolishing using an aqueous solution of ortho-phosphoric acid. (a) polishing using 0.3 µm alumina suspension (b) electropolishing at 2 V- 5 min (c) electropolishing at 2 V – 10 min (d) electropolishing at 2 V – 15 min (e) electro- polishing at 1.7 V – 45 sec (f) electropolishing at 1.7 V – 15 sec

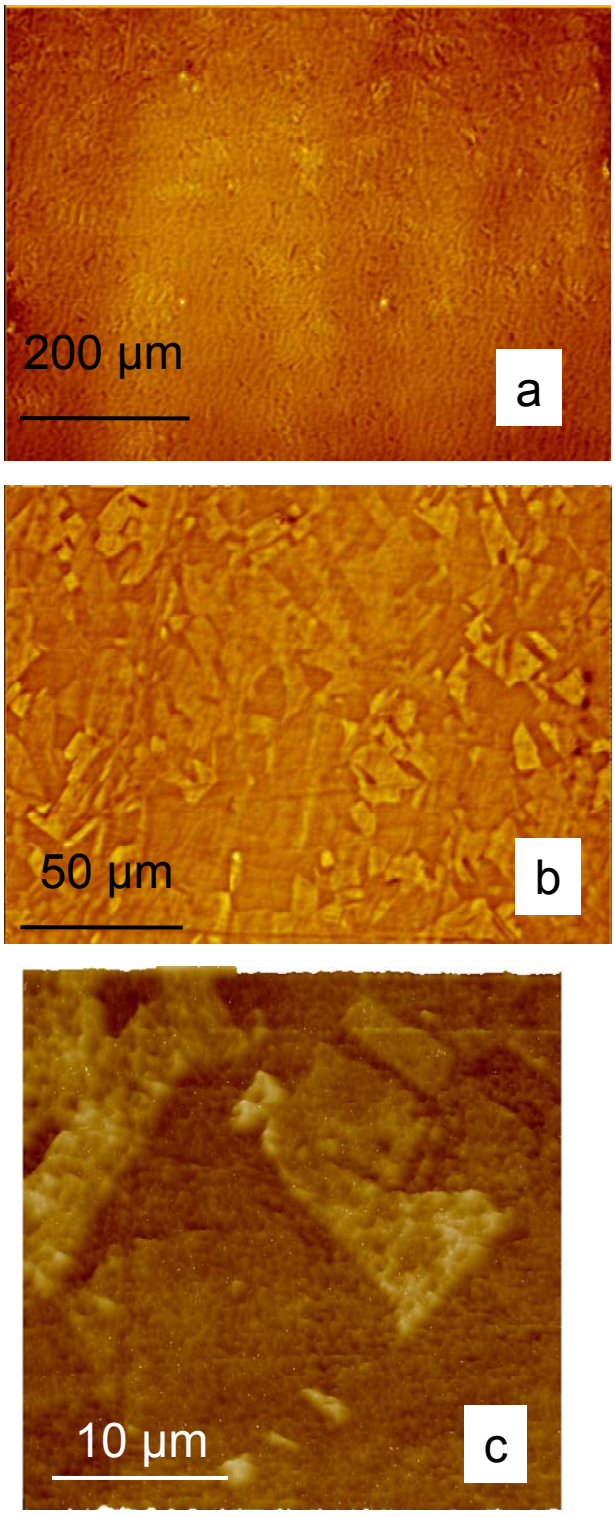

Figure 4.16: Images of the surface of H01 temper copper (C11000) after etching 1) & 2) MicroXam images 3) AFM images

CHAPTER 5

EXAMINATION OF THE TENSILE SAMPLE SURFACE USING MICROXAM AND AFM

5.1 Introduction

The tensile test is often used to provide basic design information on the strength of materials. In a typical tension test, the specimen is subjected continuously to uniaxial tensile force and the load and elongation of the specimen are recorded.

The engineering stress is obtained by dividing the load by the original cross sectional (gage) area of the tensile specimen. As mentioned earlier, the cross sectional dimensions of the gauge part of the tensile sample is 3 mm x 3 mm. Thus, the effective cross sectional area is 9 mm^2. The engineering stress, σ is given by

$$\sigma = \frac{P}{A_0} \tag{5.1}$$

where *P,* the applied tensile load and A_0 the original gage cross section.

Strain used in an engineering stress-strain curve is the average linear strain ε, which can be obtained by dividing the elongation of the gage length by the original length L_0. L is the length of the elongated sample.

$$\varepsilon = \frac{L - L_0}{L_0} \tag{5.2}$$

The magnitude and shape of the stress-strain curve of any metal depends on its processing history with regards to its composition, microstructure, heat treatment, and prior plastic deformation. Other factors that can influence the behavior are the temperature at which the experiment is performed and strain rate.

5.2 Tensile testing of polycrystalline copper to determine stress-strain behavior

Tension experiments were performed on several polycrystalline copper (C11000) samples to determine their stress - strain behavior. Figure 5.1 is a typical engineering stress- strain relationship of an ETP copper (C11000 H01 temper) sample. Since all samples tested were from the same raw material, their stress-strain behavior varied very little. Copper is an FCC metal and the stress-strain curve obtained is typical of FCC metals showing long region where strain is uniform.

The estimation of the stress at which yielding or plastic deformation begins depends largely on the sensitivity of the strain measurements. Since for most materials the transition from elastic to plastic region happens gradually, it is very difficult to determine exactly when yielding takes place. Depending on the sensitivity of the strain measurements and the intended use of the data, several criteria for the initiation of yielding are used. In the United States, the most common method of determining the yield strength is the offset yield strength method in which a line is drawn parallel to the elastic part of the stress-strain

curve at 0.02 % strain which is typically linear. The yield strength of the tensile samples used in this experiment was determined to be ~190 MPa which is very close to the values provided by the manufacturer (see Table 4-4).

The ultimate tensile strength is the maximum load divided by the original cross sectional area of the tensile specimen. The ultimate tensile strength obtained for the tensile specimens in this investigation was ~ 250 MPa.

When the load exceeds the yield strength of the material, it begins to deform plastically which means that if the load applied is released the test specimen wouldn't regain its original shape. Due to strain hardening, the stress required to cause continued plastic deformation increases with increasing plastic strain. The cross section of the specimen decreases uniformly until the ultimate tensile strength is reached. The tensile samples have relatively low elongation perhaps due to the H01 temper which is ¼ hard temper (cold worked)

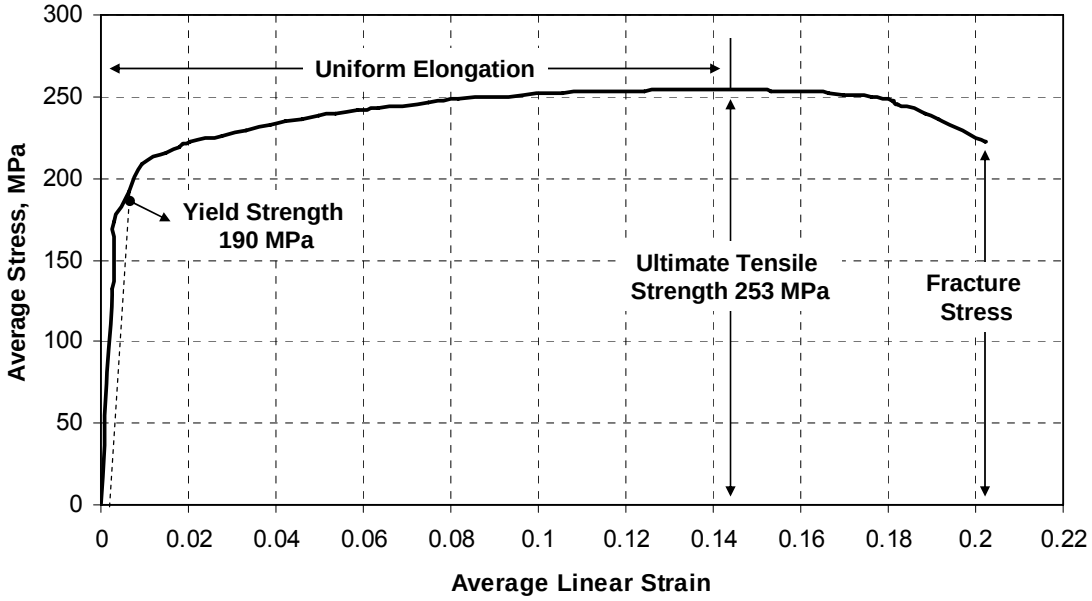

Figure 5.1 Engineering stress – strain relationship of ETP polycrystalline copper (C11000 H01 Temper)

Strain hardening more than compensates for the decrease in cross-sectional area and this results in an increase in the engineering stress with increase in strain. A point is reached when decrease in the specimen cross-sectional area is more than the increase in deformation load due to strain hardening. This usually happens at the weakest area in the specimen resulting in plastic deformation being concentrated in that region as further loading is encountered (necking). The load necessary to cause plastic deformation decreases and necking of the weak area begins to occur. Here, the cross-sectional area is decreasing more rapidly than the increase in strain hardening with deformation load. Eventually, the necked area thins down and the specimen fractures. Figure 5.2 shows photographs of the tensile sample at various stages of the tensile testing.

Loading conditions	Photographs showing deformation
a) Electropolished and etched tensile sample	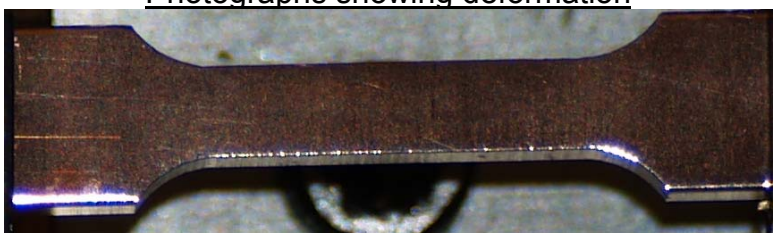
b) 178 MPa stress and 0.003 strain	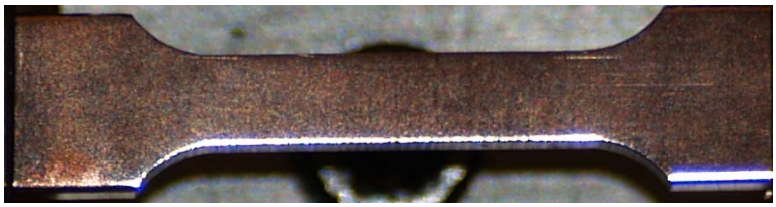
c) 190 MPa stress and 0.006 strain – Elastic Limit	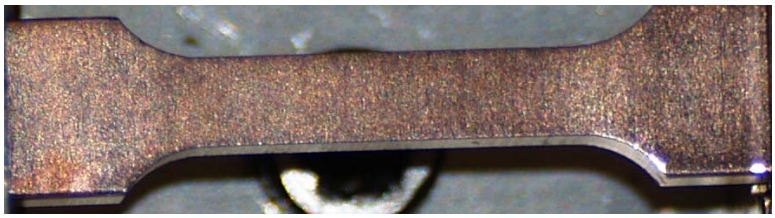

d) 226 MPa stress and 0.027 strain

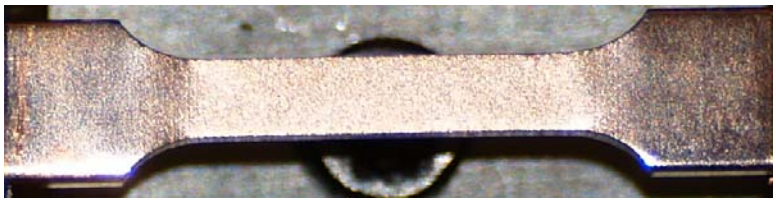

e) 234 MPa stress and 0.042 strain

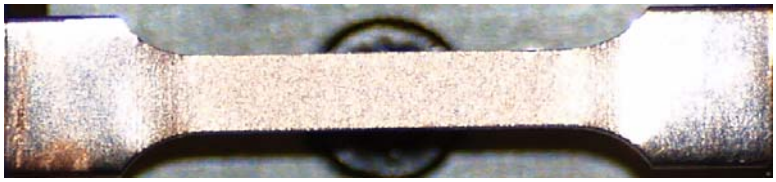

f) 243 MPa stress and 0.063 strain

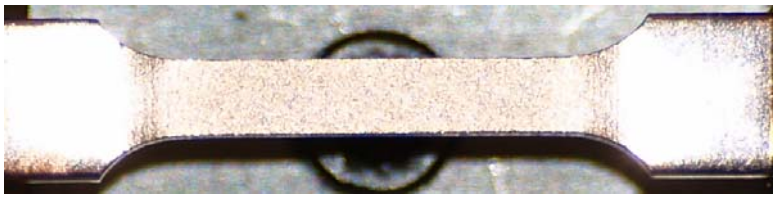

g) 248 MPa stress and 0.081 strain

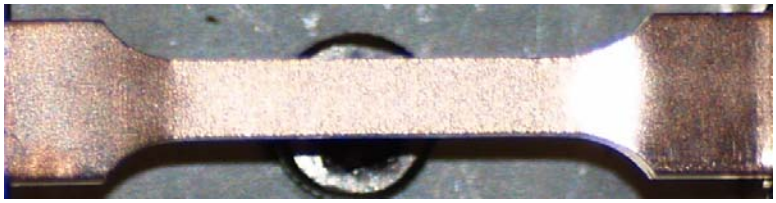

h) 252 MPa stress and 0.10 strain

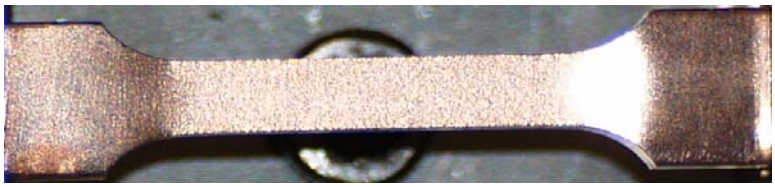

i) 254 MPa stress and 0.137 strain -UTS

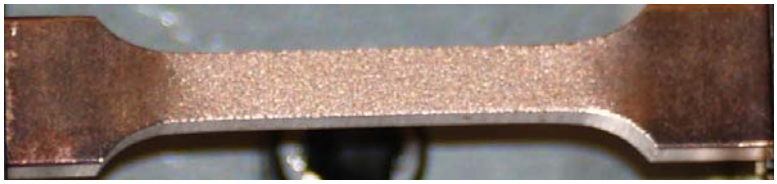

g) 253 MPa stress and 0.016 strain - Necking

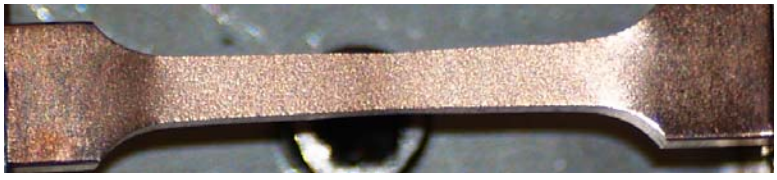

h) 236 MPa stress and 0.19 strain

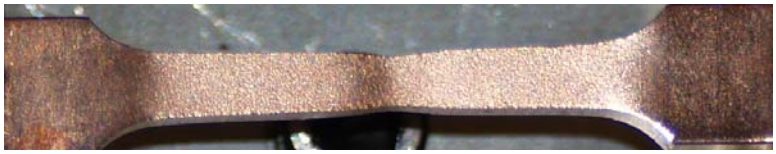

Figure 5.2 : Photographs of the deformation of the polycrystalline copper (C11000) under tensile loading

5.3 Examination of the surface using Optical Interference Microscope

An optical interference microscope (MicroXam) was used to image the surface of the tensile sample as the load was increased. Images were acquired at strain intervals similar to the ones shown in Figure 5.2, discussed earlier. In this case, the images were acquired after stopping the drive-motor. The micrographs acquired are shown in Figures 5.3 though 5.5.

Figures 5.3 (a) and (b) are MicroXam optical interference images of the surface of the copper tensile sample taken at two magnifications namely 100x and 500x, respectively. The grain structure can be seen clearly. The surface has been electropolished and etched as described earlier in Section 4.5.

During elastic deformation of the tensile sample there is stretching, rather than breaking of the bonds between the atoms. Thus, when the applied load is removed, the material will return to its original un-deformed condition. In polycrystalline materials the load at which elastic deformation ends is not well defined. As discussed earlier, the yield strength was determined to be ~190 MPa. Figure 5.3 (c) is a MicroXam image of the surface acquired at this stress. No deformation is seen in the micrograph at 500x [see Figure 5.3 (d)]. Plastic deformation, on the other hand involves breaking of bonds and making of new bonds and is therefore permanent because of the generation and propagation of dislocations. The forces involved in the breakage of the bonds of all the atoms in a crystallographic plane simultaneously is very high and therefore the movement of dislocations in metals allow atoms in crystal planes to slip at much lower stress levels. Dislocations move through the material by localized making and breaking of bonds and this reduces the yield stress. Plastic deformation thus involves

sliding or slipping layers of atoms over each other by a shearing process that occurs as close as possible to the plane of maximum shear stress. In the present case this is at 45º to the tensile axis,. The more closely packed the atoms are, the easier it is for the layers of atoms to slide. Shearing thus takes place in the close-packed plane and along the close-packed direction which are closest to the location of maximum shear stress. Figure 5.3 (e) is a micrograph of the surface soon after yielding has commenced at ~0.02 average linear strain. Some texturing of the surface can be seen. An image acquired at 500x shows that some slip systems have been activating in some grains resulting in the formation of slip bands. Single metal crystals elongate slightly when stressed in tension beyond its elastic limit and this results in the formation of a step on the surface showing relative displacement of a part of the crystal with respect to the remaining and this stops the elongation.

Most of the materials used in engineering applications are polycrystalline which means there are several crystals or grains within the material which are oriented in slightly different directions from one grain to another. Different crystals experience different patterns of slip activity because of the differences in their orientations. Several parallel slip planes group together to form slip bands that appears as a single line under an optical microscope. These are, in fact, made up of closely spaced parallel slip planes that are some 100 atom layers apart while the gaps between the slip bands are often ~10000 atom layers. All grains in a polycrystalline material do not generally undergo plastic deformation at the same time during the early stages of yielding. The grains that undergo

deformation first are the ones whose orientations have slip planes that are ~ ±45º to the tensile axis.

With increasing loads, additional steps are formed, each requiring a higher stress. The energy required to move is lowest along the densest planes of atoms and so dislocations have a preferred direction of travel that result in slip occurring along parallel planes within the crystal.

As the deformation increases, the dislocations tend to move simultaneously and this increases the probability of dislocations becoming entangled resulting in dislocation pile-ups that make further plastic deformation more difficult. The stress required to produce further deformation is increased resulting in strain hardening. This is a period during which the strain is uniform. Figures 5.4 (a) to (f) are MicroXam images of the surface at strain ranges of 0.04 to 0.1. The images show that the surface textures are getting progressively rougher. More and more grains have slip bands and the grain boundaries begin to vanish as can be seen from the MicroXam images acquired at a magnification of 500x. Figures 5.5 (a) and (b) were acquired under maximum load at ~0.12 strain. Progressive increase in load induces the formation of microvoids after large plastic deformation. Necking occurs and further elongation is restricted to the necked region. Figures 5.5 (c) and (e) are MicroXam images of the surface, after necking is initiated. A small curvature can be seen showing that the sample has begun to neck. Surface appears to be relatively smoother as the grain boundaries cannot be seen anymore. Microvoids form usually due to decohesion between the precipitates and the matrix or fracture of precipitates. With

increasing deformation, the microvoids coalesce and final failure occurs. Microvoid formation can be seen in Figure 5.5 (f) which was acquired at a strain of ~0.018, just prior to fracture. Since microvoid formation is the result of plastic deformation, failure occurs in the plane of maximum plastic deformation. This is the plane of maximum shear stress which is at 45º to the tensile axis.

5.4 Estimation of strains from MicroXam images

A polycrystalline sample under tension encounters an increase in length in the tensile direction and a decrease in area in the transverse direction. As mentioned earlier different grains with varying orientations in a tensile sample experience varying deformation patterns under an applied tensile load. Therefore, depending on the orientation, an individual grain might experience an increase or decrease in length in the tensile loading direction[72]. Furthermore, strains experienced by individual grains in a polycrystalline material could be different from the global strain experienced by the tensile sample as a whole. As discussed in the introduction, strain in materials can be determined using several techniques, one of which is digital image correlation (DIC). In this technique digital images obtained at various stages of deformation are compared using a software program that examines the relative movements of features in the images to determine strain. A brief description of DIC is given in Section 5.4.1.

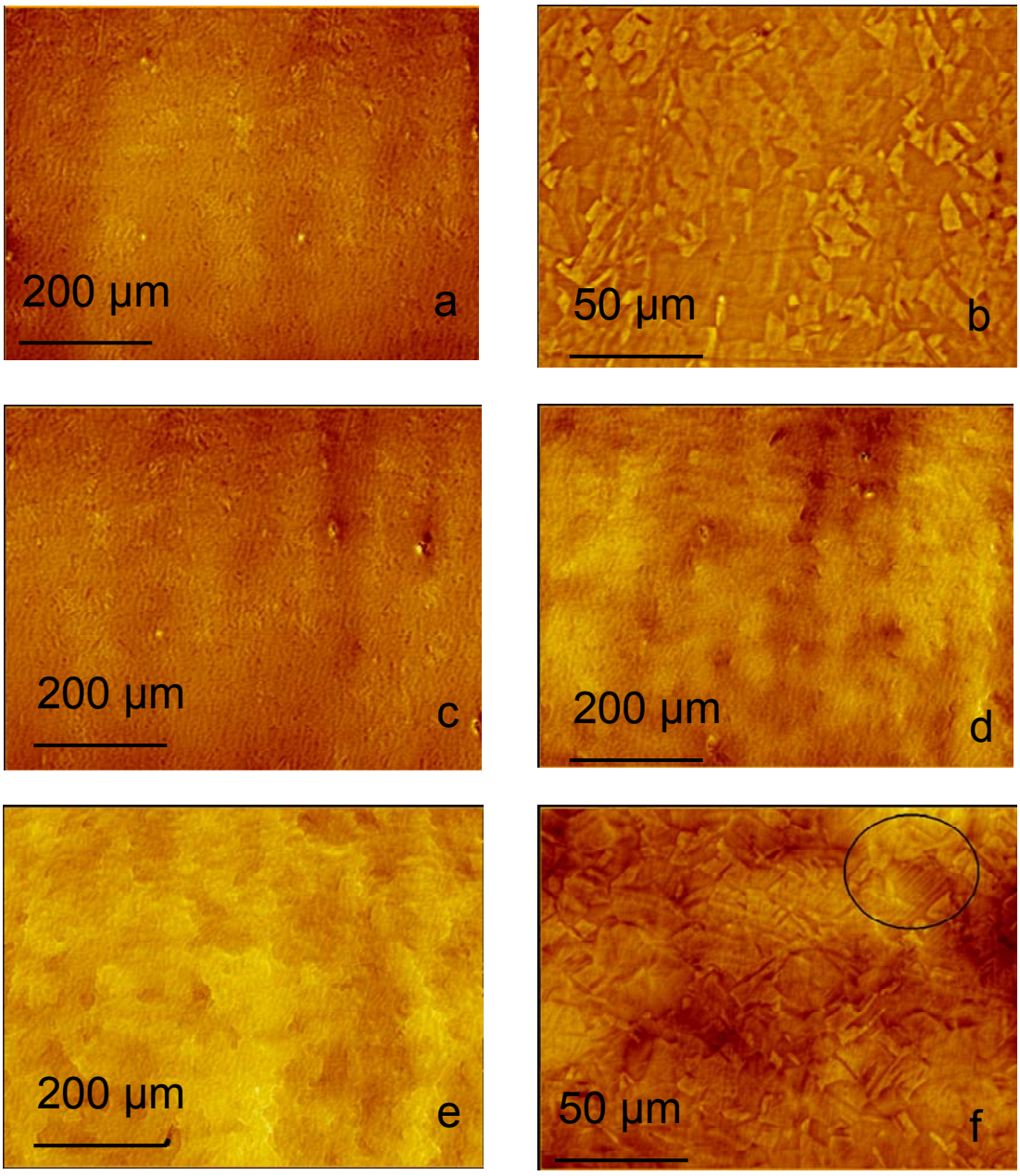

Figure 5.3: MicroXam images of the surface of C11000 copper under tension (a) electropolished and etched surface at 100x (b) at 500x showing the micro structure (c) 100x Image at 0.006 strain – elastic limit (d) beginning of yielding ~0.01 – 100x (e) 100x image 0.02 strain (f) same area at 500x

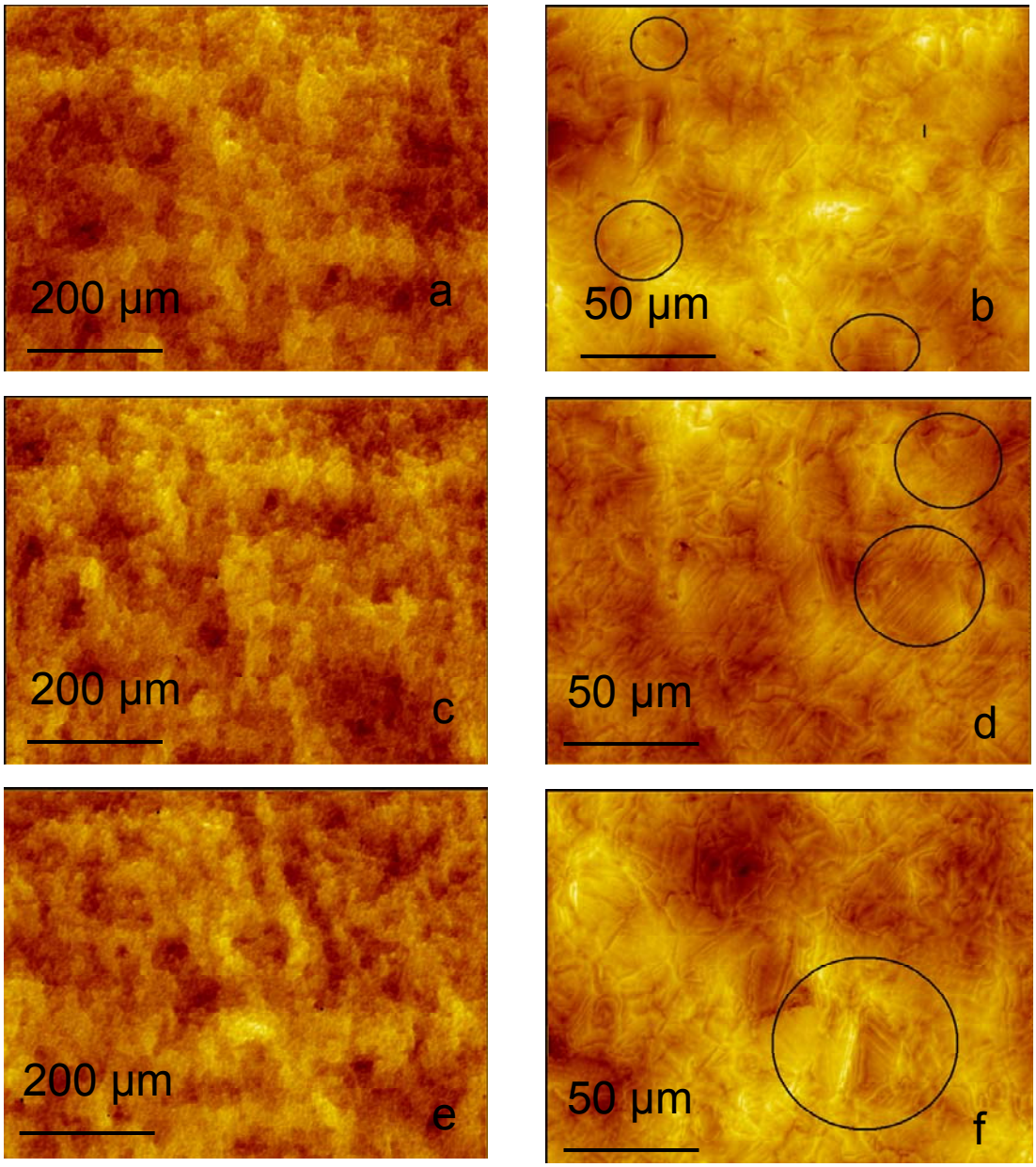

Figure 5.4: MicroXam images of the surface of C11000 copper under tension (a) 100x image 0.04 strain (b) at 500x showing more slip lines (c) 100x Image at 0.07 strain (d) same area at 500x (e) 100x image ~0.1 strain (f) At 500x – breakdown in grain structure

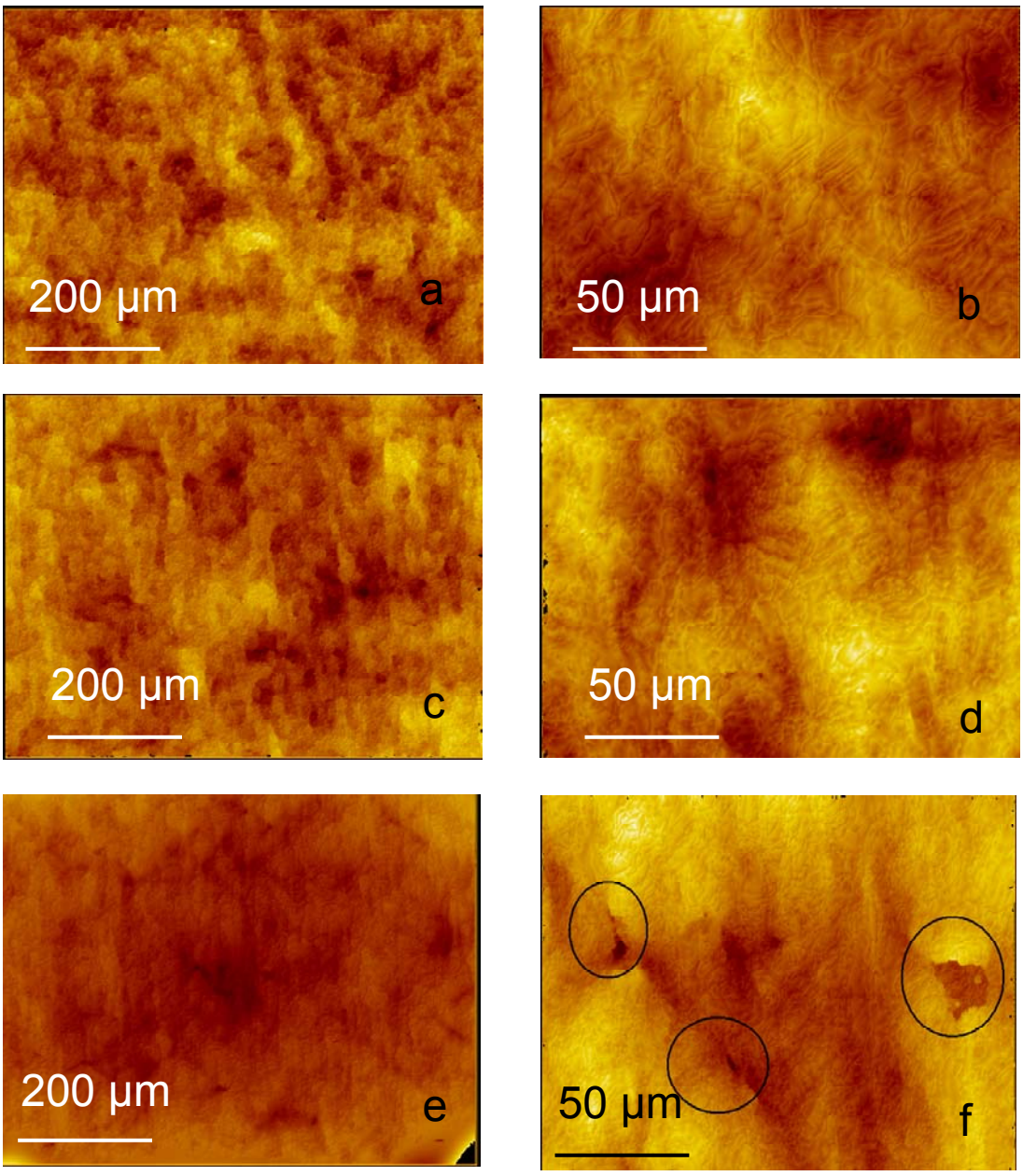

Figure 5.5: MicroXam images of the surface of C11000 copper under tension (a) 100x image 0.12 strain – maximum load(b) at 500x Grain boundaries are not seen clearly (c) 100x image at 0.14 strain – beginning of necking (d) same area at 500x (e) 100x image ~0.18 strain – before fracture (f) at 500x – microvoids can be seen

Digital image correlation (DIC) method can be used to measure surface displacements and thesis gradients in materials undergoing deformation. In this investigation, the DIC method developed by Lu and Cary[63] has been used. This method tracks the gray value pattern in small neighborhoods (subset of pixels) during deformation. DIC is performed between the subset in the reference area and its image in the deformed area. Typical subset regions are between 10 x 10 pixels and 41 x 41 pixels in size. The software incorporating this method works well with small displacements (first order displacements) as well as relatively large displacements where second order displacements are also present.

A common source for obtaining images used in this technique is an optical microscope. Variations in the images as a result of external disturbances and the imaging tool (light) are minimal[63]. Scanning electron microscope (SEM) images obtained at various stages of deformation have also been used for DIC[73]. Images obtained using AFM usually have noise that are a result of external sources such as vibrations in the air (temporal noise) and noise that is a result of the temporal noise which is translated into inconsistency or uncertainty between repetitive scans. Use of low pass filters on the images obtained, usually takes care of some of these problems[74].

Three Vickers indents were made on a polycrystalline copper tensile sample using a micro-indenter. The sample was then mounted on the tensile testing stage and *in-situ* testing was performed under an optical interference microscope (MicroXam). Sets of two images were acquired at various stages

during tensile loading. The dimensions of the images acquired were ~ 800 μm x 600 μm and ~ 150 μm x 125 μm.

Figures 5.6 through 5.9 are MicroXam images acquired at a magnification of 100x (800 μm x 600 μm) at global strains in the range of 0 to 0.14. The three Vickers indents were used as reference points so that the same area could be imaged at different stages. Figure 5.6 is a MicroXam image of the electropolished and etched copper surface just prior to the commencement of loading. Several equiaxed grains with twins can be seen. Figures 5.7 (a) through (c) are images acquired when the global strains were ~ 0.003 to 0.01. A small degree of deformation can be seen in Figures 5.8 (a) to (c) which were acquired when the strains registered by the linear shrinkage curve (LSC) were ~ 0.03, 0.06, and 0.08, respectively. The set of images in Figure 5.9 were acquired at global strains of 0.1 to 0.14. A significant amount of deformation is visible in all these images. Figure 5.9 (c), taken at 0.12 strain shows that the indents have also deformed.

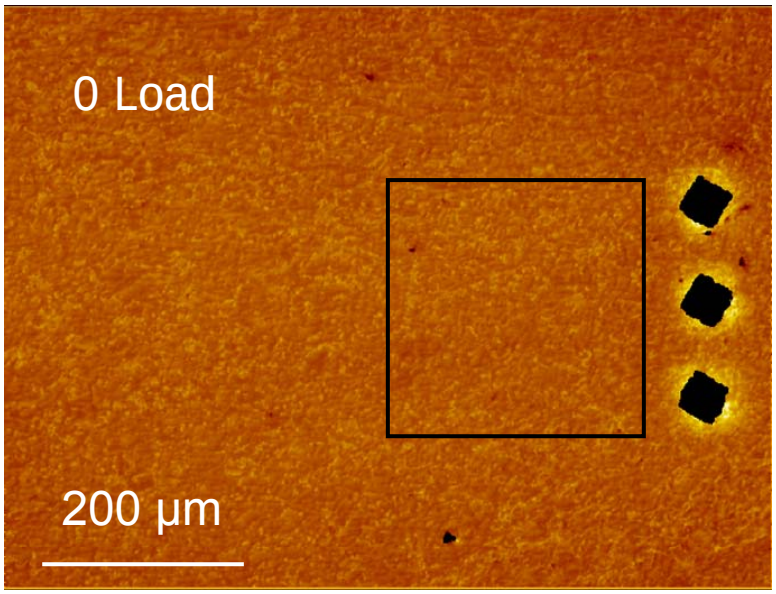

Figure 5.6: MicroXam image (800 μm x 600 μm) of the surface of C11000 copper under tensile load electropolished and etched surface at 0 load

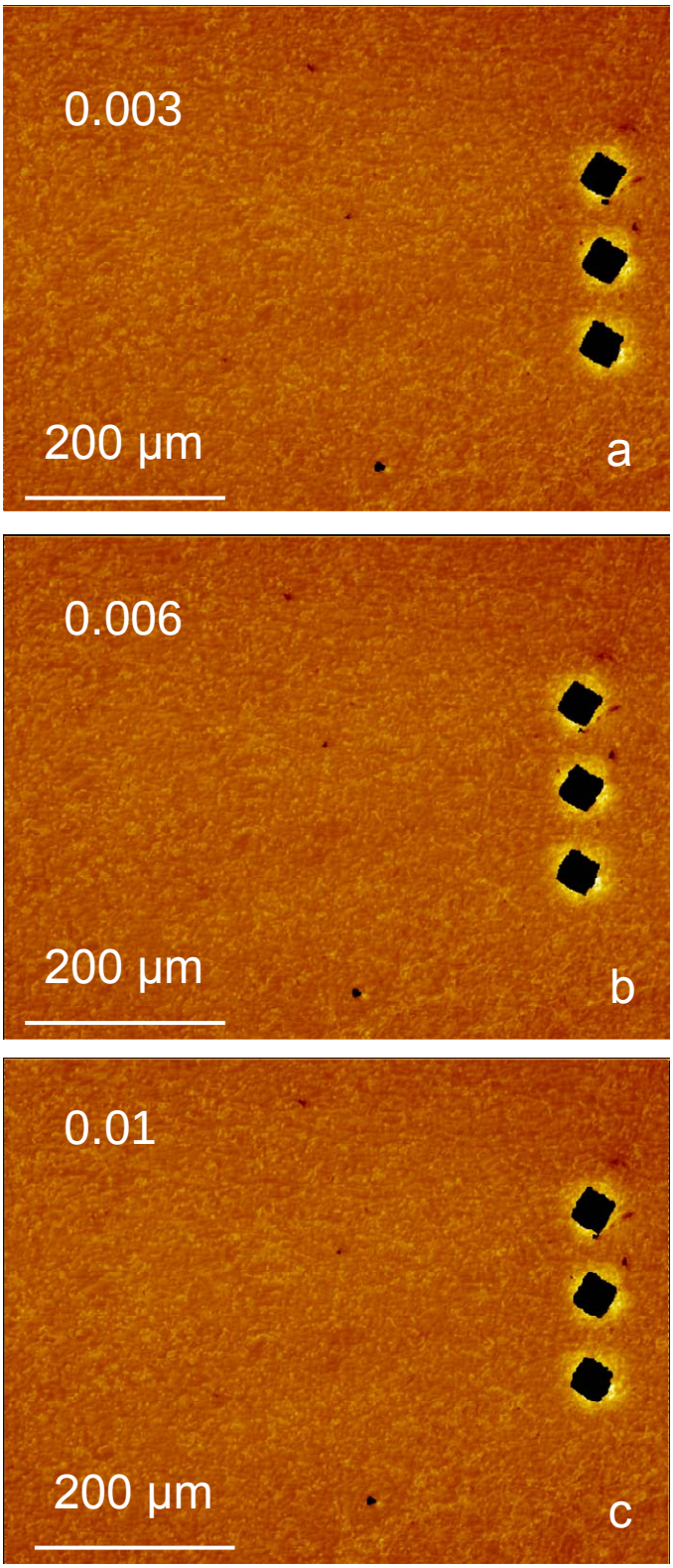

Figure 5.7:MicroXam images (800 µm x 600 µm) of the surface of C11000 copper under tensile load (a) 0.003 strain (b) Image at 0.006 strain (c) 0.01 strain

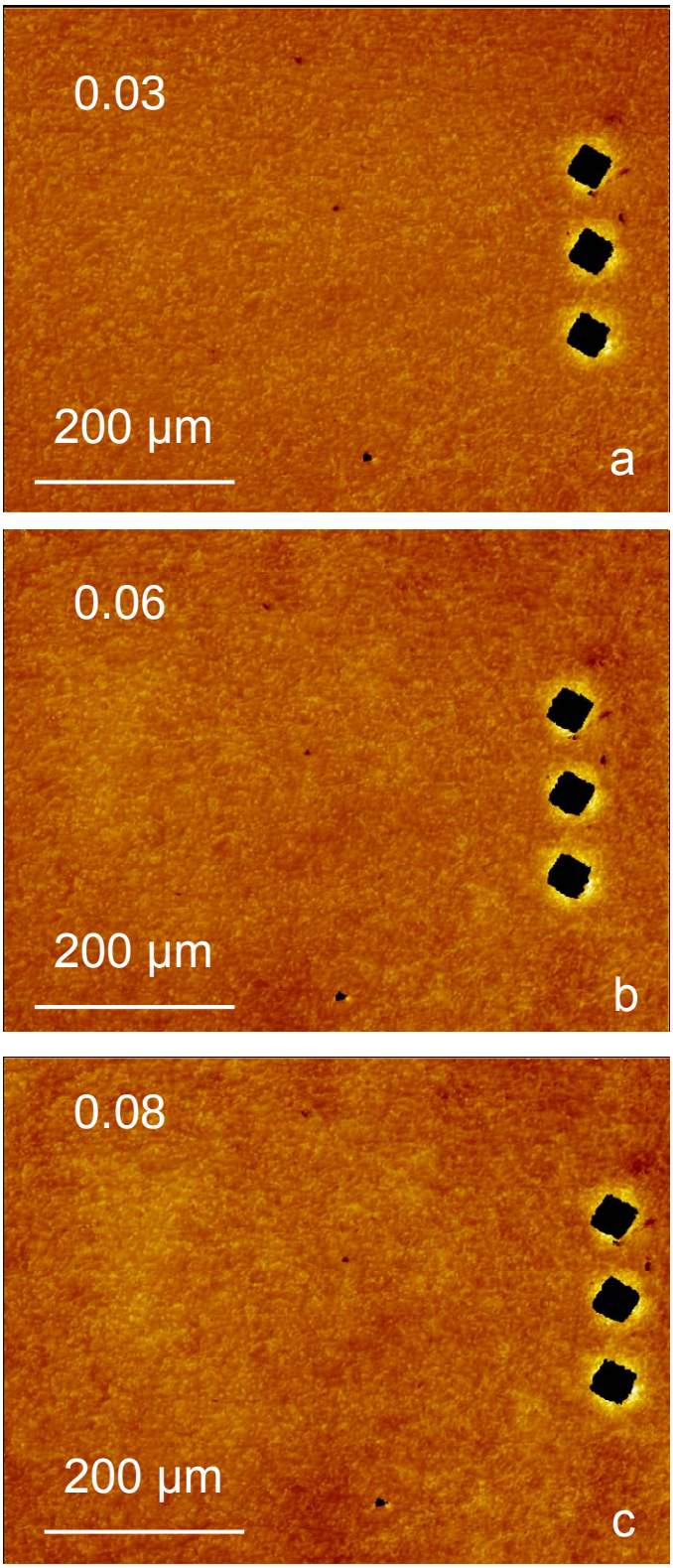

Figure 5.8: MicroXam images (800 µm x 600 µm) of the surface of C11000 copper under tensile load (a) 0.03 (b) 0.06 strain (c) Image at 0.08 strain

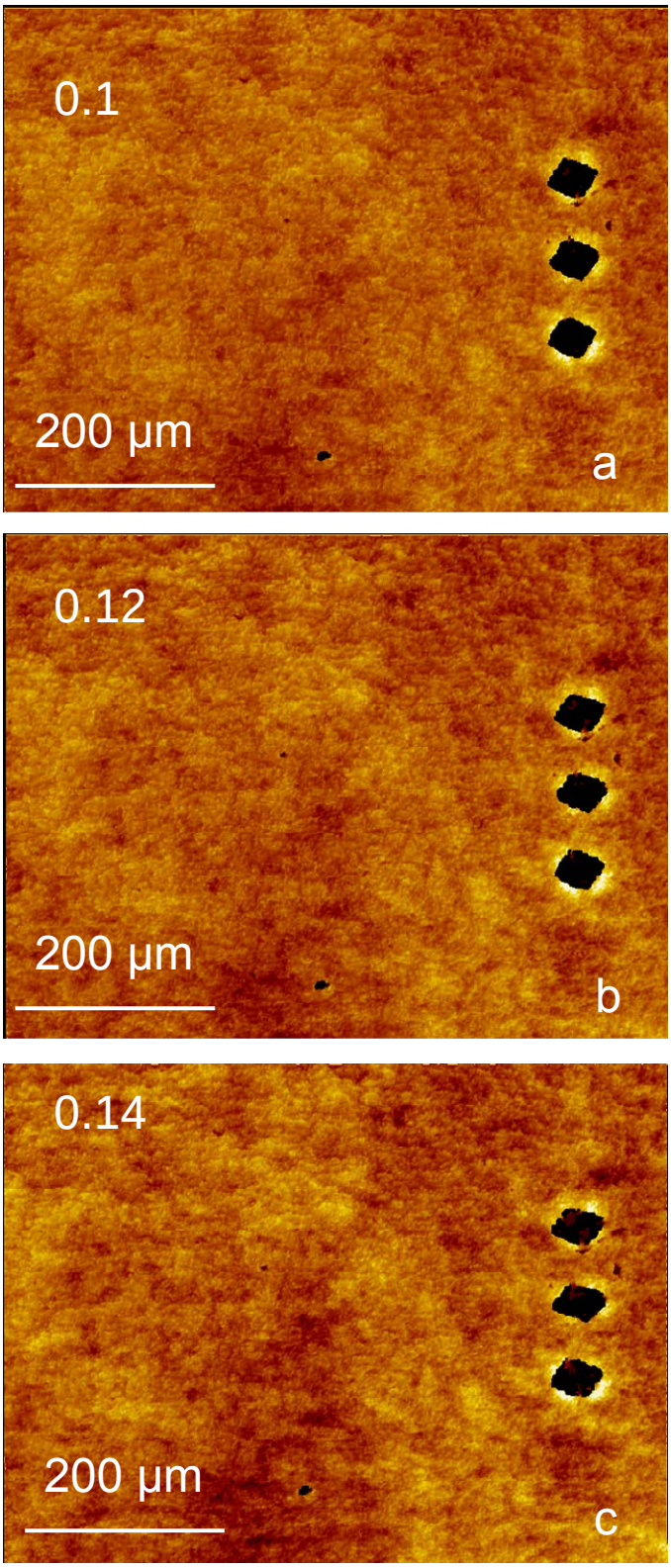

Figure 5.9: MicroXam images (800 µm x 600 µm) of the surface of C11000 copper under tensile load (a) 0.1 global strain (b) 0.12 strain (c) Image at 0.14 strain

5.4.1 Digital Image Correlation (DIC) analysis

The images of the copper sample surface acquired at various stages during the tensile test using the MicroXam were analyzed using a digital image correlation (DIC) software to investigate the distribution of strains in the sample and the effect the loading has on individual grains. An area 250 μm x 250 μm was selected near the three indents for analysis. The software uses a reference point initially to orient the features in the images for comparison. This is done by picking features easily distinguishable in all the images and selecting an initial point. An array of points or nodes, whose size is user determined, is then decided upon. The software computes the displacement of features around the node by comparing it to the same feature as in the preceding image. The area around each node, in which the software estimates strains, is called the radius which is user defined. To estimate strains due to large deformations, it is advantageous to have images that have been acquired at various intermediate stages of deformation. The software thus computes strains in increments by analyzing each image and comparing it to the previous one. Large strains can thus be estimated and the stages in which the changes in strain take place are also recorded. The data thus obtained can be outputted as a basic ASCII file that can be transferred to a plotting software at the user's discretion. The data obtained in this analysis were analyzed using TechPlot® software. Once the user defined parameters are defined, the software analyses the images to estimate strains. The software terminates the calculations at each node when it finds the feature it is analyzing or when it reaches the limit of number of iterations during

which it is attempting to locate the feature. Only the linear terms are calculated during the iterations. Table 5-1 gives the parameters used with DIC software. The main user defined control parameters are the following:

1. Nodes – The number of points at which strains have to be computed. If the strain in a larger area needs to be computed a larger array of nodes can be used.
2. Sequence of next node – This decides which node will be analyzed next. The next node that is to be analyzed could be on the sides or towards the top or bottom or diagonal.
3. Spacing – It is the distance between the nodes in the X- and Y- directions. A relatively finer mesh of nodes results in better estimation of strains in the area of interest. The choice of the number of nodes and the spacing is largely determined by the quality of the image
4. Subset radius – This determines the area around each node for which strain calculations are to be done in a rectangular format
5. Smoothing radius – This determines how much smoothing or rounding is provided around the corners of the subset radius rectangle.
6. Maximum number of iterations – This determines the maximum number of iterations that the software must make at each node to analyze the movement features before it moves to the next node. If the displacement in features between two images is larger, it will result in the software requiring more number of iteration before it converges to the feature under consideration.

7. Tolerance – Determines the tolerance in the converging process at which the iteration can be terminated.

Once the user defined parameters are entered, the software analyses the images to estimate strains. Only the linear terms are calculated during the iteration.

Table 5-1 Control parameters used with DIC software for the 250 μm x 250 μm areas

Number of nodes	30 x 30 = 900
Sequence of next node	Left - right
Spacing (pixels)	10 x 10
Subset radius (pixels)	20 x 20
Smoothing radius (pixels)	1
Maximum number of iterations	50
Tolerance	0.0001

Figures 5.10 through 5.14 are plots made using TechPlot® software that show the variation in the distribution of tensile, transverse, and shear strains from the MicroXam images acquired at global strains ranging from 0.003 to 0.14. All the images were plotted with the same overall scale. Strains in the longitudinal direction were mostly tensile while the strains in the transverse direction are compressive. Figure 5.10 shows the distribution of tensile, compressive, and shear strains for images captured at 0.003 and 0.006 global strain. Figures 5.10 (1a) and (2a) show the distribution of tensile strains in the area of interest. It is interesting to see that the strains vary between 0 and 0.05 in alternative bands in the horizontal direction. Strains in the transverse direction show similar bands in the vertical direction [see Figures 5.10 (2a) and (2b)]. When we look at the same area in the tensile and transverse strain plots, we see that if the area shows

tensile strains in the tensile plot, the corresponding area in the transverse plot is compressive. This indicates that the area of interest is being stretched in the tensile direction while having a reduction in area in the transverse direction. Shear strains have not showed too much variation at this stage of loading [see Figures 5.10 (1c) and (2c)].

With increasing loads, the strains in both longitudinal and transverse directions begin to show broadening of the bands discussed earlier. It can be seen from Figures 5.11 1(a) and 2 (a) that areas with higher tensile strain (darker green - ~0.05) have increased implying that more areas are being strained. Similarly, light green areas (~-0.05) have started to broaden in the transverse strain plots indicating that compressive stresses have become more dominant [see Figures 5.11 2 (b) and 2 (c)]. Some areas in the shear strains plots [see Figures 5.11 1(c) and 2(c)] show negative strains (light green) while others show positive strains (darker green).

Most areas in the tensile and transverse strain plots at global strains of 0.06 and 0.08 have begun to show significant changes in strain compared to images at low global strains (Figure 5.12). Strains in the tensile direction in most areas are between 0.1 and 0.15 while strains in some areas are still < 0.1 [see Figures 5.12 1(a) and 2 (a)]. Most areas in the transverse strain plot [see Figure 5.12 1(b)] for the image captured at 0.06 global strain have strains ~ -0.05. Some areas have higher compressive strains. These areas with higher compressive strains begin to broaden when the strain experienced by the tensile sample as a

whole increases to 0.08 [see Figure 5.12 (2b)]. Shear strains are still in the range of -0.05 to 0.05 at this stage [see Figures 5.12 (1c) and 2(2c)].

Strain distribution plots for images captured at global strains of 0.1 and 0.12 are shown in Figure 5.13. Most areas in the plot show strains in the tensile direction of 0.15 to 0.35 [see Figures 5.13 (1a) and (2a)]. It is interesting to note that some localized areas have experienced compressive strains too [seen in red on the bottom part of Figure 5.13 (2a)]. An area very near this region has experienced high tensile strains. This difference is due to significant differences in the orientation of the individual grains with respect to the tensile axis. The plots depicting the strains in the transverse direction have average strains of ~-0.1 at this stage [see Figures 5.13 (1b and (1c)]. It is interesting to note that areas experiencing high compressive strains (red areas) correspond to the regions in the tensile plot that have high tensile strains (blue spots). Most areas in Figures 5.13 (1c) and (2c) experience strains in the region of 0.05 to -0.05. It is interesting to note that shear strains are higher in the region that has adjacent areas (discussed earlier) that experience tensile and compressive strains. Shear strains are high because of the mis-orientation of the grains with respect to each other. The area that has high shear strain is probably the interface between the two grains where each grain is greatly influencing the neighboring grain.

Figure 5.14 compares the distribution of tensile, transverse, and shear strains for images captured at 0.003 and 0.14 global strains, respectively. These images show regions that have experienced greater deformations. It can bee seen in Figure 5.14 (2b) that some areas have experienced tensile strains as

high as 0.4. Average strains are ~ 0.2. It may also be noted that areas experiencing high tensile strains are alternating with areas with relatively lower strains which compare well with the strain distribution bands seen in Figure 5.14 (2a). Figure 5.14 (2b) shows the distribution of strains in the transverse direction. Several regions show high compressive strains (average strains ~-0.15). The shear strain distribution in Figure 5.14 (2c) shows some regions of positive shear strains while others show negative shear strains. These differences are due to orientation differences of individual grains in the neighborhood. DIC is a good way of mapping strain distribution in areas of interest when images at different stages of deformation can be obtained.

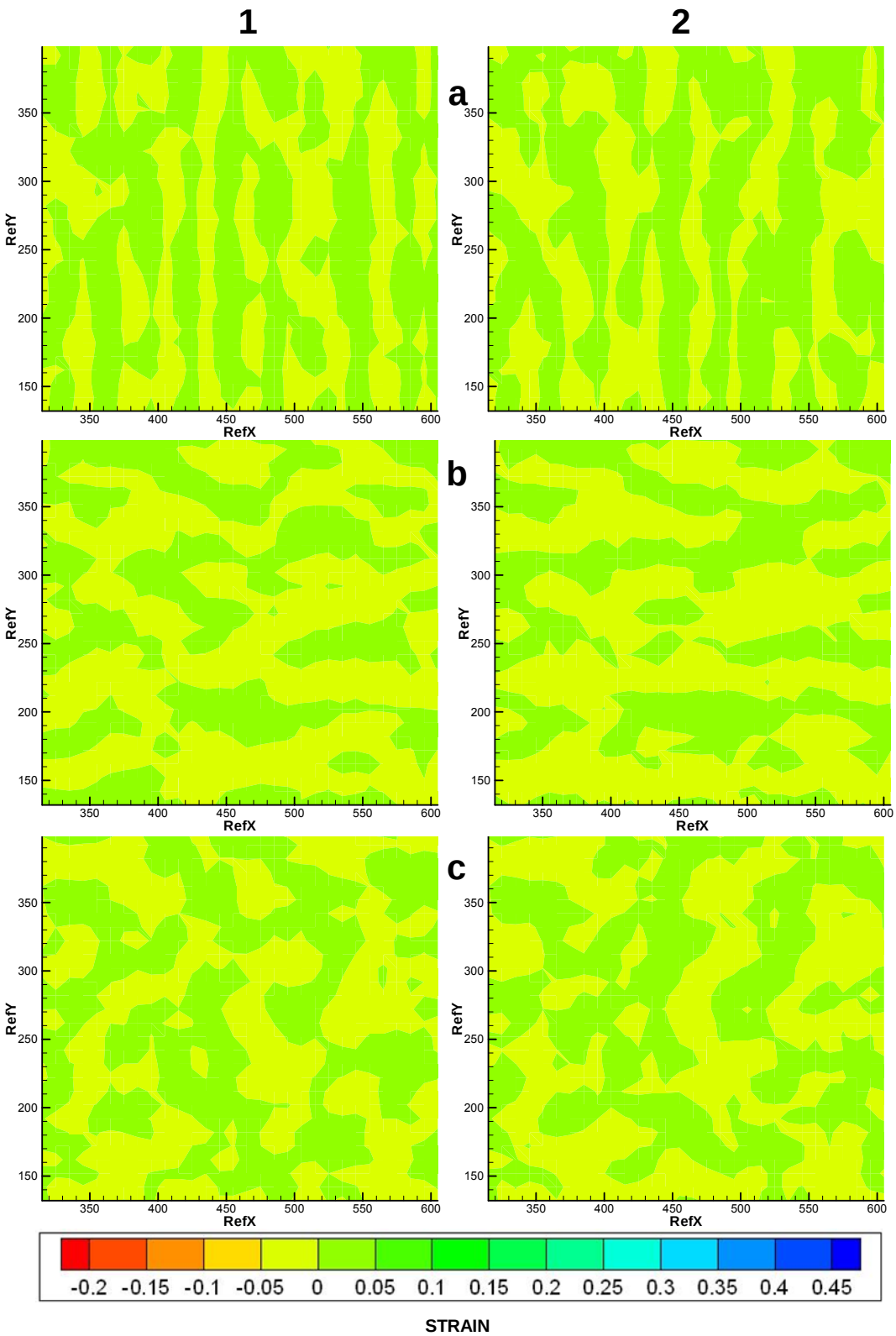

Figure 5.10: Distribution of strains in a 250 µm x 250 µm area at global strains (1) 0.003 (2) 0.006 (a) Tensile (b) Transverse (c) shear

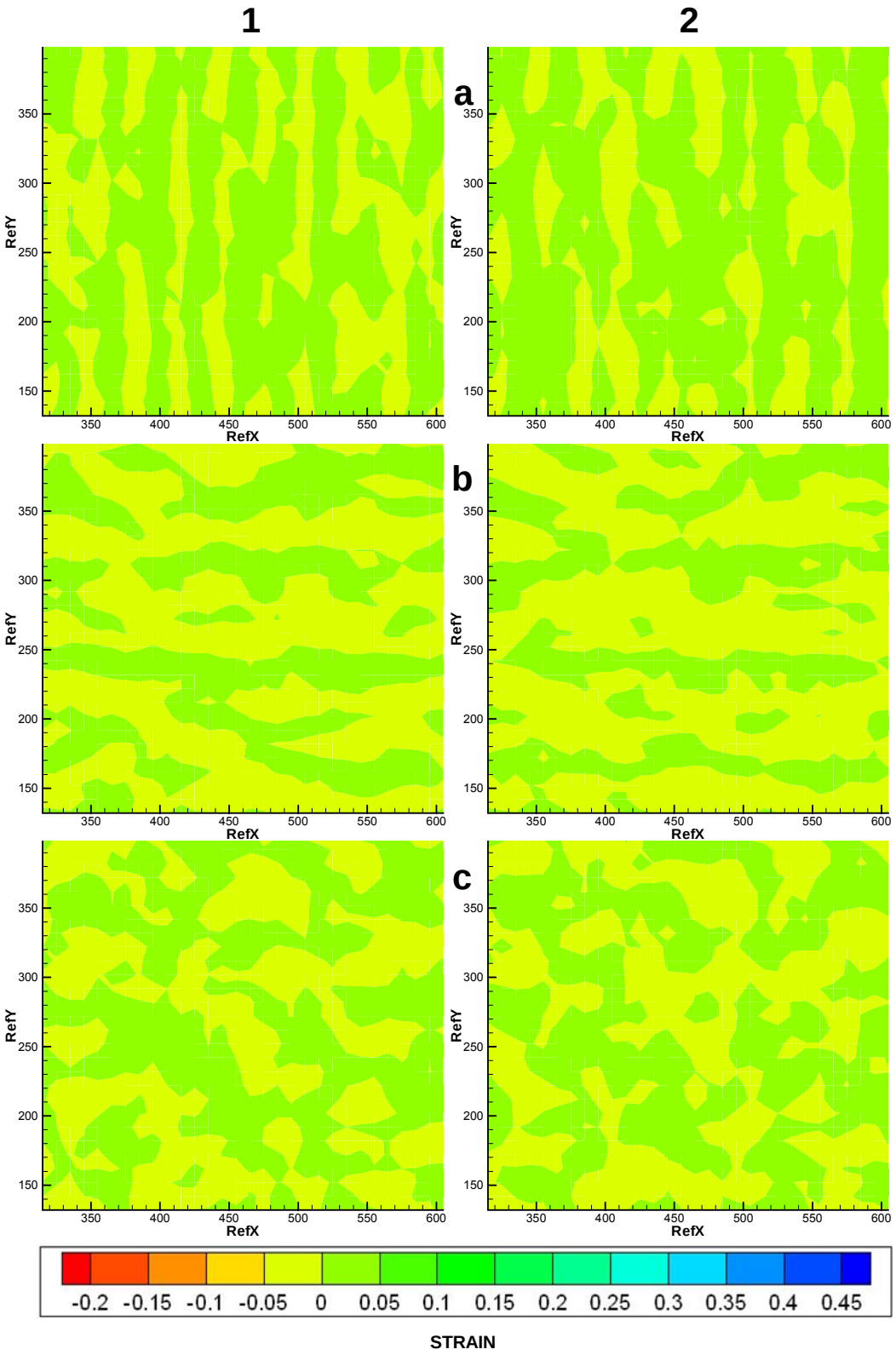

Figure 5.11: Distribution of strains in a 250 μm x 250 μm area at global strains (1) 0.01 (2) 0.03 (a) Tensile (b) Transverse (c) shear

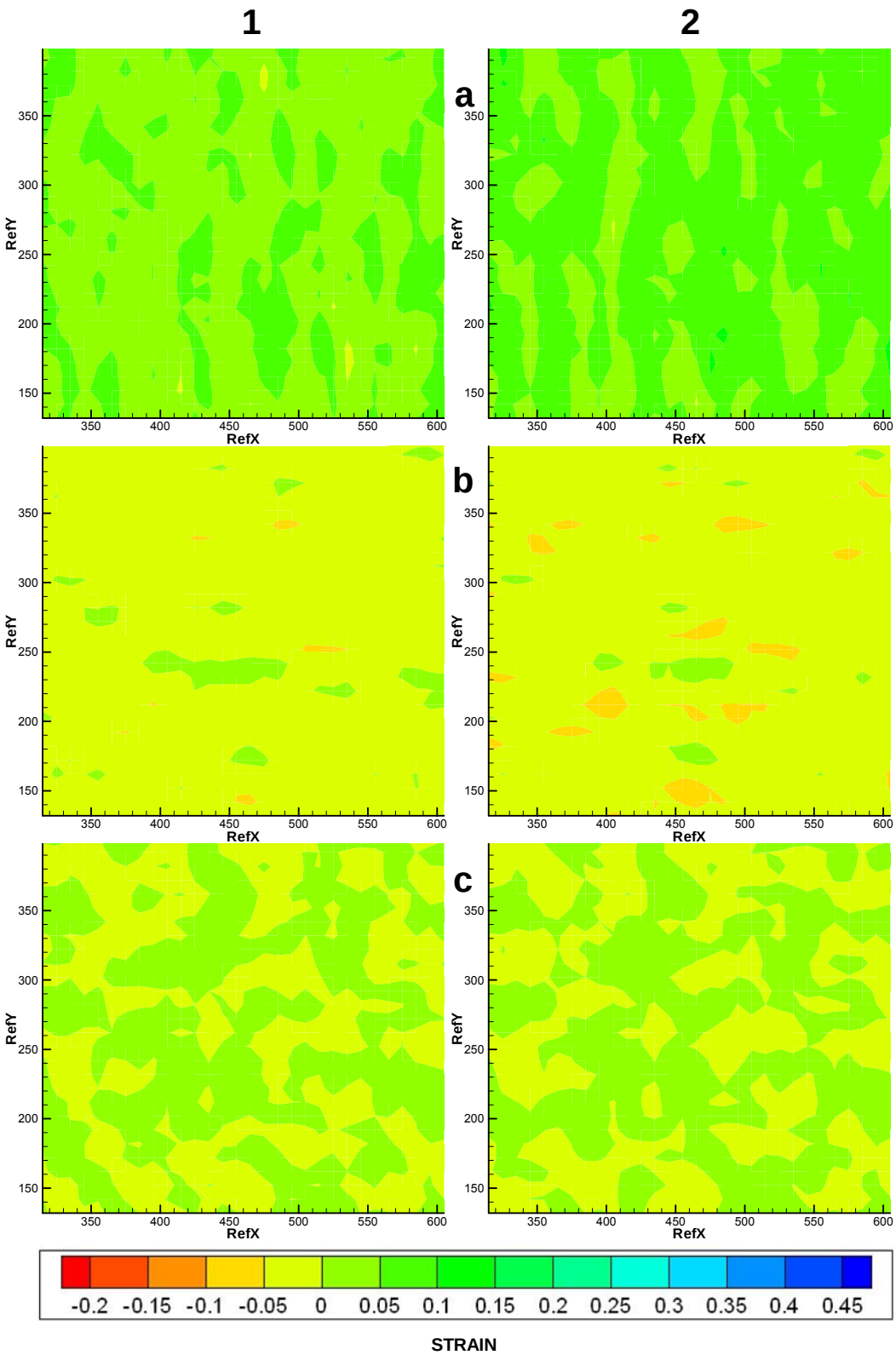

Figure 5.12: Distribution of strains in a 250 µm x 250 µm area at global strains (1) 0.06 (2) 0.08 (a) Tensile (b) Transverse (c) shear

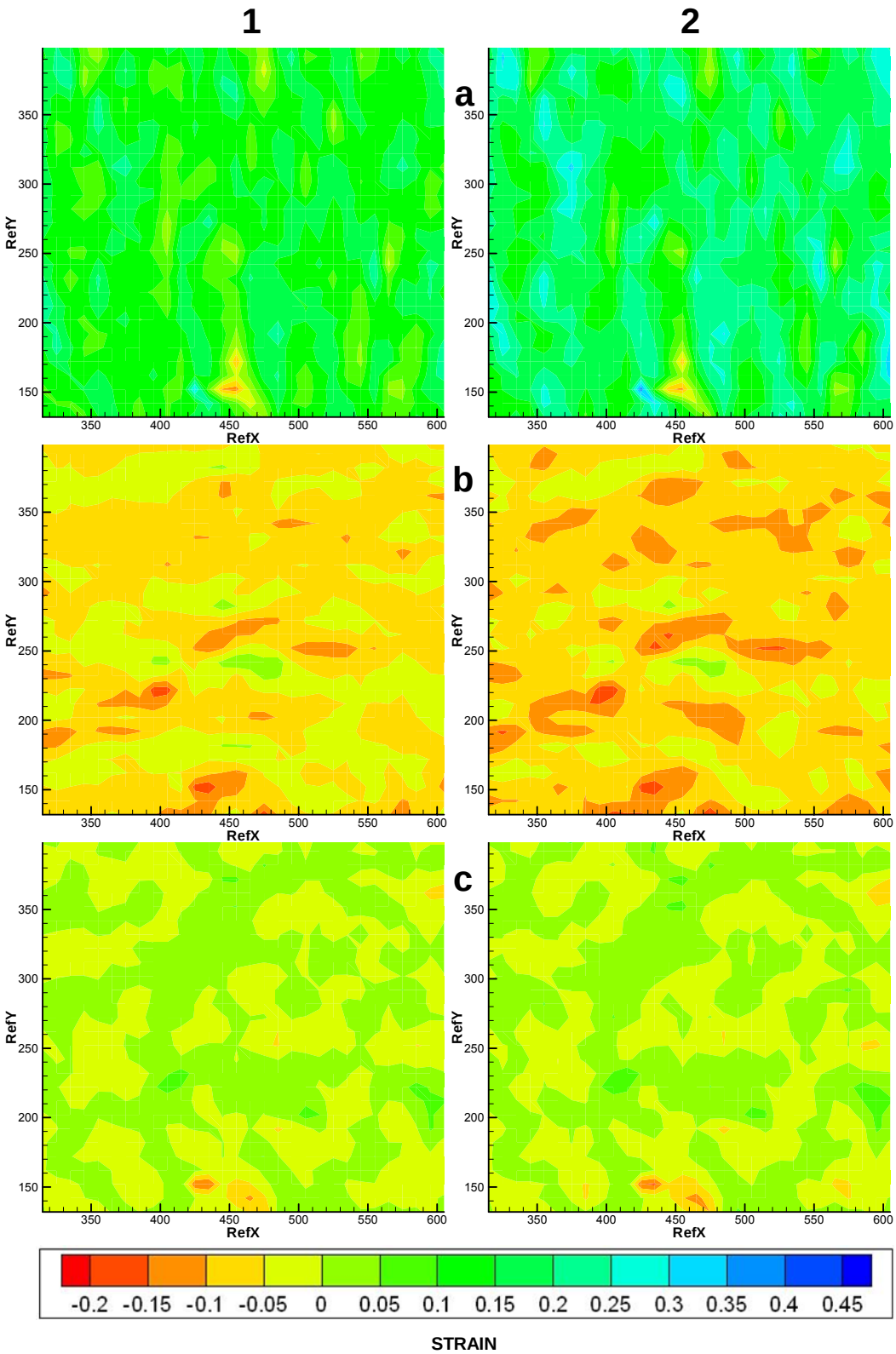

Figure 5.13 : Distribution of strains in a 250 µm x 250 µm area at global strains (1) 0.1 (2) 0.12 (a) Tensile (b) Transverse (c) shear

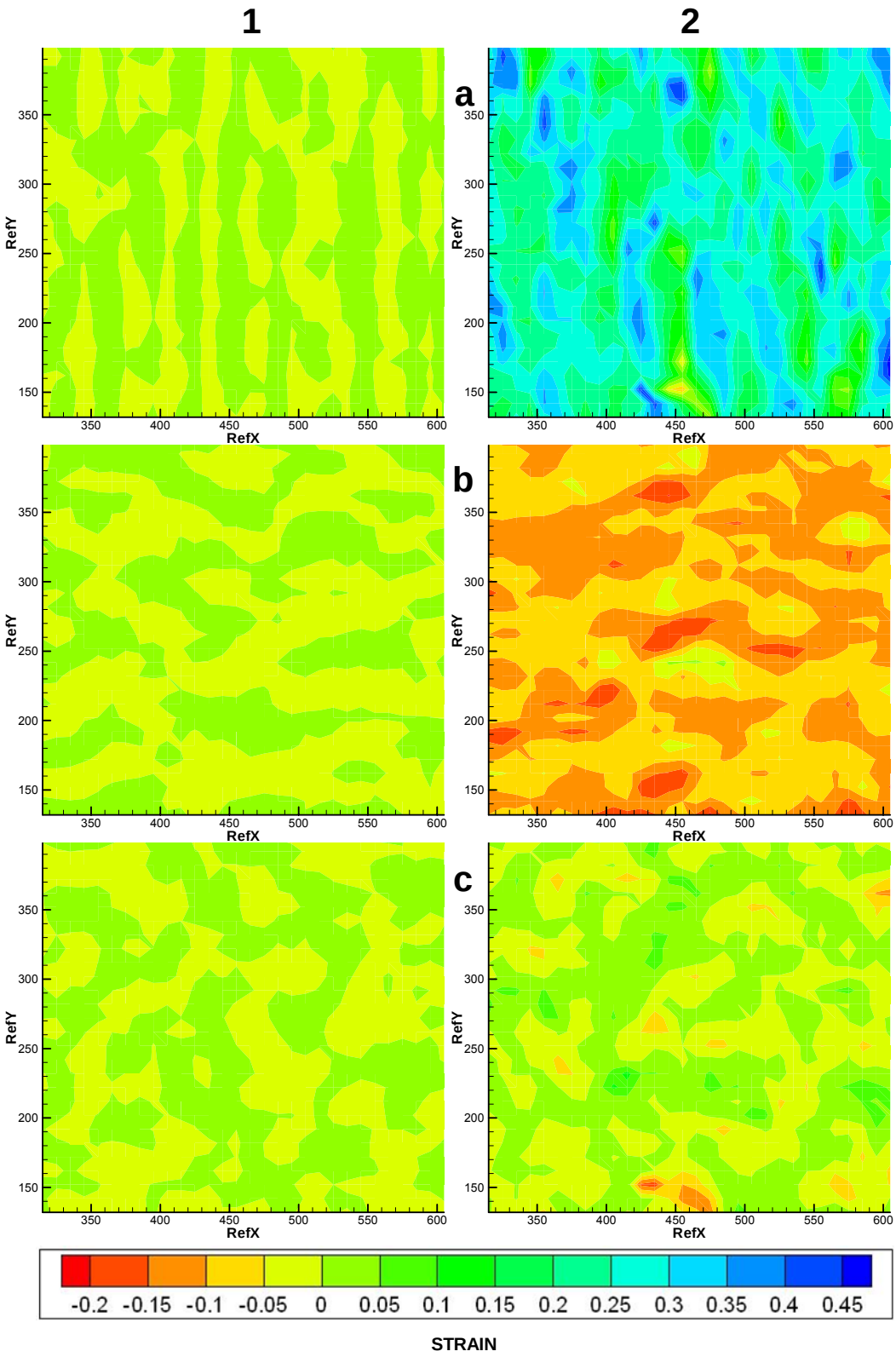

Figure 5.14: Distribution of strains in a 250 µm x 250 µm area at global strain of (1) 0.003 and (2) 0.14 (a) Tensile (b) Transverse (c) shear

5.4.2 Analysis of deformation of 150 μm x 125 μm area during tensile loading

As described earlier, three Vickers indents were made on a polycrystalline copper tensile sample using a micro-indenter. The sample was then mounted on the tensile stage and *in-situ* testing was performed under an optical interference microscope (MicroXam). Images of an area ~ 150 x 125 μm near the middle indent were captured using the interference microscope. Figures 5.15 through 5.17 are MicroXam images acquired at a magnification of 500x (150 μm x 125 μm) at global strains in the range of 0 to 0.14. The middle Vickers indent was used as a reference point so that the same area could be imaged at different stages. Figure 5.15 is a MicroXam image of an electropolished and etched copper surface prior to loading. Equiaxed grains with twins along with a part of the Vickers indent can be seen in the image. Figures 5.15 (b) and (c) are images acquired when the global strains are ~ 0.006 and 0.01. Some amount of deformation can be seen in Figures 5.16 (a), (b) and (c) that were acquired when the global strains were ~ 0.03, 0.06, and 0.08, respectively. The set of images in Figure 5.17 were acquired at global strains of 0.1 – 0.14. A significant amount of deformation is visible in all these images. It can be seen in Figure 5.9 (c) (taken at 0.14 strain) that the indents have also deformed.

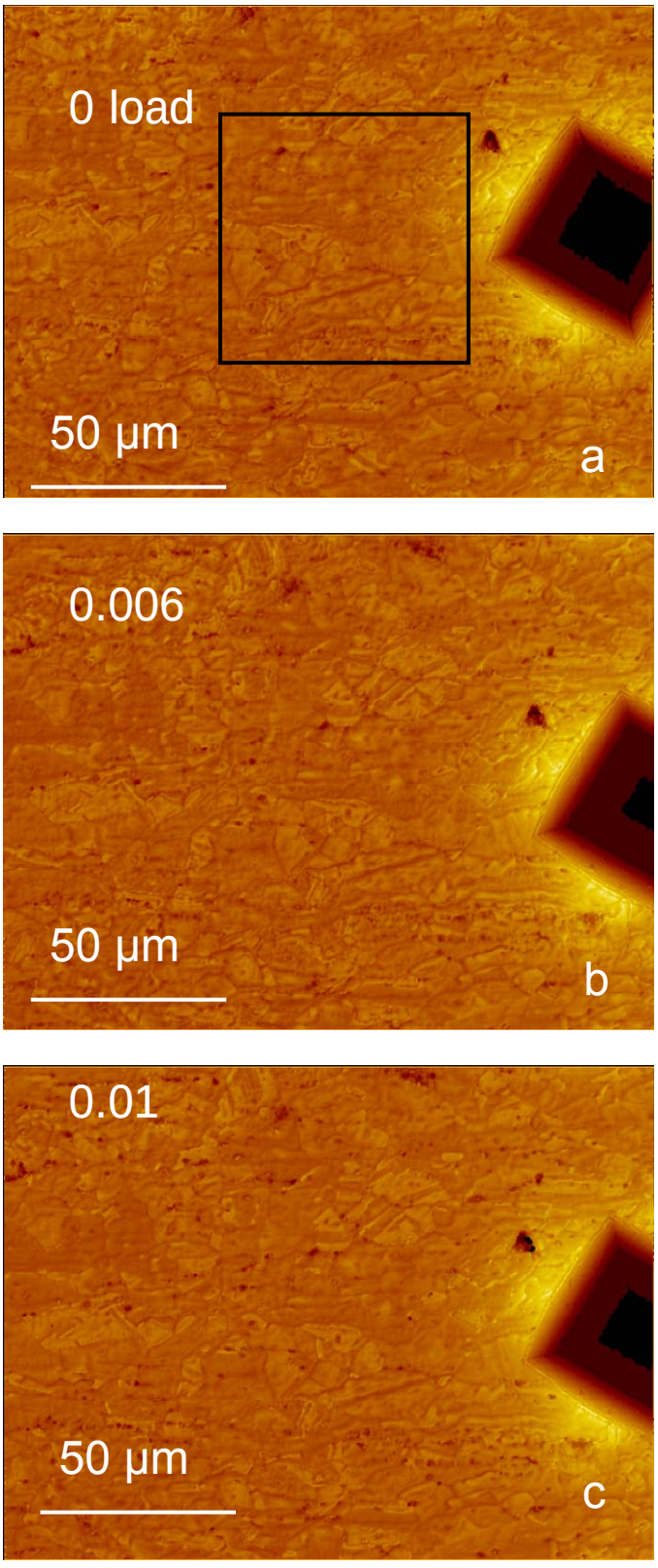

Figure 5.15: MicroXam images (150µm x 125 µm)of the surface of C11000 copper under a tensile load (a) 0 strain (b) Image at 0.006 strain (c) 0.01 strain

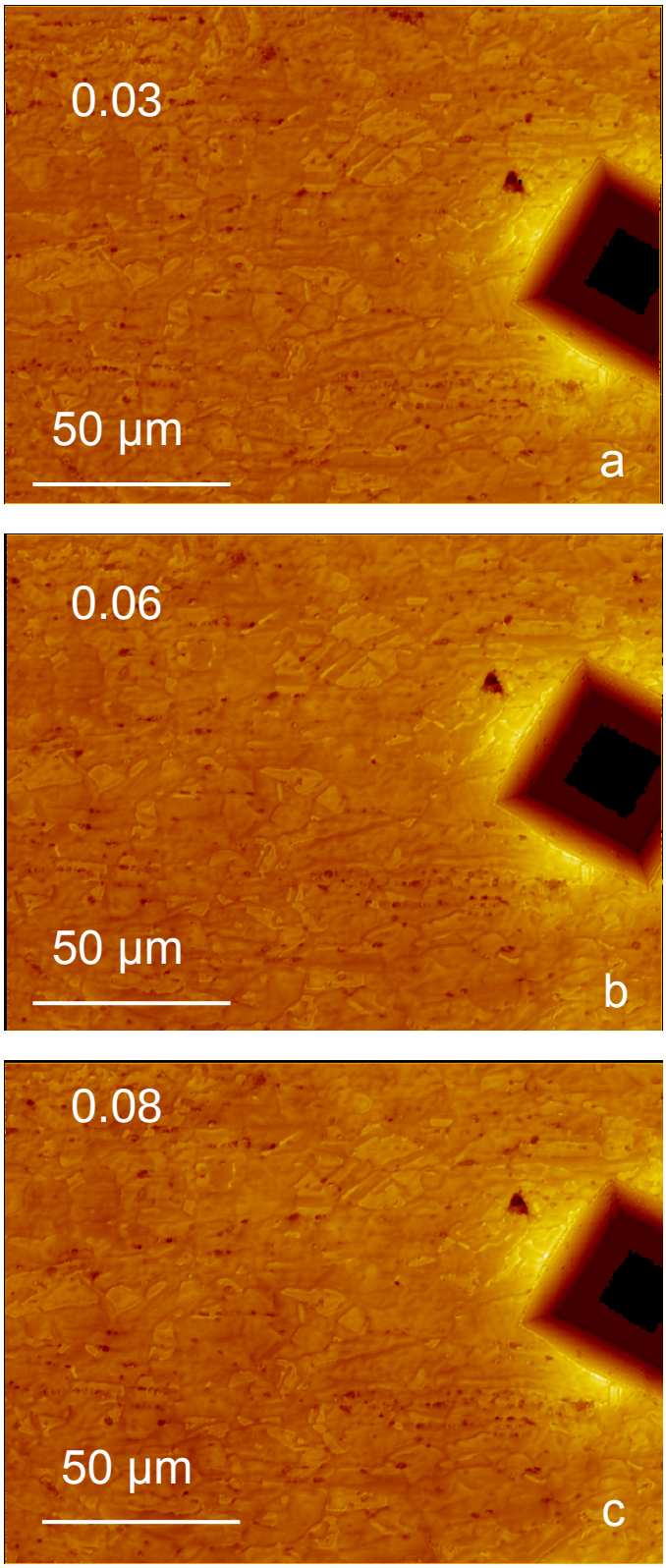

Figure 5.16 : MicroXam images (150 µm x 125 µm)of the surface of C11000 copper under a tensile load (a) 0.03 strain (b) 0.06 strain (c) 0.08 strain

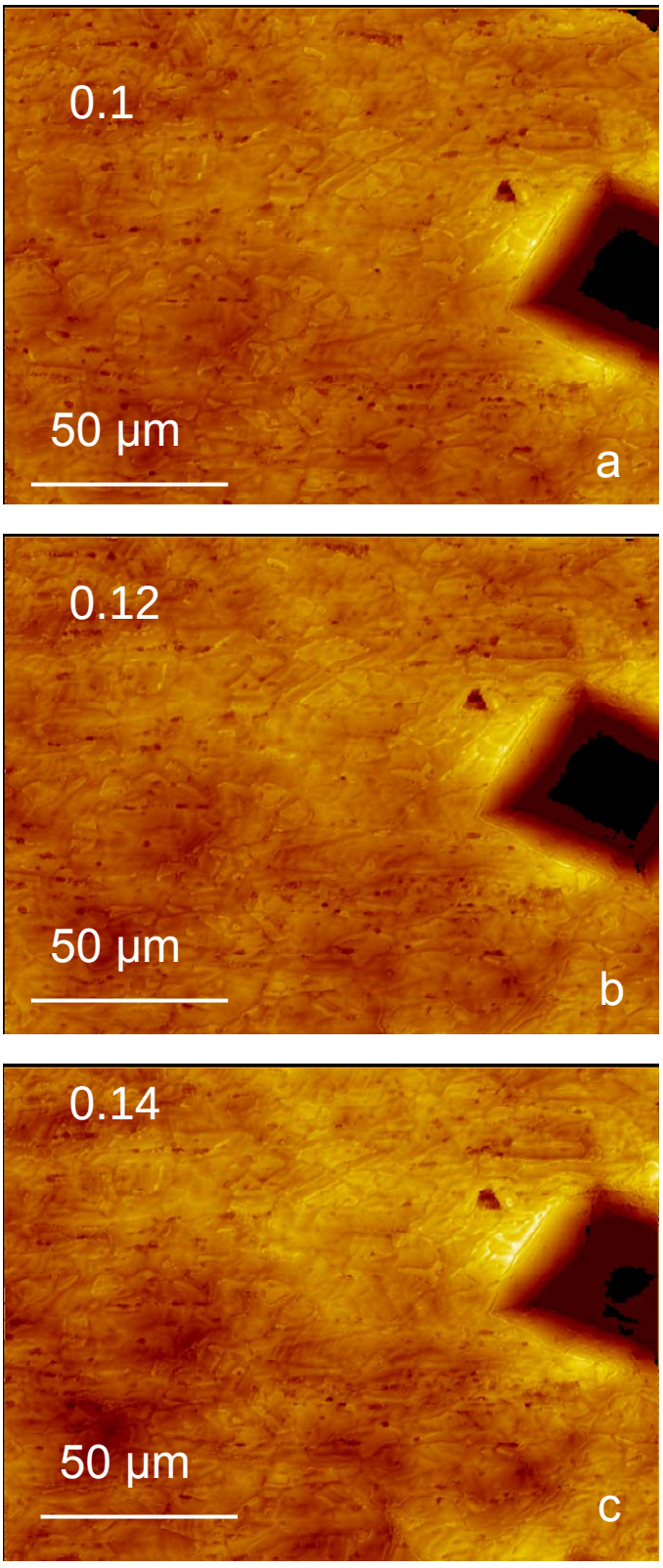

Figure 5.17 : MicroXam images (150 µm x 125 µm) of the surface of C11000 Copper under a tensile load (a) 0.1 strain (b) 0.12 strain (c) 0.14 strain

5.4.3 Digital Image Correlation (DIC) analysis

Figures 5.15 through 5.17 are photographs obtained using a MicroXam of the surface of the copper sample acquired at various stages of the tensile test. They were analyzed using DIC software to examine the distribution of strains in the sample and the effect of loading on individual grains. An area 80 μm x 80 μm was selected near the middle indent for analysis.

The control parameters used in the software are given in Table 5-2**.**

Table 5-2 Control parameters used with DIC software for the 80 μm x 80 μm

Number of nodes	20 x 20 = 400
Sequence of next node	Left - right
Spacing (pixels)	15 x 15
Subset radius (pixels)	30 x 30
Smoothing radius (pixels)	1
Maximum number of iterations	50
Tolerance	0.0001

Figures 5.18 through 5.21 are plots (using TechPlot® software) showing the variation in the distribution of tensile, transverse, and shear strains from the MicroXam images acquired at global strains ranging from 0.006 to 0.14. All the images have been plotted with the same scale. Figure 5.18 shows the distribution of tensile, compressive, and shear strain for images captured at 0.006 and 0.1 global strains. Figures 5.18 (1a) and (2a) show the distribution of tensile strains in the area of interest. It is interesting to note that the strains vary between 0 and 0.05 in alternate bands in the horizontal direction, similar to the ones seen in Figure 5.10 (2a). The main difference in these two cases is that the bands are broader in the former (smaller area). When we examine the same area

in the longitudinal and transverse strain plots, we see that area having tensile strains in the tensile plot show compressive strains in the transverse plot indicating that the area of interest is being stretched in the tensile direction while experiencing a reduction in area in the transverse direction. Shear strains have not showed too much variation at this stage of loading [see Figure 5.18 1(c) and 2(c)].

Figures 5.19 (1c) and (2c)] show negative strains (light green) while other figures in Figure 5.19 show positive strains (darker green). Most areas in the tensile and transverse strain plots at global strains of 0.08 and 0.1 have begun to show significant changes in strain compared to images at low global strains (Figure 5.20). Strains in the tensile direction are between 0.1 and 0.15 in most areas while some areas are still < 0.1 [see Figures 5.20 (1a) and (2a)]. Most areas in the transverse strain plot [see Figure 5.20 (1b)] for the image captured at 0.08 global strain have strains ~ -0.1. Some areas have higher compressive strains which begin to broaden when the strain experienced by the tensile sample as a whole increases to 0.1 [see Figure 5.20 (2b)]. Shear strains are still in the range of -0.05 to 0.05 at this stage [see Figures 5.20 (1c) and 2(2c)].

Figure 5.21 shows strain distribution plots for images captured at global strains of 0.12 and 0.14. Most areas in the plot show strains in the tensile direction to be between 0.15 to 0.35 at this stage [see Figures 5.21 (1a) and (2a)]. The plots depicting the strains in the transverse direction have average strains ~-0.15 at this stage [see Figures 5.21 (1b and (2b)]. It is interesting to note that areas experiencing high compressive strains (red areas) correspond to

the regions in the tensile plot that have high tensile strains (blue spots) as seen in Figures 5.13 (1b) and (2b) when the larger area was being analyzed. Most areas in Figure 5.21 (1c) and (2c) experience strains in the region of 0.1 to -0.1 It can be seen from Figure 5.21 (1b) that some areas have experienced tensile strains as high as 0.4 (average strains are ~ 0.2). It may also be noted that areas experiencing high tensile strains are alternating with areas with relatively lower strains which compare well with the strain distribution bands seen in Figure 5.14 (2b). Figure 5.21 (2b) shows the distribution of strains in the transverse direction. Some regions show high compressive strains and average strains of ~-0.15. Most regions in the shear strain distribution plot show positive shear strains while a few show negative shear strains. This is probably due to the fact that most grains in this region have similar orientations or very small differences in the orientation. The results obtained in this analysis are comparable to the strains estimated for the larger image that also included the present area.

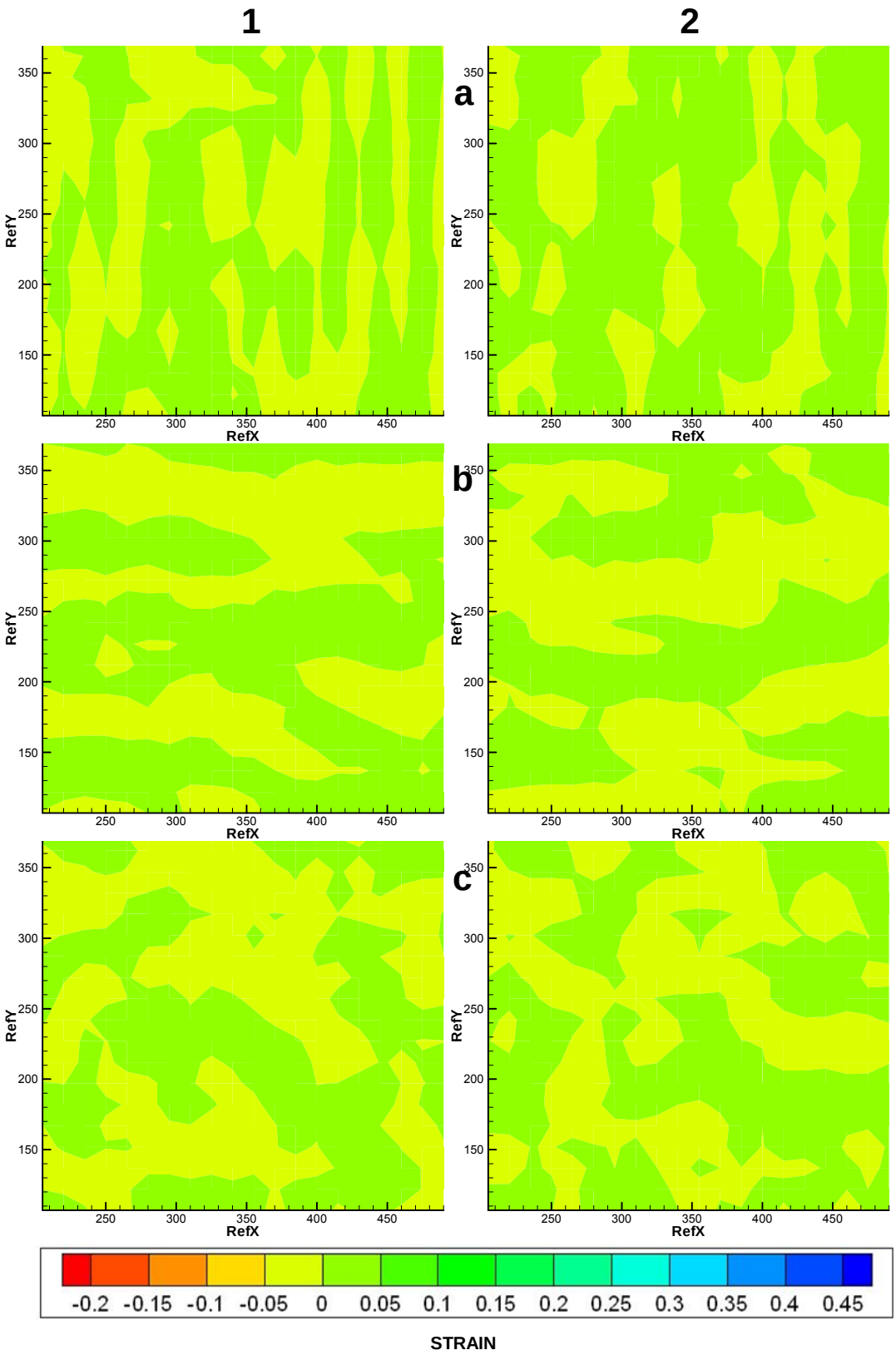

Figure 5.18: Distribution of strains in a 80 µm x 80 µm area at global strain of (1) 0.006 and (2) 0.01 (a) Tensile (b) Transverse (c) Shear

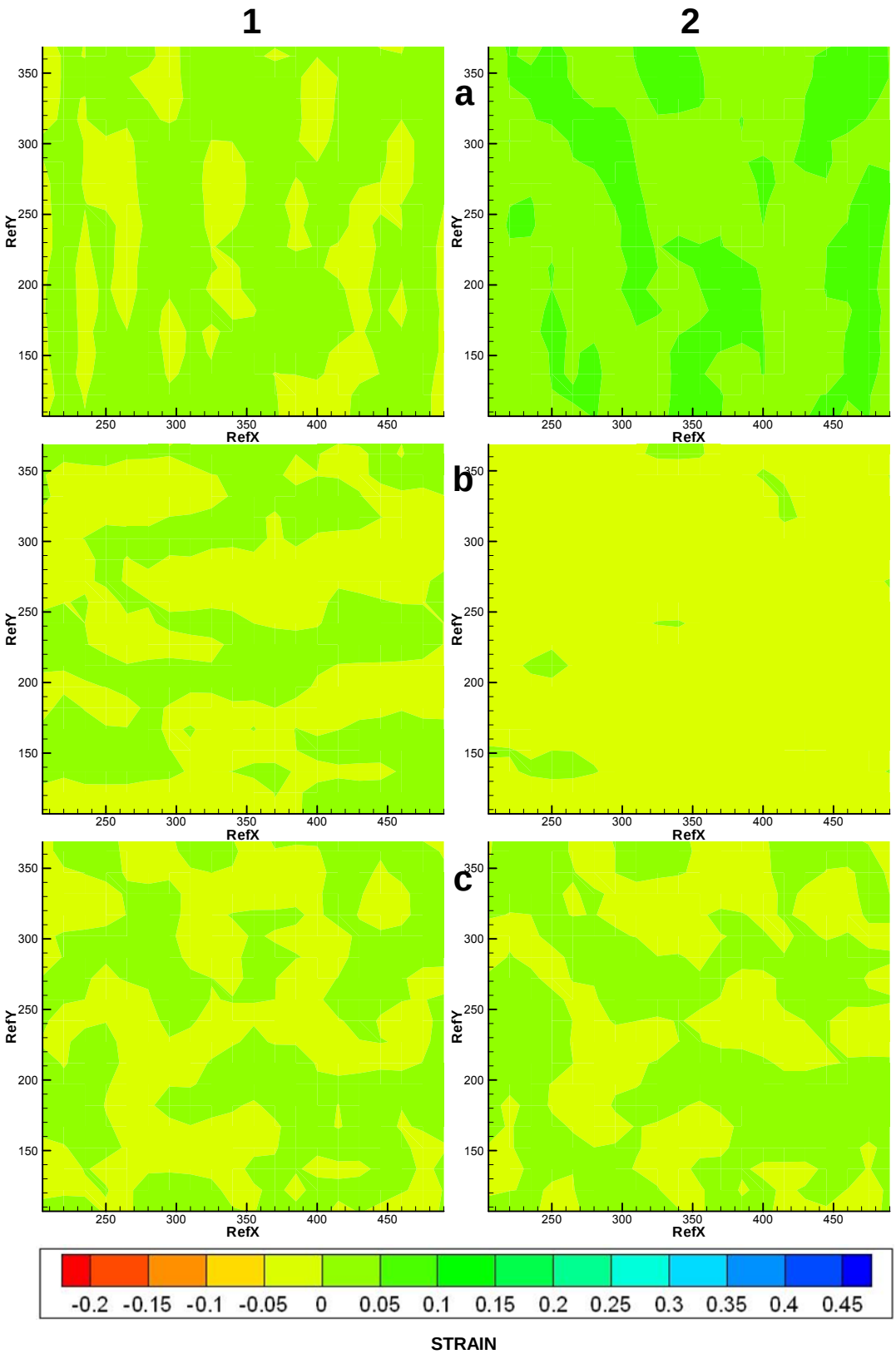

Figure 5.19: Distribution of strains in a 80 µm x 80 µm area at global strain of (1) 0.03 and (2) 0.06 (a) Tensile (b) Transverse (c) Shear

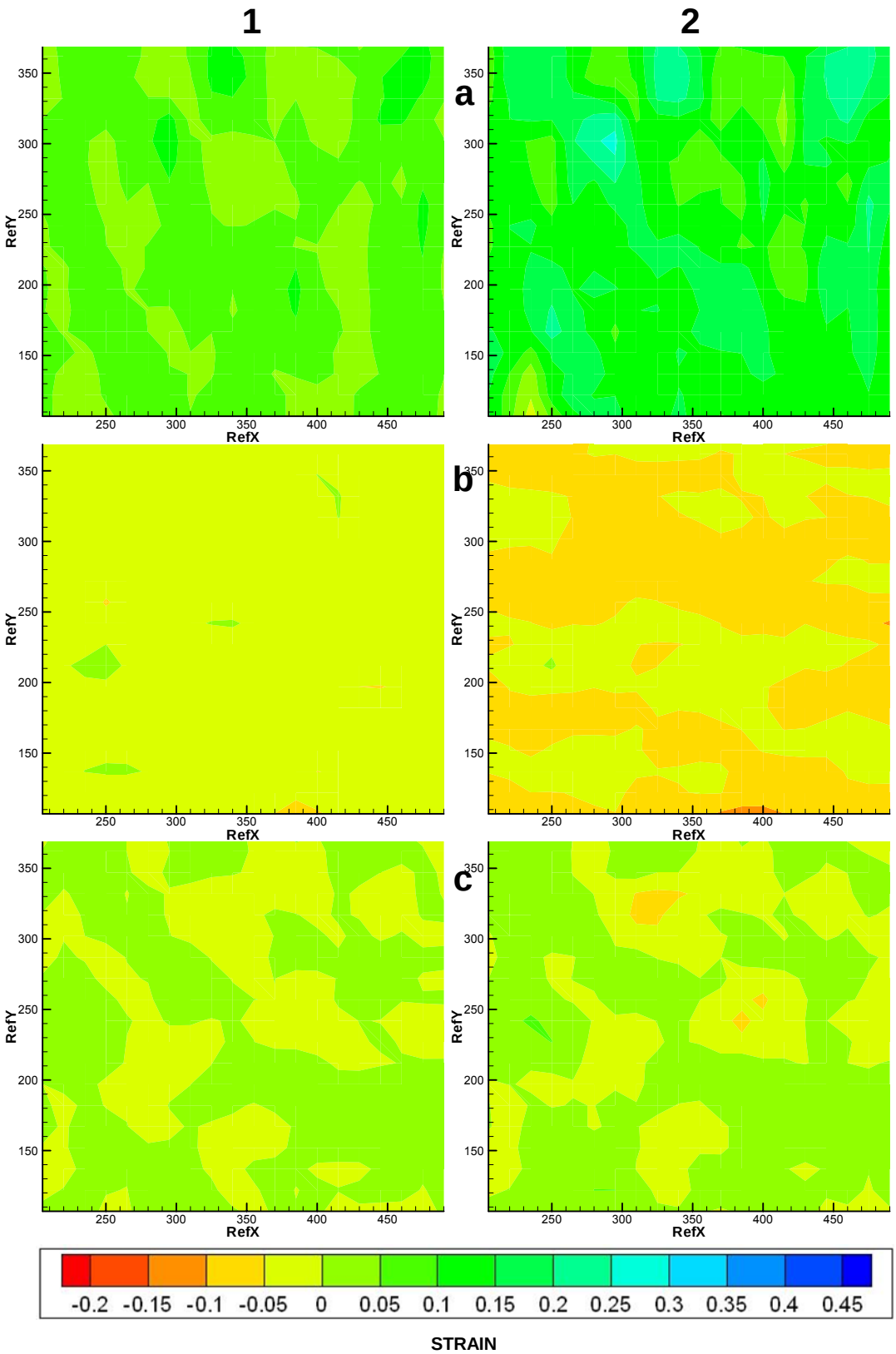

Figure 5.20: Distribution of strains in a 80 µm x 80 µm area at global strain of (1) 0.08 and (2) 0.1 (a) Tensile (b) Transverse (c) Shear

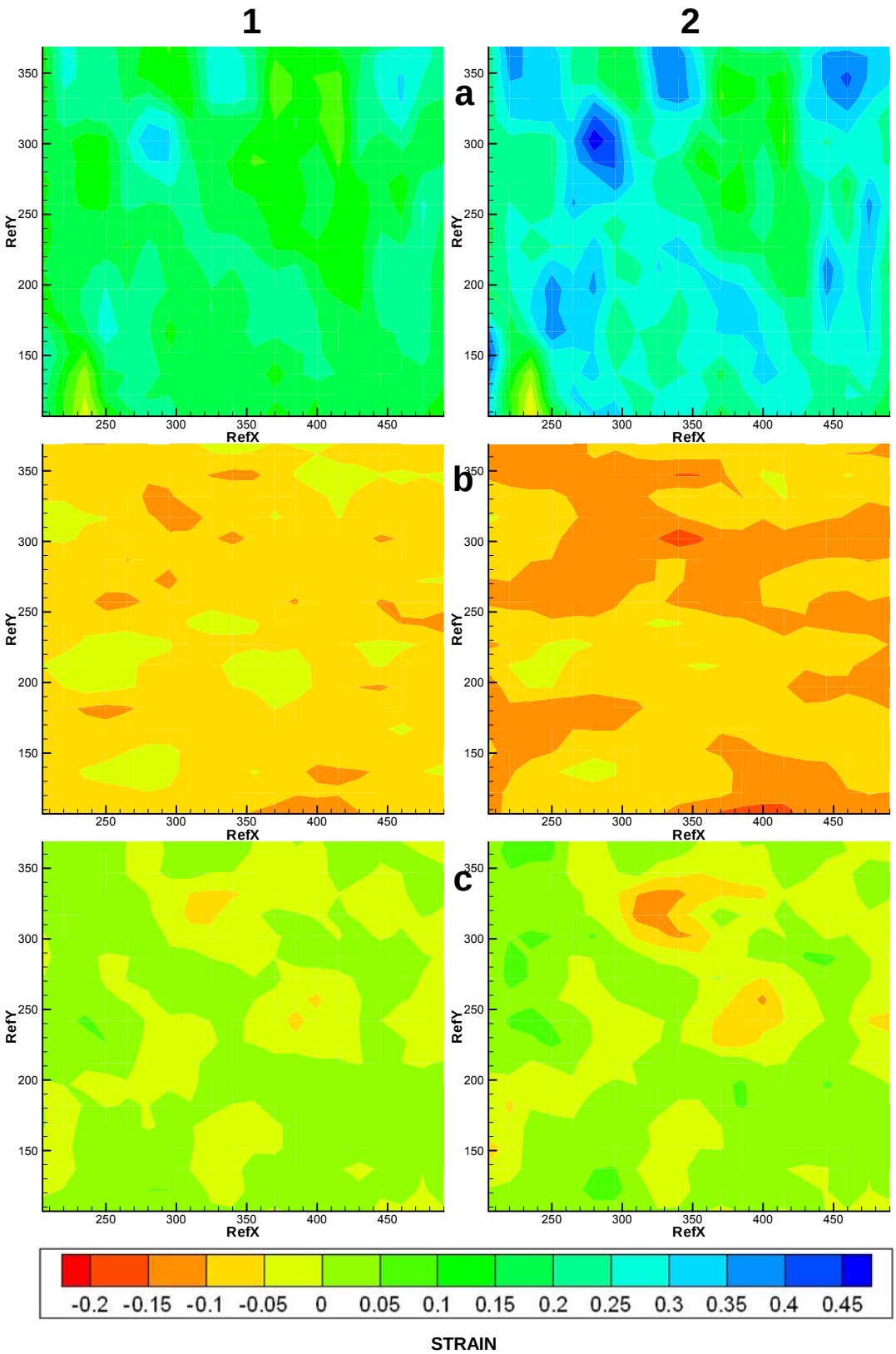

Figure 5.21: Distribution of strains in a 80 μm x 80 μm area at global strain of (1) 0.12 and (2) 0.14 (a) Tensile (b) Transverse (c) Shear

5.5 *In-situ* examination of the tensile sample surface using AFM

To study the deformation of the surface of polycrystalline copper (C11000) specimen in more detail, several tension experiments were performed using an AFM. The tensile samples were electropolished and subsequently etched lightly using an acidified ferric chloride solution to reveal the grain boundaries.

5.5.1 Results and Discussion

Figures 5.22 (a) and (b) are AFM 3D images of the surface of the tensile sample after it has been positioned on the tensile stage. The grain boundaries can be clearly seen in these images. The drive motor was stopped when the stress equaled the estimated yield stress of the sample and the AFM tip was engaged. Figures 5.22 (c) and (d) are AFM 3D images of the surface of the sample that were acquired at this stage.

Images were also acquired at ~ 0.02 strain i.e., after the onset of yielding. Faint slip bands can be seen in Figures 5.22 (e) and (f). As dislocations multiply in the material, a plastically strained lattice will become progressively more distorted. It thus becomes more difficult for dislocations to move through a distorted lattice and so the activation stresses will be increasing, making it harder to cause plastic flow (strain hardening). This, along with the dislocation pile ups at grain boundaries, interaction of dislocations undergoing slip in intersecting planes and other factors result in further hardening of the material. Grain size affects strain hardening in the early stages of plastic deformation but has less effect as the grain structure breaks down at high strains.

Flow starts first at the slip systems with the maximum resolved shear stress and this will continue until these slip systems are used up or until the increase in resistance to flow causes other systems to become stressed enough for them to be activated. Figures 5.23 (a) to (c) are AFM 3D images taken at different magnifications showing slip-lines in detail. The slip-lines in the grain at 0.04 strain are about 1μm apart. At 0.06 strain, more slip systems are seen to be active as seen in Figures 5.23 (d), (e) and (f) that result in slip lines forming about 500 nm apart. It can also be seen that one of the grains has several slip lines while the other appears to be hardly deformed.

Figures 5.24 (a) to (c) show several grains with slip lines. At strains of ~0.08, the tensile sample has undergone severe strain hardening and slip lines begin to jump across grain boundaries. It can also been seen that grains have began to separate.

Intersecting slip becomes more and more complex as more slip systems are activated. Cross slip can be seen in Figures 5.24 (d) to (f) at a strain of ~0.1. Several slip lines can be seen perpendicular to the slip lines that were initiated earlier. New slip lines are interacting with the slip lines that were formed earlier [see Figure 5.24 (f)].

At ~ 0.12 strain, almost all the grains in the polycrystalline copper have undergone deformation and the sample has reached its ultimate tensile strength. Several slip lines from different grains have started meeting at the grain boundaries that appear to be no more existent [see Figures 5.25 (a) and (b)]. A closer examination of these bands in Figure 5.25 (c) show slip lines that are ~ 50

nm apart. Intersecting shear bands can also be seen in Figures 5.25 (d), (e) and (f) (taken at ~0.13 strain) when the sample reached its ultimate tensile strength.

Microvoid formation during necking, as discussed in Section 5.3, is a result of separation of grain boundaries and void formation at weaker locations in the polycrystal. It can be seen in Figures 5.26 (a) and (b) that grain boundaries appear to be non-existent at necking, which started at ~0.15 strain. Large grooves can be seen. Figures 5.26 (c) through (f) are AFM 3D images of the area very close to the fractured region of the tensile sample. No clear grain structure can be seen. Very fine grooves that run in the tensile direction can be seen that show plastic deformation in the final stages just prior to fracture.

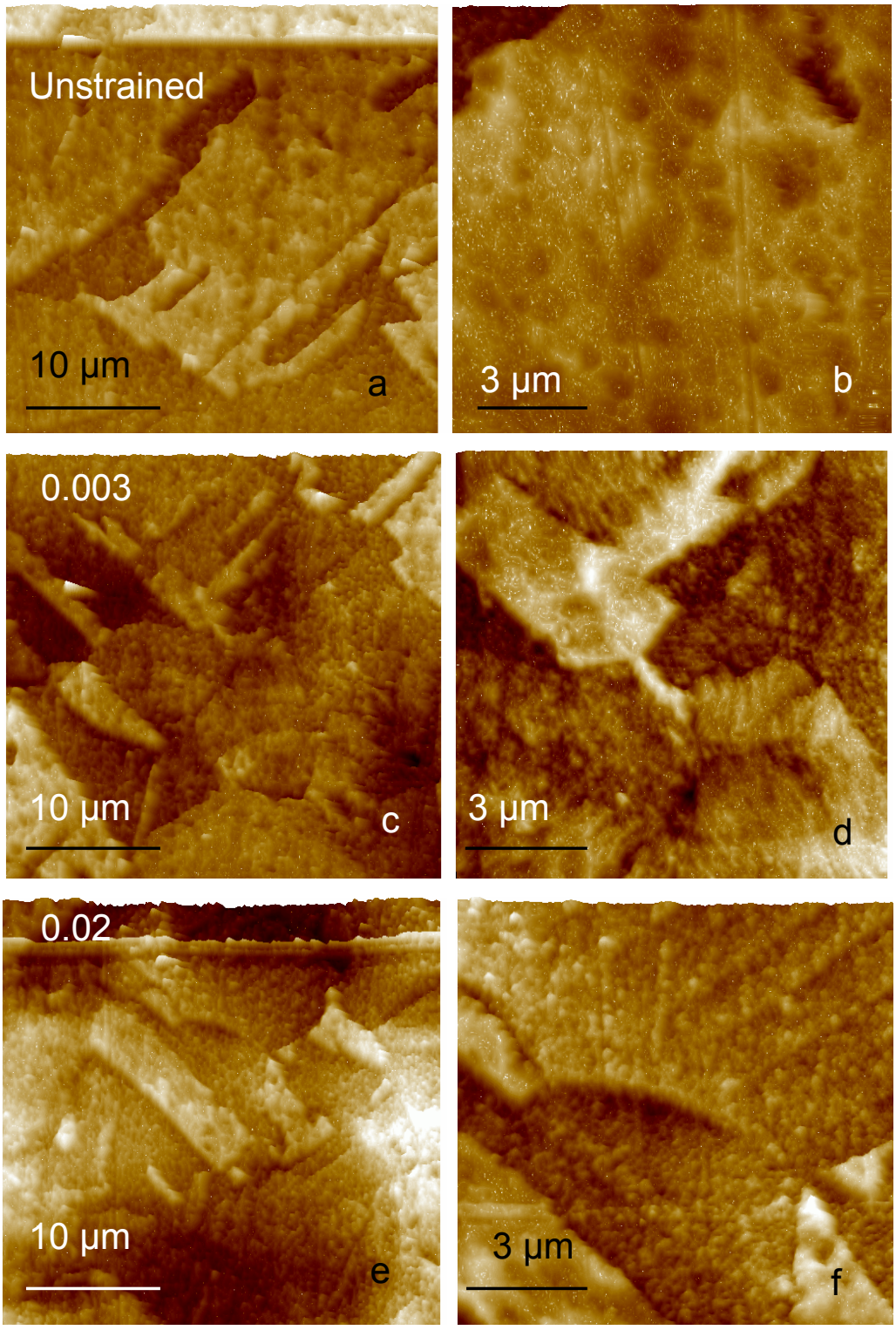

Figure 5.22: AFM 3D images of copper (C11000) under axial loading 0 - 0.02 strain (a) 30 μm x 30 μm area of electropolished etched copper (b) 10 μmx 10 μm area of a grain (c) 30 μm x 30 μm area at elastic limit (d) 10 x 10 μm area (e) 30 μm x 30 μm area at ~0.02 strain (f) 10 μm x 10 μm of the same area showing slip lines

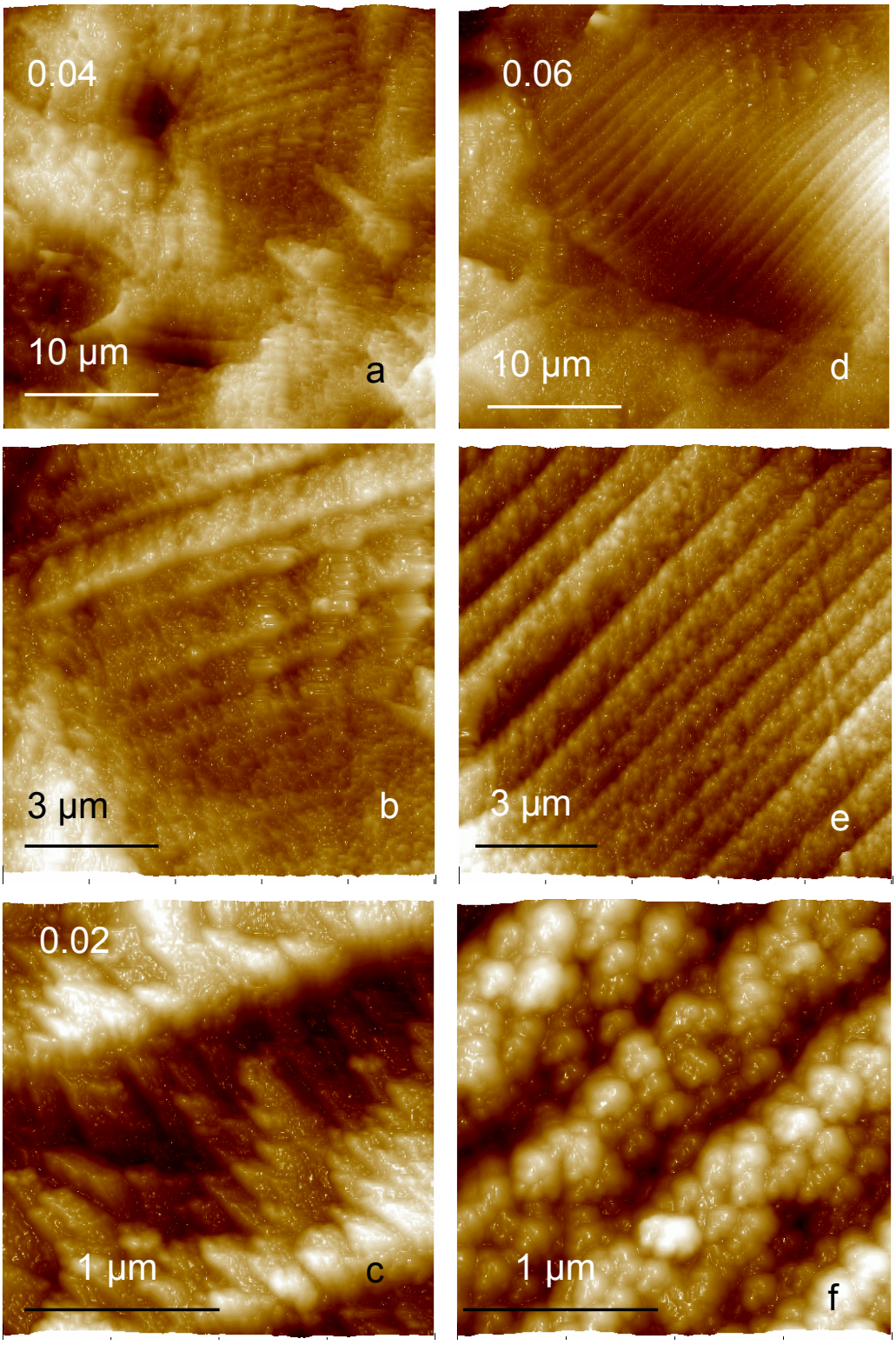

Figure 5.23 : AFM 3D images of copper (C11000) under axial loading at 0.04 – 0.06 strain (a) 30 x 30 µm area of surface at ~0.04 strain (b) 10 x 10 µm area showing slip bands (c) 2 x 2 µm area showing the slip lines clearly (d) 30 x 30µm area of surface at ~0.06 strain (e) 10 x 10 µm area showing slip bands (f) 2 x 2 µm area showing the slip lines that 500 nm apart

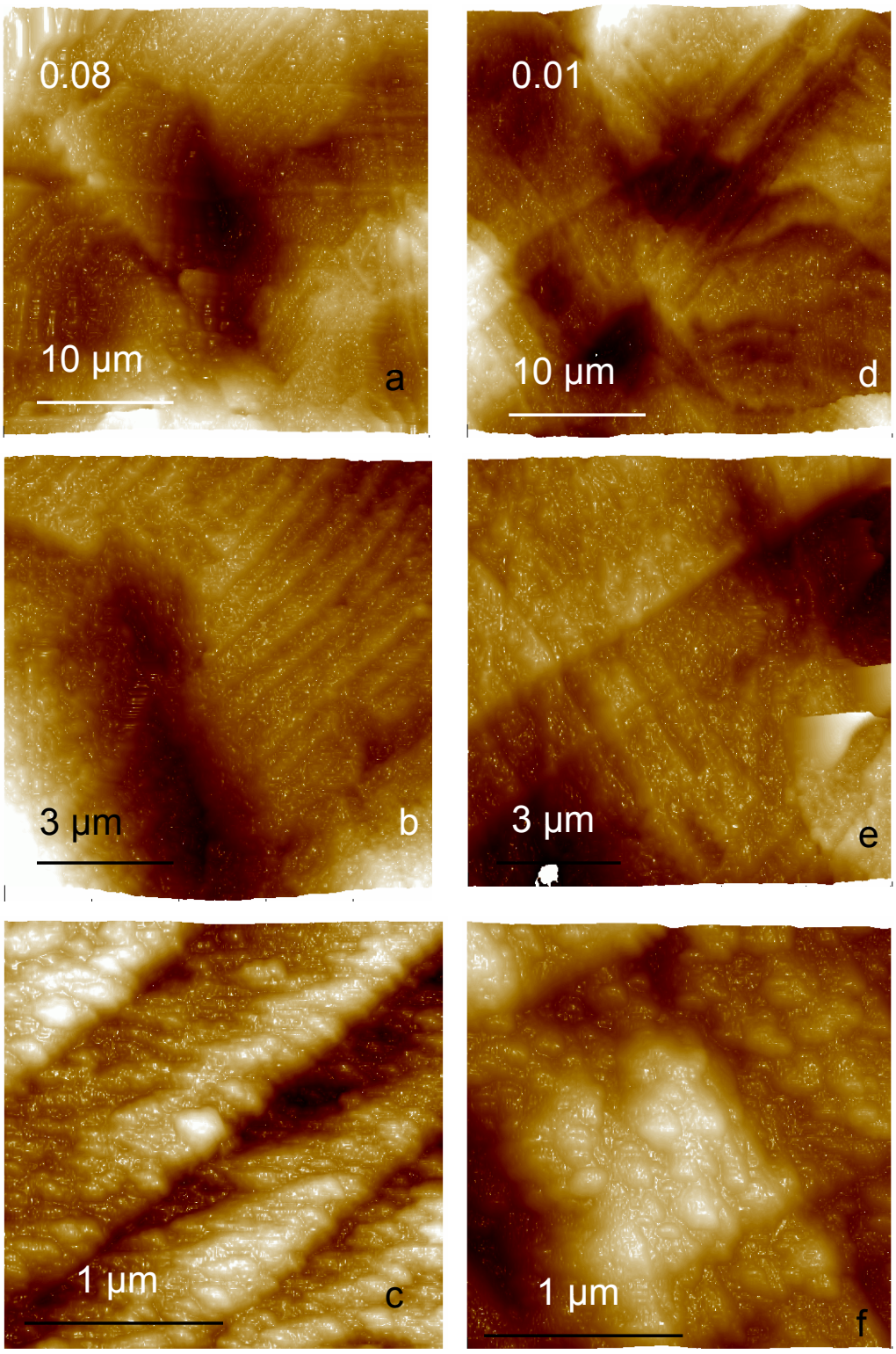

Figure 5.24 : AFM 3D images of copper (C11000) under axial loading at 0.08 and 0.1 strain (a) 30 x 30 µm area of surface at ~0.08 strain (b) 10 x 10 µm area showing slip bands (c) 2 x 2µm area showing the slip lines clearly (d) 30 x 30 µm area at ~0.1strain (e) 10 x 10 µm area showing cross slip (f) 2 x 2 µm area showing the cross slip with slip lines perpendicular to each other

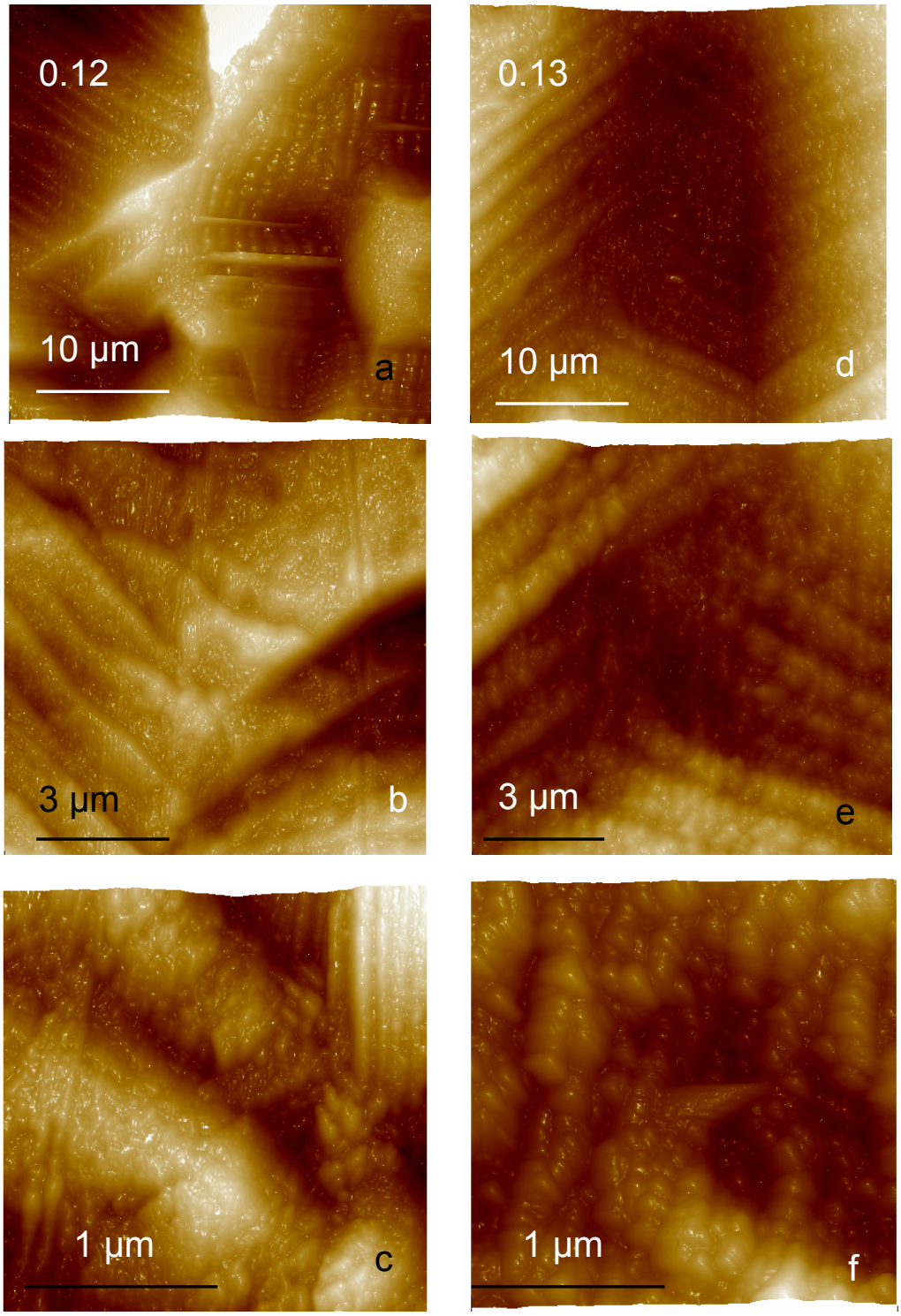

Figure 5.25 : AFM 3D images of copper (C11000) under axial loading at 0.12 and 0.13 strain (a) 30 µm x 30 µm area of surface at ~0.12 strain (b) 10 µm x 10 µm area intersecting slip bands (c) 2 µm x 2 µm area showing the slip lines 50 nm apart on slip bands (d) 10 µm x 10 µm area at ~0.13 strain showing slip in several grains (e) 5 µm x 5 µm area (f) 2 µm x 2 µm area showing some slip lines

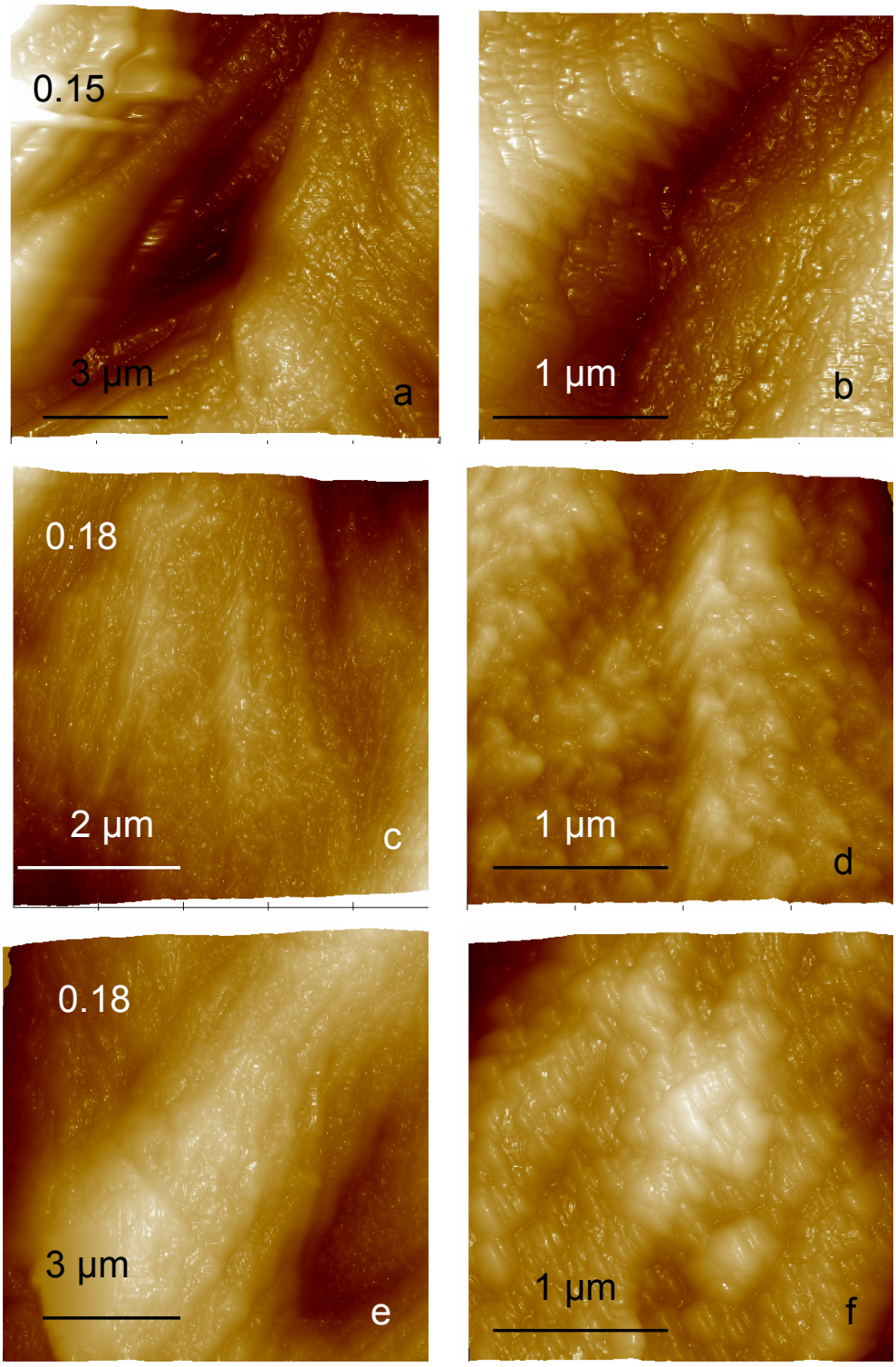

Figure 5.26: AFM 3D images of copper (C11000) under axial loading 0.15 and 0.18 strain (a) 10 μm x10 μm area of the necked region at ~0.15 strain (b) 2 μm x 2 μm area showing microvoids (c) 10 μm x 10 μm of an area near fracture (d) 2 μm x 2 μm area (e) another 10 μm x10 μm area near the fracture (d) 2 μm x 2 μm area showing groves in the tensile direction.

CHAPTER 6

ESTIMATION OF STRAINS BY RELATIVE DISPLACEMENTS OF NANOINDENTS

6.1 Introduction

To investigate strain in localized regions of a C11000 copper sample during a tension test, it was necessary to see how individual areas of the grain move under tensile load. As discussed earlier, polycrystalline materials take considerable time to begin necking due to the presence of different grains that have different orientations and yield only when the forces are high enough to start activating slip systems in them. Thus different areas would have different strain histories.

6.2 AFM imaging of nanoindents conducted using an MTS indenter

An area of about 40 μm x 40 μm of the sample was examined to see if the overall tensile loading of the sample has affected the strains locally. To keep track of individual points in the area under interest, nanoindents were used as markers. A 3 x 3 array of 9 indents each 600 nm deep and 10 μm apart were made in the area of interest. It was found from other experiments that the tensile sample failed at about the center of its gage area as expected. The indents were therefore made at the center of the tensile sample. Details of the nanoindentation process have been discussed earlier in section 4.2. The nanoindents made using

a Berkovich indenter had one of the triangular sides parallel to the tensile direction.

6.2.1 Estimation of strains by analyzing the relative displacements of the nanoindentations

To investigate the change in strain with load, the change in the distance between the indents in the diagonal directions and in the transverse directions were measured using the AFM software. The angles that each of these directions make with the X-axis were also measured. The Y-axis was oriented in the tensile direction as illustrated in Figure 6.1

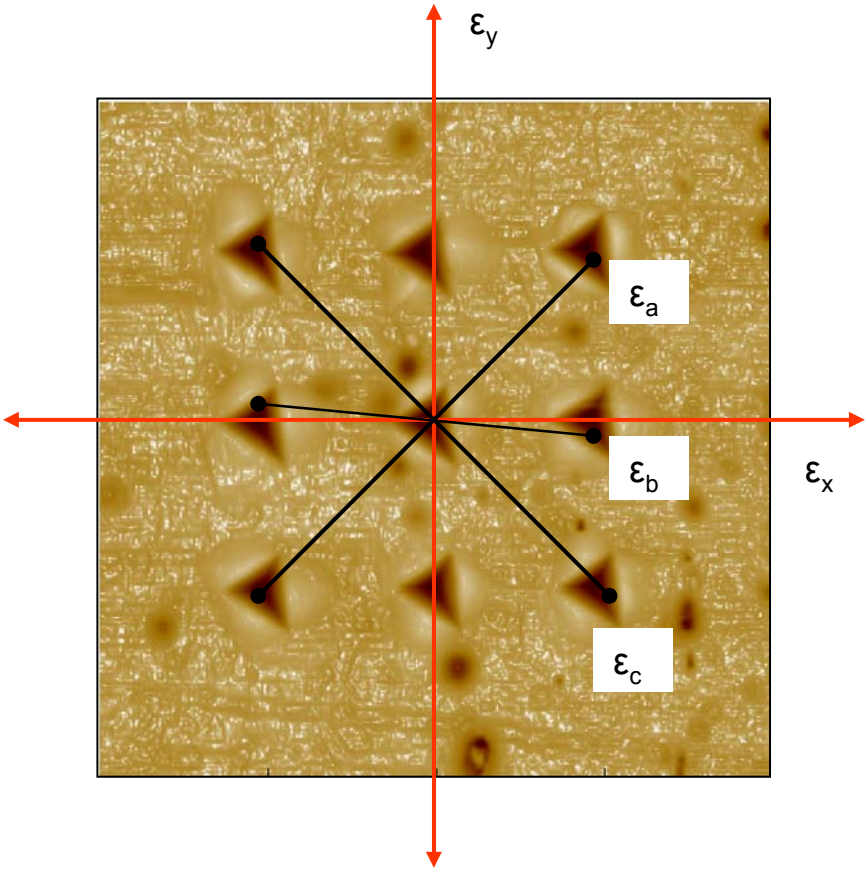

Figure 6.1 : Strain estimation from an array of nanoindents

The distances between each of the indents in the directions indicated earlier were measured for the same set of indents at various stages of deformation during the tensile test. Let A_0, B_0, and C_0 be the distances between the indent centers before the deformation. A, B, and C are the distances between the same set of indents after deformation. Let ε_a ,ε_b, and ε_c be the strains measured in the directions shown in Figure 6.1.

The strains are estimated as

$$\varepsilon_a = \frac{A - A_0}{A_0} \tag{6.1}$$

$$\varepsilon_b = \frac{B - B_0}{B_0} \tag{6.2}$$

$$\varepsilon_c = \frac{C - C_0}{C_0} \tag{6.3}$$

Let α, β, and γ be the angles that these strains make with the X-axis, respectively. Also, let ε_x and ε_y be the strains in the transverse and longitudinal directions. Let ε_{xy} be the shear strain.

The strains in the transverse and tensile directions can be estimated from the following relationships:

$$\varepsilon_a = \varepsilon_x(\cos^2\alpha) + \varepsilon y(\sin^2\alpha) + 2(\varepsilon_{xy})(\sin\alpha)(\cos\alpha) \tag{6.4}$$

$$\varepsilon_b = \varepsilon_x(\cos^2\beta) + \varepsilon y(\sin^2\beta) + 2(\varepsilon_{xy})(\sin\beta)(\cos\beta) \tag{6.5}$$

$$\varepsilon_c = \varepsilon_x(\cos^2\gamma) + \varepsilon y(\sin^2\gamma) + 2(\varepsilon_{xy})(\sin\gamma)(\cos\gamma) \tag{6.6}$$

6.2.2 Measurement of features using AFM software

To estimate strains using the relative indent movement (RIM) method, it is important to determine the feature lengths with minimal error so that the there is minimal error in the calculated strains. The first step in minimizing errors is to ensure that the AFM is calibrated. The procedure for the calibration of the AFM has been presented earlier, in section 4.1.2. In this investigation, it was necessary to estimate the distances between the indents so that the relative displacements between the same could be estimated. It was found that error in measurements can be minimized by measuring distances between the deepest parts of the indents. By inverting the images, the deepest points will appear as the highest points (or apex). The residual indents now appear as tetrahedral pyramids.

Using the AFM software, contour plots, were made which clearly identify regions of the same height with the same colors. The highest part of the pyramid would be clearly seen as a point [see Figure 6.2 (a)]. This greatly reduces the error in the measurement of feature distances. Figure 6.2 (b) is a frequency distribution plot showing the variation in the measured values of ten measurements for the same feature length. It can be seen that the variation is minimal as the error in measurements was < 0.1 %. Consequently, the effect of this error on the final strain values would also be < 1 %.

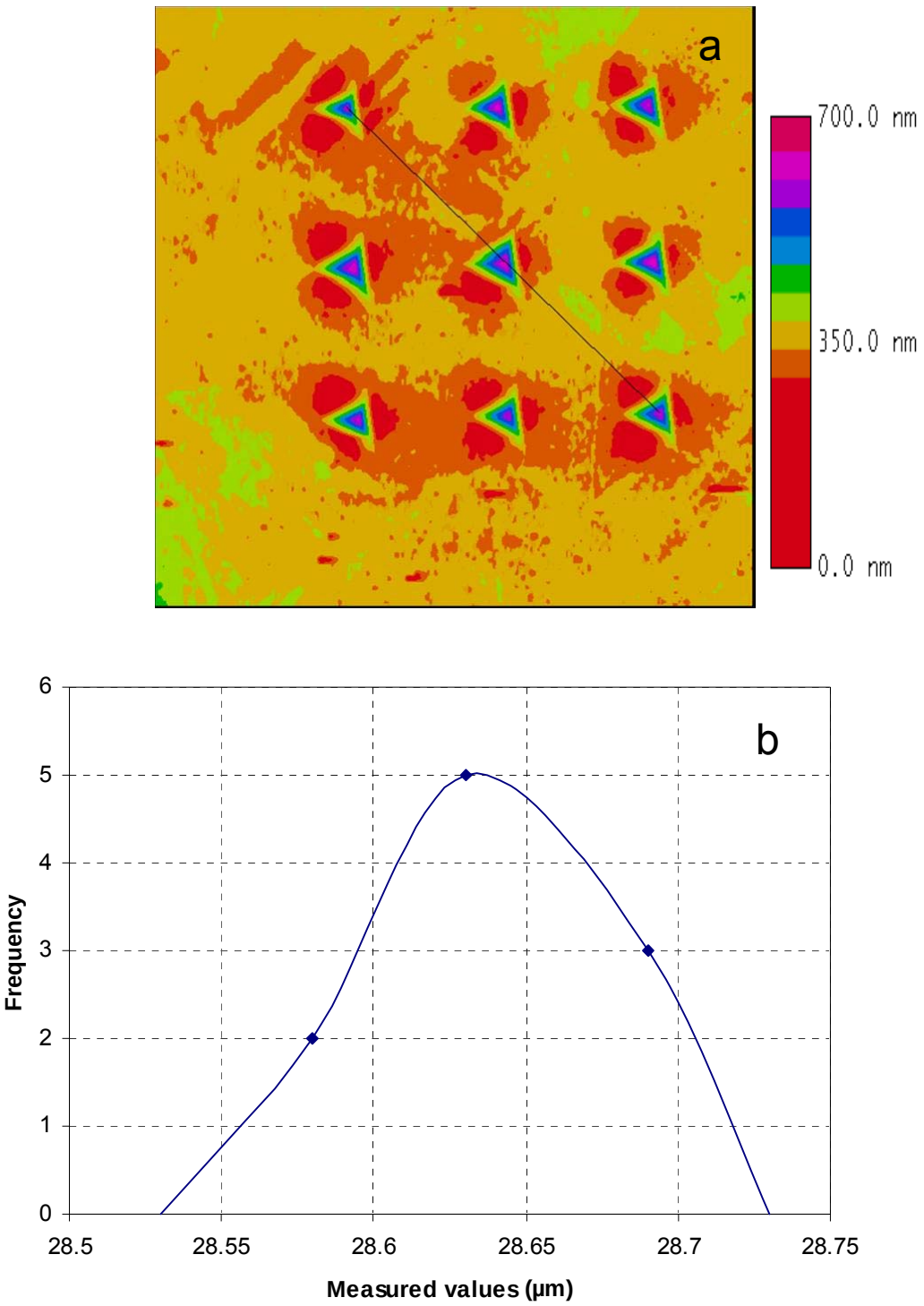

Figure 6.2 : (a) AFM image for the measurement of feature size using AFM software (b) variation in the measured values of distance between indents

6.2.3 Validation of strains estimated using Relative Indent Movement (RIM) method and Digital Image Correlation (DIC) method

When a new method is developed, it is necessary that the results obtained using this method is comparable with other known methods. Several approaches were considered to validate the new method, namely RIM for strain with an existing method namely, Digital Image Correlation (DIC) method. Validation is accomplished by comparing the measured value to a known value or to a value estimated by a known method. In this investigation, the DIC method as well as the RIM method was compared for known values of strains. This was done by performing a virtual "digital" tensile test during which an image is stretched in the longitudinal (tensile) direction and shrunk in the transverse direction by know values. The images thus modified are then analyzed using the methods that need to be validated. Table 6-1 lists the control parameters used with DIC software for the "digital" tensile test.

Figures 6.3 through 6.5 show digitally stretched images in the Y-direction in steps of 2.5 % and shrunk in the X- direction in steps of 2.5 % from the original image as shown in Figure 6.1. Details of each of the modified images are given in a tabular form beside each of the figures. These images were analyzed using DIC software and the RIM method to determine strains. Figure 6.6 shows that the strains estimated by the software were in agreement with known values of deformation that were digitally imposed. Figure 6.6 (a) shows the variation of the estimated strains with actual strains in the tensile direction. The difference in strains estimated using the DIC software was higher at higher strains. The results

obtained using the RIM technique had lesser deviations from the actual strains but were slightly higher. The error at the highest strains was ~ 1 %.

Table 6-1 Control parameters used with DIC software for "digital" tensile test

Number of nodes	3 x 3 = 9
Sequence of next node	Left - right
Spacing (pixels)	128 x 128
Subset radius (pixels)	30 x 30
Smoothing radius (pixels)	1
Maximum number of iterations	50
Tolerance	0.0001

Strains that were estimated as a result of shrinkage in the transverse direction are shown in Figure 6.6 (b). The strains estimated by both DIC and RIM were comparable with the actual compressive strains. At strains > 0.1, the variation with actual values was about 1- 2 % for the RIM technique. The error for the DIC software was about 3%. Since the RIM and DIC techniques were able to estimate strains quiet accurately, these techniques can be used for strain estimation.

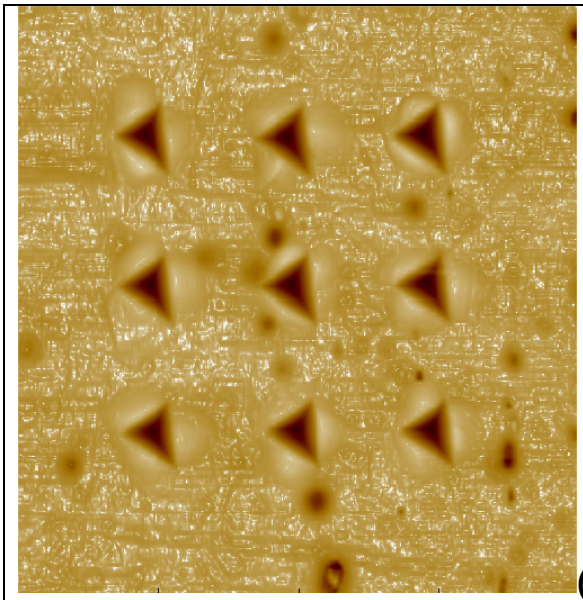

(a)

	Transverse	Tensile
Image size	497	523
Change in size	-0.025	+0.025
Est. Strain using DIC	-0.0245	0.021
Est. Strain using RIM	-0.025	0.026

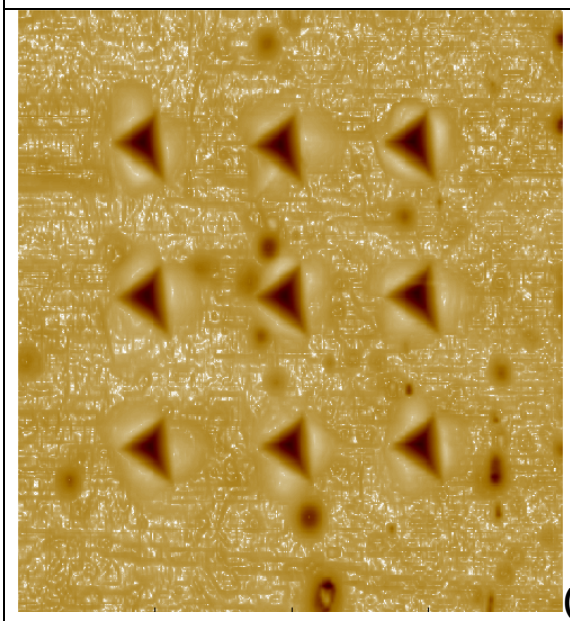

(b)

	Transverse	Tensile
Image size	485	536
Change in size	-0.05	+0.05
Est. Strain using DIC	-0.048	0.055
Est. Strain using RIM	-0.048	0.052

Figure 6.3 : Digital stretching (Y-axis) and shrinking (X-axis) of image for validation by (a) 2.5 % (b) 5 %

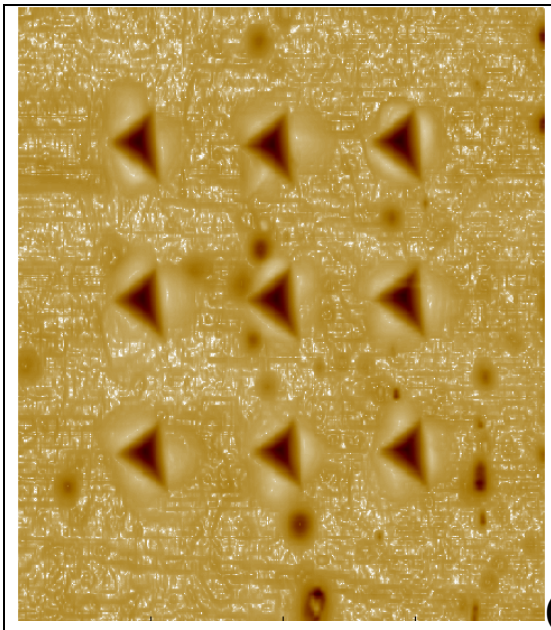

(a)

	Transverse	Tensile
Image size	472	549
Change in size	-0.075	+0.075
Est. Strain using DIC	-0.072	0.077
Est. Strain using RIM	-0.073	0.077

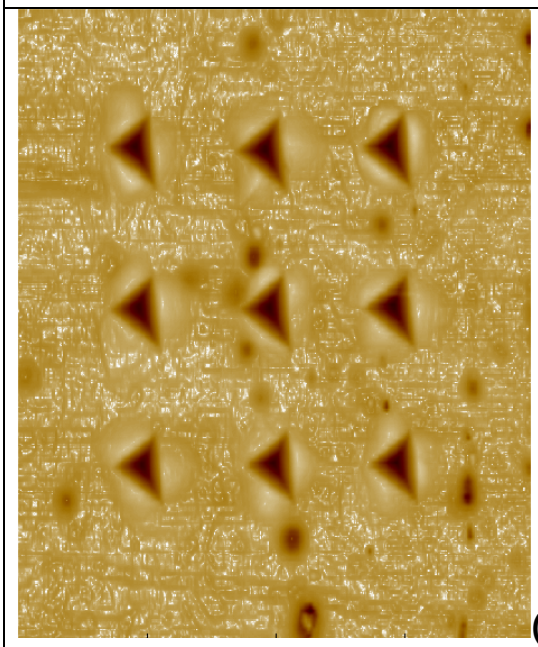

(b)

	Transverse	Tensile
Image size	459	561
Change in size	-0.1	+0.1
Est. Strain using DIC	-0.095	0.107
Est. Strain using RIM	-0.097	0.102

Figure 6.4 : Digital stretching (Y-axis) and shrinking (X-axis) of image for validation by (a) 7.5 % (b) 10 %

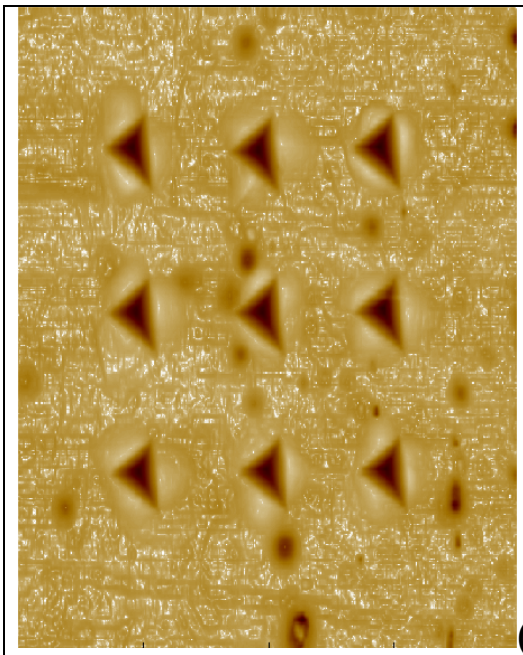

(a)

	Transverse	Tensile
Image size	446	574
Change in size	-0.125	+0.125
Est. Strain using DIC	-0.119	0.133
Est. Strain using indent	-0.122	0.127

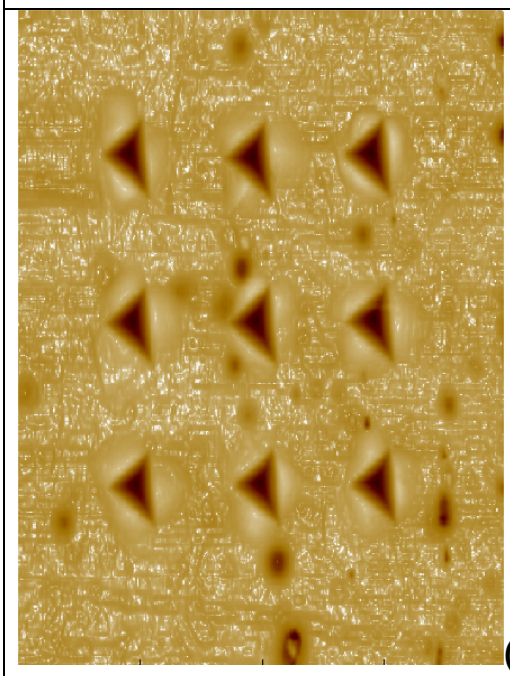

(b)

	Transverse	Tensile
Image size	434	586
Change in size	-0.15	+0.15
Est. Strain using DIC	-0.141	0.16
Est. Strain using indent	-0.147	0.155

Figure 6.5 : Digital stretching (Y-axis) and shrinking (X-axis) of image for validation by (a) 12.5 % (b) 15 %

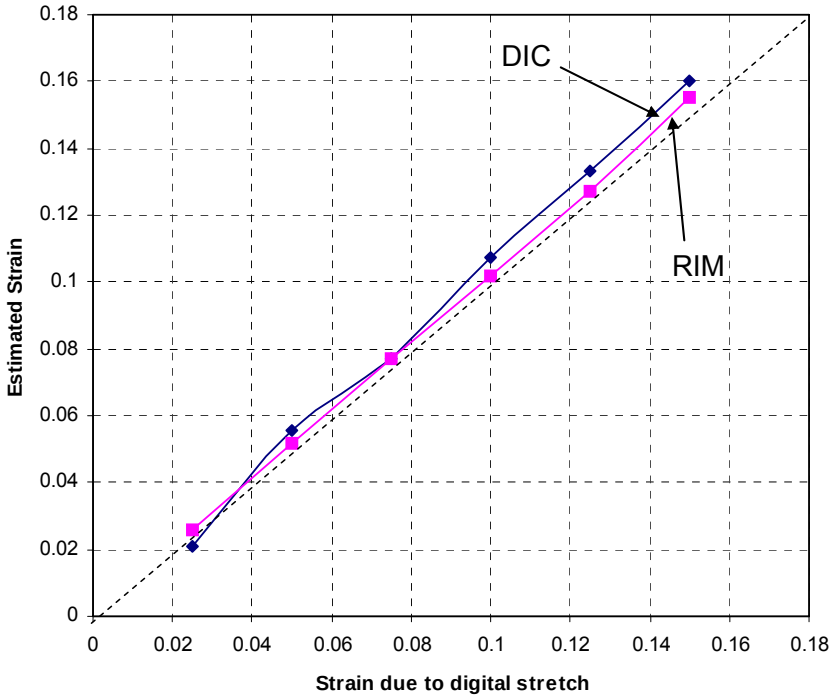

(**a**)

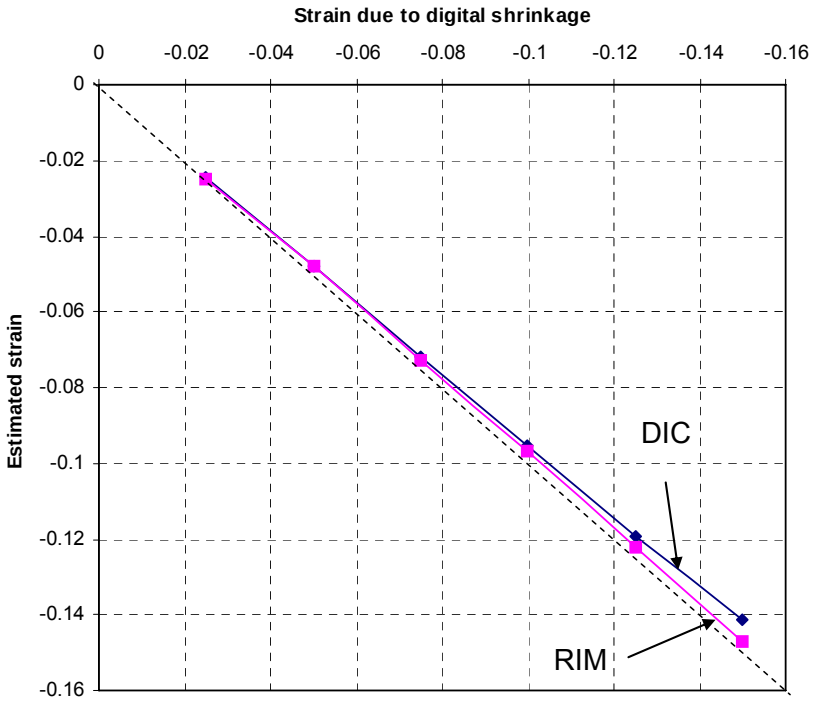

(**b**)

Figure 6.6: Results of strain analysis by DIC and RIM on digitally altered images (a) Stretch in tensile direction (b) Shrinkage in transverse direction

6.2.4 Experimental validation of RIM method - Tensile testing of polycarbonate

To test the validity of the Relative Indent Movement (RIM) method additional tension experiments were performed on polycarbonate samples. Polycarbonate was chosen because of its uniform elongation during tensile testing. The resemblance of its tensile response to that of some metallic materials such as copper in spite of fundamental differences that exist at the atomic/molecular and micro structural level, [both in terms of structural (long range order) and micro mechanisms that governs the deformation at the local level] is also another reason for selecting this material[75].

The main aim in performing experiments on a polymeric sample was to overcome issues associated with testing polycrystalline materials, namely, the differences in local strains compared to the global strain. Elongation of polymeric materials, such as polycarbonates is relatively longer (~ 3-5%) in the initial stages, when compared to metals and is uniform until yielding takes place[75]. The elongation becomes uniform again after yielding is initiated and necking starts, up until when the material begins to strain harden.

Polycarbonate Lexan® tensile samples of the same dimensions as copper samples (Section 4.5) were tested on a tensile testing setup that could be used to perform *in-situ* tension tests with an AFM. Details of the experimental setup and procedure have been discussed in Sections 4.4 and 6.2.3, respectively. Samples of Lexan polycarbonate were machined to specifications at the Petroleum Building of OSU by Prof. Warren Lewis of the Mechanical Engineering Technology and his group. Figure 6.7 shows the images of an untested Lexan

sample and a sample after necking has started. These samples were cut out from cast polycarbonate sheets.

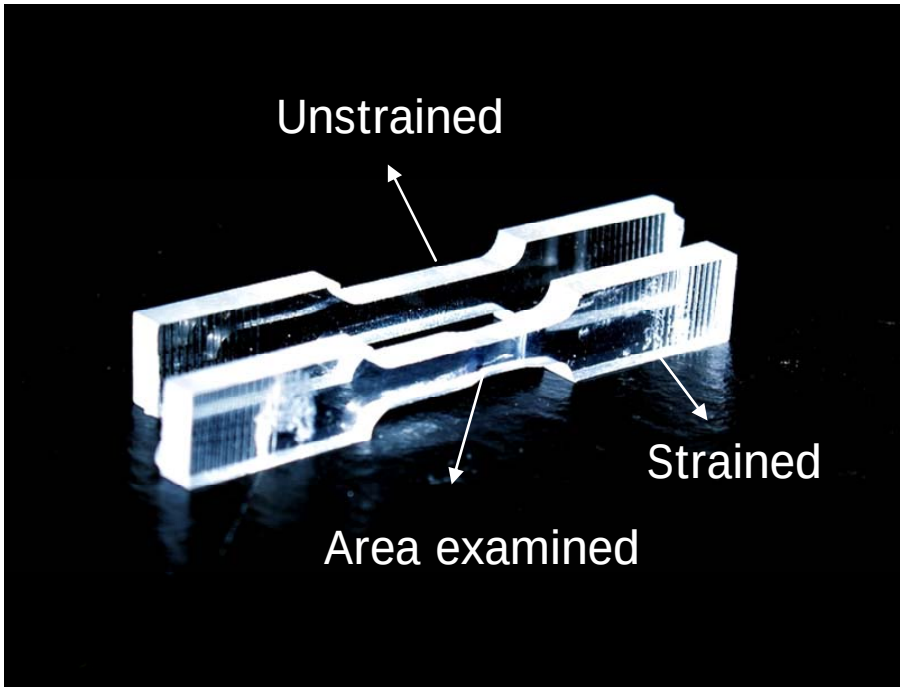

Figure 6.7 Polycarbonate samples before and after tensile testing

LEXAN® is a registered trademark of General Electric's highly-durable polycarbonate resin thermoplastic with a unique combination of high impact strength, flame retardancy, and thermoformability making it ideal for security applications. It is made up of chains of Bisphenol A alternating with phosgene, or carbonyl chloride [76].

Lexan is similar to polymethyl methacrylate (PMMA) — commonly know as Acrylic, in appearance but it is far more durable. It is typically used in the aerospace industry for items such as aircraft canopies, windscreens and other windows and also in household items, such as bottles, compact discs, and DVDs. It is also one of the most common products used to make Bullet-resistant

glass[76]. Elongation of samples during tensile tests can be as high as 130 %.

Figure 6.8 shows the stress-strain plot of the Lexan sample. The tensile testing setup, used in this investigation, is shown in Figure 4.14. It can be seen from Figure 6.8 that there are distinct regions in the stress strain curve of Lexan, namely, the region before yielding takes place and the long elongated region during which necking starts and plastic deformation takes place. The experiment has terminated after the elongation of the sample reached ~ 0.55 since this is the maximum limit to which the sample can be stretched using the tensile setup used.

A 3 x 3 array of 9 indents each 600 nm deep and 10 μm apart were made in the center of sample gauge area using a Berkovich indenter using an MTS indenter. An area of ~ 45 μm x 45 μm on the sample was examined using an AFM to see how the overall tensile loading of the sample affected the strains locally. To keep track of individual points in the area under interest, the nanoindents were used as markers, as discussed in section 6.2. The nanoindents made had one of the triangular sides parallel to the tensile direction.

Global strain in the tensile sample was monitored using a LSC displacement transducer discussed in section 4.4. The elongation rate during the tension experiment was ~ 14 μm/s. The tensile testing setup was placed under the AFM and images of the area on the surface of the sample where the nanoindents were made were imaged at different strain intervals until necking was initiated in the sample. No cleaning of the sample was performed before it was mounted on the tensile stage. The polycarbonate sheets are received with a

plastic film or paper that covers the surface to prevent accidental scratches. This film is pealed off just before the experiment is performed.

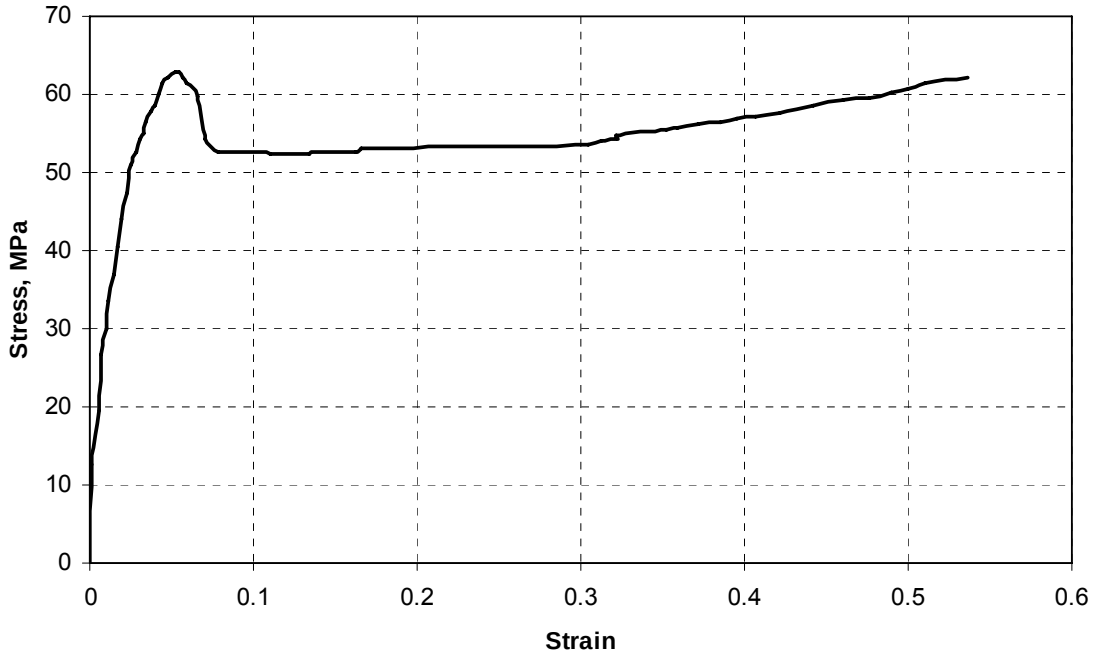

Figure 6.8 Stress- strain curve of Lexan Polycarbonate

Extra attention needs to given while imaging the surface of clear samples such as glasses and plastics. The imaging procedure of the AFM has been described in section 4.1. The imaging tip of the AFM approaches the surface to be imaged based on the focus position of the tip relative to the surface. The distance to be traveled by the tip before it comes in contact with the surface is determined by the difference between these two focus points. Since light transmits through transparent samples, it is difficult to focus the top surface of the sample especially samples that are “very clean”. There is a very good possibility that the lower surface is focused and when the tip approaches the surface, it comes in contact with the top surface since it assumes that the lower surface is

the top part of the surface. This can result in damage to the AFM head and can also result in the destruction of expensive tips such as the diamond nanoindenter tip. Sometimes a dirt particle or markers on the surface to be imaged is good, as this helps in focusing the surface by the optical microscope with the AFM.

Figure 6.9 (a) shows the array of nanoindents on the polycarbonate sample before the tensile load is applied. Figures 6.9 (b) and (c) are higher magnification AFM 3D images of one of the indents at 0 strain and at 0.07 strain. The area around the indent at 0.07 strain shows some deformation [see Figure 6.9 (c)]. Figure 6.10 shows the same set of indents at various global strains. Figure 6.10 (a) is 3D AFM image of the nanoindents at a global strain of ~ 0.003. No visible deformation can be seen at this stage. Small changes in the texture of the surface can be seen at strains of 0.012 and 0.024. Some deformation can be seen in Figure 6.10 (d) around the indents at a strain of ~ 0.048. Figure 6.10 (e) was captured at a strain of ~ 0.056 just before the sample began to yield. Deformation around the indents has increased. Figure 6.10 (f) is an AFM 3D image of the nanoindents after yielding began but just before any significant necking has started at a strain of ~ 0.064. It can be seen that there is uniform deformation around each of the indents showing that the material is uniform in composition. Soon after this stage, the sample began to neck and indents were in the curved region just where the necking took place. More images could not be captured since the surface is not flat anymore. The curved surface can be seen in Figure 6.7 (small area near the necked region of the sample).

The images obtained were analyzed using the RIM method described in Section 6.2.1. The distance between the indents was measured using the technique described in Section 6.2.2.

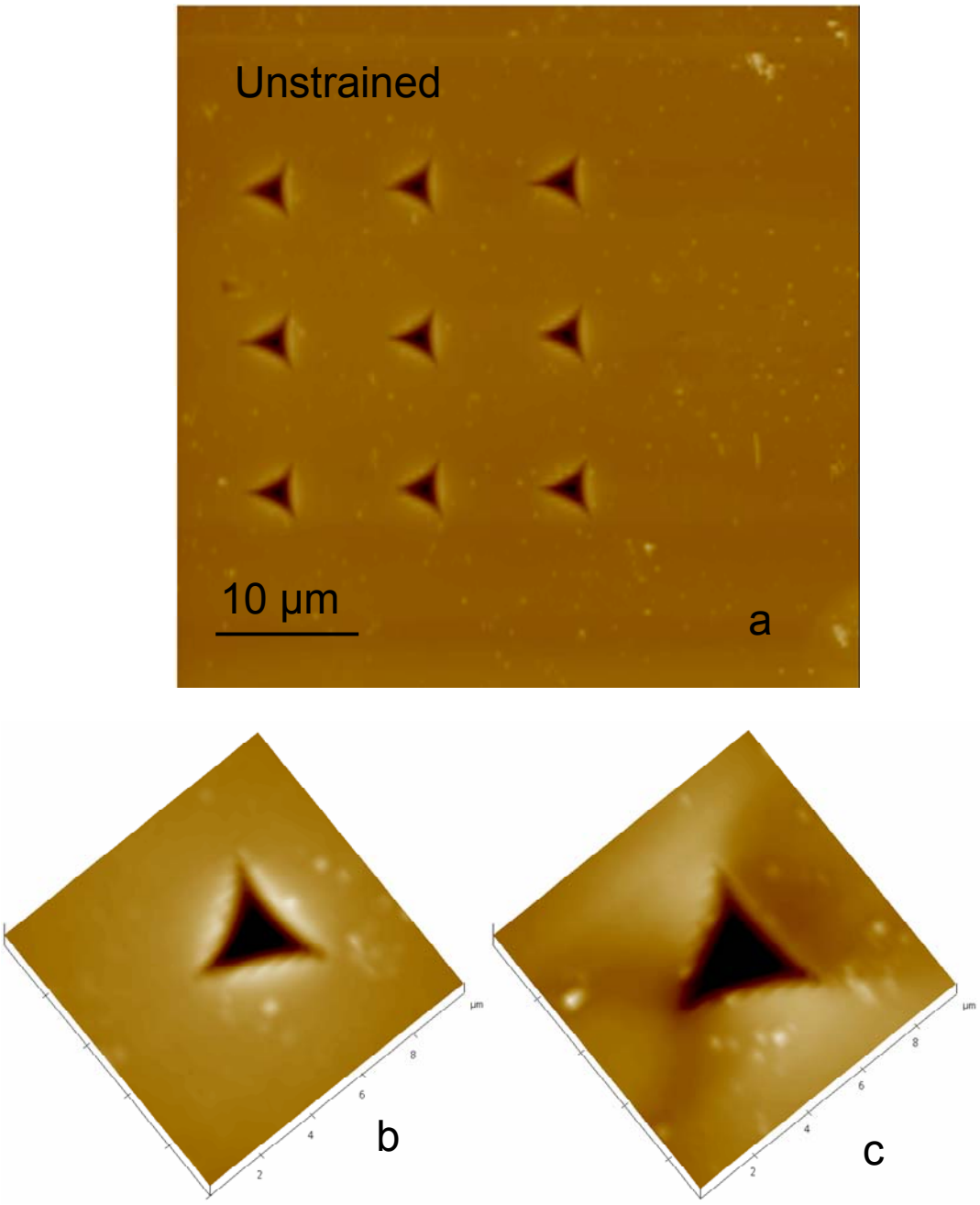

Figure 6.9 (a) Surface of the Lexan polycarbonate with 9, 600nm deep indents 10 µm apart (b) one of the indents at 0 strain (c) same indent at 0.07 strain

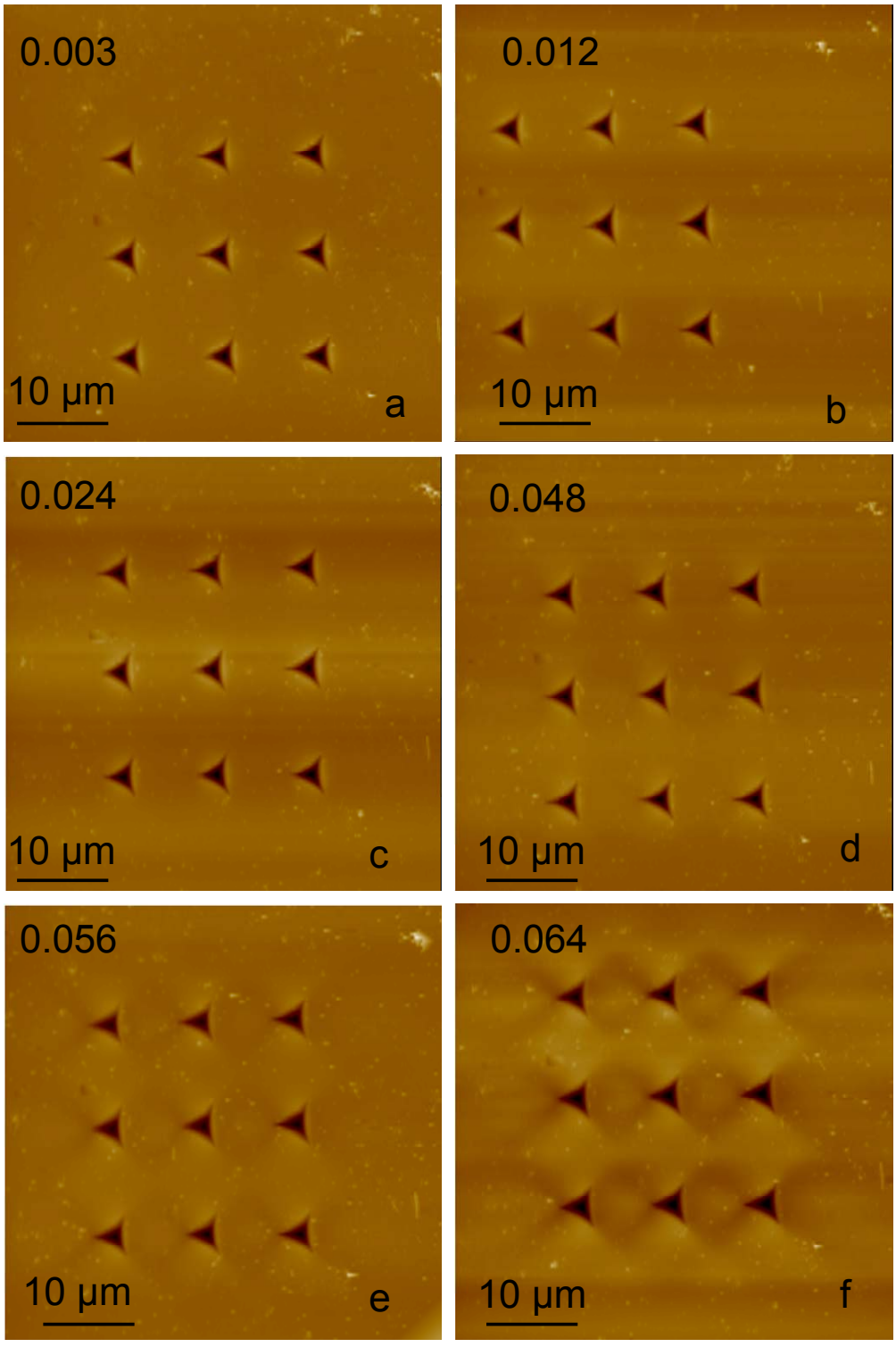

Figure 6.10 AFM 3D images of the a 3 x 3 array of 600 nm indents at various stages of axial loading at engineering strains of 0.003 – 0.07(a) 0.003 (b) ~0.012 (c) ~0.024 (d) ~0.038 deformation around indents (e)~0.056 (f) ~0.07 – yielding starts

Figure 6.11 shows the variation of the tensile, transverse, and shear strains estimated using the RIM method with respect to the global strain measured using the LSC transducer. It can be seen that the tensile strains have a very good match with the global strains. Variation of the local strain with global strain begins after yielding starts. The local strains are higher than that of the global tensile strains. It is also interesting to note that there is no variation in the shear strain and is almost zero. Some changes in the transverse strain can be seen with increase in global strain which is the result of reduction in the width of the sample. It can, therefore, be concluded from these experiments that the RIM method can be used to measure strains locally and it agrees well with strains measured using a calibrated LSC transducer.

The images in Figure 6.10 were also analyzed by the DIC method described in section 6.2.3. Figure 6.12 shows the comparison of strains estimated by the RIM method and the DIC method with respect to the global strains measured by the LSC transducer. The values of strains estimated by the DIC are similar to the values of the RIM method until the global strain is ~0.05. This is the stage at which deformation can be seen to increase around each indent. It can be seen from Figures 6.10 (d) through (f) that deformation around the indents results in the squeezing of the indent edges inwards. Though the sample is stretching the indents themselves are getting squeezed. This results in the edges moving towards the center of the indents and corners of the indents moving outwards. Since the DIC method averages the strains measured around each indent, the final strain values are lower, as can be seen from Figure 6.12.

The RIM method and the DIC method show comparable results until just prior to yielding.

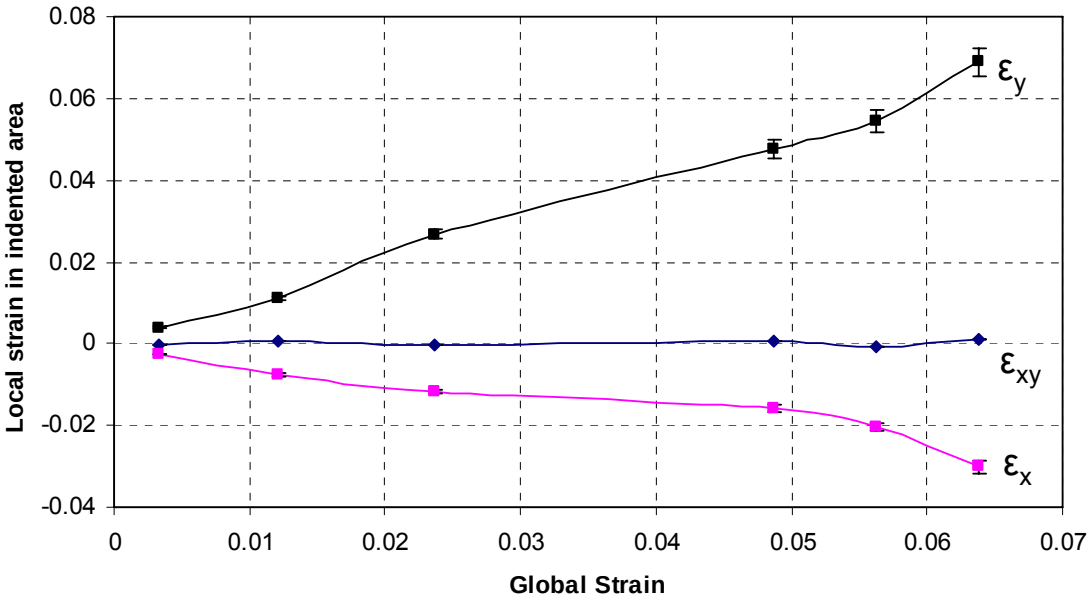

Figure 6.11 Local strains estimated in polycarbonate sample by RIM method

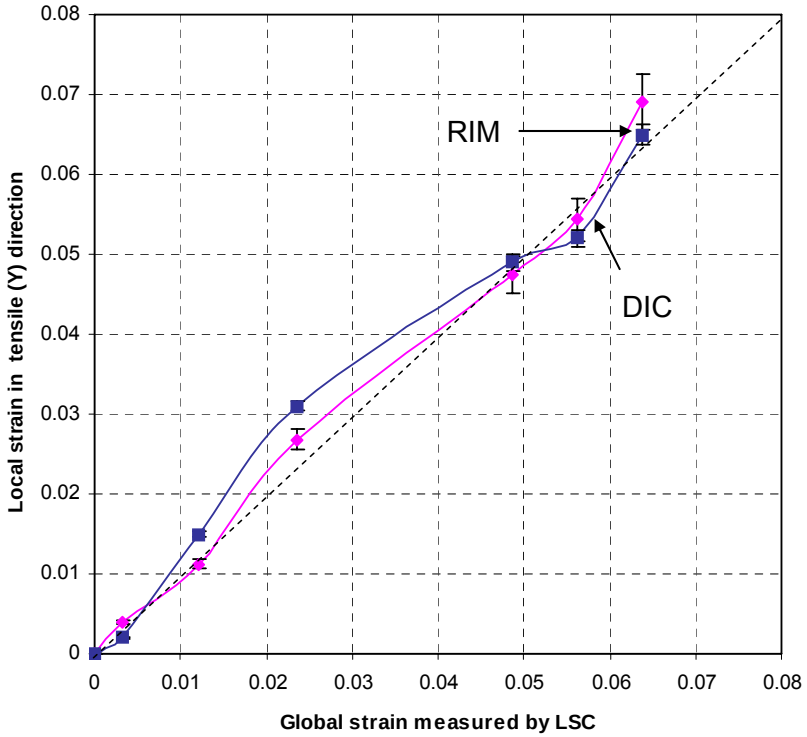

Figure 6.12 Comparisons of strains estimated by RIM and DIC methods

6.3 Results and Discussion

AFM images were acquired at 13 different stages starting from zero load to the maximum load. The relative movements and the deformation of the indents at various stages of the tensile test are shown in Figure 6.13. Only some of the images acquired are shown here since the variation between intermediate images were incremental. Figure 6.13 (a) is the indented surface after the sample has been mounted on the tensile stage. Since the surface was not etched, no grain boundaries can be seen. Figure 6.13 (b) is an image taken in the elastic region of the tensile sample at ~ 0.003 average strain. No slip lines are seen even at strains of ~0.01 - 0.02, which is well past the elastic limit as in Figures 5.13 (c) and (d). First signs of any deformation in the form of slip bands can be seen in Figure 6.13 (e) at a strain of ~0.04. More slip bands can be seen to form in the same area at ~ 0.07 strain [see Figure 6.13 (f)].

At ~0.1 strain more grains show slip bands as shown in Figure 6.14 (a). Some of the indents have been distorted due to the effect of slip bands while others have started to move up or down forming a very uneven surface. Figure 6.14 (b) shows the indents at ~0.12 average global strain. Visible displacement of the indents with respect to each other can be seen. An AFM image acquired at the maximum load applied at a strain of ~0.14 shows the surface to be very uneven. Several grains with multiple slip bands can be seen. Slip bands have moved across several indents, sometimes severely distorting their shape. Figures 6.14 (d) and (e) show AFM 3D images of the same indent before tensile loading and at maximum load, respectively.

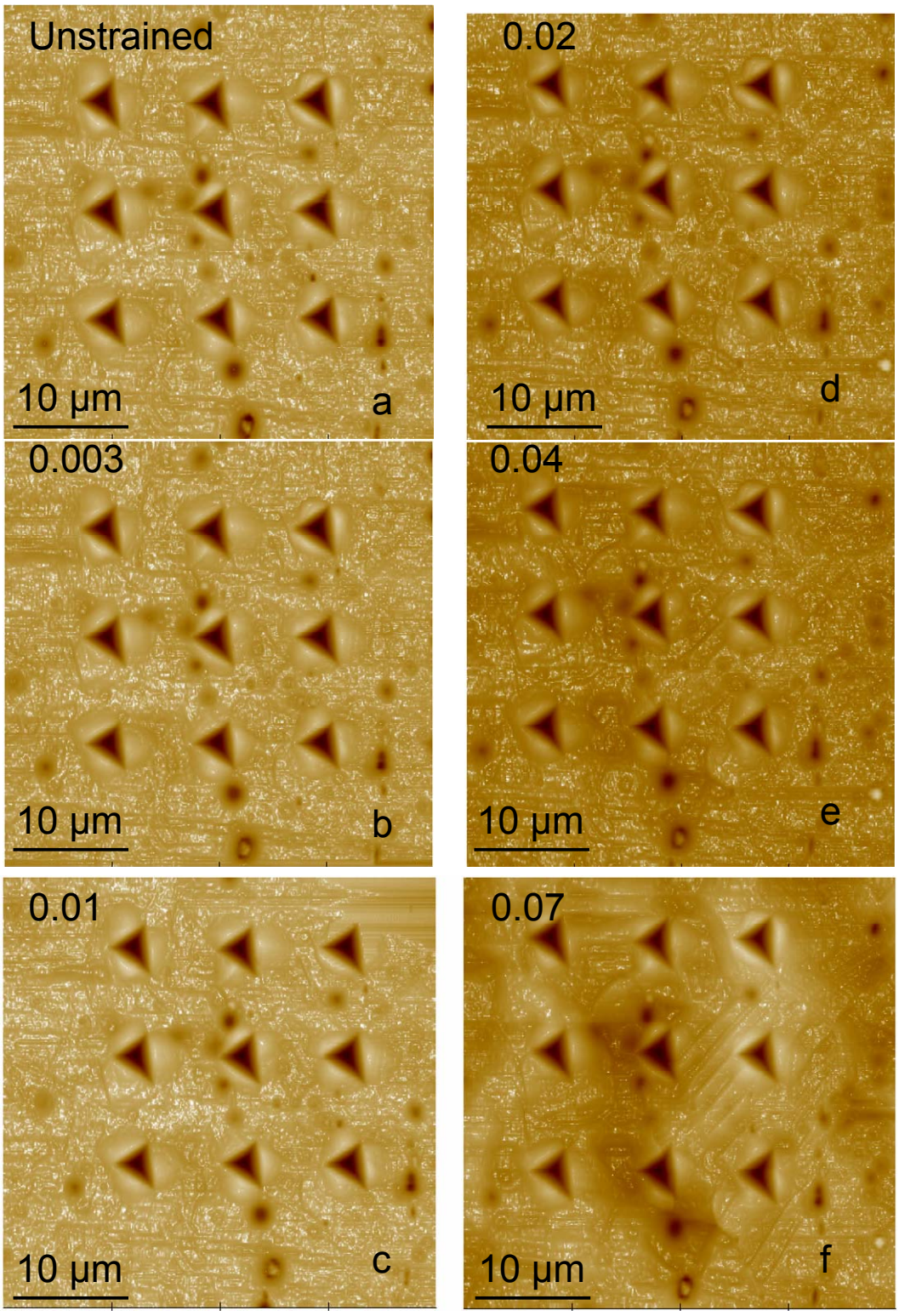

Figure 6.13 : AFM 3D images of the a 3 x 3 array of 600 nm indents at various stages of axial loading at engineering strains of 0.003 – 0.07(a) 0 - before loading (b) ~0.003 (c) ~0.01 (d) ~0.02 (e)~0.04 formation of slip bands (f) ~0.07 more slip bands seen

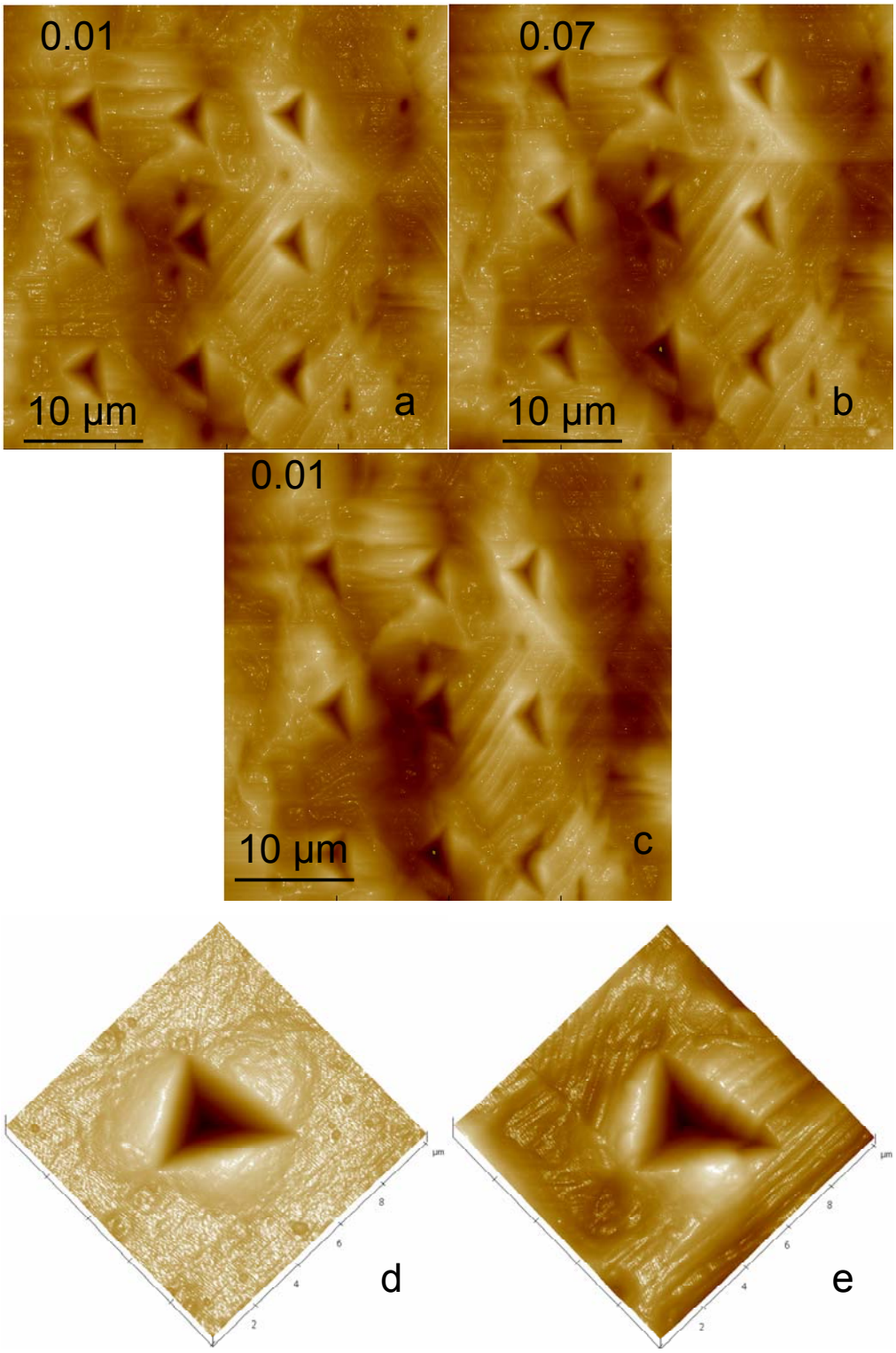

Figure 6.14: AFM 3D images of the a 3 x 3 array of 600 nm indents at various stages of axial loading at engineering strains of 0.1 – 0.14(a) ~0.1 (b) ~0.12 (c) ~0.14 - Maximum Load (d) Image of one of the indents at beginning of test (e) Same indent at maximum load – Slip bands moving over indent.

Slip lines can be seen running across the indent walls at the maximum load [Figure 6.14 (e)]. A grain boundary which was not visible in the image of unloaded sample can be seen in the same image.

Images were acquired at various intervals of average tensile strain of the tensile sample. The measured strains ε_a ,ε_b, and ε_c along with the estimated transverse, tensile, and shear strains are also shown in Figure 6.15. The measured angles α, β, and γ were 47.73º, 0º and 315.53º. It may be noted that angle β is 0º which means the array of indents in the transverse direction are perpendicular to the tensile direction indicating that the sample has been aligned properly. Some times, the sample may not have been aligned properly in which case the offset would affect the strain measured in the transverse direction. The strains estimated for ε_x would be the same as for ε_b.

Figure 6.15 shows the tensile, shear, and transverse strains in a 40 μm x 40 μm area with respect to the engineering strain estimated for the tensile sample. It can be seen that no significant increase in the transverse and tensile strain is seen in the area until ~ 0.07 average strain has reached in the sample. This indicates that after some initial deformation at ~0.04 average strain in the area, not much deformation takes place until ~0.07. This may be due to initiation of plastic deformation in other grains in the tensile sample.

By the time the sample reaches its ultimate tensile strength at a nominal strain of ~ 0.14, much larger strains are encountered locally. The maximum strain in the tensile axis in this area is ~0.3 which is almost twice the nominal strain. A transverse strain of ~-0.11 is seen at the maximum load indicating a reduction in

area. Maximum shear strain estimated was ~ - 0.05. It is interesting to note that the tensile strain actually decreases in the initial stages suggesting that the surrounding grains are straining the grains in the area of interest resulting in the shrinkage of the grains.

Table 6-2 Results of strain estimation using 600 nm nanoindents

Average Linear Strain ε	ε_a	ε_b	ε_c	ε_x	ε_y	ε_{xy}
0.003	0	0.006098	0.007495	0.006098	0.001578	-0.00364
0.006	-0.0077	0.00813	0.01142	0.00813	-0.00393	-0.00927
0.02	-0.01751	-0.00407	-0.00821	-0.00407	-0.02093	-0.00422
0.038	-0.01751	-0.00915	0.001428	-0.00915	-0.00707	-0.00954
0.045	-0.01366	-0.00762	-0.0025	-0.00762	-0.00852	-0.00557
0.063	-0.0098	-0.00407	0.001428	-0.00407	-0.00433	-0.00562
0.074	-0.00175	-0.00915	0.007852	-0.00915	0.014206	-0.00542
0.081	0.017507	-0.03455	0.021056	-0.03455	0.068603	-0.00445
0.09	0.020658	-0.04319	0.046395	-0.04319	0.103768	-0.0167
0.1	0.031513	-0.06707	0.068522	-0.06707	0.157228	-0.02435
0.128	0.062675	-0.08689	0.103854	-0.08689	0.239089	-0.02906
0.14	0.070028	-0.11433	0.139186	-0.11433	0.305069	-0.0455

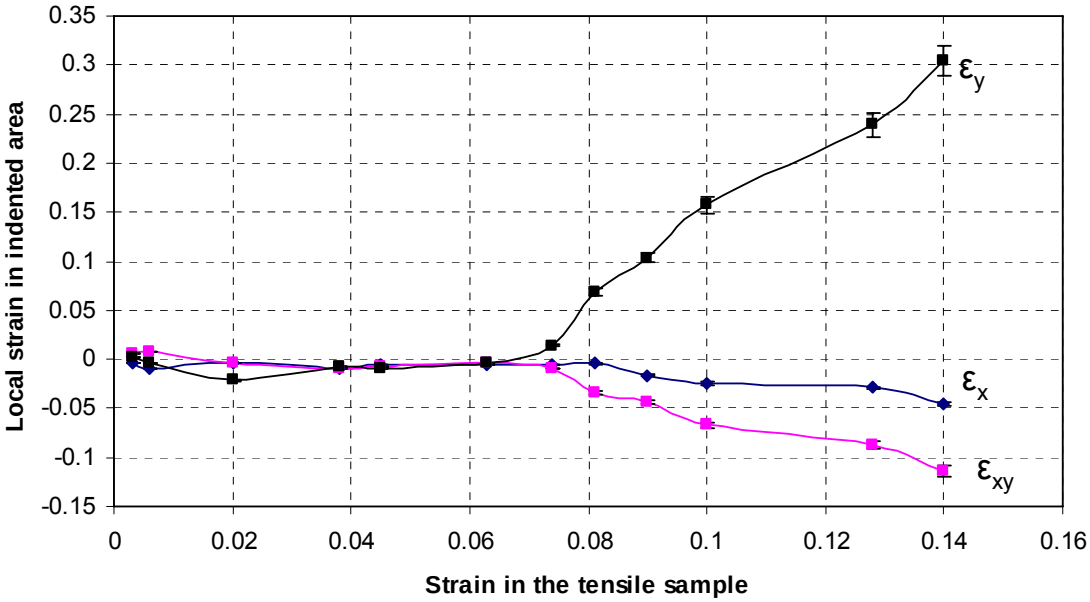

Figure 6.15 : Variation of local strains with bulk strains

6.3.1 Digital Image Correlation (DIC) Analysis

Strains were also estimated by analyzing the images using the DIC software. Nine nodes, at the center of each indent, were selected. The software estimates the strains by comparing how each point in the vicinity of the indent moves with respect to the original image. It analyzes each pixel in the image around the node. A radius of 30 pixels was selected around each node. At this radius an entire indent was included in the analysis. The strain distribution in and around the nine indents in the initial stages of loading can be seen in Figure 6.16

Not much variation in strain in either transverse or tensile directions can be seen in the initial stages, when the global strain is ~0.003 to 0.01. When the global strain increases in the range of ~0.03 to 0.065 as shown in Figure 6.17, some decrease in local strain can be seen in the tensile direction. This is consistent with our earlier analysis in which some shrinkage in the area of interest was seen. Figure 6.18 shows that in the range of ~0.075 – 0.09 global strain, the local tensile strains are ~ 0.15 in the tensile direction and ~ 0.1 in the transverse direction. Some areas experience more strain than the rest. Figure 6.19 shows the results of analysis of the area at average engineering strains of ~0.1 – 0.14. It can be seen that some areas experience maximum tensile strains ~ 0.45. Strains in the transverse direction are ~-0.2. The average strains at maximum load around the center of the area of interest are ~0.3 in the tensile direction and ~0.15 in transverse direction. These are consistent with the results obtained in our earlier analysis in section 6.2.2.

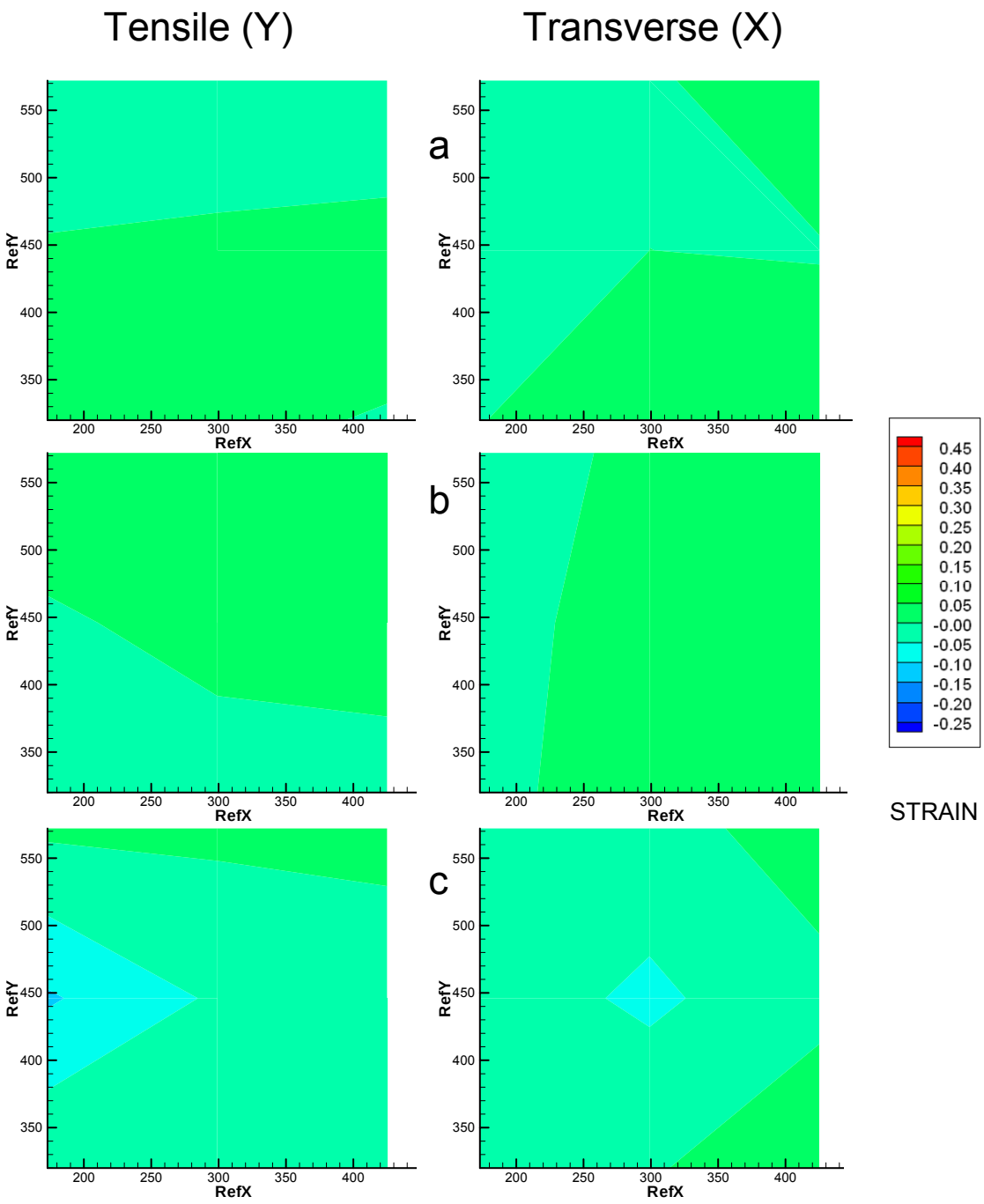

Figure 6.16 : Distribution of strains in the tensile(Y) and transverse (X) directions at various engineering strains. (a) ~0.003 (b) 0.006 (c) 0.02

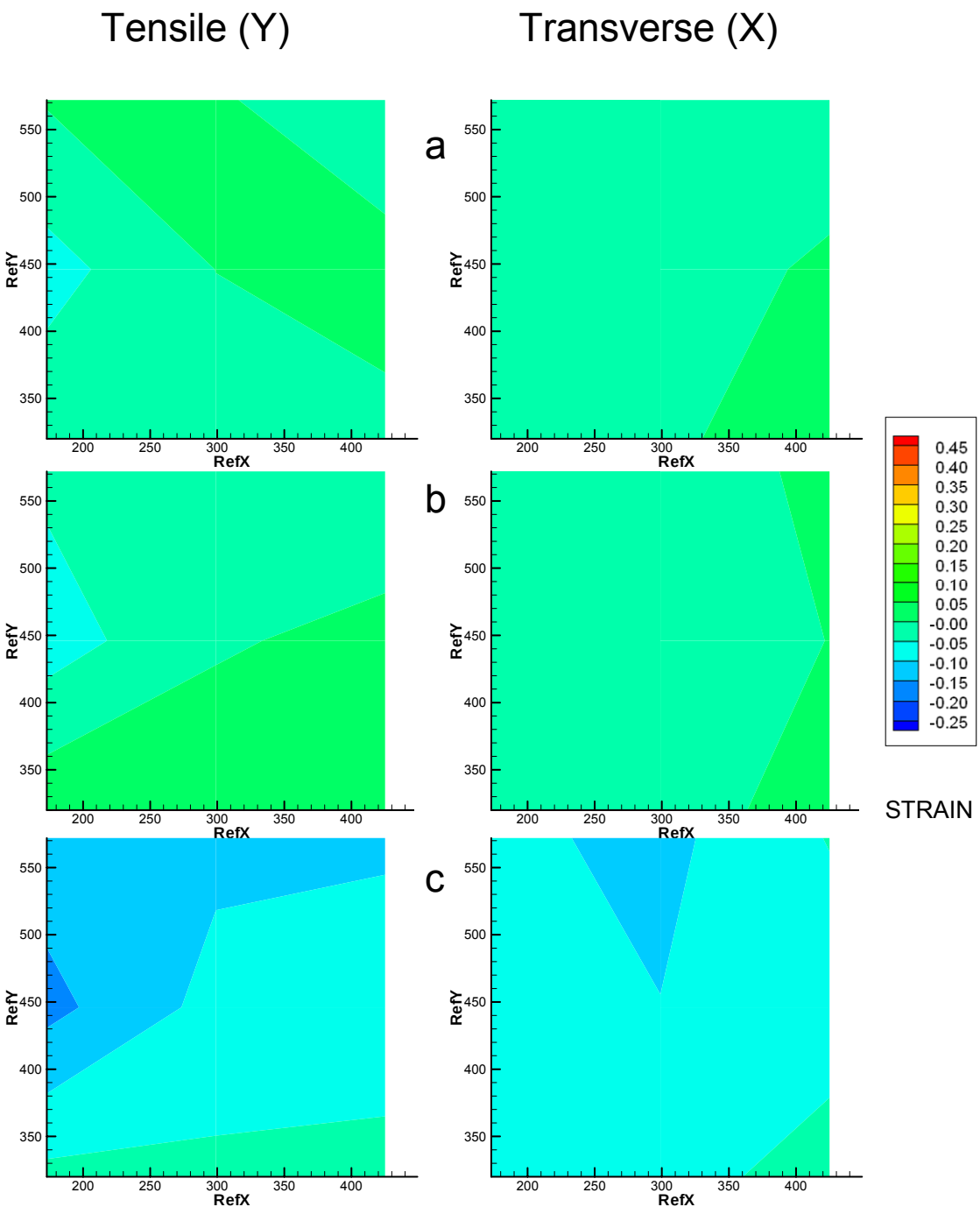

Figure 6.17 : Distribution of strains in the longitudinal (tensile -Y) and transverse (X) directions at various engineering strains ~ (a) 0.035 (b) 0.045 (c) 0.063

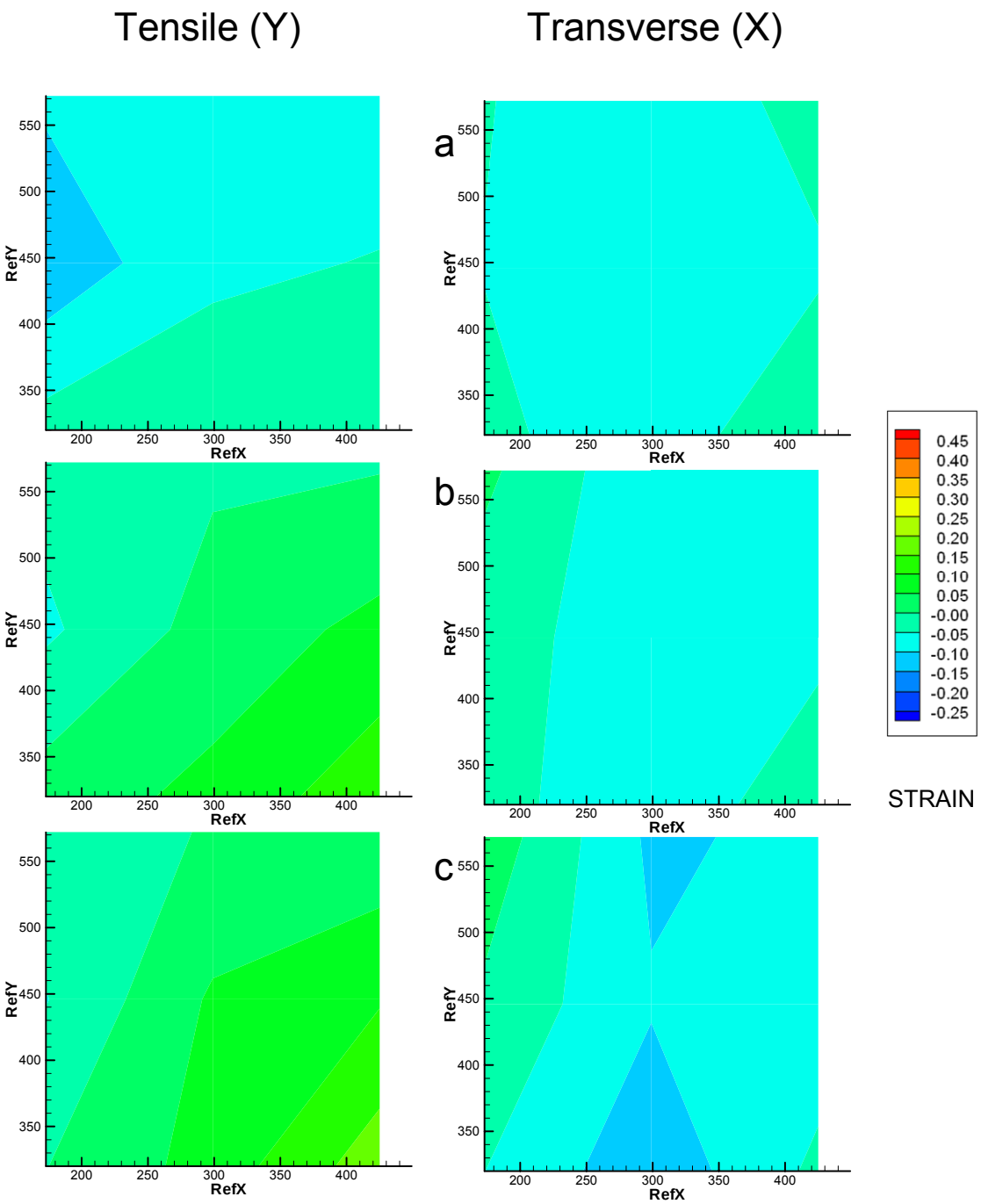

Figure 6.18 : Distribution of strains in the longitudinal (tensile -Y) and transverse (X) directions at various engineering strains ~ (a) 0.074 (b) 0.081 (c) 0.09

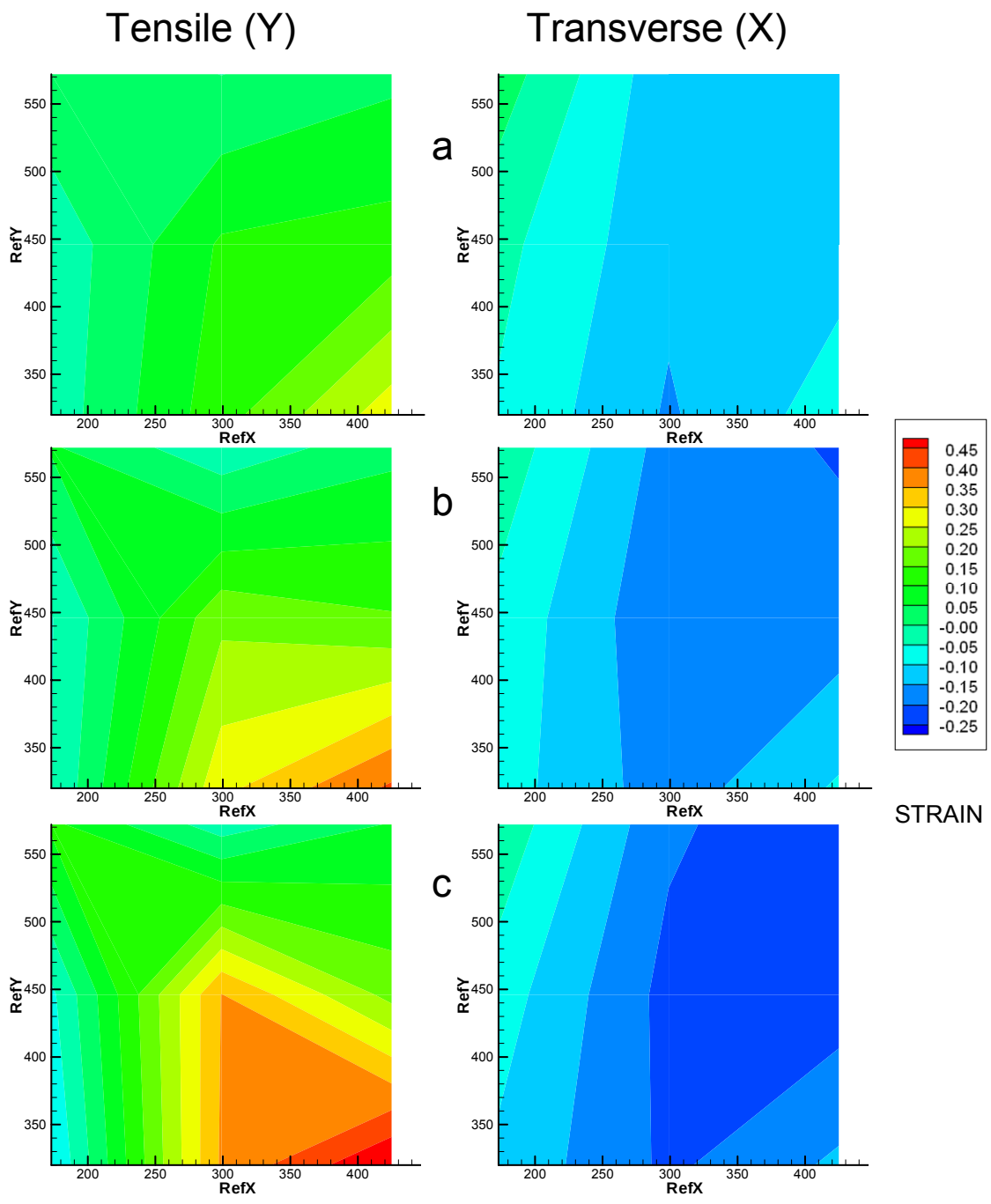

Figure 6.19 : Distribution of strains in the longitudinal (tensile -Y) and transverse (X) directions at various engineering strains ~ (a) 0.1 (b) 0.13 (c) 0.14

6.4 Variation in deformation of different grains under same load

Since the orientation of the grains in different parts of a polycrystal are different, the deformation experienced by each of them would be different under the same loading conditions. To study this phenomenon, two sets of nine nanoindents, each were made on a polycrystalline copper sample ~ 200 μm apart in the area near the center of the sample. One of the sides of each of the indents was oriented parallel to the tensile axis. Care was taken to ensure that these indents were indeed parallel to the tensile axis when the sample was mounted on the tensile testing apparatus. Let the two areas of interest be termed as “area 1” and “area 2”

Figures 6.20 and 6.21 show the deformation of the grains on the surface of a polycrystalline copper sample in area 1. Figure 6.20 (a) is an AFM 3D image of the surface just before the tensile test is performed and it shows some grain boundaries and twinned grains. It shows some slip bands can be seen at a global strain ~ 0.03 [see Figure 6.20 (d)]. With increasing load, more slip systems become active and several slip bands can be seen as a result of this (see Figure 6.21). The strains in this area were analyzed using the RIM method discussed in Section 6.2.1. The results of this analysis are shown in Figure 6.22. Strains in the tensile direction do not show large variations until the global strain is ~0.03. This coincides with the formation of slip bands as can be seen in Figure 6.20 (d).

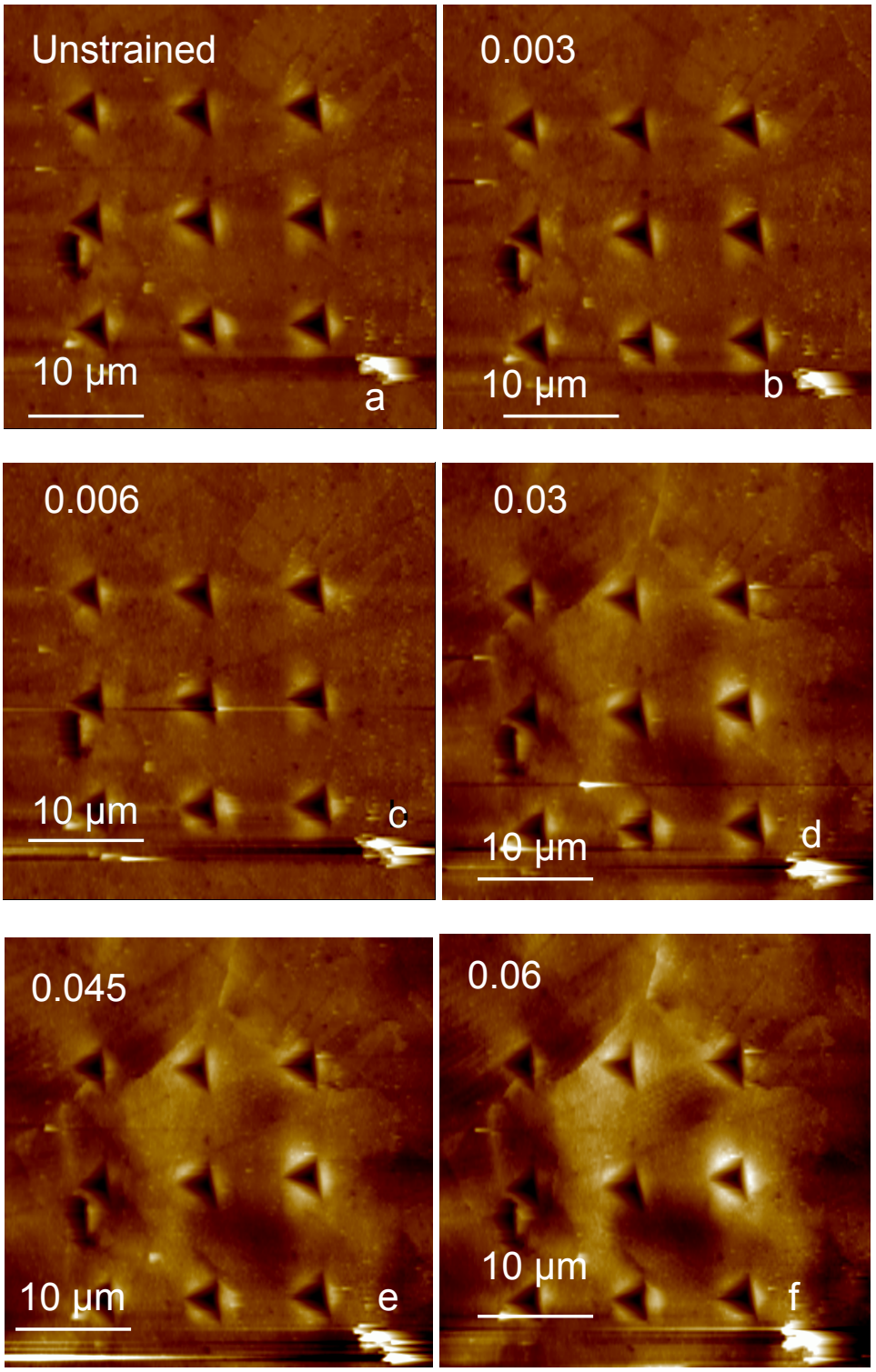

Figure 6.20 : AFM 3D images of the a 3 x 3 array of 600 nm indents at various stages of axial loading at engineering strains of 0.003 – 0.06 (a) 0 - before loading (b) ~0.003 (c) ~0.006 (d) ~0.03 formation of slip bands (e)~0.045 (f) ~0.06 more slip bands seen

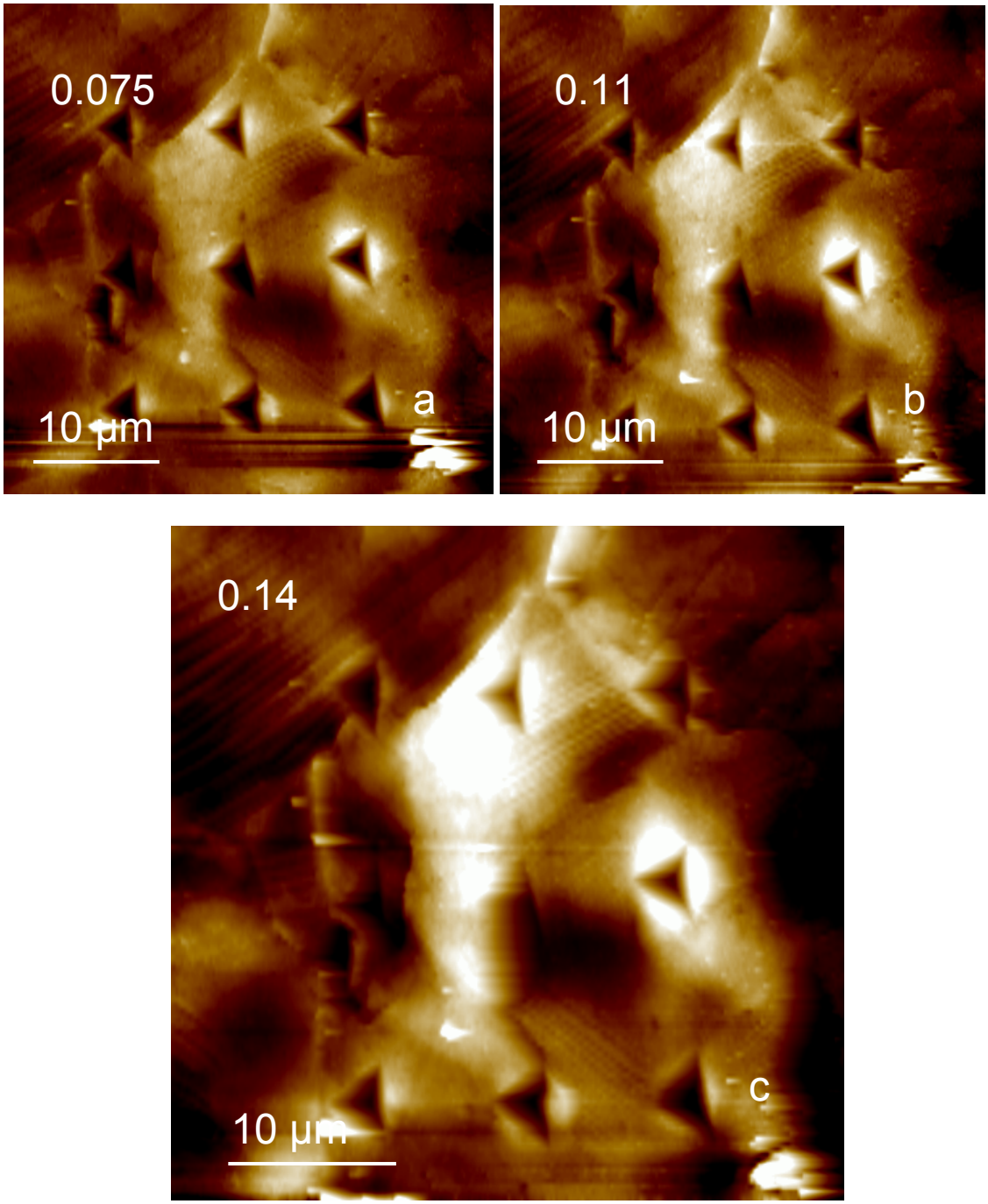

Figure 6.21 : AFM 3D images of the a 3 x 3 array of 600 nm indents at various stages of axial loading at engineering strains of 0.075 – 0.14 (a) 0.075 global strain (b) ~0.11 extensive deformation (c) 0.14 Maximum load

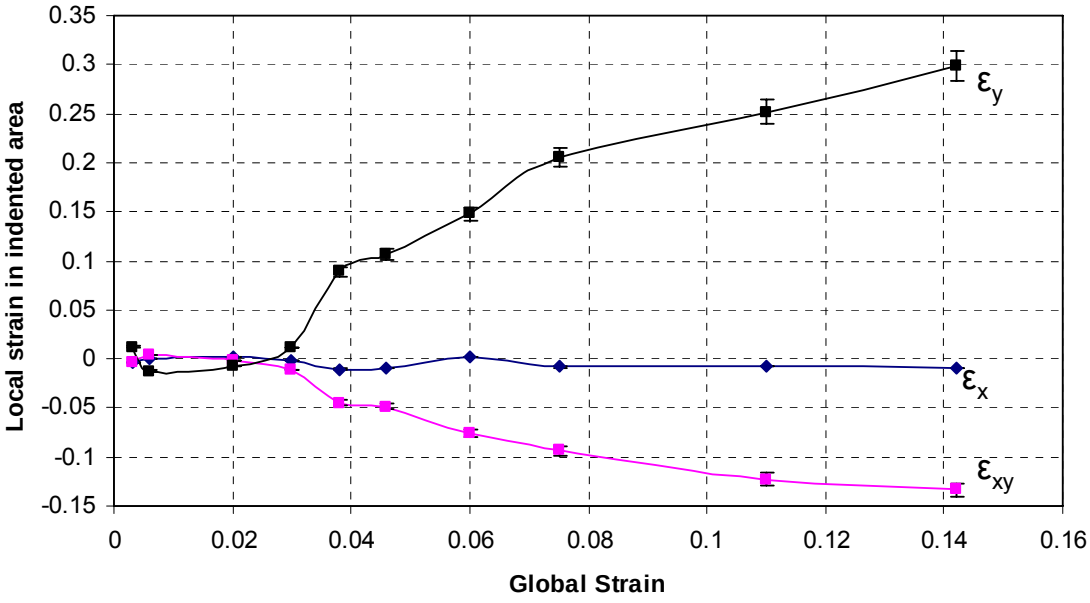

Figure 6.22 : Comparison of local strains vs. global strains in area 1 using the RIM method

The strain in the tensile direction begins to increase with increasing loads. The maximum tensile strain is ~ 0.3 when the global strain is ~0.14. These values are comparable with the values shown in Figure 6.15, namely when the local strain was ~0.3. Surface examination in both these cases show significant deformation. Transverse strains also begin to increase when the global strain is ~0.03. The maximum transverse strain is ~-0.15 when the global strain is ~0.14. This is also comparable with the strains shown in Figure 6.15. The main difference in the strains in the analysis of these two areas are seen in the values of shear strain. The shear strains in area1 do not show significant variation (~-0.002) compared to Figure 6.15 where maximum shear strains are ~-0.04. The other main difference is the global strain at which significant deformation is seen. Deformation is seen at ~0.03 global strain in this area while this happens at ~0.07 in Figure 6.15.

Strains were also analyzed in an area ~ 200 μm (area 2) away from area 1 to examine how different areas deform under the same loading conditions. Figures 6.23 and 6.24 show the deformation of area 2 with increasing tensile load. Some deformation is seen in the image only when the global strain is ~0.06, during which some slip bands can be seen to form [Figure 6.24 (a)]. The rest of the images show darkening in same areas indicating the surface is uneven. The average strains in these areas were estimated using the RIM method. Figure 6.25 shows the variation of tensile, transverse, and shear strains with respect to global strains. Tensile strains increase almost linearly soon after the loads are increased. Maximum tensile strain is ~ 0.15 when the global strain is ~ 0.14. The strains estimated in area 1 at this global strain are almost twice that of the values seen for area 2. Maximum transverse strains are ~ -0.05 at this time compared to a strain ~-0.15 for area 1. The largest difference in these two areas is seen in the values of shear strain. The shear strain values are positive and have a maximum value of ~ +0.03. The deference in the values for strains in areas 1 and 2 can be attributed to the difference in the orientation of the grains in these two areas.

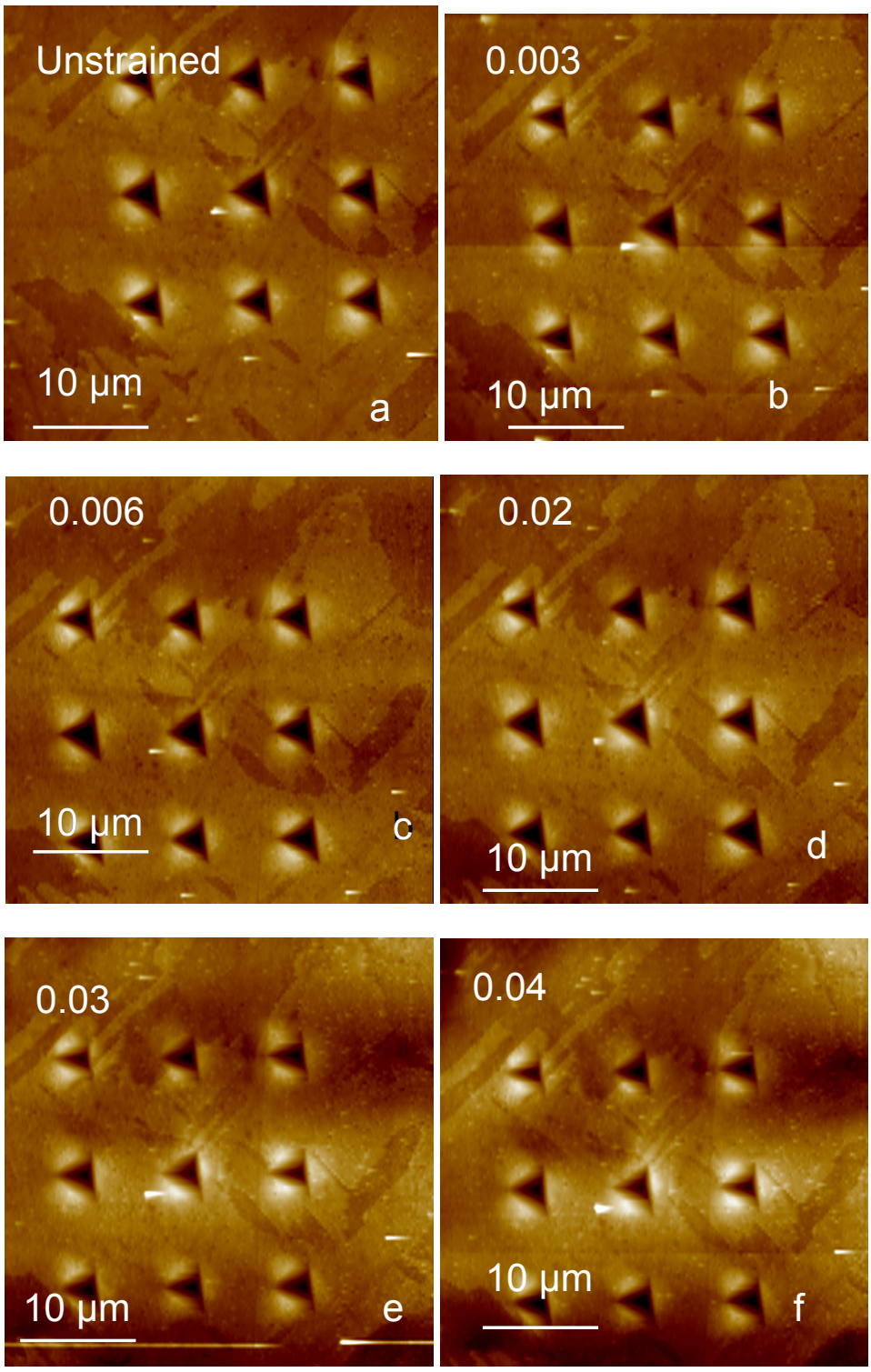

Figure 6.23 : AFM 3D images of the a 3 x 3 array of 600 nm indents at various stages of axial loading at engineering strains of 0.003 – 0.04 (a) 0 - before loading (b) ~0.003 (c) ~0.006 (d) ~0.02 (e)~0.03 small deformation seen (f) ~0.04

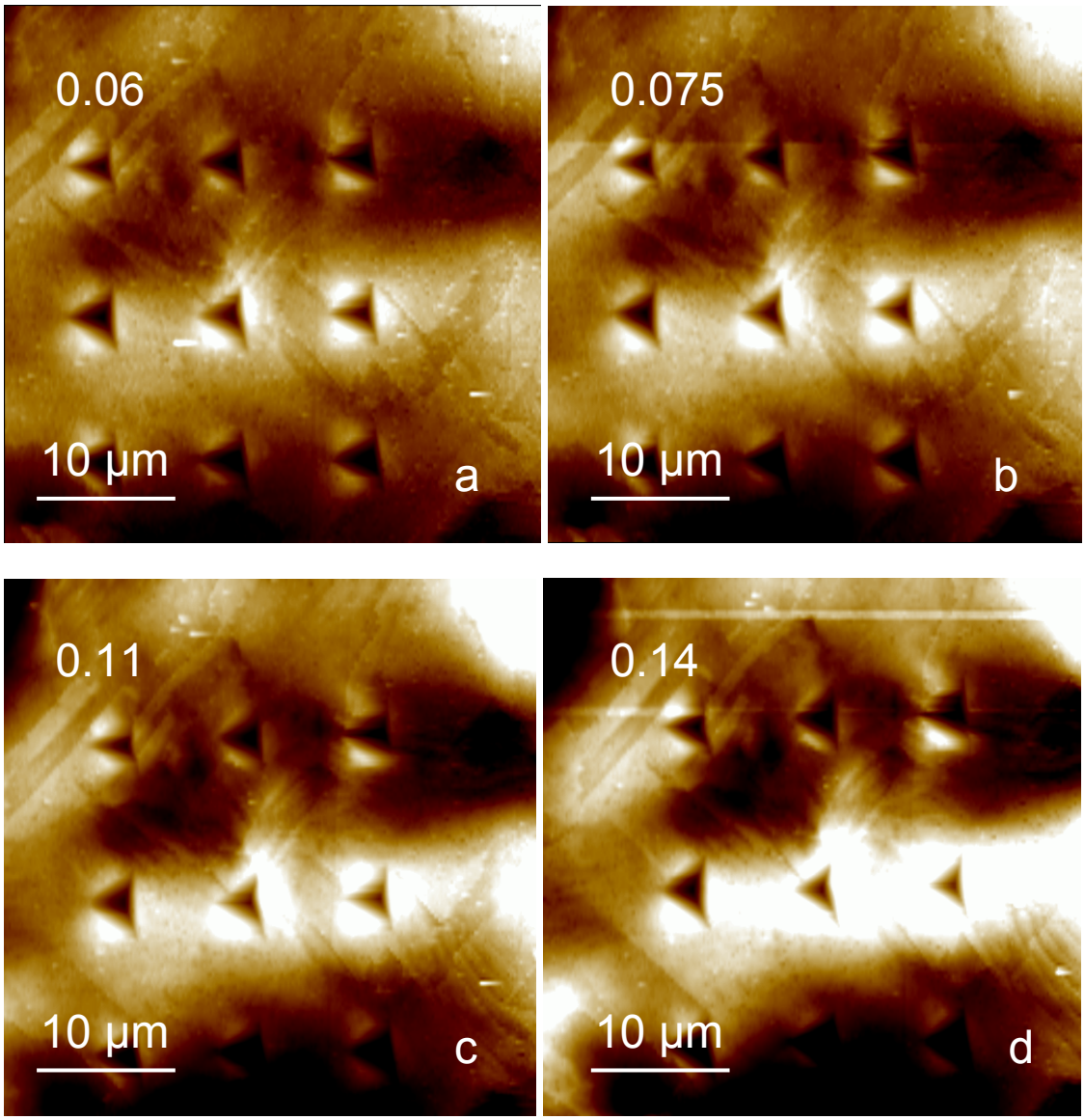

Figure 6.24 : AFM 3D images of the a 3 x 3 array of 600 nm indents at various stages of axial loading at engineering strains of 0.06 – 0.14 (a) 0.06 a few slip bands can be seen (b) 0.075 global strain (c) ~0.11 (d) 0.14 Maximum load

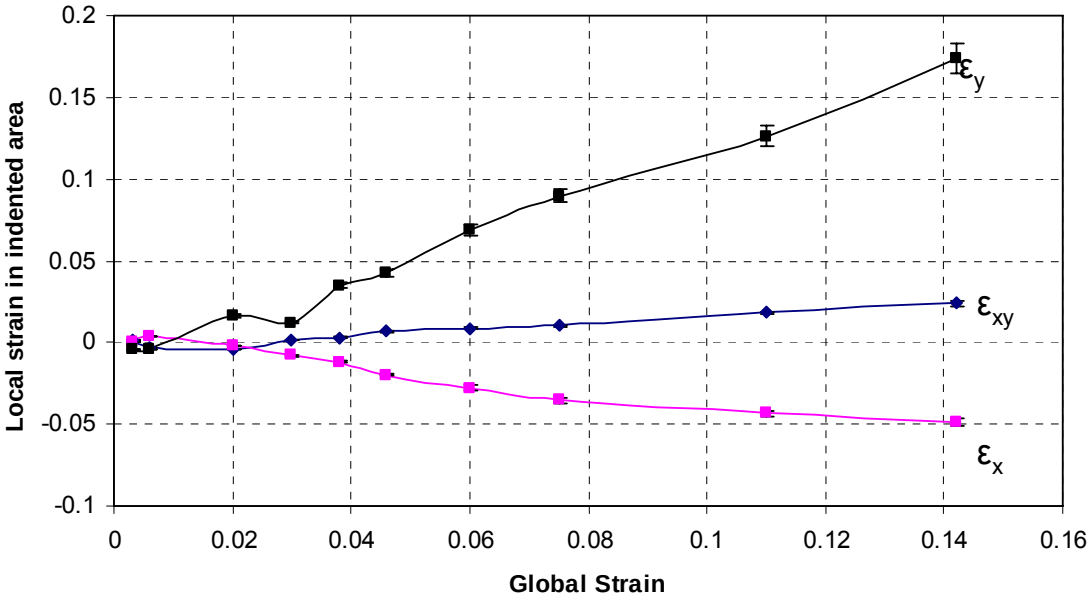

Figure 6.25 : Comparison of local strains vs. global strains in area 2 using the RIM method

6.5 Nanoindentation and imaging using AFM

Nanoindents were made on the surface of an electropolished copper (C11000) sample using an AFM. A 3 x 3 array of 9 indents ~75 nm deep and 500 nm apart were made. A 2 μm x 2 μm area that included the nine indents were imaged at engineering strain intervals between 0.003 and 0.018. This is the range in which elastic deformation changes to plastic deformation resulting in the yielding of the tensile sample.

6.5.1 Results and Discussion

Figure 6.26 (a) is an AFM 3D image of a set of nanoindents performed using an AFM tetrahedral diamond indenter. Tensile loads were applied to the sample after the indents were made and the AFM head disengaged. Details of nanoindentation using the AFM have been discussed earlier in section 4.1.1. At a

global strain of ~0.003, no significant deformation is seen around the indents [Figure 6.26 (b)] since the sample is still within its elastic limit.

Figures 6.26 (c) and (d) are images at global strains of ~0.004 and 0.005, respectively showing no visible deformation. A small amount of deformation can be seen at ~0.006 average strain in Figure 6.26 (e). Formation of a slip band at an engineering strain of ~0.008 can be seen in Figure 6.26 (f). Figure 6.27 (a) shows a slip band and a prominent step can now be seen as one of the indents has started to move along the slipped region. This indent is now lower than the rest of the indents. Engineering strain at this stage is ~0.012. Figure 6.27 (b) is an AFM 3D image when the average strain is ~0.014 It shows that two of the indents have moved with the slip band and they are lower than the rest of the indents. At ~0.017 global strain, the indent can be seen to have started to drift away from the rest of the indents [Figure 6.27 (c)]. The white areas in the image are due to missing data, but the slip plane can be easily seen. Due to surface roughening, it became difficult to keep track of the indents at higher strains. These images nicely show the formation of a slip line with increasing strains.

Local strains in the 2 μm x 2 μm area were estimated using the technique shown in Figure 6.1. The strains that were determined from the images are given in Table 6-3 and plotted in Figure 6.28. It can be seen that there are some variations in the tensile, transverse, and shear strains until ~0.008 engineering strain.

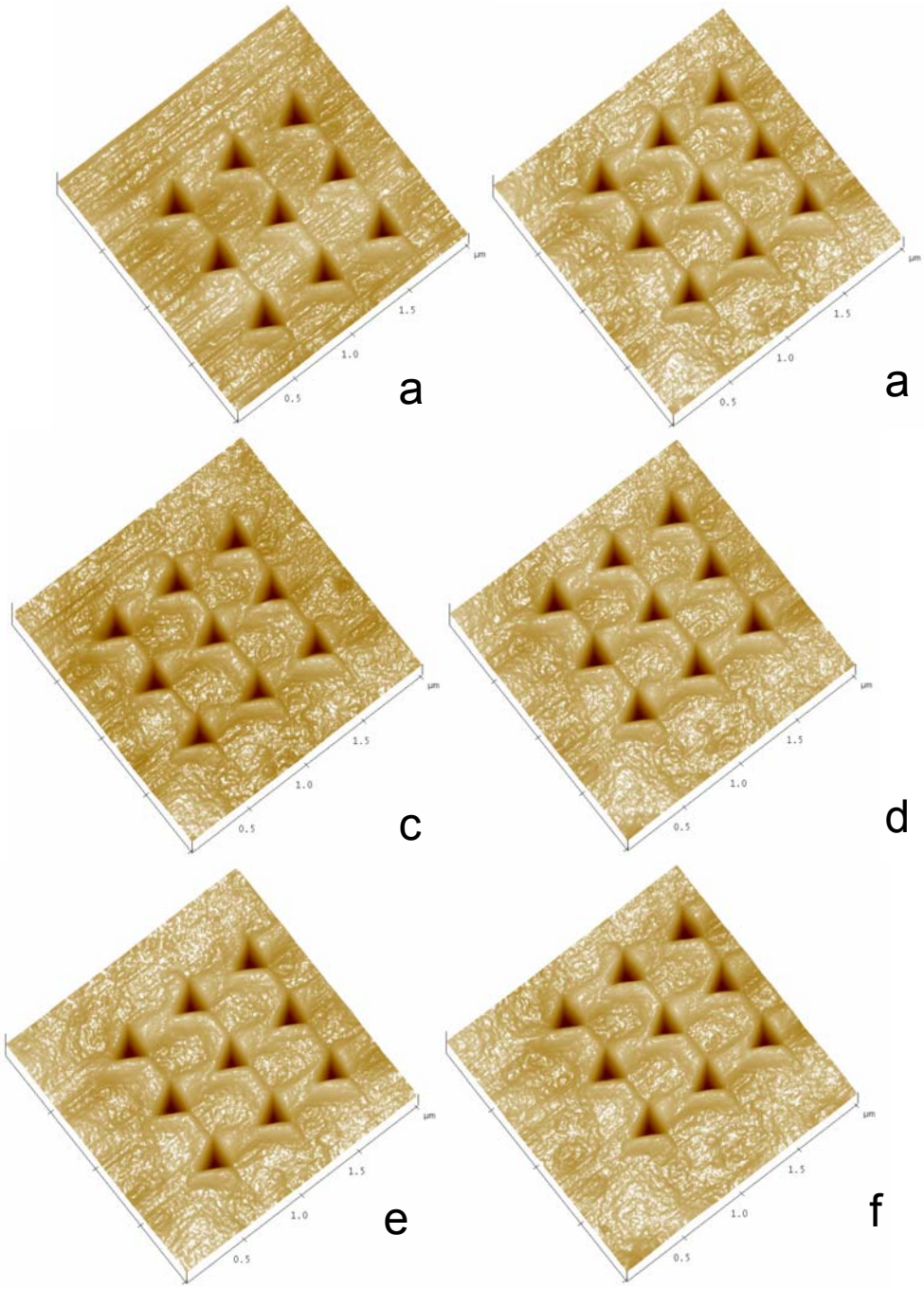

Figure 6.26 : AFM 3D images of the a 3 x 3 array of 75 nm indents at various stages of axial loading at engineering strains of 0 – 0.008(a) 0 - before loading (b) ~ 0.003 (c) ~0.004(d) ~0.005(e) ~0.006 Small deformation seen (f)~0.008 – formation slip can be seen

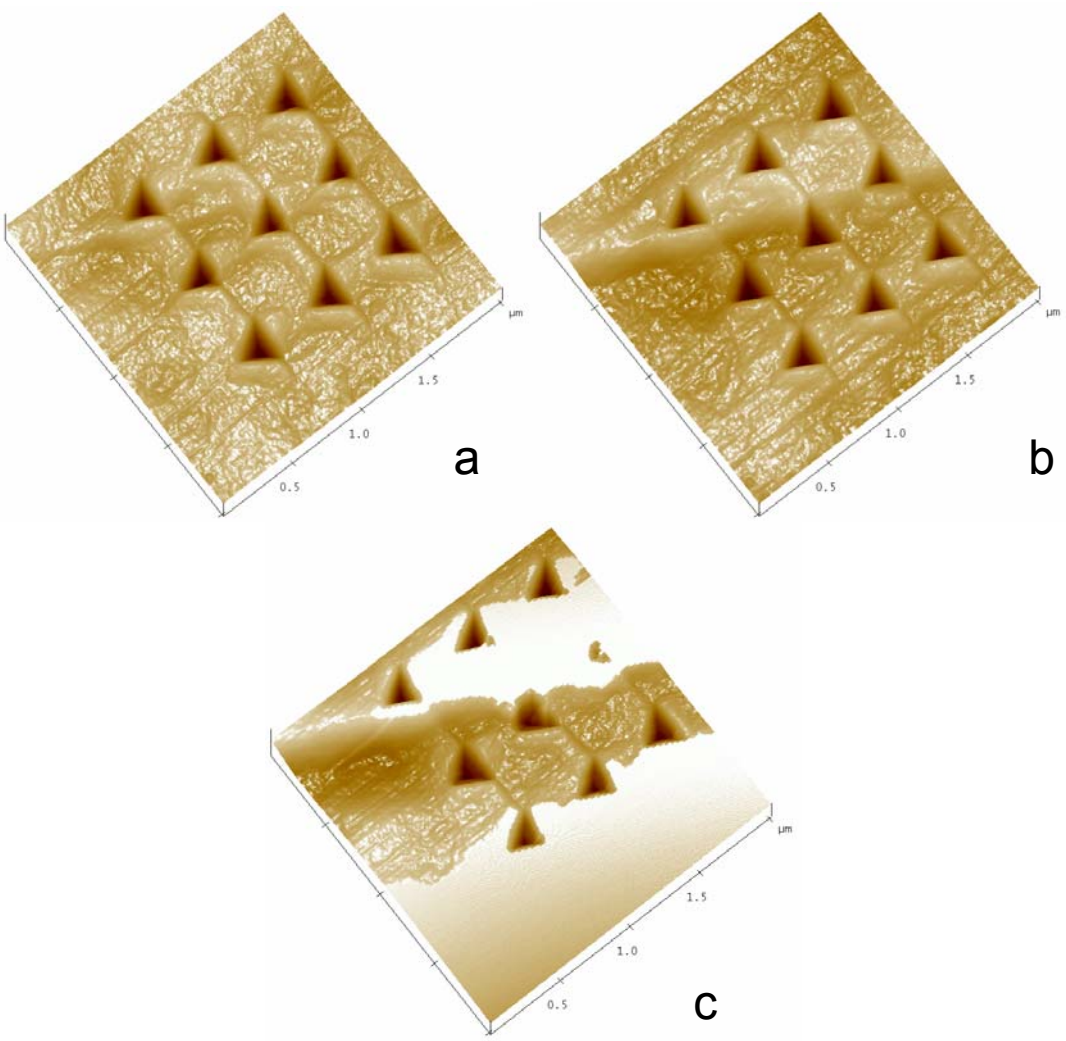

Figure 6.27 : AFM 3D images of the a 3 x 3 array of 75 nm indents at various stages of axial loading at engineering strains of 0.012 – 0.017(a) ~0.012 slip line is become more prominent (b) ~0.014 – two indents moved along with slipped region (c) ~0.017 slipped region is seen clearly, white area is due to tip reach its limit in scanning

There is a significant increase in the tensile strain at ~0.09 and this coincides with the formation of the slip band. This also shows that strains in very small areas of a polycrystalline material can be quiet high compared to the global strain estimated for the material. The strain remains almost steady, increasing to ~0.12, at an average engineering strain of ~0.017. The transverse strain did not vary very much in the initial stages. With the formation of the slip line, the strain in the X-direction decreased to ~ 0.03. This is mainly due to the formation of a step which resulted in the heights between the indents changing and thus the reduction of lateral distance. The shear strain was estimated to be ~ 0.012.

Table 6-3 Results of strain estimation using AFM nanoindents

Average Linear Strain ε	ε_a	ε_b	ε_c	ε_x	ε_y	ε_{xy}
0.003	-0.00357	0	0.007143	0	0.00383	-0.00529
0.004	-0.01214	0	-0.01714	0	-0.00317	0.001762
0.005	0.003571	0	0	0	0.003887	0.001885
0.006	0.003571	0	-0.01429	0	-0.01155	0.008693
0.008	-0.01429	-0.0294	-0.02857	-0.0294	-0.01204	0.007582
0.012	0.024286	-0.0294	0.035714	-0.0294	0.099397	-0.0027
0.014	0.014286	-0.0294	0.042857	-0.0294	0.096231	-0.01138
0.017	0.025	-0.0294	0.052143	-0.0294	0.117925	-0.01015

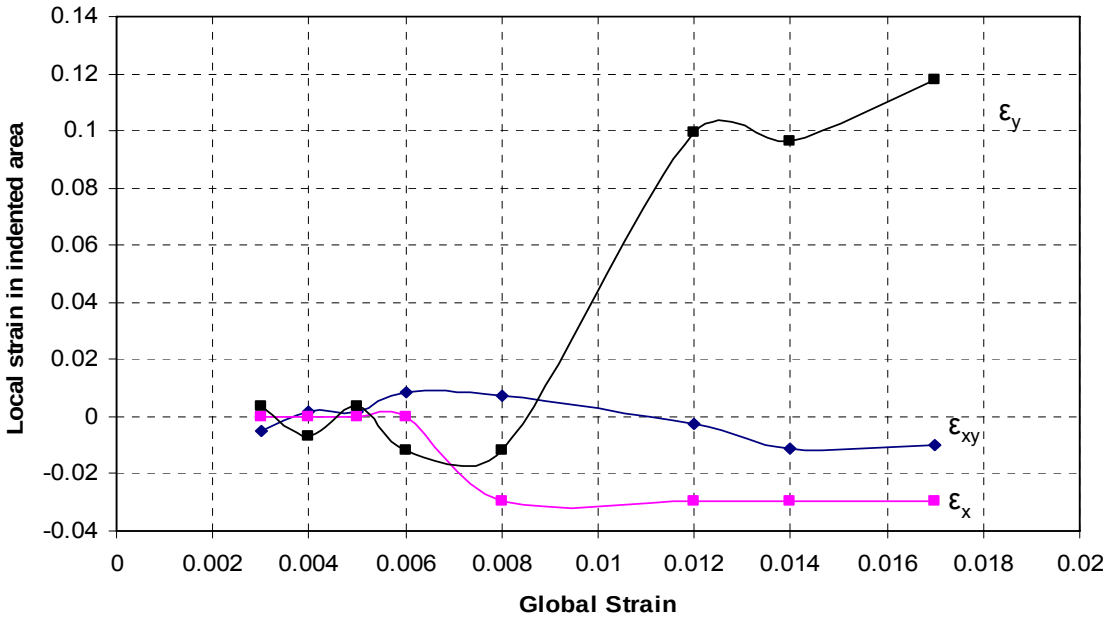

Figure 6.28 : Comparison of local strains with global strains

Surface stresses acting on a plane can be resolved into three mutually orthogonal components. One component is normal to the surface and represents the direct stress. The other two components are tangential to the surface and represent shear stresses. Direct stresses try to change the volume of the material and are resisted by the materials bulk modulus, which is dependent on the Young's modulus and the poisson ratio of the material under consideration. Shear stresses tend to change the shape of the material without a change in the volume and are resisted by the body's shear modulus.

The stress state at any point P inside a very small cube in the Cartesian coordinate system can be described relative to X-, Y-, and Z- coordinate directions, with three stress components on each of its six sides (one direct and two shear components) as shown in Figure 6.29.

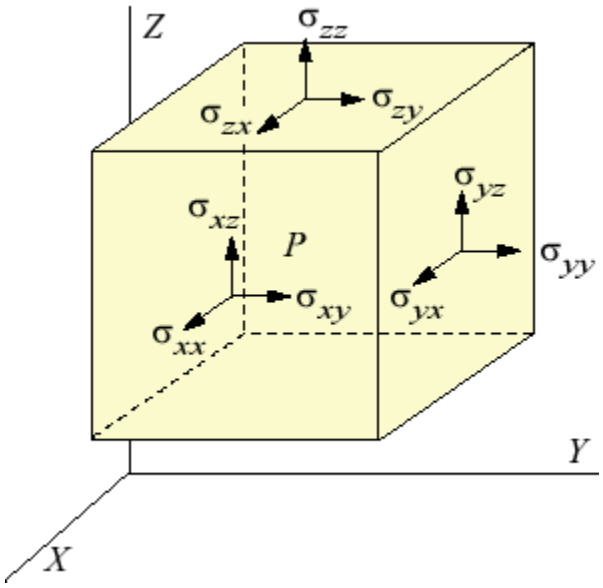

Figure 6.29 : Stresses resulting from forces acting on the faces of a volume element

Assuming that there are no body forces, each point in the body is under static equilibrium and only nine stress components from three planes are needed to describe the stress state at point P.

These nine components can be organized into a matrix form termed the stress tensor:

$$\begin{bmatrix} \sigma_{xx} & \sigma_{xy} & \sigma_{xz} \\ \sigma_{yx} & \sigma_{yy} & \sigma_{yz} \\ \sigma_{zx} & \sigma_{zy} & \sigma_{zz} \end{bmatrix}$$

The shear stresses across the diagonal are identical as a result of static equilibrium (i.e. $\sigma_{yz} = \sigma_{zy}$, $\sigma_{xy} = \sigma_{yx}$, and $\sigma_{zx} = \sigma_{xz}$).

Now, since the depth of indents are very small compared to the thickness of the tensile sample, this is an ideal plane-stress condition. This means that one

of the principal stresses would be much smaller than the other two and can be considered to be zero. Thus, the 3D stress state can be considered in a simplified form.

Assuming that the stress in the Z-direction is zero, the 3D matrix can be now written as

$$\begin{bmatrix} \sigma_x & \tau_{xy} \\ \tau_{yx} & \sigma_y \end{bmatrix}$$

where $\tau_{xy} = \tau_{yx}$ are shear stresses for static equilibrium.

The stresses in the X-, Y- and Z- direction can be calculated using the strains estimated by analyzing the relative movements of the indents

$$\sigma_x = \lambda(\varepsilon_x + \varepsilon_y + \varepsilon_z) + 2\mu\varepsilon_x \quad 6.1$$

$$\sigma_y = \lambda(\varepsilon_x + \varepsilon_y + \varepsilon_z) + 2\mu\varepsilon_y \quad 6.2$$

$$\sigma_z = \lambda(\varepsilon_x + \varepsilon_y + \varepsilon_z) + 2\mu\varepsilon_z \quad 6.3$$

Since σ_z is zero ,ε_z is

$$\varepsilon_z = \frac{-\lambda(\varepsilon_x + \varepsilon_y)}{(\lambda + 2\mu)} \quad 6.4$$

$$\tau_{xy} = 2\mu\varepsilon_{xy} \quad 6.5$$

Now, given the stress components σ_x, σ_y, and σ_{xy}, we can calculate the principal stresses σ_1, σ_2, and the principal angle θ_p (Figure 6.30) The principal stress can thus be obtained using the relationships.

$$\tan 2\theta_p = \frac{2\tau_{xy}}{\sigma_x - \sigma_y} \quad 6.6$$

$$\sigma_{1,2} = \frac{\sigma_x + \sigma_y}{2} \pm \sqrt{\left(\frac{\sigma_x - \sigma_y}{2}\right)^2 + \tau_{xy}^{\ 2}} \qquad 6.7$$

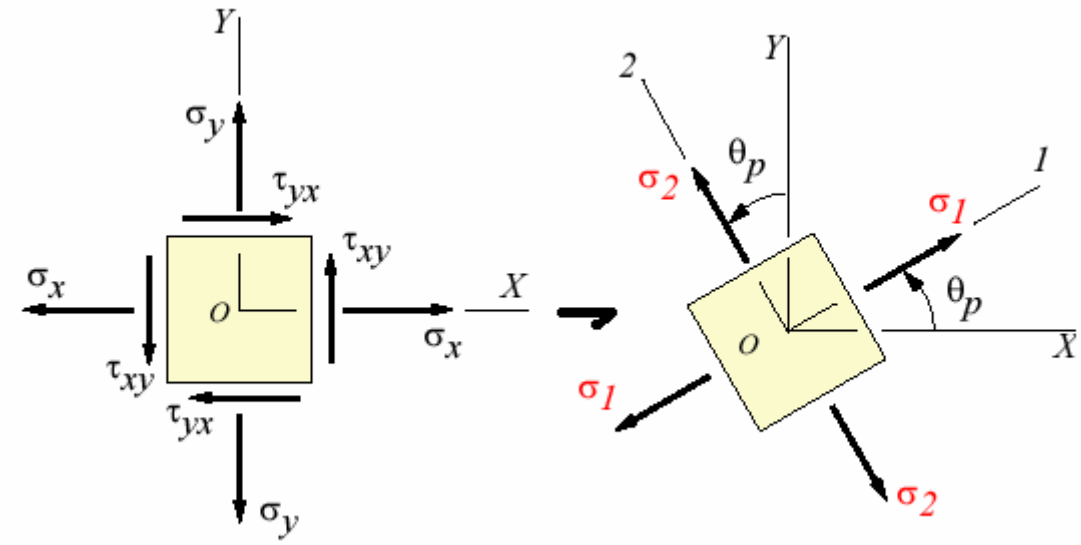

Figure 6.30 : Transformation of the stress components σ_x, σ_y, and σ_{xy}, to estimate the principal stresses σ_1, σ_2, and the principal angle θ_p

The maximum shear stress τ_{max} and its angle θ_s are calculated using the equations

$$\tau_{\max} = \sqrt{\left(\frac{\sigma_x - \sigma_y}{2}\right)^2 + \tau_{xy}^{\ 2}} = \frac{\sigma_1 - \sigma_2}{2} \qquad 6.8$$

$$\tan 2\theta_s = \frac{\sigma_x - \sigma_y}{2\tau_{xy}} \qquad 6.9$$
$$\Rightarrow \theta_s = \theta_p \pm 45°$$

6.5.2 Digital Image correlation analysis

The AFM 3D images were also used to estimate strains using the DIC software. The indents were used as markers and selected as nodes for estimating the distribution of strains around the indents. An area with a radius of 30 pixels is selected around each indent for analysis. The results of this analysis for the images acquired when the global strains were ~0.008 and ~0.014 are shown in Figure 6.31. It can be seen that the longitudinal or transverse strains around the indents increase with increasing strains. The compressive strains are ~0.02 to ~0.6, which are consistent with the strains estimated using the method in which the relative movements of the indents were used to estimate strains [Figures 6.31 (c) and (d)]. Figure 6.31 (e) shows the distribution of strains in the tensile direction at ~0.008 global strain. At this strain, the grain is undergoing transition from elastic to plastic deformation and some compressive strains can be seen. The maximum tensile strain is ~0.07 in the center of the image which corresponds to the stretching of the indent in the middle (Figure 6.31 (f)].

Figures 6.31 (g) and (h) show the distribution of shear strains at 0.008 and 0.014 global strains, respectively. The maximum shear strain changes from 0.02 from the former to ~- 0.03 for the latter. This corresponds to the formation of shear bands.

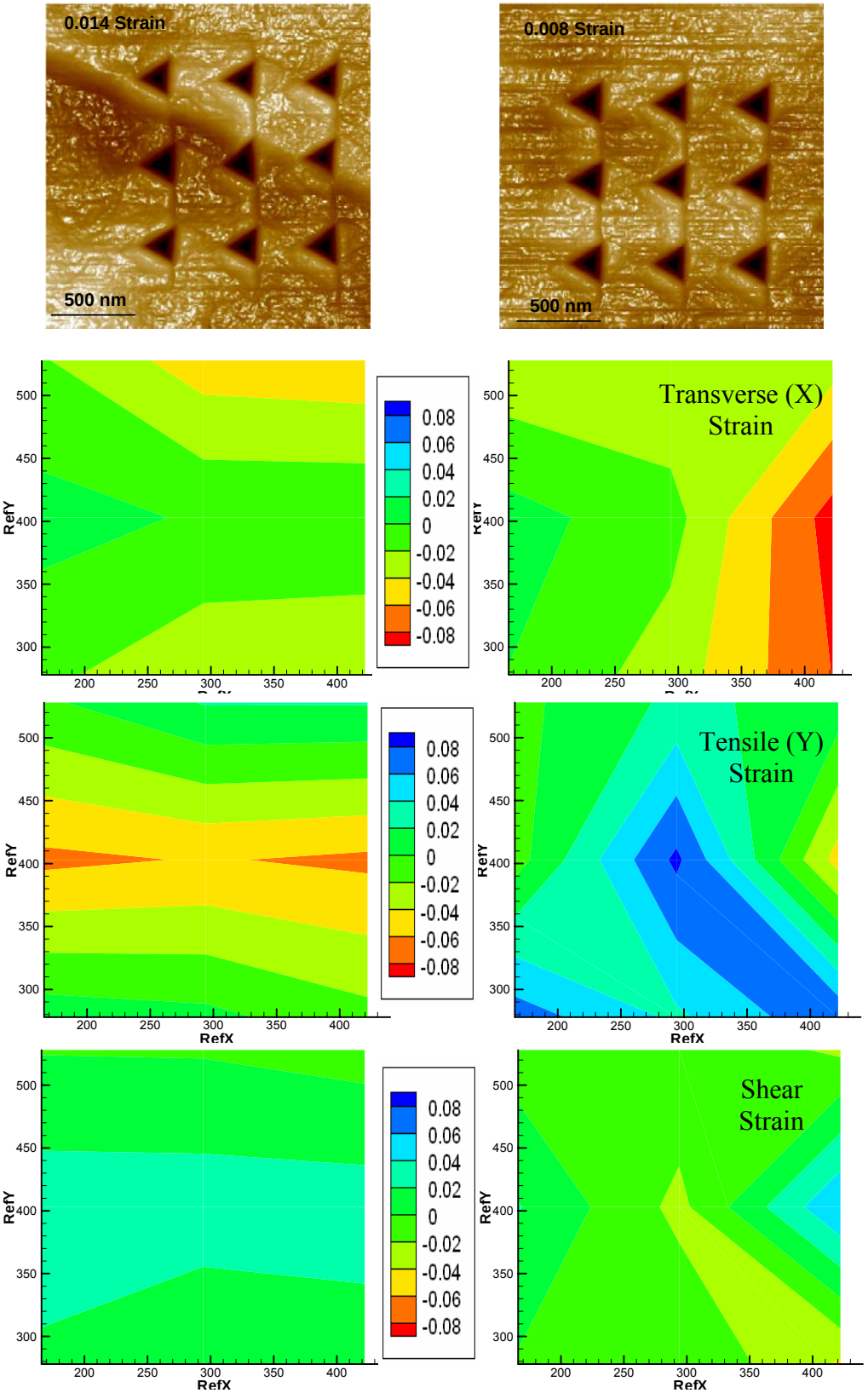

Figure 6.31 : Distribution of strains in X-, Y- and shear directions at global strains (a) 0.008 (b) 0.014

The formation of slip is associated with the formation of steps that assists in relieving the stresses locally. With increasing global strain and formation of the slip band, it can be seen that the area around which the slip band is forming begins to form a depression. This can be seen more clearly in Figure 6.32 which shows the sections perpendicular to the slip band formed at different global strains. The line in the AFM 3D image shows the area in which the sections were made. The cross section images show that at a global strain of ~0.008, the depression is about 7 nm deep (section marked 2) relative to the section before the loading process (section marked 1). At a global strain of ~0.014, the depth of the area is ~14 nm showing an increase in depth with increasing load (section marked 3). It can also be seen that projection on the surface at the point marked 1 has moved with increasing loads to points 2 and 3 at global strains of 0.008 and 0.014, respectively showing that the formation of slip bands is accompanied by the formation of a step as well as a new surface.

The slip bands have formed at an angle of ~ -65º or ~115º in the clockwise direction with respect to the tensile axis. Slip occurs easily when the shear planes are oriented at ±45º to the tensile axis. Higher loads are needed to activate shear planes in grains that are not at this orientation. These loads increase as the magnitude of this angle increases. It can thus be inferred that slip may have started in some other grain with an orientation of ±45º to the tensile axis before it initiated in the grain that was imaged. Slip started at a global strain of ~0.009 under a load of ~215 kg for the grain that was imaged. This grain was oriented at – 65º to the tensile axis. Using this information, the load at which a

grain oriented at ± 45º begins to form slip bands can be estimated. A grain with this orientation mayhave formed slip bands when the tensile load was ~150 Kg and a global strain of ~0.006.

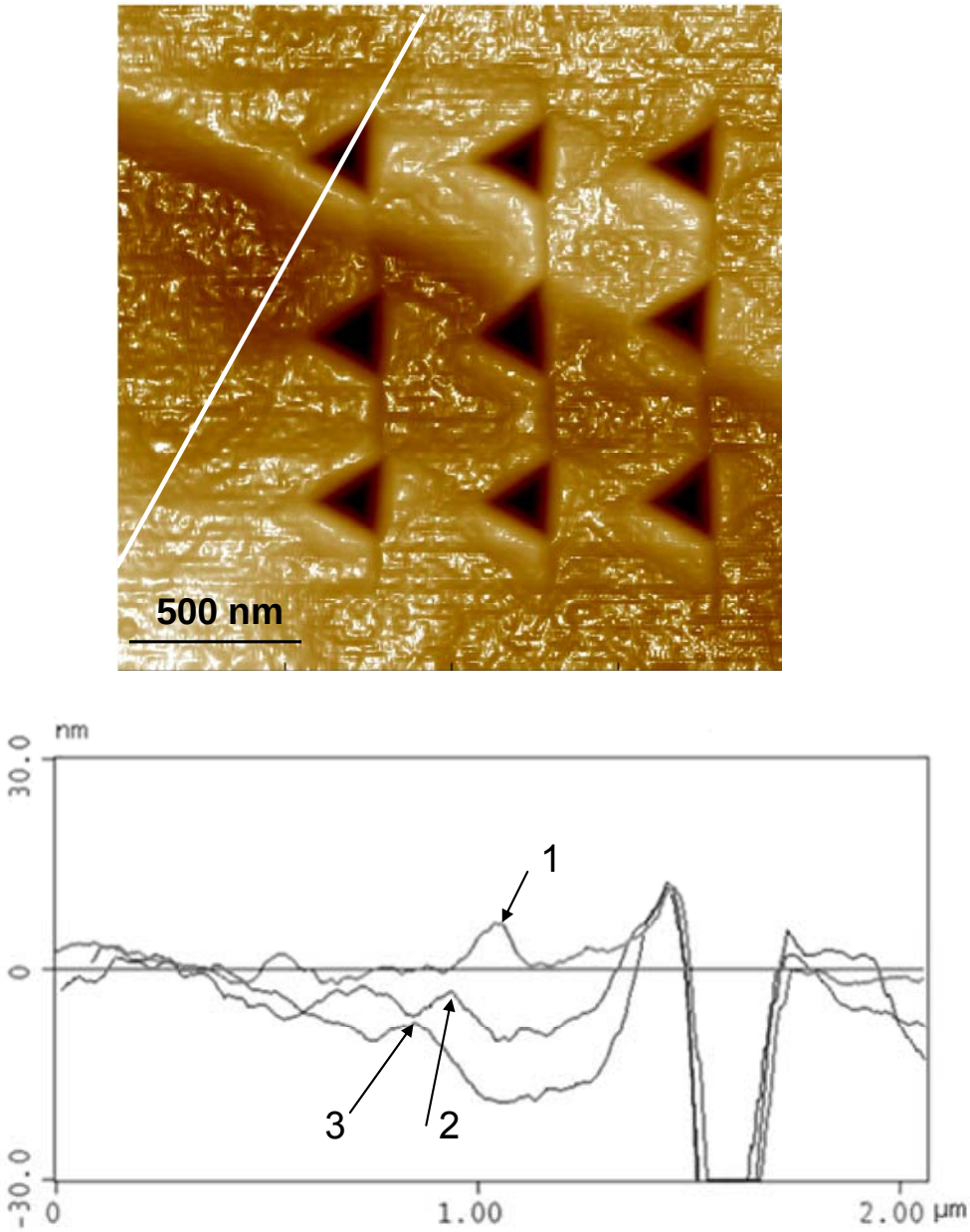

Figure 6.32 : Section perpendicular to the slip band formed showing the change in depth of the step formed due to the development of the slip band (1) unstrained (2) 0.008 global strain (3) 0.014 global strain

CHAPTER 7

ESTIMATION OF STRAINS BY ANALYZING THE CHANGE IN SHAPE OF RESIDUAL NANOINDENTS

7.1 Introduction

Nanoindentation tests were conducted on tensile samples of copper (C11000) loaded in tension. At various stages of tensile testing, the loading was stopped and a nanoindentation was made. This was done to investigate what effects the local deformation of the tensile sample may have on the shape of the residual indent. It was found that shape of the residual indent changed with change in the tensile loads.

7.2 Results and Discussion

Figures 7.1 and 7.2 show AFM 3D images of nanoindentations made on the surface of a copper sample at various tensile loads. A set of four indents, 500 nm apart were made at an indentation load of ~ 23 μN resulting in residual indents ~ 40 nm deep. Nanoindentations were made after stopping the drive motor of the tensile stage and engaging the AFM head. Both the indentation and the imaging of the indents, thereafter, were made using a tetrahedral diamond indenter. Details of the indenter are given in Section 4.1. The size of the area that was scanned was 700 nm x 700 nm that included four indents.

Figures 7.1 (a) through (f) are AFM 3D images of the indents at engineering strains ranging from ~0.003 to 0.06. Subtle changes in the shape of the indents can be seen at these strains. A more careful examination of Figure 7.1 (b) indicates that the indents look bigger than the indents in Figure 7.1 (a) which were acquired when there is no tensile load on the sample. This increase in the size of the indents is probably due to stretching of the grain by its neighbors. Indents in Figures 7.1 (c) and (d) show some shape change. These indents were made when the global strains were ~0.02 and 0.035, respectively. Figures 7.1 (e) and (f) are images of the indents made at ~0.045 and 0.065 engineering strains, respectively.

On further increase in load, the indents appear to have been stretched to one side [Figure 7.2 (a)]. This is more prominent in Figure 7.2 (b) which is an image acquired when the global strain is ~0.081. With increasing tensile load the indents were stretched to one side. The direction in which the indent is stretched is dependant on the direction of shear, which is ~ 45º. Since the area in which the indents are made is >1 μm^2, it would be difficult see any slip bands. The slip bands are generally seen to be 2 to 3 μm apart and the indents are made between two slip bands. Relative movement of the slip bands result in the rotation of the residual indents. Figures 7.2 (c) and (d) show indentations made when the engineering strains were ~0.09 and 0.01, respectively. Figure 7.2 (e) shows the indentations made at maximum load at an engineering strain of ~0.12. Necking commenced at ~0.14 strain. Figure 7.2 (f) shows that the shape of the indents has changed compared to the ones when no tensile load was applied.

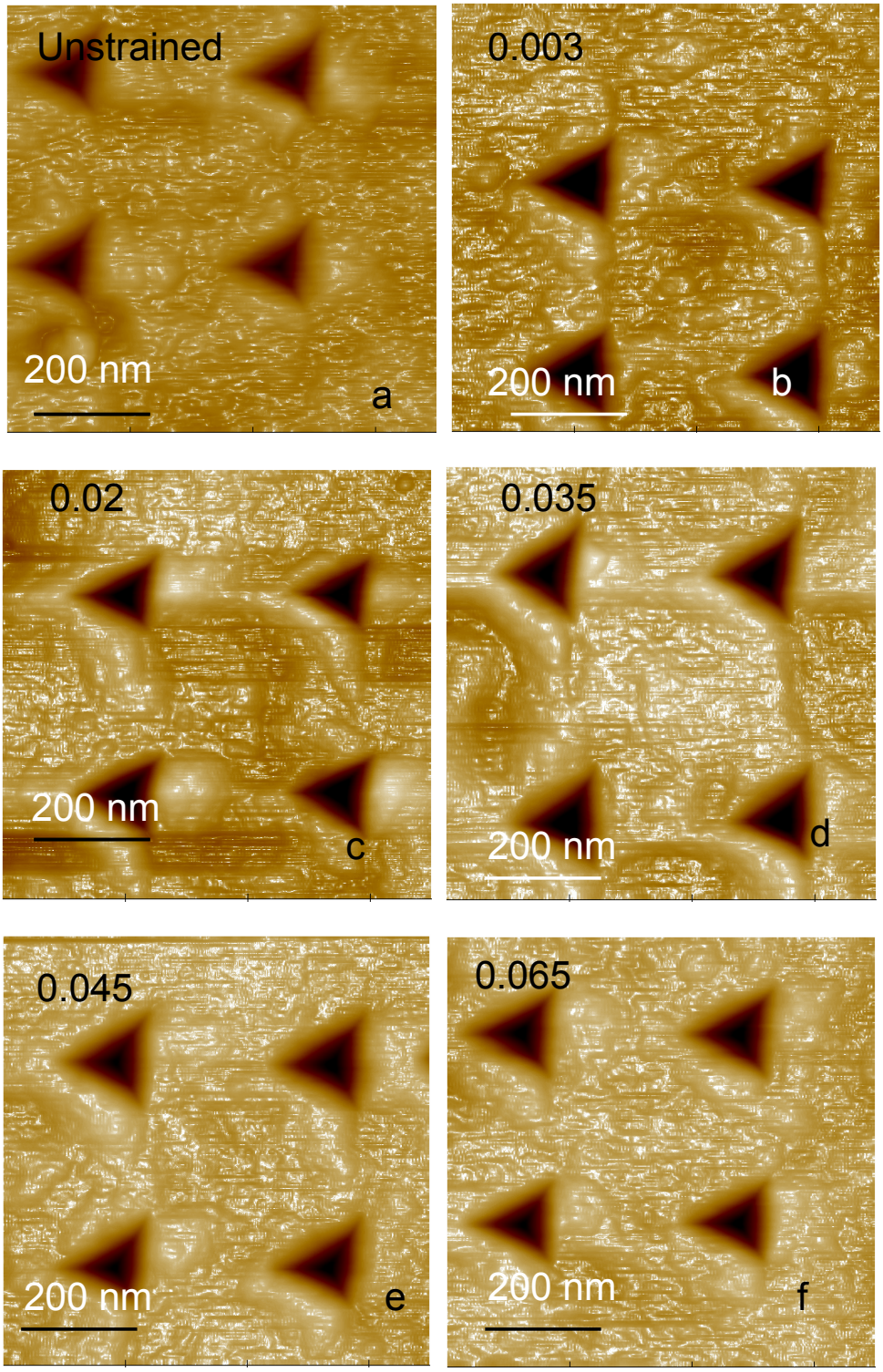

Figure 7.1 : AFM 3D images of indents under ~23 μN at each stage when axial loading was stopped at engineering strains of 0.003 – 0.065 (a) Unstrained (b) ~0.003(c) ~0.02 (d) ~0.035 (e) 0.045 (f) 0.065

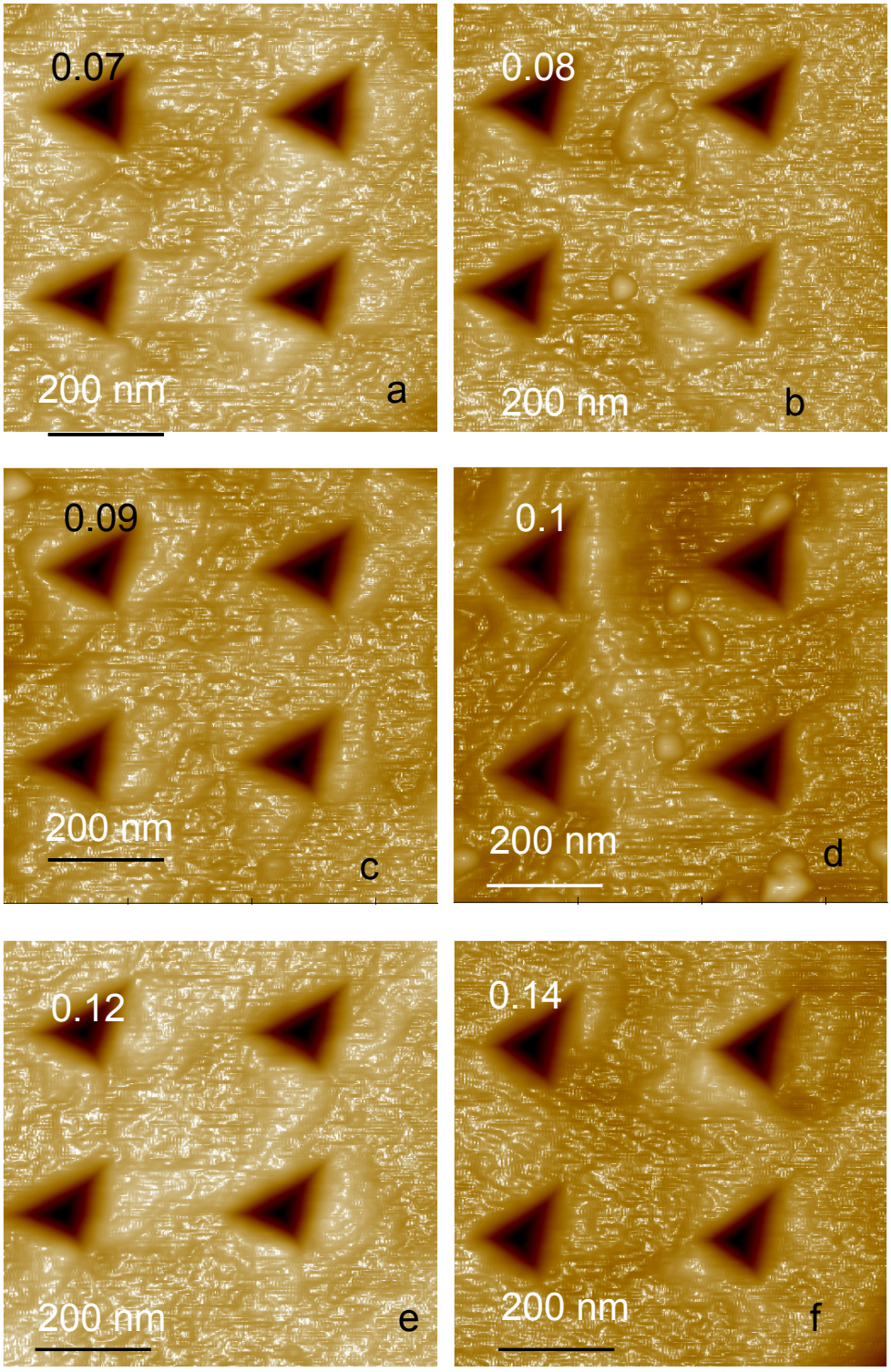

Figure 7.2 : AFM 3D images of indents under ~23 μN at each stage when axial loading was stopped at engineering strains 0.07 – 0.14(a) ~0.07 (b) ~0.08(c) ~0.09 (d) ~0.1 (e) ~0.12 (f) ~0.14

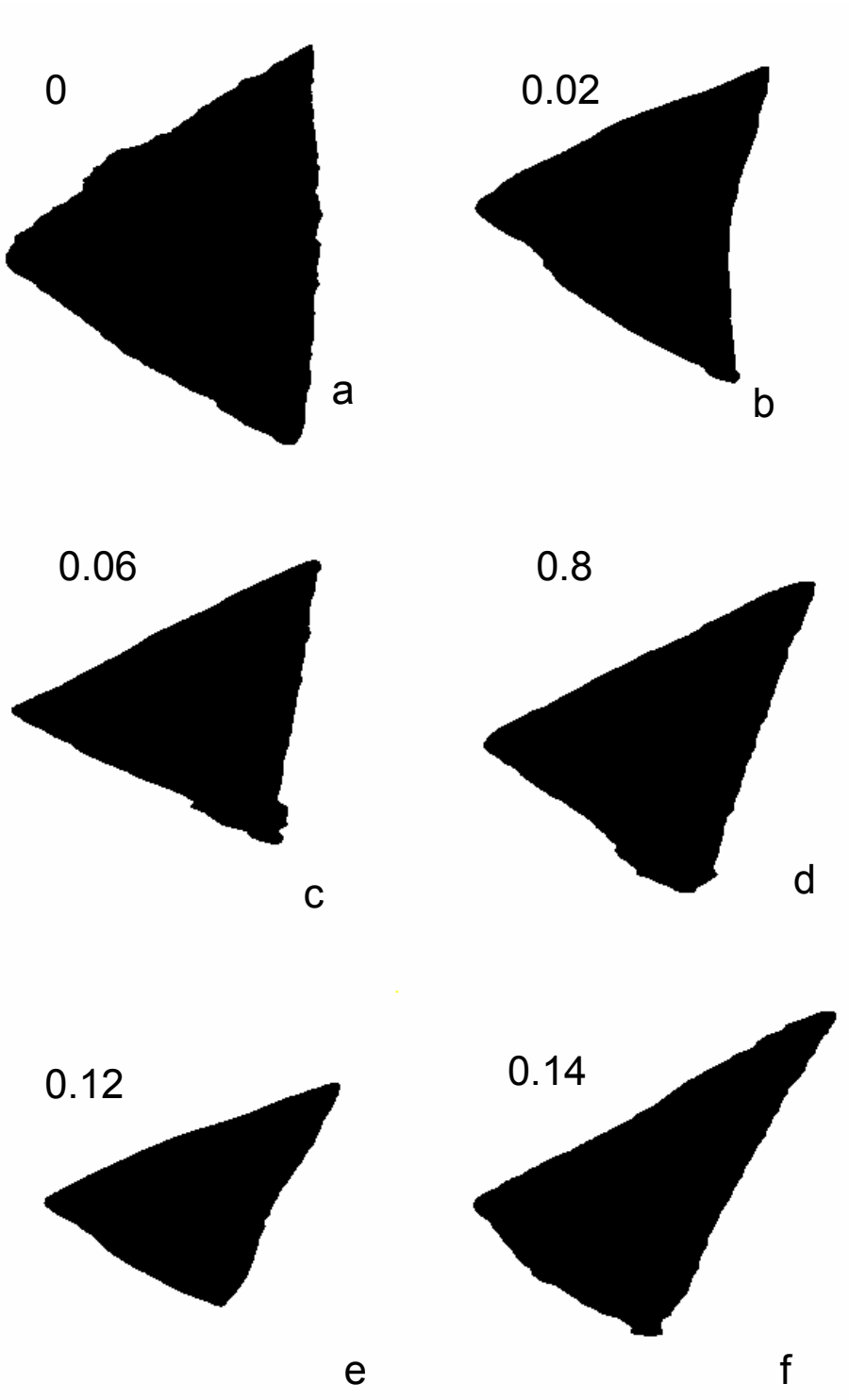

Figure 7.3 : Change in shape of indents as the tensile load is increased (a) No strain (b) ~ 0.02 strain – elastic region (c) ~0.06 plastic deformation has started (d) ~0.08 (e) 0.12- maximum load (f) 0.14 - necking begins

Figure 7.3 shows progression of the change in shape of the indents with increase in tensile load. In to order to determine the strains in the area being imaged, strains in the indents were estimated. This was done by taking a projected image of the indents and estimating the change in its dimensions. The projected image of the indent is a triangle. Since a triangle can be drawn with any three dimensions, it was decided to measure two sides of the indent and the angle between them. Using geometry, all other dimension can be estimated. The length of each of its median was thus found. This analysis was performed for all the indents.

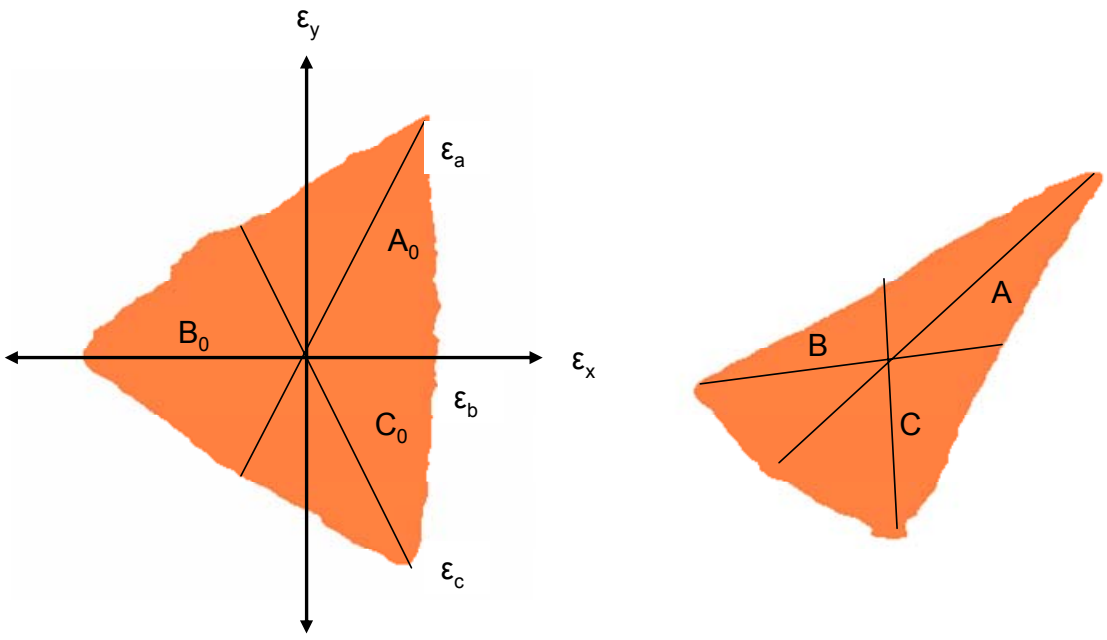

Figure 7.4 : Strain estimation by analyzing the change in the shape of indent

Figure 7.4 is a schematic showing the method used to estimate strains based on deformation of residual indents. Let A_0, B_0, and C_0 be the lengths of the medians of the triangle, i.e. the projected area of the indent when no tensile load

is acting on the sample. Let A, B, and C be the lengths of the medians of the triangle formed by the projected area of the indent that has been made on the tensile loaded specimen.

Let ε_a ,ε_b, and ε_c be the strains measured in the respective directions as shown in Figure 7.4.

The strains are estimated as

$$\varepsilon_a = \frac{A - A_0}{A_0} \qquad 7.1$$

$$\varepsilon_b = \frac{B - B_0}{B_0} \qquad 7.2$$

$$\varepsilon_c = \frac{C - C_0}{C_0} \qquad 7.3$$

Let α, β, and γ be the angles that these strains make with the X-axis, respectively. Let ε_x and ε_y be the strains in the transverse and tensile directions. Let ε_{xy} be the shear strain.

The strains in the transverse and tensile directions can be estimated from the following relationships.

$$\varepsilon_a = \varepsilon_x(\cos^2\alpha) + \varepsilon y(\sin^2\alpha) + 2(\varepsilon_{xy})(\sin\alpha)(\cos\alpha) \qquad 7.4$$

$$\varepsilon_b = \varepsilon_x(\cos^2\beta) + \varepsilon y(\sin^2\beta) + 2(\varepsilon_{xy})(\sin\beta)(\cos\beta) \qquad 7.5$$

$$\varepsilon_c = \varepsilon_x(\cos^2\gamma) + \varepsilon y(\sin^2\gamma) + 2(\varepsilon_{xy})(\sin\gamma)(\cos\gamma) \qquad 7.6$$

Results obtained from this analysis are presented in Table 7-2 and Figure 7.10.The stresses in the elastic region of the deformation in the X-, Y- and Z-

directions can be calculated using the strains estimated by analyzing the relative displacements of the indents.

$$\sigma_x = \lambda(\varepsilon_x + \varepsilon_y + \varepsilon_z) + 2\mu\varepsilon_x \quad 7.7$$

$$\sigma_y = \lambda(\varepsilon_x + \varepsilon_y + \varepsilon_z) + 2\mu\varepsilon_y \quad 7.8$$

$$\sigma_z = \lambda(\varepsilon_x + \varepsilon_y + \varepsilon_z) + 2\mu\varepsilon_z \quad 7.9$$

where λ and μ are the Lame's constants

Since σ_z is zero, ε_z is given by

$$\varepsilon_z = \frac{-\lambda(\varepsilon_x + \varepsilon_y)}{(\lambda + 2\mu)} \quad 7.10$$

$$\tau_{xy} = 2\mu\varepsilon_{xy} \quad 7.11$$

The stress components σ_x, σ_y, and σ_{xy}, it is possible to calculate the principal stresses σ_1, and σ_2, and the principal angle θ_p The principal stress is obtained using the relationships

$$\tan 2\theta_p = \frac{2\tau_{xy}}{\sigma_x - \sigma_y} \quad 7.12$$

$$\sigma_{1,2} = \frac{\sigma_x + \sigma_y}{2} \pm \sqrt{\left(\frac{\sigma_x - \sigma_y}{2}\right)^2 + \tau_{xy}^{\ 2}} \quad 7.13$$

The maximum shear stress τ_{max} and its angle θ_s are calculated using the equations

$$\tau_{\max} = \sqrt{\left(\frac{\sigma_x - \sigma_y}{2}\right)^2 + \tau_{xy}{}^2} = \frac{\sigma_1 - \sigma_2}{2} \qquad 7.15$$

$$\tan 2\theta_s = \frac{\sigma_x - \sigma_y}{2\tau_{xy}}$$
$$\Rightarrow \theta_s = \theta_p \pm 45° \qquad 7.16$$

The elastic modulus of the copper sample was determined from nanoindentation experiments to be ~ 125 GPa and the Poisson's ratio is taken to be 0.33. Using these elastic properties, the stresses in the elastic region of the deformation were estimated to be in the range of 400 – 600 MPa, which are consistent with some of the results for thin films of copper given in the literature[77].

7.3 Validation of strains estimated using the indent shape change (ISC) method

An analysis similar to the one performed in Figures 6.3 through 6.5 for validating the relative indent method (RIM) was also used for the validation of strains estimated using the indent shape change (ISC) method. Several steps were taken to validate the new ISC method for strain with an existing method (DIC). Validation was done by comparing it's measured value to a known value or to a value estimated by a known method. In this investigation, the digital image correlation (DIC) method as well as the indent shape change (ISC) method were used to compare known strains. This was done by performing a virtual "Digital" tensile test during which an image is stretched in one direction and shrunk in the direction normal to it by know values. The images thus modified were then analyzed using the methods that need to be validated.

Figures 7.6 through 7.8 show images that have been digitally stretched in the Y-direction in steps of 2.5 % and shrunk in the X- direction in steps of 2.5 % from the original image shown in Figure 7.5. Details of each of the modified images are given in a tabular form beside each of them. These images were analyzed using the digital image correlation (DIC) software and the indent shape change method to determine strains. The results are shown in Figure 7.9. The strains estimated by the software were in agreement with the known values of deformation. The parameters used in the software are given in Table 7-1. Figure 7.9 (a) shows the variation of the estimated strains with actual strains in the tensile direction as seen in the analysis by RIM method in Figure 6.6. The differences in strains estimated using the DIC software were higher at higher strains. The results obtained using the ISC technique had lesser deviations from actual strains but were slightly higher. The error at the highest strains was ~ 1 %.

Table 7-1 Control parameters used with the DIC software for "digital" tensile test

Number of nodes	3 x 3 = 9
Sequence of next node	Left - right
Spacing (pixels)	128 x 128
Subset radius (pixels)	30 x 30
Smoothing radius (pixels)	1
Maximum number of iterations	50
Tolerance	0.0001

Strains that were estimated as a result of shrinkage in the transverse direction are shown in Figure 7.9 (b). The strains estimated by both DIC and ISC were comparable with the actual compressive strains. The error for the DIC software was about 3%. The strains estimated using both the ISC method and DIC techniques showed good agreement with actual values of strain. The indent

shape change method can therefore be used for estimating strains in small areas by analyzing the change in shape of indents.

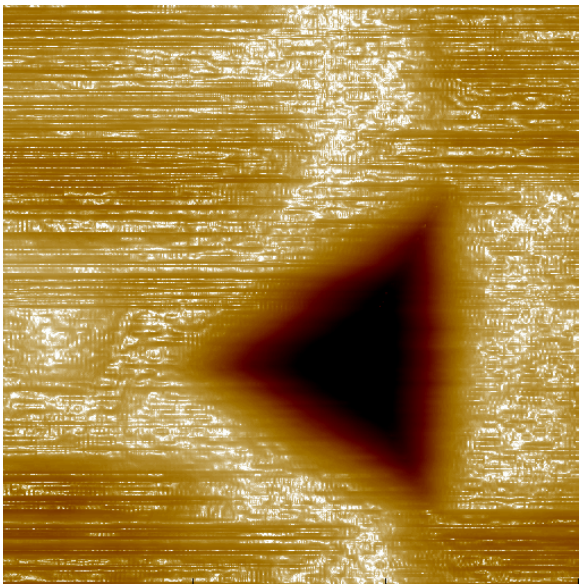

	Transverse	Tensile
Image size	509	510
Change in size	0	0
Est. Strain using DIC	0	0
Est. Strain using indent	0	0

Figure 7.5 : Undeformed image of the indent for validation of ISC method

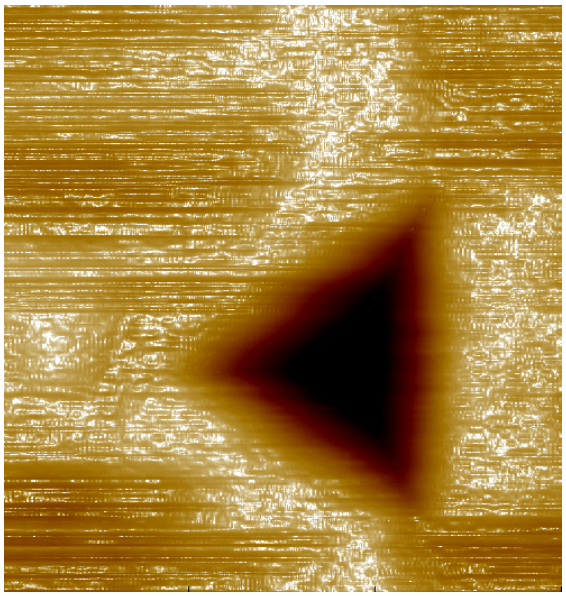

a

	Transverse	Tensile
Image size	497	510
Change in size	-0.025	+0.025
Est. Strain using DIC	-0.023	0.027
Est. Strain using indent	-0.0247	0.026

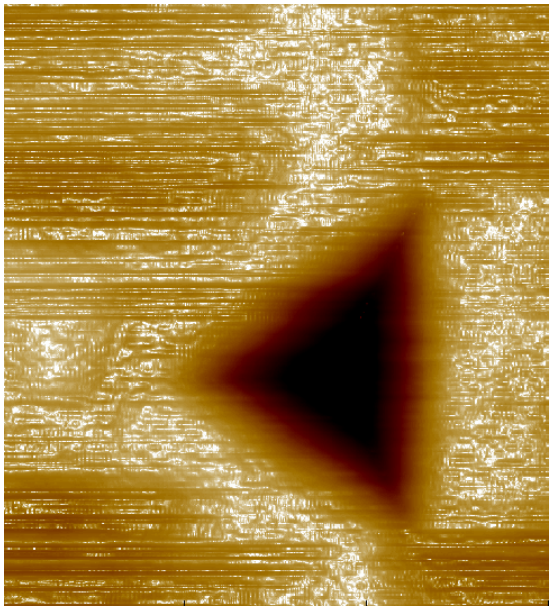

b

	Transverse	Tensile
Image size	485	536
Change in size	-0.05	+0.05
Est. Strain using DIC	-0.047	+0.048
Est. Strain using indent	-0.049	0.051

Figure 7.6: Digital stretching (Y-axis) and shrinking (X-axis) of image for validation of ISC method (a) 2.5 % (b) 5 %

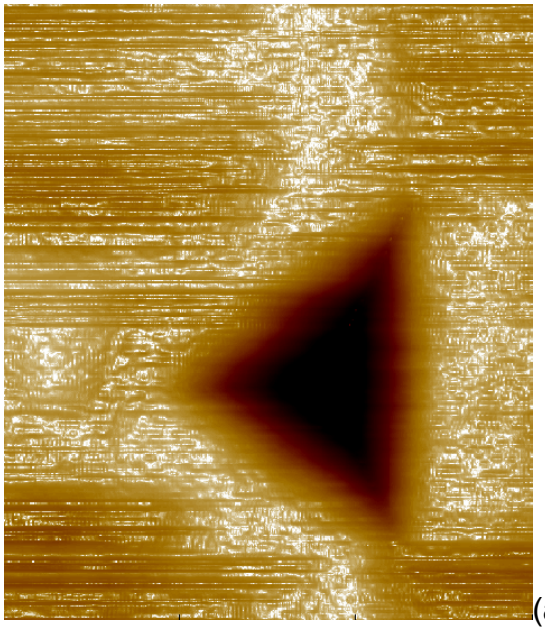

(**a**)

	Transverse	Tensile
Image size	472	549
Change in size	-0.075	+0.075
Est. Strain using DIC	-0.071	+0.076
Est. Strain using indent	-0.076	0.074

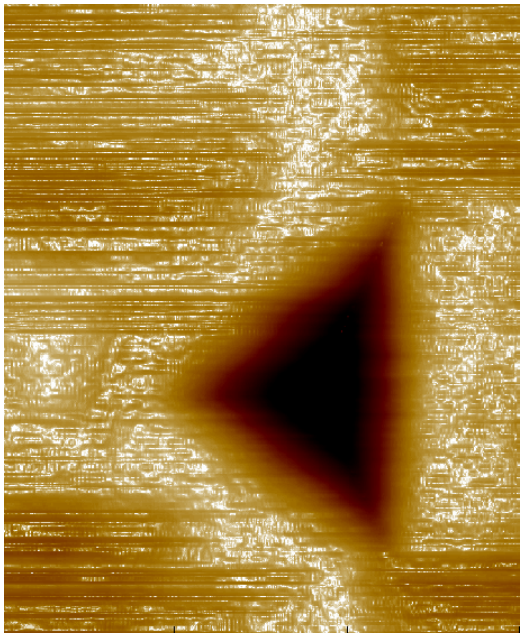

(**b**)

	Transverse	Tensile
Image size	459	561
Change in size	-0.1	+0.1
Est. Strain using DIC	-0.097	+0.103
Est. Strain using indent	-0.1	0.098

Figure 7.7 : Digital stretching (Y-axis) and shrinking (X-axis) of image for validation of ISC method (a) 7.5 % (b) 10 %

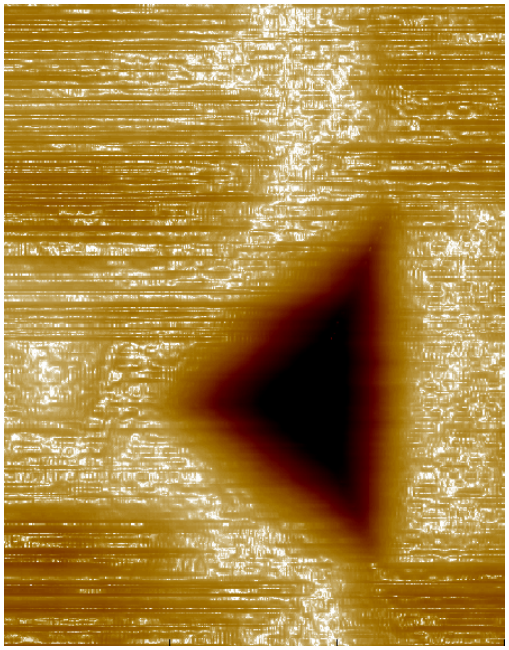

(**a**)

	Transverse	Tensile
Image size	446	574
Change in size	-0.125	+0.125
Est. Strain using DIC	-0.121	+0.127
Est. Strain using indent	-0.128	0.123

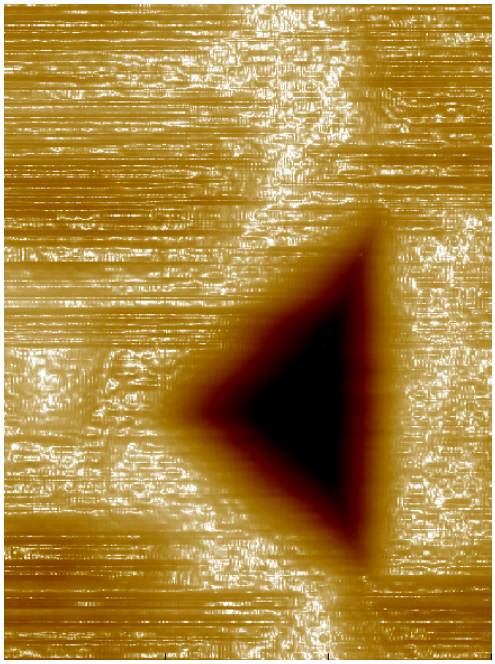

(**b**)

	Transverse	Tensile
Image size	434	586
Change in size	-0.15	+0.15
Est. Strain using DIC	-0.135	0.177
Est. Strain using indent	-0.16	0.147

Figure 7.8 : Digital stretching (Y-axis) and shrinking (X-axis) of image for validation of ISC method (a) 12.5 % (b) 15 %

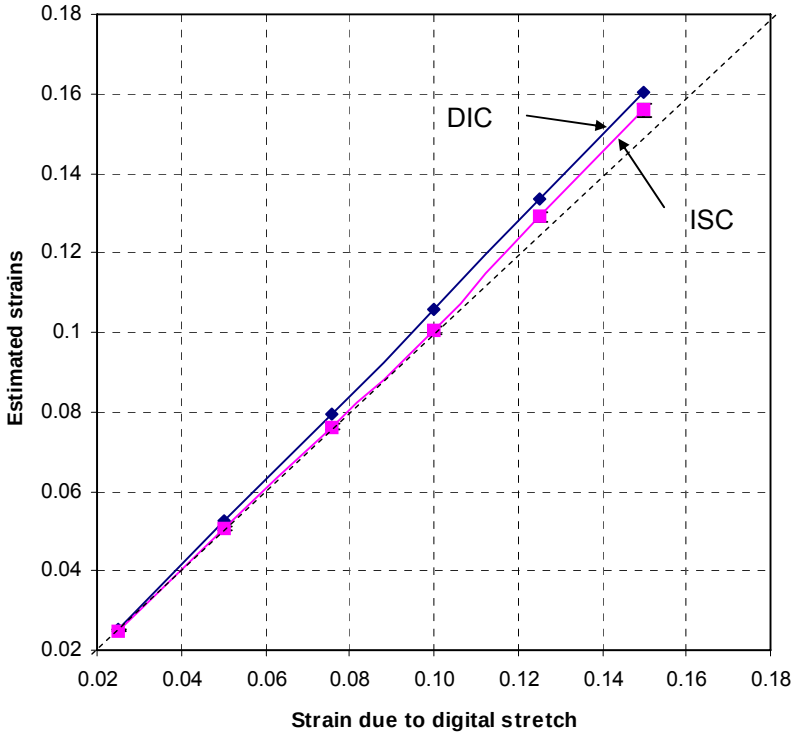

(**a**)

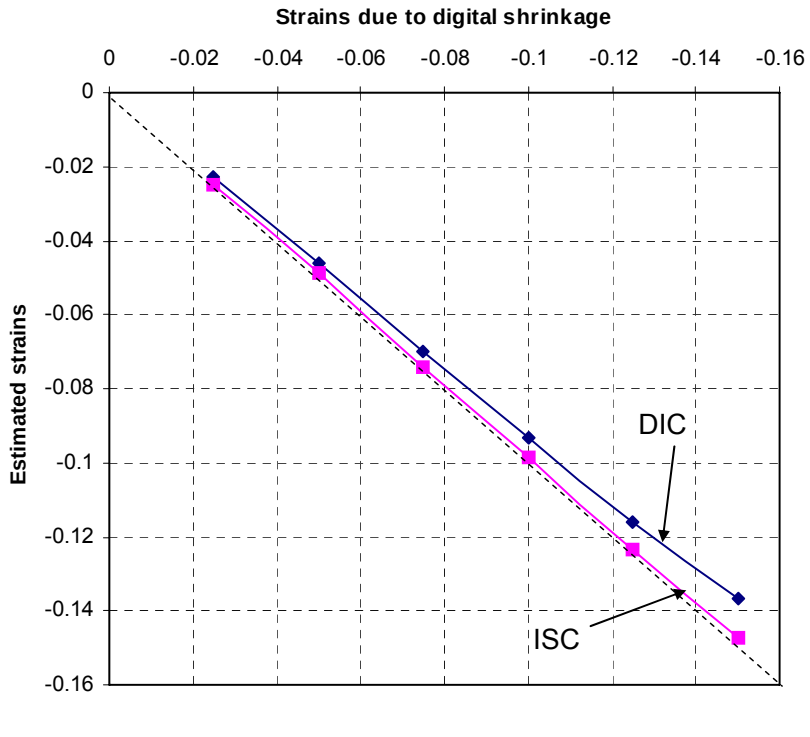

(**b**)

Figure 7.9 : Results of strain analysis by DIC and ISC on digitally altered images (a)Stretch in tensile direction (b) Shrinkage in transverse direction

Table 7-2 Strains estimated by analyzing the change in shape of the indents

Average Engineering Strain	ε_x	ε_y	ε_{xy}
0.003	-0.0193	0.11035	-0.06892
0.006	-0.0662	0.07384	-0.06102
0.02	0.0537	-0.0324	-0.07162
0.038	-0.0785	0.01622	-0.03926
0.045	-0.0024	0.01854	-0.02551
0.063	-0.1493	-0.0075	0.03088
0.074	-0.0697	-0.0825	0.08767
0.081	-0.1922	-0.0066	0.0453
0.09	-0.1477	-0.0317	0.04901
0.1	-0.2579	0.05474	0.02498
0.128	-0.2242	-0.1525	0.10336
0.14	-0.034	-0.1982	0.15787

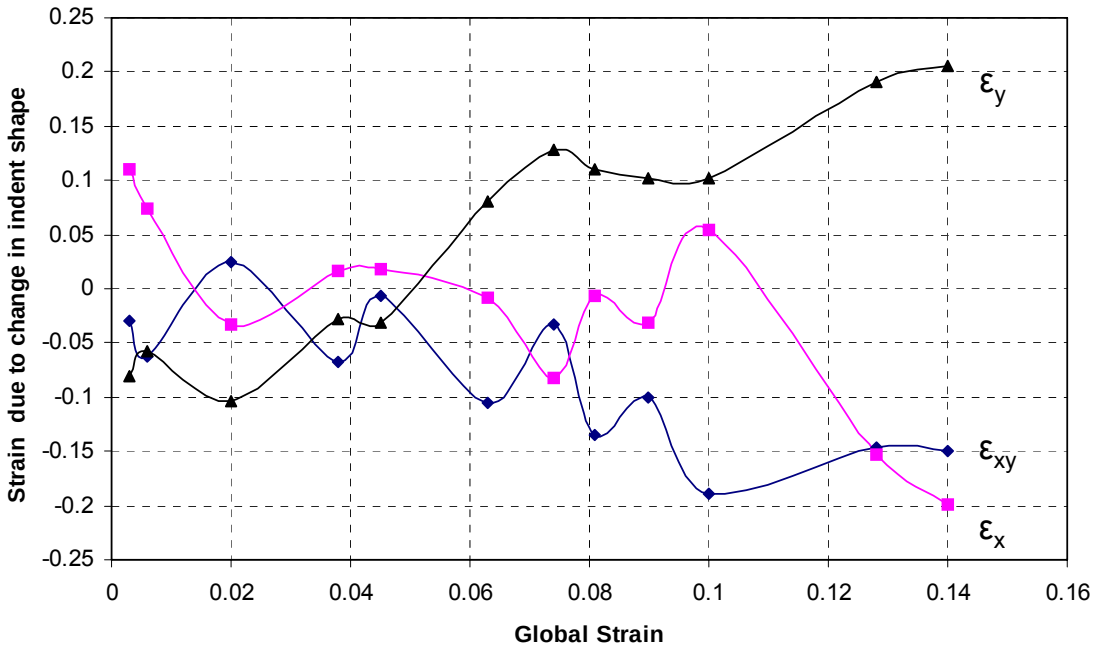

Figure 7.10 : Variation in tensile, transverse and shear strains estimated from the deformation of nanoindents with the engineering strain

It can be seen that during these investigations the shape of the residual indent was affected by the direction of the slip bands formed in the grains. In order to better understand this phenomenon, several sets of nanoindentations

were made on grains with different orientations. Since all grains in a polycrystalline material do not deform at the same time and thereby do not form slip bands at the same time, the indentations were performed at different tensile loads when individual grains of interest started showing slip bands. Figures 7.11 and 7.12 are AFM 3D images of nanoindentations performed on grains with different orientations as determined by the angles of their slip bands.

Figures 7.11 (a) and (b) are AFM 3D images of a grain that has slip bands formed at +40º to the tensile axis. The residual images of the nanoindents in Figure 7.11 (b) show that the top edge of the indents have stretched in the direction of the shear band. The residual indent on the lower right hand side has been formed at the junction of two slip bands. The shape of the indent has therefore been influenced by both the bands resulting in stretching in two directions.

The grain shown in Figure 7.11 (c) has the slip bands at an angle of -50º or +130º with respect to the tensile axis when measured in a clockwise direction. The residual indents in Figure 7.11 (d) have the lower corners stretched in the direction of shear. The indent in the upper right corner is partially on an adjacent slip band. This has resulted in the indent getting stretched in that direction too. Rest of the indents show that they have been stretched in the downward direction.

All the grains in a polycrystalline material do not deform at the same time during a tensile test. This is due to the fact that only grains, that have their slip planes oriented at ±45º to the tensile axis deform first. Thus, grains that have slip

planes at angles closer to this condition slip with increasing loads. The further away the angles of the slip planes are from ±45º, the longer it takes for that grain to deform. Figure 7.11 (e) is an AFM 3D image of a grain which is an example of such a condition. The slip bands in this grain are ~+5º with respect to the tensile axis and thus were almost vertical. The residual indents in Figure 7.11 (f) show only a small amount of stretching because stretching is mainly happening on the vertical side of the residual indent. The indents have been made at almost the center of the slip band were the effect of shear is least.

With increasing tensile loads several grains exhibit multiple slip bands. These are mostly the result of slip bands jumping across grain boundaries from other grains. Figure 7.12 (a) is an example of such a condition. The grain has slip bands formed at an angle of +48º. These bands may have been formed early in the tension experiment as this grain meets the ±45º criterion for slip formation. With increasing loads, other grains with different orientations begin to plastically deform. Figure 7.12 was acquired almost when the tensile sample had reached its ultimate tensile strength. When this happens, there are almost no grain boundaries in existence and slip bands begin jumping to the neighboring grains. It can be seen from Figure 7.12 (a) that +48º slip bands were formed earlier as they are lower than the second set of slip bands. The newer slip bands are at an angle of + 85º to the tensile axis and therefore are almost perpendicular to the tensile axis. Figure 7.12 (b) is an AFM 3D image of nanoindents made on this grain. The residual indents on the top half of the image show that the left corner has been stretched in the direction of shear. The other two indents have been

performed on the edge of the slip band and therefore have been influenced by both the bands.

Figure 7.13 is a schematic showing the influence of the slip band direction on the shape of the residual indent. It can be seen that the residual indents on grains that have their slip planes oriented close to the ±45º criterion show maximum stretching. It can be concluded from this examination that slip bands with positive angles with respect to the tensile direction tend to have the top corner of the residual indent stretching as shown in Figure 7.11 (b) while grains with negative slip plane angles show that the lower corner of the residual indent stretches. The further away the grain is from satisfying the ±45º slip plane criterion, the lesser is the stretch of the residual indent corners. When the orientation of the slip planes are closer to the vertical axis, very little stretching is seen in the residual indent mainly because the stretching action is on the vertical side of the indent where very little movement is possible. It has also been noted that closer the orientation of the slip planes of the grain to the perpendicular to the tensile axis, further would be the stretching of the left corner of the residual indent opposite to the vertical side.

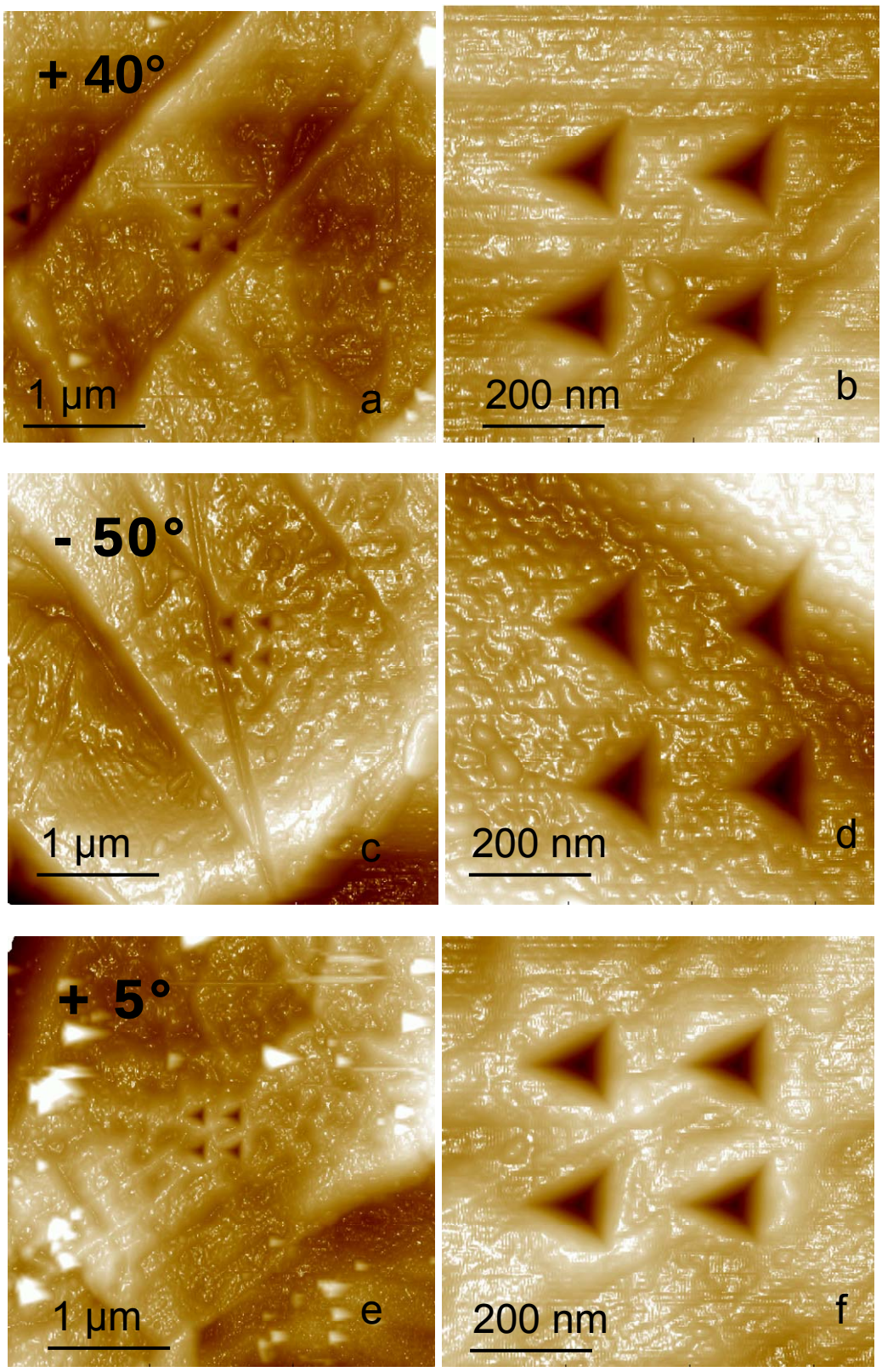

Figure 7.11 : Effect of slip band direction on the shape of residual indents

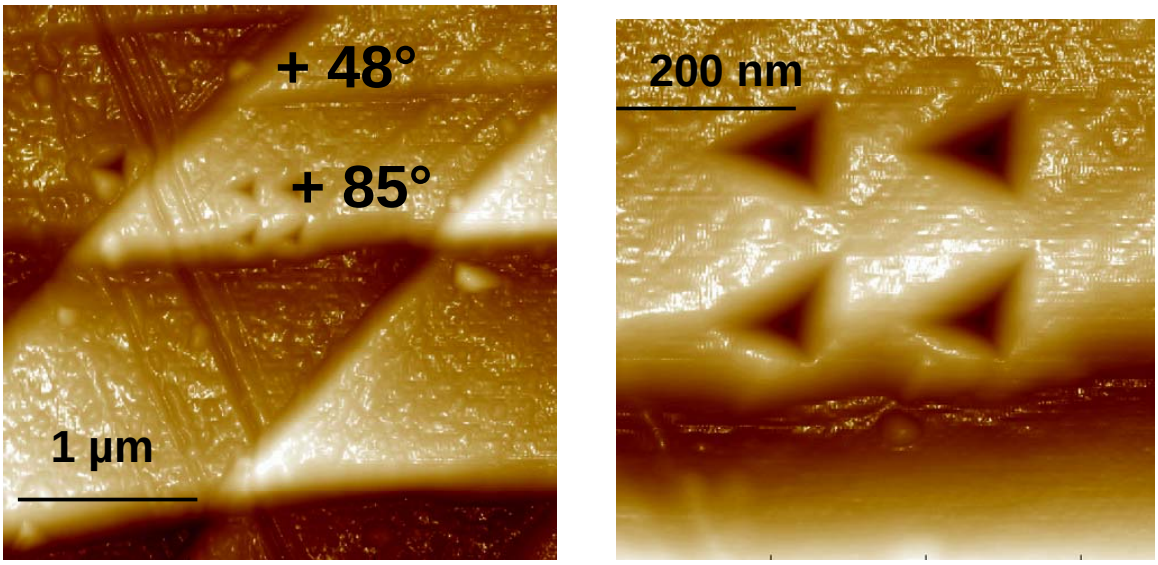

Figure 7.12 : Effect of Intersecting shear bands on the shape of residual indents

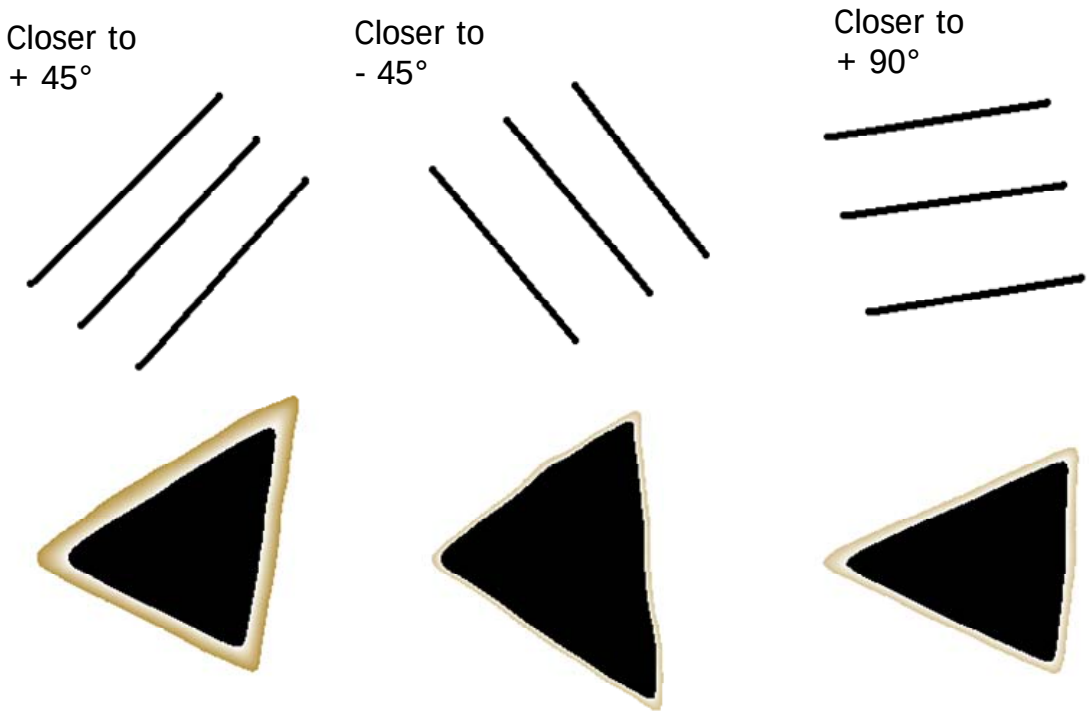

Figure 7.13 : Comparison of slip band directions and shapes of residual indents

CHAPTER 8

CONCLUSIONS AND FUTURE WORK

1. A new method has been developed for determining strains in very small regions using a micro-tensile stage and nanoindentation as a tool. Nanoindentation experiments were performed at various stages using a micro-tensile stage to investigate the effect of tensile loading on the shape of the residual indent. Both the shape and size of the indents were found to vary with increasing loads. The size was mostly affected by the local stresses. The shear strain and the local stresses affected the shape of the indent resulting in the residual indent getting pulled in the direction of shear strain. A method known as the indent shape change (ISC) method was developed to analyze the change in the shape and size of the residual indent to determine local strains. The maximum tensile, transverse, and shear strains were estimated to be ~ 0.15, -0.19, and -0.25, respectively.

2. Tensile tests were performed *in-situ* on a polycrystalline copper (C11000, H01 temper) specimen with an atomic force microscope (AFM) to study the deformation on the surface and to measure local strains in very small regions. An *in-situ* micro-tensile stage, originally developed for *in-situ* testing inside an SEM, was modified and adapted so that it can be placed under an AFM and the

surface can be imaged under different tensile loading conditions. The AFM head was engaged after stopping the tensile test at various engineering strain values.

A good surface finish (Ra ~0.85 nm and Rq ~ 1.09 nm) for AFM imaging was obtained for polycrystalline copper by using a combination of polishing using abrasives and electropolishing in an orthophosphoric acid bath. It was determined that electropolishing copper for 15-20 seconds at a voltage ~1.7 V in an othophosphric acid bath resulted in the best surface conditions for AFM imaging.

3. Some modifications were made to accommodate the tensile stage under the AFM. A new X-Y stage was made to mount the tensile testing setup so that fine movements can be made to locate the area of interest. This setup can be easily disassembled so that the AFM can be used for imaging other samples as and when necessary.

4. The ISC method was theoretically validated by performing a virtual “digital” tensile test in which an image of a residual indent was digitally stretched along the longitudinal (tensile) direction and shrunk in the transverse direction by known quantities. The images thus obtained were analyzed using a Digital Image Correlation (DIC) software developed by Lu and Cary[63] and ISC method to estimate strains. The strains estimated were found to be in good agreement with the actual strains applied.

5. A method, called the relative indent movement (RIM) method, was developed to study strains in a 40 μm x 40 μm area using an array of nine, 600 nm deep indents in a 3 x 3 arrangement. They were made on the tensile sample

with a Berkovich indenter using an MTS nanoindenter. The sample was then subjected to a tensile test during which the surface was imaged using an AFM. By analyzing the relative displacements of the indents, the tensile strain at maximum load in the area was estimated to be ~0.3 which is almost twice the global strain at that location and time. A compressive strain of ~0.11 was also noted in the X-direction. The shear strain was estimated to be ~0.04.

6. The relative displacements of the indents were measured with the AFM software using a new technique that is not covered in the AFM manual. This was done by first inverting the images so that all the deepest points would appear as the highest points (or apex) and then using contour plots so that areas with same the heights are of the same color. This enabled identification of the center of each indent more accurately aiding in quick and accurate measurement of lengths. This was done because the built-in option used for measuring the step heights in the AFM software did not yield satisfactory results.

7. The calculated strains were theoretically validated by performing a virtual “digital” tensile test. The images obtained were analyzed using digital image correlation (DIC) software and the relative indent method (RIM) method to determine strains. Strains calculated by the RIM method and DIC methods were found to be in good agreement with the actual strains obtained from the virtual “digital” tensile test.

8. Experimental validation of the strains calculated by the DIC and RIM methods was done by tensile testing a polycarbonate sample. This material was selected because it has uniform elongation under tension upto large strains.

Relative displacements of nanoindents made on the polycarbonate sample under a tensile load were analyzed using the RIM and DIC methods. Local strains calculated by these methods were found to be consistent with global strain values measured by the LSC transducer until necking began in the sample. Beyond this stage, the local tensile strains were higher than global strains.

9. Strains were analyzed in different areas of the tensile sample using the RIM method by analyzing sets of nanoindents made in these areas. It was found that local strains varied from one area to another and depended on the orientation of grains in the indented area.

10. Nanoindentations (~ 75 nm) were also made in an area 2 μm x 2 μm with a tetrahedral diamond indenter using an AFM. The surface was examined after stopping the tensile test at various stages. The development of a slip band was observed during this experiment. Very little variations in the tensile and transverse strains were observed in the earlier stages of the tensile test. A change in these strains was observed with the development of the slip band. The maximum tensile strain and transverse strain (estimated by the RIM and DIC method) of these indents were ~0.11 and ~-0.02 when the engineering strain was ~0.017. A reduction in the local area in the transverse direction was thus observed.

11. It was determined that grains with slip bands with positive angles (with respect to the tensile direction) tend to have the top corner of the residual indent stretching while grains with negative slip plane angles showed that the lower corner of the residual indent stretches. The further away the grain is from

satisfying the ±45º slip plane criterion, the lesser is the stretch of the residual indent corners. When the orientation of the slip planes are closer to the vertical axis, very little stretching is seen in the residual indent mainly because the stretching action is on the vertical side of the indent where very little movement is possible. It has also been noted that closer the orientation of the slip planes of the grain to the normal to the tensile axis, the further would be the stretching of the left corner of the residual indent opposite to the vertical side.

12. Surface of polycrystalline copper was examined using an optical interference microscope (MicroXam) at magnifications of 100x and 500x. Vickers indents were used as reference points to keep track of the area being imaged. Micrographs obtained were analyzed using DIC software to analyze the distribution of strains in the area being examined. The effect of global strain on local strains (longitudinal, transverse, and shear) was mapped and analyzed using the TechPlot® software. It was seen that different grains experienced different strains during tensile loading.

13. High resolution images of the change in the surface morphology of the surface when the tensile loads were applied were captured using an AFM. Formation of slip bands and cross slip are observed in several grains. Individual slip lines ~50 nm apart were also imaged. It was observed that several grains had slip bands at different angles with the tensile axis

FUTURE WORK

1. Estimate strains in the polycrystalline copper sample under the same conditions as used in the AFM experiments using X-ray diffraction, or μ-Raman spectroscopy to corroborate the results obtained in this investigation. This may be accomplished by fabricating a setup in which the present tensile stage could me mounted on the XRD goniometer or the stage under the μ-Raman spectroscope. Since the present stage has already been used with an optical interference microscope (MicroXam), it can be easily adopted for use with μ-Raman spectroscopy equipment.

2. A large array of nanoindents(~200 indents or more) on a tensile sample made using an AFM or MTS nanoindenter can be imaged and analyzed using the RIM method to study how strains in different areas vary relative to the global strain. Software can be developed to analyze the relative displacements of all the nanoindents with respect to each other to estimate strains at different scales. This information can also be used to study grain rotation relative to each other. The method used to measure the relative distances, using the AFM software (described in Section 6.2.2), can also be incorporated in this software.

3. The surface of a sample under tensile loading undergoes deformation and the image changes from a 2D to a 3D condition (ridging). This is especially true when large areas (multiple grains, 40 μm x 40 μm or larger area) are examined. There will therefore be strains in the vertical (z-direction) in addition to the strains in the longitudinal and transverse directions. Indents on individual grains show a

small amount of ridging. An investigation into the effect of ridging on the overall local strain could be considered.

4. Multiple nanoindents (depending on the area being imaged) could be made using the AFM diamond indenter over multiple grains that have deformed under a tensile or compressive load. Each indent could then be analyzed using the ISC method to determine strains. The information from this could be used to make strain maps (longitudinal, transverse, and shear) of the area being examined. If larger areas (> 90 x 90 μm) need to be studied, movement of the AFM X-Y stage can be programmed to move a fixed and known distance and indentations can then be performed. The area can be subsequently imaged in various steps and, if necessary, these images may be “stitched” using imaging software. The analysis of a large area can take several hours or days depending on the area being analyzed.

5. This investigation has examined at the effect of strains on the shape of residual indents made at a depth of ~75 nm. The effect of strain on residual indents at different depths can be analyzed. Strain can be estimated using the ISC method. Since nanoindents cannot be made on the same exact point repeatedly, indents made when global strains are higher, need to be made close to the earlier indents

6. Nanoindentation experiments can be performed on thin coatings under a tensile load and the effect of global strains on local strains can be investigated using both the RIM as well as the ISC method. Since the minimum thickness of a tensile sample that can be tested on the present tensile setup is ~ 3 mm,

coatings have to be made on thick substrates. One good method of depositing coatings on tensile substrates, such as copper could be electroless plating of metals with nickel. Other methods of coating can also be employed. By adjusting the depth of indentation, the effect of strain in the substrate on the strains in the coatings can be analyzed. This could also possibly reveal strains at coating-substrate interfaces.

7. A detailed study of strains measured in the elastic region of the deformation of metals can be made to determine stresses. A plasticity-based model could be developed to determine stresses due to change in the shape of residual indents due to plastic deformation. With the development of an appropriate model that takes into effect the depth of indentation, load vs indentation depth curves along with the shape changes caused due to local stresses, a new method for the measurement residual stress can be developed. A residual stress measurement technique that employs nanoindentation, using AFM, would be of great advantage in the microelectronics industry. The main advantage of this technique would be the ability of this method to locate and image the area of interest and determine residual stresses in very small regions (> 200nm).

REFERENCES

1 Withers, P. J.; Bhadeshia, H. K. D. H., Residual stress. Part 1 – Measurement techniques. *Materials Science and Technology* 2001, 17, (4), 355-365.

2 C.Fischer-Cripps, A., *Nanoindentation*. Springer: 2002.

3 Dahmani, F.; Lambropoulos, J. C.; Schmid, A. W.; Burns, S. J.; Pratt, C., Nanoindentation technique for measuring residual stress field around a laser-induced crack in fused silica. *Journal of Materials Science* 1998, 33, (19), 4677.

4 Han, S. W.; Lee, H. W.; Lee, H. J.; Kim, J. Y.; Kim, J. H.; Oh, C. S.; Choa, S. H., Mechanical properties of Au thin film for application in MEMS/NEMS using microtensile test. *Current Applied Physics* In Press, Corrected Proof.

5 Bolshakov, A.; Oliver, W. C.; Pharr, G. M., Influences of stress on the measurement of mechanical properties using nanoindentation: Part II. Finite element simulations. *Journal of Materials Research* 1996, 11, (3), 760.

6 Taylor, C. A.; Wayne, M. F.; Chiu, W. K. S., Residual stress measurement in thin carbon films by Raman spectroscopy and nanoindentation. *Thin Solid Films* 2003, 429, (1-2), 190.

7 Tsui, T. Y.; Oliver, W. C.; Pharr, G. M., Influences of stress on the measurement of mechanical properties using nanoindentation: Part I.

Experimental studies in an aluminum alloy. *Journal of Materials Research* 1996, 11, (3), 752-759.

8 Shultz, W. L.; Conte, J. P.; Udd, E., Long gage fiber optic bragg gratting strain sensors to monitor civil structures. *www.bluerr.com*.

9 George, D. T.; Bogen, D. K., A low-cost fiber-optic strain gage system for biological applications. *IEEE transactions in Biomedical Engineering* 1991, 38, (9), 919-924.

10 Beilis, I. I.; Shashurin, A.; Boxman, R. L.; Goldsmith, S., Influence of background gas pressure on copper film deposition and ion current in a hot refractory anode vacuum ARC. *Surface and Coatings Technology* 2005, 200, (5-6), 1395.

11 Wang, G.; Zhao, J. H.; Ding, M.; Ho, P. S. In Thermal deformation analysis on flip-chip packages using high resulution moire interferometry, *Intersociety conference on thermal phenomena*, 2002; IEEE: 2002; pp 869-875.

12 Silva Gomes, J. F.; Monteiro, J. M.; Vaz, M. A. P., NDI of interfaces in coating systems using digital interferometry. *Mechanics of Materials* 2000, 32, (12), 837.

13 Guelorget, B.; Francois, M.; Vial-Edwards, C.; Montay, G.; Daniel, L.; Lu, J., Strain rate measurement by Electronic Speckle Pattern Interferometry: A new look at the strain localization onset. *Materials Science and Engineering: A* 2006, 415, (1-2), 234.

14 Joo, H. D.; Kim, J. S.; Kim, K. H.; Tamura, N.; Koo, Y. M., *In situ* synchrotron X-ray microdiffraction study of deformation behavior in

polycrystalline coppers during uniaxial deformations. *Scripta Materialia* 2004, 51, (12), 1183.

15 Kim, K. H.; Koo, Y. M., *In-situ* X-ray diffraction study about uniaxial deformation behavior in a copper single crystal. *Materials Science and Engineering A* 2002, 335, (1-2), 309.

16 Kretschmann, A.; Kuschke, W.-M.; Baker, S. P.; Arzt, E. In Plastic deformation in thin copper films determined by X-ray microtensile tests, *Proceedings of the Symposium on Thin Films: Stresses and mechanical properties VI;, San Francisco, CA*, 1996; San Francisco, CA, 1996; pp 59-64.

17 Pantleon, W.; Poulsen, H. F.; Almer, J.; Lienert, U., *In situ* X-ray peak shape analysis of embedded individual grains during plastic deformation of metals. *Materials Science and Engineering A* 2004, 387-389, 339.

18 Hanan, J. C.; Bale, H.; Smay, J. E.; Chu, Y. S.; DeCarlo, S., Combined diffraction and tomogrphy analyzing controlled stress in solid free form fabrication. *Synchrotron Radiation in Materials Science* 2006.

19 Rizzo, A.; Capodieci, L.; Rizzo, D.; Galietti, U., Low cost technique for measuring *in-situ* strain of nanostructures. *Materials Science and Engineering: C* 2005, 25, (5-8), 820.

20 Carlsson, S.; Larsson, P. L., On the determination of residual stress and strain fields by sharp indentation testing.: Part I: theoretical and numerical analysis. *Acta Materialia* 2001, 49, (12), 2179.

21 Sines, G.; Carlson, R., Hardness measurements for determination of residual stresses. *ASTM bulletin* 1952, 180, 35.

22 Doerner, M. F.; Gardner, D. S.; Nix, W. D., Plastic properties of thin films on substrates as measured by submicron indentation hardness and substrate curvature techniques. *Journal of Materials Research* 1986, 1, 845-851.

23 LaFontaine, W. R.; Paszkiet, C. A.; Korhonen, M. A.; Li, C.-Y., Residual stress measurements of thin aluminum metallizations by continuous indentation and x-ray stress measurement techniques. *Journal of Materials Research* 1991, 6, (10), 2084-2090.

24 LaFontaine, W. R.; Yost, B.; Li, C.-Y., Effect of residual stress and adhesion on the hardness of copper films deposited on silicon. 1990, 5, (4), 776-783.

25 Suresh, S.; Giannakopoulos, A. E., A new method for estimating residual stresses by instrumented sharp indentation. *Acta Materialia* 1998, 46, (16), 5755.

26 Venkatesh, T. A.; Van Vliet, K. J.; Giannakopoulos, A. E.; Suresh, S., Determination of elasto-plastic properties by instrumented sharp indentation: guidelines for property extraction. *Scripta Materialia* 2000, 42, (9), 833.

27 Carlsson, S.; Larsson, P. L., On the determination of residual stress and strain fields by sharp indentation testing.: Part II: experimental investigation. *Acta Materialia* 2001, 49, (12), 2193.

28 Lee, Y.-H.; Kwon, D., Estimation of biaxial surface stress by instrumented indentation with sharp indenters. *Acta Materialia* 2004, 52, (6), 1555.

29 Atar, E.; Sarioglu, C.; Demirler, U.; Sabri Kayali, E.; Cimenoglu, H., Residual stress estimation of ceramic thin films by X-ray diffraction and indentation techniques. *Scripta Materialia* 2003, 48, (9), 1331.

30 Guelorget, B.; Francois, M.; Lu, J., Microindentation as a local damage measurement technique. *Materials Letters* In Press, Corrected Proof.

31 Smith, B. W., *Sixty centuries of copper*. UK Copper Development Association: 1965.

32 Streiter, R.; Gener, T.; Wolf, H., Geometrical optimization of multilevel interconnects using Cu and low-k dielectrics. *Microelectronic Engineering* 1997, 33, (1-4), 429.

33 Lloyd, J. R.; Clemens, J.; Snede, R., Copper metallization reliability. *Microelectronics Reliability* 1999, 39, (11), 1595.

34 Eichenlaub, S.; Chan, C.; Beaudoin, S. P., Hamaker Constants in Integrated Circuit Metalization. *Journal of Colloid and Interface Science* 2002, 248, (2), 389.

35 Shen, Y. L., Thermo-mechanical stresses in copper interconnects - A modeling analysis. *Microelectronic Engineering* 2006, 83, (3), 446.

36 Cheng, Y.-W.; Read, D. T.; McColskey, J. D.; Wright, J. E., A tensile-testing technique for micrometer-sized free-standing thin films. *Thin Solid Films* 2005, 484, (1-2), 426.

37 Keller, R. R.; Phelps, J. M.; Read, D. T., Tensile and fracture behavior of free-standing copper films. *Materials Science and Engineering A* 1996, 214, (1-2), 42.

38 Borbely, A.; Szabo, P. J.; Groma, I., Orientation correlation in tensile deformed [0 1 1] Cu single crystals. *Materials Science and Engineering A* 2005, 400-401, 132.

39 Simons, G.; Weippert, C.; Dual, J.; Villain, J., Size effects in tensile testing of thin cold rolled and annealed Cu foils. *Materials Science and Engineering: A* 2006, 416, (1-2), 290.

40 Yu, D. Y. W.; Spaepen, F., The yield strength of thin copper films on Kapton. *Journal of Applied Physics* 2004, 95, (6), 2991-2997.

41 Cheng, S.; Ma, E.; Wang, Y. M.; Kecskes, L. J.; Youssef, K. M.; Koch, C. C.; Trociewitz, U. P.; Han, K., Tensile properties of in situ consolidated nanocrystalline Cu. *Acta Materialia* 2005, 53, (5), 1521.

42 Wang, Y. M.; Wang, K.; Pan, D.; Lu, K.; Hemker, K. J.; Ma, E., Microsample tensile testing of nanocrystalline copper. *Scripta Materialia* 2003, 48, (12), 1581.

43 Weertman, J. R., *Nanostructured materials: processing, properties and applications*. William Andrews Publishing, Norwich (NY): 2002; p 397.

44 Capolungo, L.; Jochum, C.; Cherkaoui, M.; Qu, J., Homogenization method for strength and inelastic behavior of nanocrystalline materials. *International Journal of Plasticity* 2005, 21, (1), 67.

45 Van Swygenhoven, H.; Weertman, J. R., Deformation in nanocrystalline metals. *Materials Today* 2006, 9, (5), 24.

46 Kalidindi, S. R.; Bhattacharya, A.; Doherty, R. D., How do Polycrystalline Materials Deform Plastically? *Advanced Materials* 2003, 15, (16), 1345-1348.

47 J.G.Tweeddale *The Mechanical Properties of Metals*, American Elsevier Publishing Company, Inc.: 1964.

48 McLean, D., *Mechanical Properties of Metals*. John Wiley & Sons, Inc.: 1962.

49 Niewczas, M.; Embury, J. D. In Approaching the theoretical sttength in ductile copper, *The integration of material, process and product design*, 1999; Zabaras, Ed. Balkema, Roterdam: 1999; pp 1-10.

50 Van Houtte, P.; Delannay, L.; Kalidindi, S. R., Comparison of two grain interaction models for polycrystal plasticity and deformation texture prediction. *International Journal of Plasticity* 2002, 18, (3), 359.

51 Ogata, S.; Li, J.; Yip, S., Ideal pure shear strength of aluminum and copper. *Science* 2002, 298, 807-811.

52 Cerney, M.; Sob, M.; Pokluda, J.; Sandera, P., *Ab initio* calculations of ideal tensile strength and mechanical stability of copper. *Journal of Physics: Condensed Matter* 2004, 16, 1045-1052.

53 Paul, H.; Morawiec, A.; Bouzy, E.; Fundenberger, J.-J.; Piatkowski, A., TEM Orientation Mapping Applied to the Study of Shear Band Formation. *Microchimica Acta* 2004, 147, (3), 181.

54 Small, M. K.; Coupeau, C.; Grilh, J., Atomic force microscopy of *in situ* deformed LiF. *Scripta Metallurgica et Materialia* 1995, 32, (10), 1573.

55 Goken, M.; Vehoff, H.; Neumann, P., Investigations of loaded crack tips in NiAl by atomic force microscopy. *Scripta Metallurgica et Materialia* 1995, 33, (7), 1187.

56 Long, W.; Hector, J. L. G.; Weiland, H.; Wieserman, L. F., *In-situ* surface characterization of a binary aluminum alloy during tensile deformation. *Scripta Materialia* 1997, 36, (11), 1339.

57 Bobji, M. S.; Bhushan, B., Atomic force microscopic study of the micro-cracking of magnetic thin films under tension. *Scripta Materialia* 2001, 44, (1), 37.

58 Renault, P. O.; Villain, P.; Coupeau, C.; Goudeau, P.; Badawi, K. F., Damage mode tensile testing of thin gold films on polyimide substrates by X-ray diffraction and atomic force microscopy. *Thin Solid Films* 2003, 424, (2), 267.

59 George, M.; Coupeau, C.; Colin, J.; Grilhe, J., Mechanical behaviour of metallic thin films on polymeric substrates and the effect of ion beam assistance on crack propagation. *Acta Materialia* 2005, 53, (2), 411.

60 Tambe, N. S.; Bhushan, B., *In situ* study of nano-cracking in multilayered magnetic tapes under monotonic and fatigue loading using an AFM. *Ultramicroscopy* 2004, 100, (3-4), 359.

61 Bamberg, E.; Grippo, C. P.; Wanakamol, P.; Slocum, A. H.; Boyce, M. C.; Thomas, E. L., A tensile test device for *in situ* atomic force microscope mechanical testing. *Precision Engineering* 2006, 30, (1), 71.

62 Vettegren, V.; Svetlov, V., Dynamics of slip lines on the surface of polycrystalline copper. *Physics of the Solid State* 2004, 46, (11), 2063.

63 Lu, H.; Cary, P. D., Deformation Measurements by Digital Image Correlation: Implementation of a Second-Order Displacement Gradient. *Experimental Mechanics* 2000, 40, (4), 393.

64 *DI 3100 Atomic Force Microscope - Reference Manual*. Digital Instruments, Santa Barbara, CA: 1999.

65 Tabor, D., Indentation hardness and Its measurement: some cautionary comments. *American Society for Testing and Materials*: 1986; p 129-159.

66 *Fine calibration procedures for the SPM- a users's guide*. Digital Instruments: 1996; Vol. Support Note No.217, Rev.D.

67 *Nanoindenter XP - Instruction Manual*. MTS Instruments.

68 Oliver, W. C.; Pharr, G. M., An improved technique for determining hardness and elastic modulus using load and displacement sensing indentation experiments. *Journal of Materials Research* 1992, 7, (6), 1564.

69 Chemical and Electrolytic Polishing, Metallography and Microstructures, *ASM Handbook*. ASM International: 2004; Vol. 9, p 281-293.

70 www.matweb.com referenced 30, Nov. 2005

71 *Metallography and Microstructures of Copper and its Alloys, ASM Handbook*. ASM International: 2004; Vol. 9, p 775-788.

72 Kalidindi, S. R.; Schoenfeld, S. E., On the prediction of yield surfaces by the crystal plasticity models for fcc polycrystals. *Materials Science and Engineering A* 2000, 293, (1-2), 120.

73 Lagattu, F.; Bridier, F.; Villechaise, P.; Brillaud, J., In-plane strain measurements on a microscopic scale by coupling digital image correlation and an in situ SEM technique. *Materials Characterization* 2006, 56, (1), 10.

74 Knauss, W. G.; Chasiotis, I.; Huang, Y., Mechanical measurements at the micron and nanometer scales. *Mechanics of Materials* 2003, 35, (3-6), 217.

75 Lu, J.; Ravi-Chandar, K., Inelastic deformation and localization in polycarbonate under tension. *International Journal of Solids and Structures* 1999, 36, (3), 391.

76 Lexan referenced June 3, 2006 In Wikipedia, The Free Encyclopedia, from http://en.wikipedia.org/w/index.php?title=Lexan&oldid=56899841.

77 Zhang, X.; A.Misra, Residual stresses in sputter-deposited copper/330 stainless steel multilayers. *Journal of Applied Physics* 2004, 96, (12), 7173-7178.

APPENDIX

Procedure for estimating local strains using nanoindentation and atomic force microscopy (AFM):

Sample Preparation

1. Only tensile samples of the dimensions described in Section 4.5 can be imaged using the AFM by *in-situ* tensile testing using the present setup. Though small variations in the length and width of the sample can be accommodated, the thickness of the sample cannot be less than 3 mm since the AFM head assembly would come in contact with tension stage setup.

2. Surfaces being imaged must have the best surface finish possible (Ra < 3 nm, Rq < 5 nm). This ensures that asperities do not interfere with the indentation and imaging process.

3. Polymer tensile samples made from cast sheets usually have very good surface and can be imaged as is. Metal samples need to be polished and electropolished, if necessary. Details of copper sample surface preparation are given in Section 4.5. Getting the right conditions for electropolishing usually involves considerable trial and error before the optimum combination of process variables is achieved. This optimization is preferably not done on the sample to be imaged but rather on test coupons of the same material. ASM Handbook electropolishing recommendations can be used as a starting point but optimum conditions vary from material to material. Moreover these recommendations are

usually intended for improving the appearance of big samples on a macro to micro scale and this may not be the best condition for AFM surface imaging.

Use of tensile stage in conjunction with the AFM

This step usually takes about one and a half hours to accomplish for an experienced user.

1. It must be always remembered that the AFM is a delicate instrument and utmost care must be taken when any movement around the AFM head is involved. The AFM head has to be moved away from the granite stage before the tensile stage can be mounted. The cable connecting the AFM head to the system has to remain connected if the tensile stage has to be moved using the AFM X-Y stage.

2. The jaws of the tensile stage have to be brought closer to each other before the tensile sample can be mounted on it. Use the limit switch on the tensile stage to position the jaws, as this will prevent repeatability problems when testing different samples. The samples have to be fixed on the stage by tightening the jaws in increments alternating on both sides. This ensures that the sample doesn't move when the screws are being tightened.

3. Turn the AFM software on. Use the appropriate tip needed for the experiment. AFM nanoindentation tip has to be used only if nanoindentation experiments need to be done. For all other imaging applications silicon tips would be adequate.

4. Before placing the tensile stage under the AFM head, the original AFM stage has to be removed slowly and placed on the side of the AFM. The vacuum tube connecting the stage to the system should not be separated.

5. Once the tensile stage has been screwed on to the X-Y translation arms of the AFM, it has to be moved by invoking the “focus surface” option in the AFM software. The stage has to be moved in small increments making sure that the tensile stage doesn’t hit the AFM head as there is very little clearance between the two. Use the optical microscope attachment with AFM to focus the tip being used and then the surface to be examined.

***In-situ* AFM imaging of tensile testing**

One AFM image of a surface usually takes about 10 minutes from initial approach, to adjusting parameters, to imaging, to final retraction of the tip. Typically an imaging sequence in which an area of interest is located using the optical microscope attachment, engaging AFM for imaging, adjusting imaging parameters, acquiring images at different magnifications and subsequent retraction of the AFM takes ~ ½ - ¾ hr. The loading of the tensile sample has to be performed only when the AFM head is disengaged. Thus an *in-situ* examination of a sample under tensile loads during which images are acquired at, at least a minimum of 10 stages will need about 11 hours with an hour break.

1. The AFM has to be calibrated every 3 - 4 months to maintain the accuracy of the dimensions of features being examined. The details of the right procedure to install the tip, calibrate the AFM and imaging using the AFM can be obtained from the Digital Instruments instruction manual.

2. The surface of the tensile sample after mounting on the stage has to be imaged before any loads are applied, so that the image of the un-deformed surface can be used as a reference image to estimate strains. An area of interest can be located using the optical microscope attachment by using scratches or easily distinguishable macroscopic features. At least 3 features around the area of interest can be selected so that their relative positions will facilitate in locating the point of interest. Care has to be taken so that AFM head doesn't hit the surface being imaged or the tensile stage when the area of interest is being located.

3. After the AFM head is retracted, tensile loads can be applied by deciding the strain intervals at which the surface needs to be imaged. The area of interest must only be imaged after the drive motor has stopped and the main power supply to it has been turned off. This precaution has to be taken to prevent any accidental starting of the motor which might result in damage to the AFM head.

4. Extra attention needs to given while imaging the surface of clear samples like glasses and plastics. The imaging tip of the AFM approaches the surface to be imaged based on the focus position of the tip relative to the surface. The distance to be traveled by the tip before it comes in contact with the surface is determined by the difference between these two focus points. Since light transmits through transparent samples it is difficult to focus the top surface of the sample especially samples that are "very clean". There is a very good possibility that the lower surface is focused and when the tip approaches the surface, it comes in contact with the top surface since it assumes that the lower surface is

the top part of the surface. This can result in damage to the AFM head and can also result in the destruction of expensive tips like the nanoindenter tip. Sometimes a little “dirt” or markers on the surface to be imaged is good, as this helps in focusing the surface by the optical microscope with the AFM.

Nanoindentation and imaging using AFM

The procedure for using nanoindents for strain estimation on tensile samples has been described in detail in Chapter 6. The imaging of the area of interest can be performed in the same way as described earlier in this appendix. Some extra attention needs to be paid while imaging nanoindents made using the AFM nanoindenter. First and foremost areas larger than 10 x 10 μm should not be imaged using the diamond indenter. Secondly AFM nanoindents have to be made near some features that can be easily identified once the area to be imaged has been located and imaged with the AFM. Any necessary translation to locate the area of interest may be done by moving the tip while the imaging is being done. This is accomplished by using the AFM software to command the tip to move by the required distance. The maximum distance a tip can be moved is ~ 90 μm but this depends on the location of the tip and scan size at the time imaging is being done. It is preferable that no movements larger than 20 μm be made when the diamond tip is being used, to prevent any damage to the tip.

If experiments similar to the one described in Chapter 7 are to be performed in which indents are made after the loading is done, the area in which strain has to be estimated has to be chosen first. Any number of indents can be made and the indented area can be imaged. Individual indents can be imaged to

get more detailed information about the deformation in that area. Strain can be estimated using the ISC method described in Section 7.3.

Processing of AFM images

Images acquired by the AFM are in a raw data format and can be processed using the software that accompanies the AFM equipment. Raw images from the AFM are processed to remove scan lines, correct for any tilt or any such noise. Images can be viewed in a 2D format or in 3D. If these images are to be used in different softwares for example digital image correlation (DIC), Microsoft word or powerpoint, they need to be exported in a tiff format using the export option in the AFM software. When exporting images care must be taken to save all the images with same brightness and contrast combinations, especially when using them for analysis using DIC.

VITA

SONY VARGHESE

Candidate for the Degree of

Doctor of Philosophy

Thesis: NEW METHOD FOR ESTIMATING LOCAL STRAINS USING NANOINDENTATION AND ATOMIC FORCE MICROSCOPY

Major Field: Mechanical Engineering

Biographical:

Personal Data: Born in Ranni, Kerala, India, on Jan. 29, 1975, the son of K. V. Varghese and Mariamma Varghese

Education: Received Bachelor of Engineering degree in Mechanical Engineering from Basaveshwar Engineering College, Bagalkot, Karnataka, India, in July 1996. Master of Technology in Materials Engineering from Karnataka Regional Engineering College, Suratkal, Karnataka, India, in July, 1998. Completed the requirements for the degree of Doctor of Philosophy at Oklahoma State University, Stillwater, Oklahoma in July, 2006

Experience: Graduate Research Assistant in Mechanical Engineering Department, Oklahoma State University, Stillwater, Oklahoma